Iron ore deposits in the Eastern Tianshan orogenic belt (China) : the magnetite-skarn-magmatism association

Guangrong Li

UNIVERSITÉ D'ORLÉANS

ÉCOLE DOCTORALE SCIENCES ET TECHNOLOGIES

INSTITUT DES SCIENCES DE LA TERRE D'ORLÉANS

THÈSE présentée par :

Guangrong LI

soutenue le : **5er juillet 2012**
pour obtenir le grade de : **Docteur de l'université d'Orléans**

Discipline/ Spécialité : Sciences de la Terre et de l'Univers

Gisements de fer dans la ceinture orogénique de l'Est Tianshan (Chine):l'Association Magnétite-Skarn-Magmatisme

THÈSE dirigée par :
Luc BARBANSON Maître de conférences, Université d'Orléans - CNRS
Bo WANG Professeur, Nanjing University

RAPPORTEURS :
Alain CHAUVET Chargé de recherche,Université Montpellier 2 - CNRS
Changzhi WU Professeur, Nanjing University

JURY :
Yan CHEN Professeur, Université d'Orleans
Bo WANG Professeur, Nanjing University
Alain CHAUVET Chargé de recherche,Université Montpellier 2 - CNRS
Changzhi WU Professeur, Nanjing University
Luc BARBANSON Maître de conférences, Université d'Orléans - CNRS
Giada IACONO MARZIANO Chargé de recherche, CNRS
Bei XU Professeur, Peking University
Stanislas SIZARET Maître de Conférences, Université d'Orleans

INVITÉS :
Yannick BRANQUET Maître de Conférences, Université d'Orleans

好好学习，天天向上。

----毛泽东 MAO Zedong

(Work harder to survive in the hard environment.)

用出世的精神做入世的事业。

----a Buddhistic saying

（To be earnest to in our pursuit of worthiness in this world, yet embarking on the journey with eyes on the path that life takes us, not the destination.）

心累，就是常常徘徊在坚持和放弃之间，举棋不定。烦恼，就是记性太好，该记的，不该记的都会留在记忆里。

----anonymous

(Tired heart is always hovering between adhering to and giving up, indecisive. Trouble is that memory is good, the mind should not mind will stay in memory.)

This dissertation is dedicated to my wife and my son.

REMERCIEMENTS

Mes premiers remerciements s'adressent tout naturellement à mes directeurs de thèse, Luc Barbanson, Yannick Branquet et Stanislas Sizaret qui m'ont accueilli au sein de leur équipe. Merci infiniment pour votre grande disponibilité, votre enthousiasme ainsi que pour vos précieux conseils qui ont fait progresser ce travail. Cette thèse n'aurait jamais vu le jour sans leur confiance, leur patience et leur sympathie. Ils m'a apporté sa confiance et son expérience de terrain. Au-delà de leurs qualités scientifiques, je les remercie également pour leurs qualités humaines. Je leur exprime donc toute ma gratitude et leur dis mille mercis.

Je souhaite exprimer un merci tout particulier à Yan Chen qui m'a fait bénéficier de ses compétences et de ces précieux conseils. Il m'a initié aux méthodes magnétiques (ASM, paléomagnétisme…) avec beaucoup de gentillesse et de patience, et a toujours été présent lors de mes réunions de thèse pour des discussions scientifiques efficaces, objectives et souvent décisives.

Merci également à Changzhi Wu et Alain Chauvet d'avoir acceptés de rapporter cette thèse.

J'adresse également de profonds remerciements au Professeur Bo Wang, Lianxing Gu et Liangshu shu, qui, malgré la distance, a su insuffler une orientation originale et attractive à cette étude. Son experience de terrain a permis d'élaborer une vision alternative à l'origine d'un débat scientifique permanent et stimulant pour ces quatre années.

Je remercie également toutes les personnes qui ont assuré le côté technique des différentes analyses réalisées au laboratoire, à commencer par les litholamelleurs, Jean-Gabriel Badin et Sylvain Janiec (champion de sections polies doubles faces, dont l'amitié restera ancrée, autant que son caractère revendicatif et son humour décalé) ; Dominique Panis et Philippe Penhoud pour la goniométrie de texture et la diffractométrie des rayons X, ainsi que Olivier Rouer pour le MEB et Giada Iacono Marziano pour le sonde.

De nombreux chercheurs et enseignants-chercheurs de l'ISTO m'ont aidé, par de fructueuses discussions, à avancer dans mes travaux de recherche. Merci à Michel Faure, Romain Augier et Nicole Le Breton. Je n'oublie pas de remercier tous mes collègues présents ou passés, doctorants ou docteurs pour ces quatre années superbes : Nicolas Charles, Flavien Choulet, Boris Sterligov, Ke Chen, Wei Wei, Guangzhong Shi, Pan Zhao, Aurore Dissaux, Emmanuelle Joignaux, Frédéric Delarue, Audrey Gallaud, Paul Turrillot, Gérardo Soto, Julie Machaults, Nicolas Bost, Anaëlle Simonneau, Mathieu Bellanger et Mickaël Laumonier…

Merci aussi à mes amis avec qui j'ai passé de bons moments en dehors et dedans du labo, je pense en premier lieu àNathalie Lottier et Longlong Xie, Hefeng Zhang.

Enfin, de tout mon coeur, je remercie ma famille.

SOMMAIRE

Chapter 1 Skarn and iron oxides ore deposits: the state of art and problems

Résumé:

En se basant sur une étude bibliographique, on donnera dans ce chapitre, d'abord une série de définitions relatives aux "skarns". Le problème des skarns associés à des gisements est ensuite abordé à travers une revue bibliographique portant sur: les assemblages minéralogiques observés, les successions paragénétiques mises en évidence, les zonalités, tant à l'échelle des grains qu'à celle du gisement, les conditions de formations (inclusions fluides, l'apport des paragenèses, les données isotopiques et les études expérimentales).

Une attention particulière est accordée aux skarns à magnétite. Dans cette partie sont présentés des gisements de taille internationale et les deux modèles classiquement invoqués pour expliquer la formation de ce type de gisement. D'un point de vue statistique, ces concentrations sont plutôt associées à des intrusions basiques à ultrabasique, les processus de genèse variant entre deux pôles: un pôle où l'accent est mis sur les fluides exsolvés du magma, un pôle où le rôle des processus intervenant dans la chambre magmatique est soulignés, ces processus pouvant inclure la formation d'un magma immiscible riche en oxyde de fer. Enfin, les relations entre skarns à magnétite et IOCG sont discutées.

Cette thèse concerne les skarns à magnétite du Tianshan oriental. L'évolution géodynamique de cette zone peut être décrite en termes d'accrétion progressive de différents terranes sur la marge sud du block sibérien durant le paléozoïque (Wand et al. 2010, Charvet et al., 2011). Dans cette région, les gisements de fer sont encaissés par: des formations volcano-sédimentaires précambriennes (gisement de Tianshu par

exemple), des formations volcano-sédimentaires carbonifères (gisements de Wutongguo et Tianshu par exemple), des gabbros comme à Cihai et des gabbros à V-Ti-Fe à Weiha. Deux gisements ont été sélectionnés comme objets de nos recherches. Il s'agit des gisements à magnétite de Yamnasu (32Mt à 51%TFe) et de Cihai (23Mt à 45.7% TFe), deux des plus grands gisements de fer de la partie orientale du Tianshan (Yu et al. 1999; Mao et al. 2005).

L'objectif de l'étude de ces deux gisements est: (1) d'apporter notre contribution à la compréhension de la formation de ce type de concentration et (2) de préciser les relations entre ces minéralisations et l'évolution géodynamique du Tianshan.

Abstract:

Skarn have been scientifically recognized as a distinct class of rock for more than 100 years, however, the definition of skarn is loose. Recently, mineralogy was proposed to be the key to define a skarn: a mineral assemblage including a wide variety of calc-silicate and associated minerals, but is usually dominated by garnet and pyroxene; it was form in almost all age and variety of tectonic setting. This pure "descriptive" definition is not genetic and does not account for processes as "metasomatism" or "replacement". As for the genetic aspect, diverse models have been proposed: from a general dictionary definition of contact metamorphic-metasomatic interactions with intruding granitic magma in early times to interactions with mafic-ultramafic magma and high temperature magmatic skarn in recent years. It seems that genetic geological domain of skarn could be controversial and is also expanding with time. Melt inclusion in skarn minerals and assimilation experiments studies provides new research insight on the skarn. Skarn-related iron deposits are of largest types among the others, which may reach 5000Mt with grade 45%. Skarn-related iron deposits mostly associated with mafic-ultramafic magmatism, alkaline alteration extensively developed, and were low in contain of Au comparing to IOCG. These deposits of Precambrian age are rare. This chapter also summarizes some features of skarn-related iron deposit which promote our understanding of different iron ore deposits.

1.1 General definitions

Meinert et al. (1992, 2005) and Pirajno (2009) explicitly indicated that skarn can form during regional or contact metamorphism. In addition, skarn and metasomatic rocks share similar features (Barton et al., 1991). Therefore, although metamorphism, metasomatism and skarnization present overlapping concepts, it seems necessary to defined precisely each concepts to avoid any confusion in the following chapters of this memoir.

1.1.1 Metamorphic rocks

The terms metamorphic rocks and metamorphism were first used by Boue in 1820, and they were defined and systematically improved by Lyell in 1833 in Callegari and Pertsev (2007). Metamorphism leads to the forming of metamorphic rocks. The metamorphism is defined as the solid-state mineralogical/textural/chemical transformations of pre-existing rocks undergoing variations of physical and chemical conditions such as temperature, pressure, and active fluid flows. Mineralogical and textural changes occurring just beneath Earth's surface due to weathering and/or diagenesis are not referred as metamorphism (Vernon and Clarke, 2008; Bucher and Grapes, 2011). Three types of metamorphism are distinguished: (1) the regional metamorphism (i.e. Barrovian metamorphism) during mountain building; (2) the contact metamorphism owing to thermal anomaly often related to magma intrusion; (3) the dynamic metamorphism mainly resulting from mechanical deformation associated with short duration and overprinting processes. Metamorphism which characterized by increasing pressure and temperature conditions is known as prograde metamorphism. Conversely, decreasing temperatures and pressure call retrograde metamorphism. The lower temperature limit of metamorphism is considered to be between 100-200°C; the upper limit temperature is about 900°C (Bucher and Grapes, 2011). Migmatites are thought to be formed at or near this upper limit, which contain pods and veins of the protoliths

that has started to melt but has not fully segregated from the refractory residues (Ashworth, 1985; Vielzeuf and Holloway, 1988). If exceed this upper limit, it become magmatism. Recrystallization or occurrences of metamorphic minerals which originally not present in a rock are important criterions of metamorphism. The new mineral assemblages grow at the expense of old ones. Involved processes could be subdivided into: coarsening, neocrystallization, metasomatism, anatexis and deformation (Derrill and Kerrick, 1991).

For metamorphism types, the new mineral assemblages mostly depend on the chemical composition of the protloliths. This is particularly well-expressed during contact metamorphism. For example, within siliceous wall rocks as sandstones and shales, anhydrous minerals such as andalousite growths close to the intrusion with associated hydrated minerals such as biotite, amphibole, epidote, chlorite. Within carbonated host rocks as limestones or dolostones, a calc-silicate "skarn" paragenesis (e.g. garnet, Ca-pyroxene) and oxides (e.g. periclase) may form resulting from carbonate-silica reactions. This process includes an early anhydrous stage (generally prograde) followed by a later hydrous stage (retrograde).

Among the three types of metamorphism, contact metamorphism seems to initially associate with skarn. Contact and regional metamorphism have traditionally been separated according to scale and the spatial relationship to intrusive heat sources (Fig. 1-1A). Rather than pressure, temperature anomaly, protolith chemistry and magma composition are the key controls in contact metamorphic rocks forming (also called thermo-metamorphic rocks). It typically occurs around magmatic intrusions due to the strong thermal gradient between the hot intrusion and the cooler wall rocks. As the result, a metamorphic aureole forms sometimes associated with deformation. From a broad point of view, the heat of the intrusive, its dimension, and the temperature difference with the wall rocks control the size of metamorphic aureole. Dykes generally have small aureoles whereas large ultramafic intrusions can have significantly thick and well-zoned contact metamorphic aureole.

During emplacement of the intrusion, fluids of different origins may also contribute to the metamorphic reactions. In that case, the chemical system is potentially open, and metamorphism might not be isochemical (i.e. allochemical metamorphism). This can significantly modify the geochemistry of the affected rocks including the pluton and the wall rocks. In this case, the metamorphism might be partially achieved through metasomatism. If the intruded rock is rich in $CaCO_3$, skarnization is expected (see details below). Rocks issues from contact metamorphism include hornfels, quartzite, marble and skarn, indicating a relative high temperature and low pressure metamorphic facies (Fig. 1-1B).

A

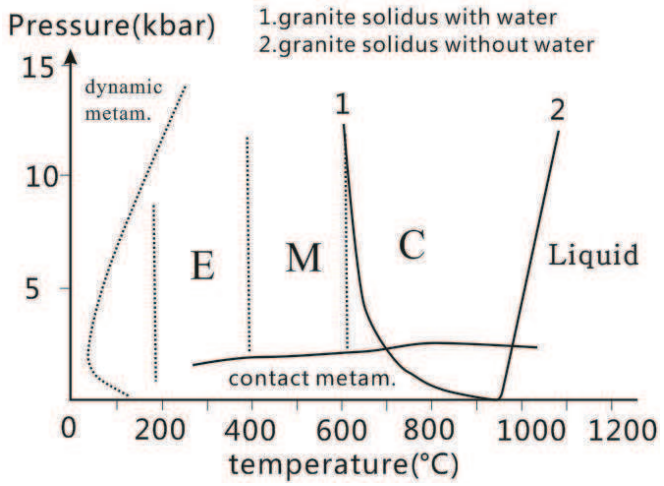

B

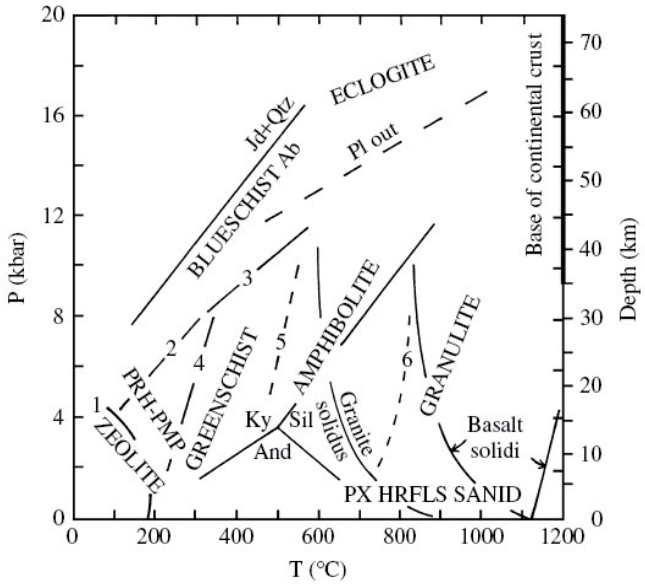

Fig. 1-1: Temperature-pressure bivariate diagrams.
(A) Diagram displaying contact metamorphism is characterized by low pressure. E=epithermal zone, M=mesothermal zone, C=high temperature contact zone; (B) Schematic representation of metamorphic facies (Best, 2003).

In (B), P–T boundaries between facies are not precisely defined as shown by the fact that some reaction lines pass through a facies field and because reactions involving solid solutions are smeared over a range of P and T, rather than being a univariant reaction line as for end-member compositions. “Pl out” line indicates maximum P stability of plagioclase in mafic rocks. Numbers on curves refer to following reactions, where reactant phases on left are stable at lower T:

1. Analcite + quartz=albite + H_2O
2. 2lawsonite + 5glaucophane= tremolite + 10albite + 2chlorite
3. 6tremolite + 50albite + 9chlorite=25glaucophane + 6zoisite + 7quartz + 14H_2O.
Also 13albite + 3chlorit + quartz=5glaucophane + 3paragonite + 4H_2O
4. 25pumpellyite + 2chlorite + 29quartz=7tremolite + 43zoisite + 67H_2O
5. 4chlorite + 18zoisite + 21quartz=5Al-amphibole + 26anorthite + 20H_2O.
Also 7chlorite + 13tremolite + 12zoisite + 14quartz=25Al-amphibole + 22H_2O.
Also albite + tremolite=Al-amphibole + quartz (approximate reaction)
6. Hornblende=clinopyroxene + orthopyroxene + Ca-plagioclase + H_2O (approximate reaction).

1.1.2 Metasomatic rocks

The metasomatism is an allochemical metamorphism during which composition of rocks is modified through reactions implying cationic exchanges between host rocks and external chemical fluxes. The resulting texture and mineralogical composition are generally very different from the protolith, with exception of some preserved "ghost textures". One major characteristic of metasomatites is that replacement and mineral changes are pervasive (i.e. at the grain-scale of matrix). It is noteworthy that, for many authors, "metasomatism" is only used when a monomineralic rocks is formed (e.g. albitites, phlogopitites, tourmalinites, serpentinites…) (Zharikov et al., web version 01.02.07).

Two end-member processes for metasomatic transfer are distinguished: (1) the diffusion-based metasomatism is driven by differences in chemical potential and promoted by high temperatures and prolonged times. Ionic diffusion through solid mineral phases is a slow process and thus required long-lived favourable conditions; (2) fluid advection-based metasomatism (i.e. infiltration metasomatism) is very widespread in upper crust plutonic environment (contact metamorphism), where circulation of external and magmatic fluids is promoted by high permeability. This advective metasomatism is also called "hydrothermal metamorphism" and corresponds in many studies to the "hydrothermal alteration" described along fluids drains (faults, veins etc⋯).

Consequently, relatively to regional metamorphism, metasomatism is spatially restricted to small area or rock volumes without being restricted to contact metamorphism. Skarn was thought to be one member of the metasomatic family (Fig. 1-2).

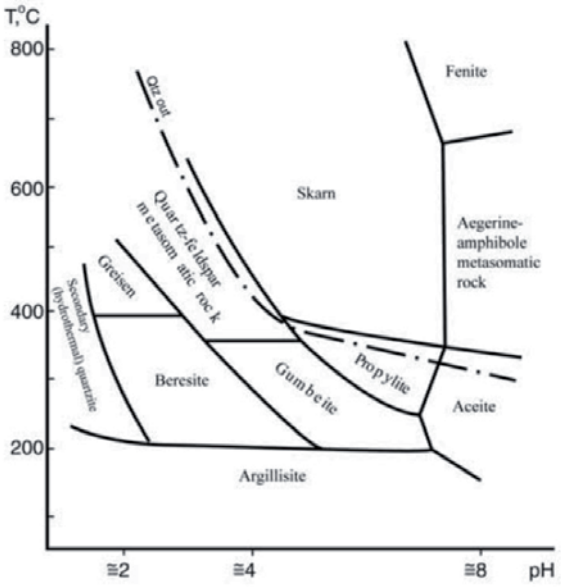

Fig. 1-2: Diagram illustrating the general T-qualitative pH fields of the metasomatic families. The dot-dash line separates acidic and neutral-alkaline families (with and without quartz) (Zharikov et al., web version 01.02.07).

1.1.3 Skarn

The word “skarn” was firstly used by the miner of centre Sweden, to describe coarse green calc silicate rocks (Ca-rich garnet, pyroxene, amphibole and epidote) which accompanied the ore. Skarn have been scientifically recognized as a distinct class of rock for more than 100 years (Burt, 1982) and thousands of scientific papers are related to those peculiar and sometimes “spectacular” rocks. However, the definition of skarn is loose. In the most recent reviews of skarn, Meinert et al. (2005) proposed that the characteristic mineral assemblage is the key to define a skarn: a mineral assemblage including a wide variety of calc-silicate and associated minerals, but is usually dominated by garnet and pyroxene; it was form in almost all age and variety of tectonic setting. This pure “descriptive” definition is not genetic and does not account for processes as “metasomatism” or “replacement”.

Another review (Ray and Webster, 1991) gives a more explicit definition: the term skarn describes coarse-grain calcium or magnesium silicate alteration, commonly

rich in Fe, Al, and possibly Mn, formed at relatively high temperatures by the replacement of original, often carbonate-rich rocks. Thus, these authors introduce the replacement process (i.e. “the skarnization”) into their definition of skarn.

Finally, a general dictionary definition of skarn is: skarn is a coarse-grained contact metamorphic-metasomatic rock developed within magnesian limestone/dolostone host rocks and resulting from interactions with intruding granitic magma. The modified carbonate-rich host rocks are called exoskarn, the modified granite is named endoskarn (Foucault and Raoult, 2001). These assumption and definition are supported by numerous studies, including experimental works (Liang, 2000) and field observations (Meinert, 1992).

Those three definitions among others show that the concept of skarn can be controversial and is also expanding with time. For example, in the earliest time, skarn was thought to be only caused by granitic magmas (causing excess of Si and Al); nowadays we know that skarn might develop around mafic and ultramafic intrusions (e.g. Ganino et al. 2008).

Currently, it is generally admitted that mineralogy or mineral assemblage defines a rock as skarn, without genetic information. The most common skarn minerals include Ca-pyroxene, garnet, forsterite, calcite, wollastonite, idocrase, actinolite, magnetite, chlorite and epidote, as well as some accessory minerals, such as: tourmaline, beryl, topaz, corundum, fluorite, apatite, barite, strontianite, tantalite… which concentrates incompatible elements in a siliceous aqueous environment. Usually, feldspathoids and rare calc-silicates (such as scapolite) are found.

Although Liang (2000), basing on more then 6000 experimental studies, explicitly indicated that skarn is a metasomatic rock, rather than a metamorphic rock; in addition, Zharikov et al (2003) devoted the skarn was one member of the metasomatic family. In the book of “Igneous and metamorphic petrology”, Best

(2003) also address similar opinion: “skarn is a metasomatic calc-silicate rock”. The following section summarizes precisely and illustrates the major key-points and concepts dealing with skarns after Meinert et al. (1992, 2005), Einaudi (1981) and Ray and Webster (1991).

Classically, four types of skarn are distinguished relatively to the role of fluid advection (Fig. 1-3) (Meinert et al., 2005) which expands the concept of skarn, but in certain sense, they make the “skarn” chaos:

(i) Calc-silicate hornfels is a fine-grained metamorphic rock containing a high percentage of calc-silicate minerals and resulted from metamorphism of impure carbonate, such as silty limestone or calcareous shale. Hornfels are aphanitic to fine phaneritic, granoblastic product of thermal metamorphism in contact metamorphic aureoles. Relict bedding may be present. Common pelitic hornfels may contain poikiloblastic cordierite and/or andalusite. They are generally dark brown to black, tough, and may have conchoidal fracture if the texture is aphanitic. This type represents the “diffusion-based” end member, with very poorly-expressed fluid percolations.

(ii) Reaction skarn or bi-metasomatism is also a metamorphic rock which is formed from large scale isochemical metamorphism of thinly interlayered shale and carbonate units. These units transfer at small layer scale elements between them to form skarn (Vidale, 1969; Zarayskiy et al., 1987). Whether the metasomatism is diffusion-based or advective (fluid-assisted) is not evident to establish in many cases. Ray and Webster (1991) indicated that skarns issue form regional metamorphism could ascribe to this reaction skarn type.

(iii) “Skarnoid” is a descriptive term to qualify a fine-grained and iron-poor calc-silicated rock, which thus appears genetically intermediate between “diffusion-dominant” calc-silicated hornfels and “fluid advection-dominant” or percolation skarn (Zharikov, 1970). According to Meinert et al. (2005), it seems that skarnoid is the result of fluid flows. However, protolith chemistry

and textures are still controlling in part the skarnization. The mineral assemblage is relative simple which is mostly composed by garnet and pyroxene lacking hydrous minerals. Some researchers classify the vein-like skarn into this “skarnoïd” type.

(iv) The coarsed-grained skarns are supposed to represent the fluid advection-based type end member (i.e. “pure metasomatic skarn”). Nevertheless, this assumption is a first order approximation which has to be carefully applied: crystal growth laws are complex and does not only depend on mass equation of cations within fluids.

In recent 30 years, some researchers devoted to extremely high temperature skarn which was largely supported by melt inclusion in the skarn minerals (Lin and Xu, 1989; Wu and Chang, 1998; Fulignati et al., 2000; Fulignati et al., 2001; Zhao et al., 2003; Zhao et al., 2003; Gaeta et al., 2009). These studies displayed that the skarn probably formed at about 1000°C (Zhao et al., 2003).

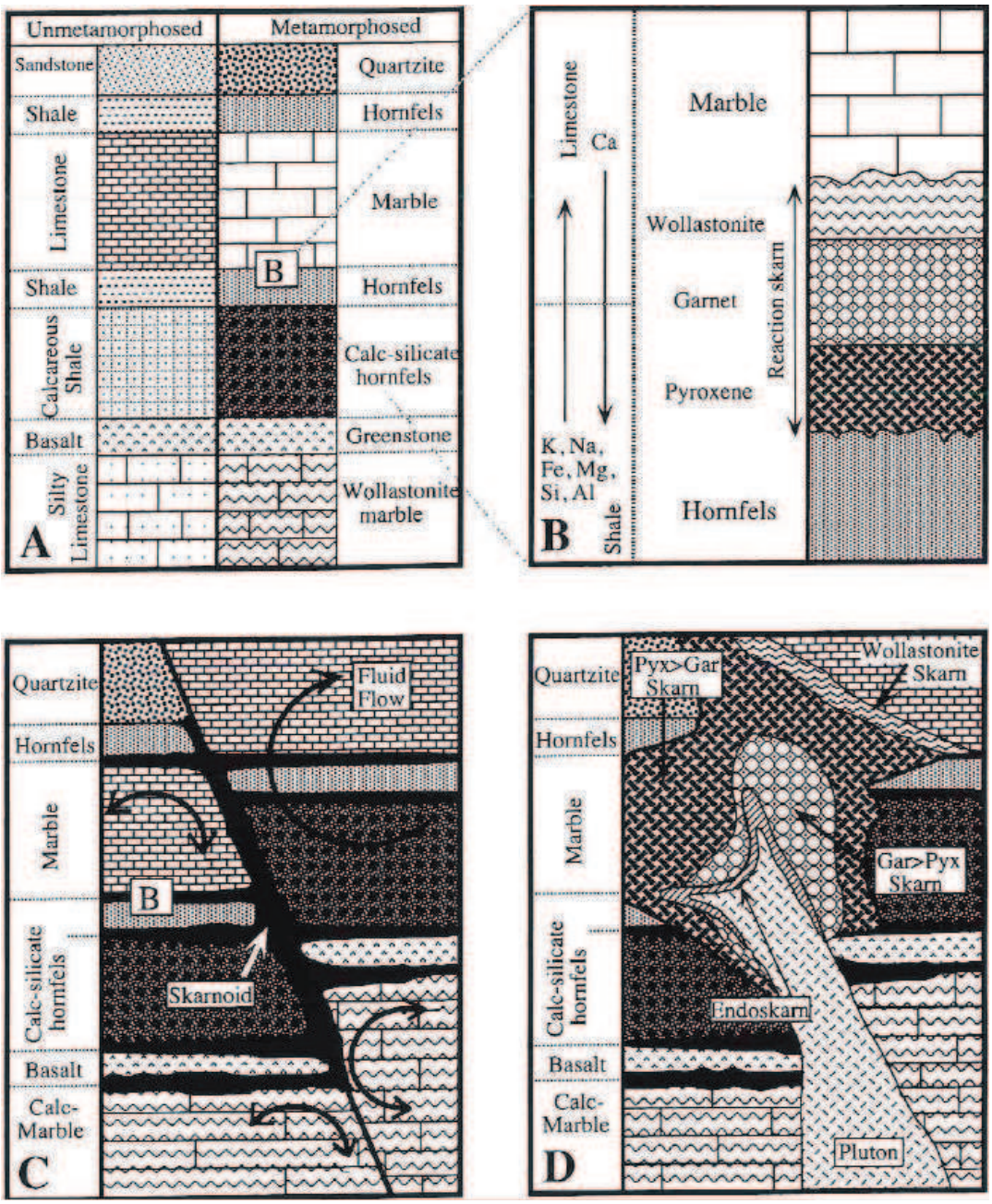

Fig. 1-3: Types of skarn formation (Meinert et al., 2005): (A) Isochemical metamorphism involves recrystallization and changes in mineral stability without significant mass transfer. (B) Reaction skarn results from metamorphism of interlayered lithologies, such as shale and limestone, with mass transfer between layers on a small scale (bimetasomatism), (C) Skarnoid results from metamorphism of impure lithologies with some mass transfer by small scale fluid movement. (D) The fluid-controlled metasomatic skarn typically is coarser grained and does not as closely reflect the composition or texture of the immediately surrounding rocks.

1.1.4 Skarn-related ore deposits (SROD)

The “skarnization” processes are often associated with economic metal deposition and concentration. In such cases these deposits are grouped into skarn deposits (Einaudi et al., 1981; Meinert et al., 2005). The term “skarn deposits” used by theses authors is ambiguous because mineralization is not necessary genetically and/or temporary linked with the skarnization processes. As “intrusion-related gold deposits” has been defined by Thompson et al. (1999), in the following sections of this manuscript the term “skarn-related ore deposit” (SROD) will be used to characterize an ore deposit associated, at least spatially, with a skarn.

SROD are widespread over the world and constitute important reserves in Fe, W, Pb/Zn, Cu, Au, Mo and Sn. Some skarn are caused by porphyry, which leaded Jebrak and Marcoux (2008) classified part of the so-call porphyry deposits into skarn. Pirajno (2009) also indicated that in the lower Yangtz area of South-East Chine, skarn-type deposits and porphyry deposits were initiallly linked. Tonnage and grade relations in porphyry and non porphyry environment for Au, Cu-Au and Pb-Zn-Au of world class deposits of SROD are listed (Fig. 1-4). Most skarn deposits are associated with intrusions, but distal skarn/skarnoid–related ore deposits are found spatially disconnected from plutons or intrusions. To classify or to establish a typology of SROD is not easy and not unequivocal because too many parameters interact (substance, depth of deposition, telescoping with porphyries etc…). The different metals found in skarn deposits are a product of the different composition of the protoliths, oxidation state, etc…According to Zhao et al. (1990), reserves of 25% iron, 50% W, 30% Pb-Zn, 100% phlogopite, and 100% vermiculite of the world would be contributed by skarn-related deposits. Skarn deposits are also important sources for the non-metallic elements and minerals, such as: tourmaline, phlogopite, diopside, wollastonite, tremolite etc..

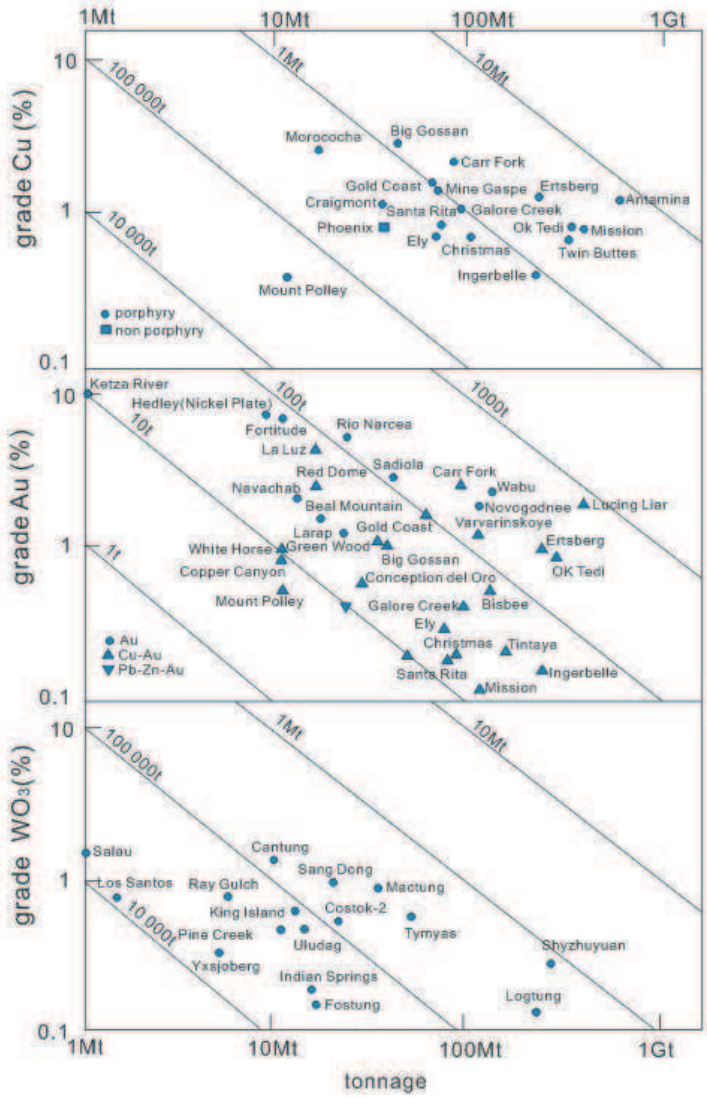

Fig. 1-4: Major skarn-type deposits in the world (Jebrak and Marcoux, 2008).

1.2 Skarns: from objects to processes

The objects of skarn could include country rocks (wall rocks), skarn, pluton, mineral assemblage, ore, fluid, zonation etc. In this section, we present major characteristics of skarn, not always related to ore forming processes. However, some data presented here come from skarn-related ore deposits (those objects receiving peculiar intention in regard of economic interests). Specific points on skarn-related ore deposits are detailed in section 1.3.

1.2.1 Wall rocks

The country sedimentary rocks of skarn could be composed of mainly limestone, dolostone, limestone-dolomite, marl, tuff, sandstone, siltstone, schist, gneiss etc. The empirical statistics show that when the MgO content is less than 2% in the carbonate rocks, only calcic skarn may be formed, which is exemplified by the majority of skarn deposits in China; when the MgO content is higher than 10-15%, will occur more typical magnesian skarn mineral assemblages such as forsterite, diopside, spinel, humite family and phlogopite; when the MgO content is about 2-10%, mainly diopside and phlogopite are developed with very little Mg-rich minerals (Zhao et al., 1990; Liang and Qiao, 1991; Liang, 2000).

The plutons are not always presenting in or nearby the skarn, however, plutons varied from mafic-ultramafic rocks to high fractional magma.

1.2.2 Mineralogy: paragenesis, evolution and mineral zonation

1.2.2.1 Mineral paragenetic evolution

Due to the strong temperature gradients from the magmatic intrusions or hot reative fluid toward the sediment wall rock and large fluid circulation cells caused by intrusion of magma intruding, many skarn deposits have zonations (Bowers et al., 1990). Mostly skarn displayed zonation that garnet-pyroxene and vesuvianite-(chlorite) assemblage close and far from the heat source, respectively. This zonation is characterized by mineral assemblage which evolves in different stage during the skarnization. Durand (2006) did a synthesis of the major mineral phases encountered within skarn systems caused by granitic intrusions (Fig. 1-5). As we can see on this figure, skarn is characterized by an extreme mineralogical variety, with a dominance of calc-silicated minerals. And, it seems that from the pluton into the limestone wall rock, zonation generally could be recognized. Garnet-pyroxene anhydrous minerals dominantly occur in the early and close to the pluton. For the

garnet, it occurred preferably in the exoskarn side; whereas the K-feldspar alteration occurred in the endoskarn side. The epidote-chlorite-sulphide presents in the distal and later.

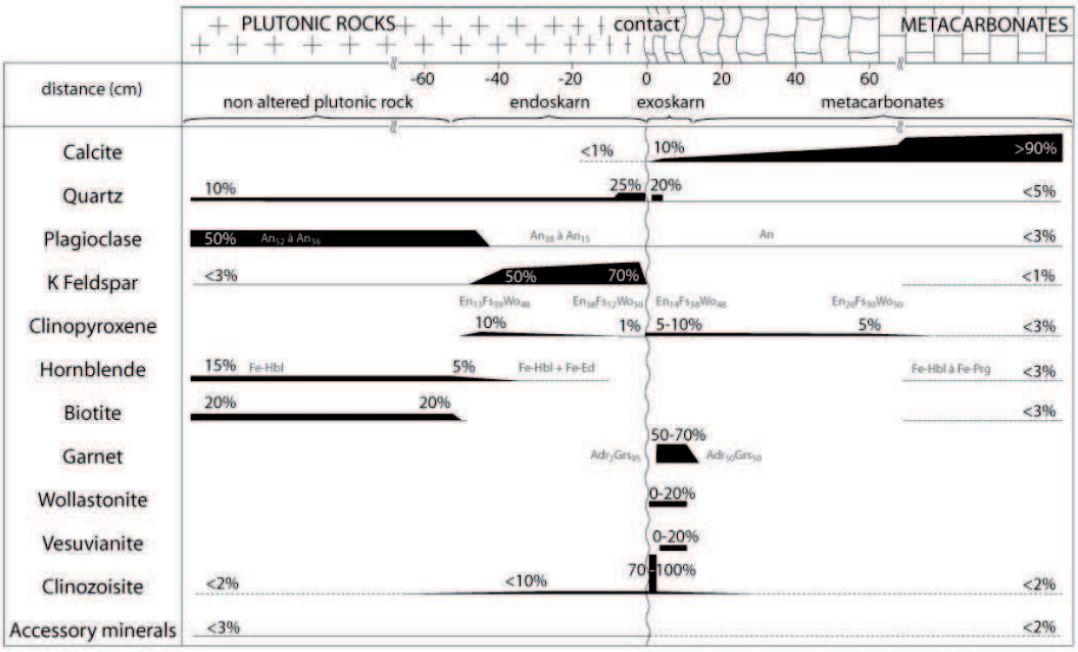

Fig. 1-5: Synthese of mineral evolution along the zones of contact between granodiorites and carbonates (Durand, 2006). This trend is valid for 90% of the contact zones between the observable silicate intrusives and septa metacarbonates pure marble massif of Quérigut. Accessory minerals are represented by sphene, apatite, allanite and / or muscovite. Under the figure, list of different minerals encountered in skarns is companied.

In addition, zonations composed by ore minerals also occurred, such as the Fe-Cu-Zn-Pb skarn in the Ocna de Fier-Dognecea orefield: it showed Fe zone, Fe-Cu zone and Zn-Pb zone with increase distance from the intrusion (Ciobanu and Cook, 2004).

1.2.2.2 Mineral zonation

Mineralogical zonation pattern is very common in skarn minerals of which garnet and pyroxene are in proximal, as well as epidote, tourmaline etc. Currently, there are three popular hypotheses for their forming.

Firstly, it was caused by diffusion. According to the diffusion theory, they may be interpreted in terms of the cooling rate of the system, in particular the partitioning of Fe and Mg in garnet/pyroxene. The partitioning has been recognized as geologically relevant for long time. A number of studies have applied this method to determine cooling histories of metamorphic terrains (Ehlers et al., 1994; Ito and Ganguly, 2006; Brady and Cherniak, 2010). This was first described by a seminal work of Dodson (Dodson, 1973) and has since been popularized by Lasaga (Lasaga, 1983). However, many geologists typically measure chemical zoning profiles of single mineral by analyzing minerals thin sections using the electron microprobe. Their work probably increases the uncertainty of cooling rate by the sectioning effect (Robl et al., 2007).

Secondly, the zonation is controlled by the hydrothermal ambient (Jamtveit et al., 1993; Jamtveit and Hervig, 1994). It means the compositional change in a single grain would synchronize with the ambient. It probably provides a continuous record of the geochemical evolution of the hydrothermal system in which they form and helps to delimit the range of external vs. internal controls of the fluid composition. In 1993, Jamteit et al. (1993) published their widely cited paper to show zoned garnet formed in hydrothermal system (Fig. 1-6A and B).

Thirdly, dissolve-reprecipitation model. Because of some mineral elements in which the diffusion rate is very slow and can not re-equilibrium in the geological conditions. A typical example is plagioclase. It has two immiscible end members: An and Ab. If X_{An} diffuse, it requires the exchange of Al and Si in the tetrahedron. It is a very slow process. The X_{An} zonation could not be caused by diffusion, but probably dissolve-reprecipitation process. Garnet and plagioclase are commonly rich in Ca. From Fig. 1-6C, Ca distributions show smooth decreases toward garnet rims, whereas it increases in plagioclase from cores to rims. It indicates that released Ca from garnets precipice into the plagioclase during the retrograde metamorphism (Kohn et al., 2001).

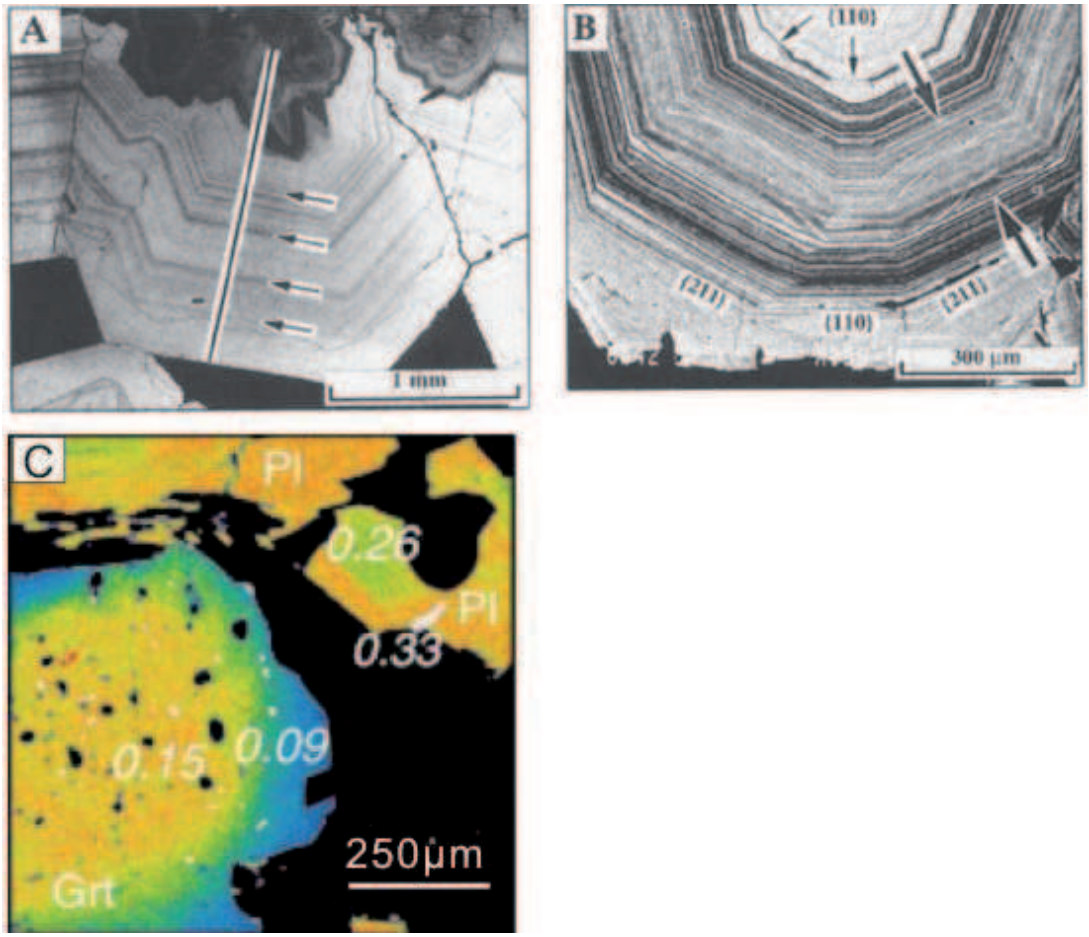

Fig. 1-6: (A) Back scattered electron (BSE) image showing andradite-rich garnet (light) growing epitaxially on preexisting more grossular-rich core (dark). Garnet grew into void that was later filled by quartz. Oscillatory zonation seen in andradite-rich rim reflects different relative proportions of major components andradite and grossular. Major and trace element line scans were obtained along the bar (~1800 µm), arrows indicate major changes in trace element (Jamtveit et al., 1993). (B) BSE image of zoned andradite-rich garnet (diameter ~1.5mm) that shows increasing development of dodecahedral {110} faces. Dissolution structures on {211} surfaces are most clearly seen in region between large arrows (Jamtveit et al., 1993). (C) Ca content map of garnet and plagioclase from gneiss. Warmer color indicates higher content. Pl=plagioclase, Grt=garnet. Numbers refer to mole fractions Xgrossular, and Xanorthite.(Kohn et al., 2001).

1.2.3 Mass transfer

During the infiltrative skarn formation, mass transfer is bound to occur both in the carbonate and pluton side. Study on the Santa Rita stock and related skarn (Ague and van Haren, 1996) showed (Fig. 1-7A) that the Fe, S, Si, Al, Mg, K, H^+ and Na

immigrate from the pluton to the limestone, whereas the Ca and CO_2 immigrate inversely. Research done in the granitoids in Querigut massif companied by isotopes study show similar result but chemical mass transfer seems to be restricted to a few centimeters in the K-feldspar rich zone (Fig. 1-7B) (Durand, 2006; Durand et al., 2009). Some study showed that the assumption of constant volume (Lindgren's law) is not entirely justified; net mass changes, however, are generally small except in the most proximal endoskarn and exoskarn, although this depends a lot on the nature of the infiltrative magmatic system (Lentz, 2005). Lentz (2005) also suggested that the infiltrative decarbonation front enhanced by the dissolution of excess carbonates by carbonic acid generated by the skarn reactions, as well as the acidity (HCl) of the magmatically-dominated hydrothermal fluid.

A

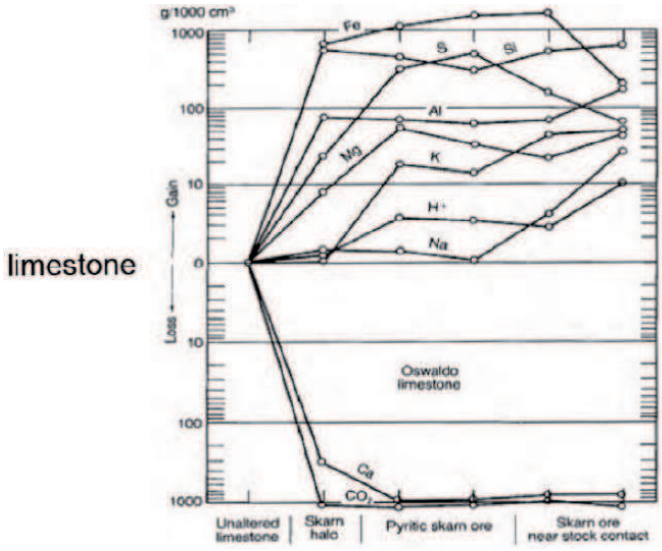

B

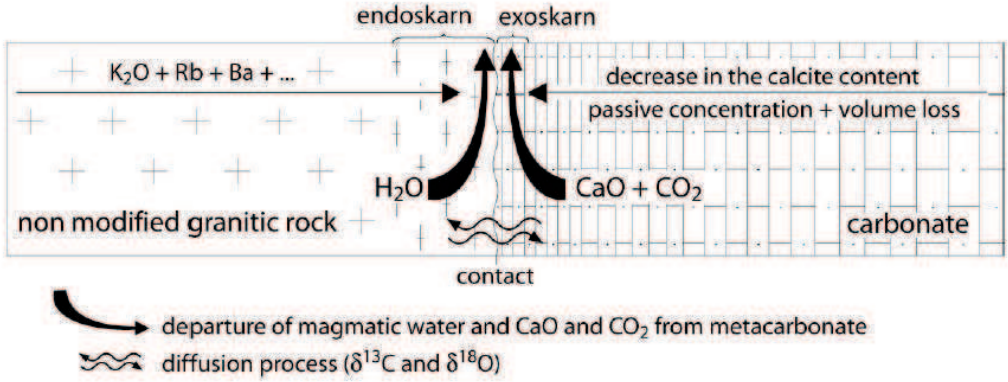

Fig. 1-7: (A) gain and loss of elements from the Oswaldo limestone, Santa rita stock; (B) schema showing the elements immigrate direction (Ague and van Haren, 1996; Durand, 2006; Durand et al., 2009).

1.2.4 Skarn forming conditions

1.2.4.1 Temperature

Skarn forming temperature was mainly derived from mineral stability experiments and fluid inclusion studies. Some mineral thermomters are useful, such as chlorite (Cathelineau and Nieva, 1985; Cathelineau, 1988; Vidal et al., 2005). The

low-temperature stability of andradite was a function of temperature, X_{CO_2}, and fO_2. Experimental results indicated that the reaction

3quartz + 3calcite + (1/4)hematite + (1/2)magnetite + (1/8)O_2 = andradite + 3CO_2

occurs at: T=550°C at X_{CO_2}=0.22 (Fig. 1-8).

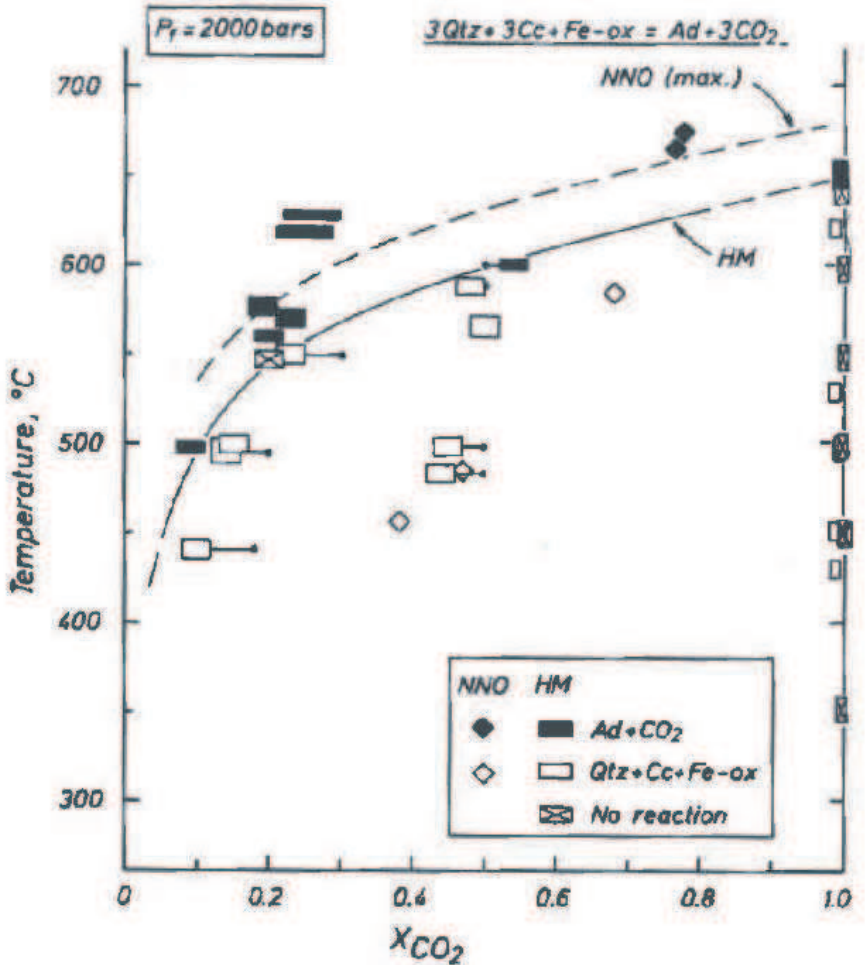

Fig. 1-8: Experimentally determined T- X_{CO_2} diagram for the reaction: 3quartz+3calcite+(1/4)hematite+(1/2)magnetite+(1/8)O_2=andradite+3CO_2.

The magnitude of experimental error is indicated by the size of the rectangles (HM buffer only). The initial X_{CO_2} in the experimental fluid (dots) and direction and magnitude of shift in fluid composition due to crystallization of calcite (indicated by bars) are shown for runs in which a change in fluid composition was detected after the run. Diamond-shape symbols are reconnaissance run data of Gustafson (Gustafson, 1972). The dashed line indicates the maximum possible temperature for the reaction with oxygen fugacity determined by the NNO buffer (Taylor and Liou, 1978).

Wollastonite often occurs as a result of the reaction of quartz and calcite in metamorphosed limestone. Harker and Tuttle (1956) [recited from (Deer et al., 1982)] conducted experiments, for the reaction $CaCO_3+SiO_2 \leftrightarrow CaSiO_3+CO_2$, indicating that at atmospheric pressure the reaction takes place at, or slightly below, 400°C. The tendency seems to be that lower the pressure, the lower the temperature of the formation.

Inclusions in skarn minerals reflect the physical-chemical nature of the solutions present during the skarn-forming process. Homogenization temperature of inclusions in skarn minerals displayed a wide range: from about 1000°C to 200°C. It should note that even for the same process of skarnization, different stages have different temperatures. The upper temperature limit was mainly supported by melt inclusions in the skarn minerals (Fulignati et al., 2000; Fulignati et al., 2001; Lu et al., 2003; Zhao et al., 2003; Iacono Marziano et al., 2007; Yang et al., 2009; Maher, 2010; Soloviev, 2011).

1.2.4.1.1 Homogenization temperature of fluid inclusions

Fluid inclusion studies are mainly on the minerals which contain numerous of fluid inclusions and are relative transparent, such as quartz, carbonate and fluorite. Most high temperature skarn minerals such as forsterite, garnet, diopside, etc. are unlikely to trap later low temperature fluids without visible evidence of alteration (Meinert, 1992). Thus, fluid inclusions in skarn minerals provide a relatively unambiguous opportunity to measure temperature, pressure, and composition of skarn-forming fluids. Fluid inclusion studies displayed that the homogenization of fluid inclusions of ore skarn solutions have much higher $CaCl_2$ contents and usually very high formation temperatures (>500°C); temperatures generally decrease away from the solution source, both in time and distance; the gradients found at greater distances from the source in distal (far from contact) skarns tend to be less (e.g. 210–350°C) for a particular skarn stage to that in proximal (near contact) skarns (e.g. 400–650°C)

(Kwak, 1986); temperatures also tend to decrease with time, which is reflected by the superimposition of various overprinting, retrograde mineral stages.

1.2.4.1.2 Homogenization temperature of melt inclusions

In recent 30 years, some researchers devoted to high temperature skarns (Lin and Xu, 1989; Wu and Chang, 1998; Fulignati et al., 2000; Fulignati et al., 2001; Zhao et al., 2003; Zhao et al., 2003; Gaeta et al., 2009). It is strongly supported by melt inclusion research (Fulignati et al., 2001; Zhao et al., 2003; Zhao et al., 2003). Melt inclusions in skarn minerals could hold silicate glass and non-silicate, vapor-bearing globules (Fig. 1-9) (Fulignati et al., 2001; Zhao et al., 2003; Zhao et al., 2003). Melt inclusions were thought to represent silicate melts at the time of skarn formation in magma (Zhang and Ling, 1993; Zhao et al., 2003). Therefore, some researchers believed that the skarn could be form directly by magmatic crystallization (Lin and Xu, 1989; Wu and Chang, 1998). Skarn rocks which are component of tephra ejected by Vesuvius were studied by Fulignati et al. (2000). Fulignati et al. (2000) found that skarn formed at temperatures of about 800~1000°C which leading them to concluded these rocks record in-situ endoskarn genesis at the interface between magma and carbonate rocks.

A B

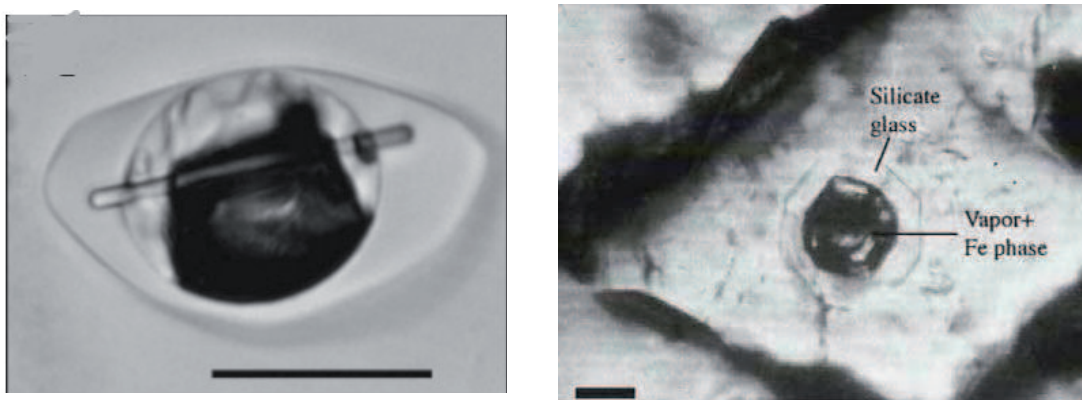

Fig. 1-9: Melt inclusions in skarn minerals. (A)Inclusion from endoskarn with variable proportions of silicate glass and nonsilicate, vapor-bearing globules (Fulignati et al., 2001). (B) Melt inclusion in garnet from Tonguanshan, China Fe-Cu skarn (Zhao et al., 2003) (recited from Meinert 2005). All scale bars are 20 μ m .

The melt inclusions could vary in shape (Zhao et al. 2003). They mainly consist of crystallized silicate phases (C_{Si}), iron phases (Fe), amorphous silicate phases (A_{Si}) and vapor (V) with different volume percentages, and some of them contain several crystallized silicate phases (Zhao et al., 2003). The sizes are commonly (10--46)*(6--15) μm^2 with homogenization temperatures ranging from 745-1115°C in the Yangtze district, China. The high homogenization temperatures lead Zhao et al. (2003) to conclude to the magmatic origin of these skarns.

1.2.4.2 Pressure

Skarn size, geometry, and style of alteration probably associated with their forming pressure. Because the pressure controls the fO_2, pH, X_{CO_2}, as well as decomposition of calcite and formation of skarn minerals. In the relative shallow environment, some fracture would be observed, however, most early skarn minerals are altered by later minerals during retrograde alteration. In a deep skarn environment, rocks will tend to deform in a ductile manner rather than fracture. Generally, the following structures may help to tell the relatively shallow and deep environments: chilled margins, porphyry groundmass grain size, mineral assemblage, deformation, pluton morphology, and brecciation and brittle fracture etc. Most research results showed that skarns form at depth of 1~4.5km, basing on mineral equilibria, fluid inclusion, as well as texture study (Hames et al., 1989; Anovitz and Essene, 1990; Ciobanu and Cook, 2004; Soloviev, 2011). In this ambient, calcite would decompose into CaO and CO_2 (Einaudi et al., 1981).

Some skarn may form at the depth exceed 5-10km (Taylor, 1976; Nicolescu and Cornell, 1999). In Italy, it seems that some deep buried limestone and dolostone in the sedimentary basement (more than 5km in depth) (Iacono Marziano et al., 2007) make the skarnization possible in high pressure and high temperature.

At a depth of 12 km with ambient temperatures around 400°C, skarn may not totally cool below

garnet and pyroxene stability without subsequent uplift or other tectonic changes, but it could happen. So, if the depth exceeds 12 km, even garnet and pyroxene were birthed through skarnization, these skarn minerals may not be stable. In such deepness, it seems to be rather a CaO-rich silicate melt environment, just as described by Gaeta et al. (2009). When the pressure decreases, Ca silicate melt could crystallize garnet and pyroxene. For example, the Nevoria gold skarn deposit in southern Cross Greenstone Belt, Western Australia was reported to be formed in middle crust, about 11-14km (Mueller et al., 2004).

1.2.4.3 Chemical conditions

1.2.4.3.1 Volatiles

Much discussion has been made indicating the participation of volatile components, such as F, Cl, B and H_2O (Zhao et al., 1984; E.T.C, 1993; Aksyuk, 2000). These components are very active factors in rock and ore forming process. They are also called “mineralizing agent”. They are important during the metal concentration. Most of the volatile component rich minerals (scapolit, chlorine/fluorine amphibole, phlogopite, vesuianite, chlorite, epidote, tourmaline etc.) are formed at the late stage of skarn forming. Even for the same kind of volatile-containing mineral, the volatile content could be different according to different deposits.

1.2.4.3.2 Salinity

Fluid inclusions distribute in all skarn minerals. Measurement of fluid inclusion may provide relatively unambiguous mineral forming temperatures, composition, as well as salinity (Hames et al., 1989; Lu et al., 2003; Soloviev, 2011). The salinities of ore containing fluids are rather high, ranging from 35 to 60 wt% NaCl equivalent in the early mineralization stage (Meinert, 1992). Salinities are especially high in iron skarn deposits. With the temperature decreasing, the salinities seem to have a tend of decline (Knauth, 2005). In general, magmatic fluids have KCl > $CaCl_2$ whereas

high-CaCl2 fluids appear to have interacted more with sedimentary wall rocks.

1.2.4.3.3 Redox and PH value

The composition of pyroxenes and garnets can serve as an indicator of acidity and redox environment which contain ferric iron. Skarns associated with different kinds of mineralization are formed in different conditions of oxygen fugacities and acidities. Their oxygen fugacities are declining in turn: Fe-Cu, Fe, Sn-Mo, W-Sn. Whereas the acidities, they rise on the same sequence.

1.2.5 Isotopic geochemistry

Different rocks have characteristic isotopic value, for example that the isotope composition of the carbon and oxygen of sedimentary carbonate rocks is characterized by values of $\delta^{13}C$ from +2 to -2‰ and $\delta^{18}O_{smow}$ from 30‰-20‰ for both dolomites and limestones (Karimzadeh Somarin, 2004; Baskaran, 2011). Carbonates are the initial rocks in skarn formation processes and products of all stages of formation of the deposits being discussed. Being “sulplus” minerals compensating for the changes in the volumes of all the metasomatic reactions, they are the link between processes of the magmatic replacement of the initial carbonate rocks and those of postmagmatic mineral formation. This could not fail to affect the isotope composition of carbon and oxygen of carbonate radical, thus proving the relation between skarn and ore formation.

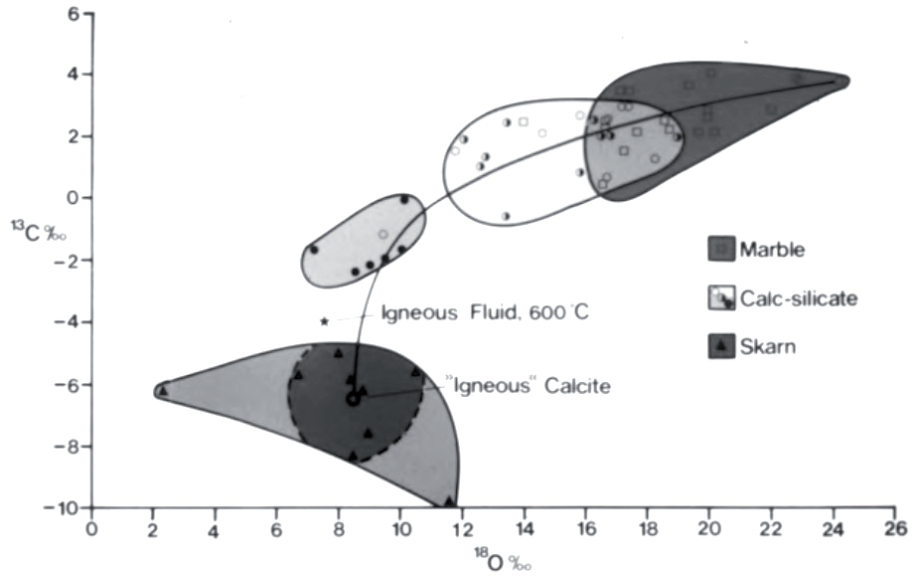

Fig. 1-10: Analytical data for calcites from marble, outer skarn, and ore-bearing skarn. The data suggest the mixing of two reservoirs of carbon and oxygen; the original marble and a fluid equilibrated with an igneous source. The curved line simply traces the observed isotopic changes from marble to igneous rock (Maher and Larson, 2007).

Mostly, using geochemistry of isotopes aimed at solving the genetic problems of metals or fluids (Shimazaki and Kusakabe, 1990; Levresse et al., 2004; Grabezhev, 2010), such as the tungsten skarn deposit in Pine Creek (Fig. 1-10) (Maher and Larson, 2007). Commonly, geochemistry of isotopes is used mainly in three aspects. Firstly, studying the isotopic composition of different protoliths and revealed the material changes between them; secondly, traced the source; thirdly, characterized the isotope composition during the alteration. Frequently, C, O and S isotopes are analyzed to archive the studying problems. Besides, Fe, Si, Ca and Sr are rarely reported. Characteristic isotope composition of carbon and oxygen in carbonates of marbles, calciphyres, skarns and products of their endogenetic and hypergenetic alteration (Aleksandrov 1998) are attached (appendix E). It is noteworthy that some isotopic studies displayed multi-source of the metals which were mostly derived from the plutons (Zhang and Pan, 1994).

1.2.6 Reconstruction of fluid flow involved in skarn

It has been recognized for more than a decade that the mineralogy of many metamorphic rocks is controlled not just by the elevated pressures and temperatures but also by pervasive flow of chemically reactive fluids during metamorphism. One-dimensional models were used to predict the spatial distribution of mineral assemblage developed in siliceous dolomitic limestones (Ferry, 1994; Hanson and Ferry, 1995). Their result emphasized that mineral assemblages in metacarbonate rocks are controlled not only by temperature, pressure, rock composition, and fluid composition but also by the amount and direction of fluid flow. Besides, fluid flow controlled by structure during contact metamorphism was reported (Ferry et al., 1998; Cole et al., 2000). In order to constrict fluid flow during skarn formation, isotopic data were used frequently. The Bungonia limestone was taken as the study target for isotopic analysis, and the result showed that the protolith of limestone did not initially contain a fluid-filled porosity, but hydrofracture play an important role in the fluid circulation (Buick and Cartwright, 2000). It is noteworthy that, for the fluid flow involved in skarn, its geometry was playing an important role during fluid circulation. That is whether fluid flow was horizontal or vertical and up-temperature or down-temperature. There could be many ways to answer this question according for specific aureoles.

1.2.7 Temporal and spatial evolution of skarn

When a pluton intrudes into $CaCO_3$-contained wall rocks, the early isochemical metamorphism and continued metasomatism at relatively high temperature is followed by retrograde alteration as temperature decline (Fig. 1-11). They are characterized by distinguished mineral assemblage. Contact metamorphism is not a typical isochemical recrystallisation (Einaudi et al., 1981; Meinert, 1984; Meinert, 1992). Heat, magmatic components such as Fe, Si, Cu, etc., transfer from the magma to the sediment wall rock, whereas the CaO and CO_2 are inverse. This is the

process that called bimetasomatism. In addition to the mineral assemblage, some mineral show compositional and colour gradients according to the distance of contact zone. For example, the garnets closed to the pluton may contain relative higher Fe and lower Ca, dark red-brown, towards the wall rock, the Fe and Ca content would systematically decrease and increase respectively (Meinert et al., 2005). Its colour becomes pale green because of appearance of epidote and chlorite. For some skarn systems, these zonation patterns can be "stretched out" over a distance of several kilometers and can provide a significant exploration guide.

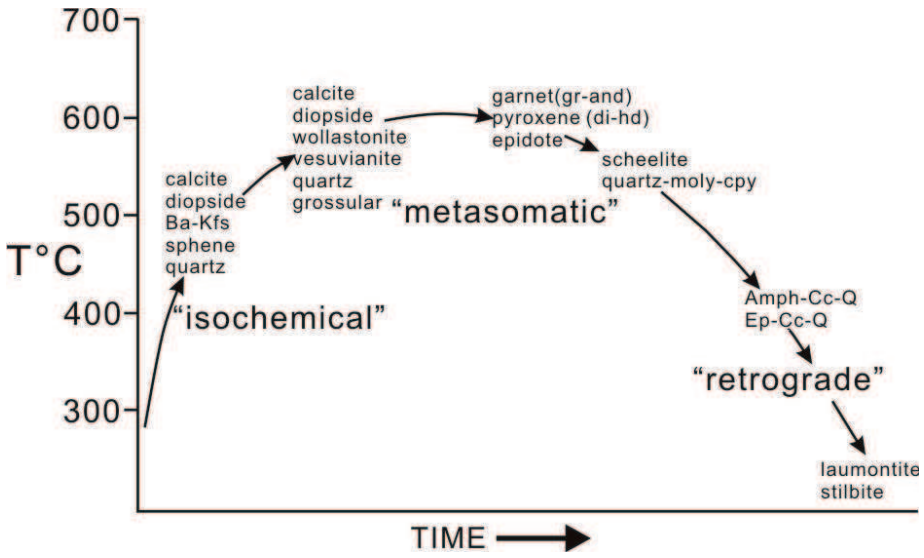

Fig. 1-11: Schematic time-temperature plot summarizing the major steps in the development of the Pine Creek skarn and ore body (Maher and Larson, 2007).

As to the decrease of the temperature, later fluid which is commonly rich in volatiles, Ca and Si would alter the earlier skarn minerals. For example, epidote and chlorite would superimpose on the garnet and pyroxene. This process of superimpose is mostly accompanied by pyrite+/-marcasite.

Most skarn ore deposits could be distinguished into two quite different alteration stages according to forming temperature and water content. The first one is characterized by anhydrous minerals, such as garnet and pyroxene, in the early prograde stage and in relatively high-temperature and hypersaline liquid; the second

one is composed by hydrous minerals, such as epidote, amphibole, and chlorite plus sulphide ore minerals which are formed in relative low temperature and lower salinity in a retrograde stage. These two different alteration stages probably reflect a dominance of magmatic and meteoric water, respectively (Meinert et al., 2003).

1.2.8 Experimental studies of "skarnization"

Many experimental studies have been done concerning forming processes of skarn, such as solid solution studies of pyroxene (Burton and Taylor, 1982; Gamble, 1982; Hochella et al., 1982); stabilization of garnet (Liou, 1973; Taylor and Liou, 1978); decomposition of calcite (Harker and Tuttle, 1956) [recited from (Deer et al., 1982)]); artificial synthesize of vesuvianite (Hochella et al., 1982); sulfidation reactions involving andradite and hedenbergite (Gamble, 1982). Those experimental studies restrict the skarn forming conditions. However, most of them place particular emphasis upon the synthesis of individual skarn minerals, ignoring mineral assemblage. The systematic formations of skarns have been experimentally studied by Zharikov and Zaraisky (2003). Their results show that the temperature range of the epidote skarns formation was found to be 350-550^{o}C. Their formation is favored by the enhanced potassium content in the starting granitoids and low ($NaCl+CaCl_2$)/KCl ratio in the affecting solutions. Epidote skarn facies can be indicators of low partial CO_2 pressure corresponding to the mole fraction of CO_2 to 0.04 at P(H_2O+CO_2)=1 kbar; in the direction from granitoid to limestone, ore minerals deposit in a certain sequence: pyrite→chalcopyrite→sphalerite→galena. Zonation in an experimental skarn formed at the contact between granodiorite and limestone at 600°C, P_{fluid} = 0.1 GPa (X_{CO_2} = 0.07) also has been studied (Fig. 1-12A) (Zharikov and Zaraisky, 2003). Fe and Si transfer toward the carbonate, whereas the Ca does the inverse. The bimetasomatism is proved. Experimental formation of carbonate metasomatic zones in a column of comminuted quartz diorite as a function of temperature shows that when temperature increases, the widths of metasomatic zone synchronously increase (Fig. 1-12B).

Liang (2000) conducted more than 6000 experiments on skarn formation and concluded that skarn could be also formed in the process of migmatization and assimilation, as well as contact metasomatism. In his book “Experimental studies on the mechanism of the formation of skarns and skarn ore deposits in China”, he wrote that “No matter what type and composition of rocks are and no matter what tectonic location, as long as with Si, Al, Ca, Mg, Fe, and their proportion is appropriate [SiO_2:Al_2O_3:CaO:MgO:T Fe_2O_3=30~50:10~15:30~40:5~10:3~6], pH = 2.0~11.0, in 265~750°C, 200.105~2000.105Pa, weak redox environment, skarns and skarn ore deposits can be formed by metasomatism in the presence of hydrothermal fluids containing volatile (CO_2, Cl, F etc.) and K, Na. Or, in 850~1200°C, 3000.105~6000.105Pa, skarn magma differentiation, limestone or dolomitic limestone assimilation of alkali-rich magma can produce Ca-skarn-type magma and skarn-type deposit.” From the results of all his experiments, skarn is a metasomatic rock, rather than a metamorphic rock (Burt, 1982; Gamble, 1982; Zhao et al., 1985; Liang, 2000). A recent integration of experiment, petrology and geochemistry study shows that limestone assimilation of mafic magma could cause desilicated and alkali-rich magmas which may relate to skarn formation (Iacono Marziano et al., 2008). According to these experimental study, there is a general impression that skarn could be caused by metasomatism and the magmatism-sediment-interaction-related causation.

A

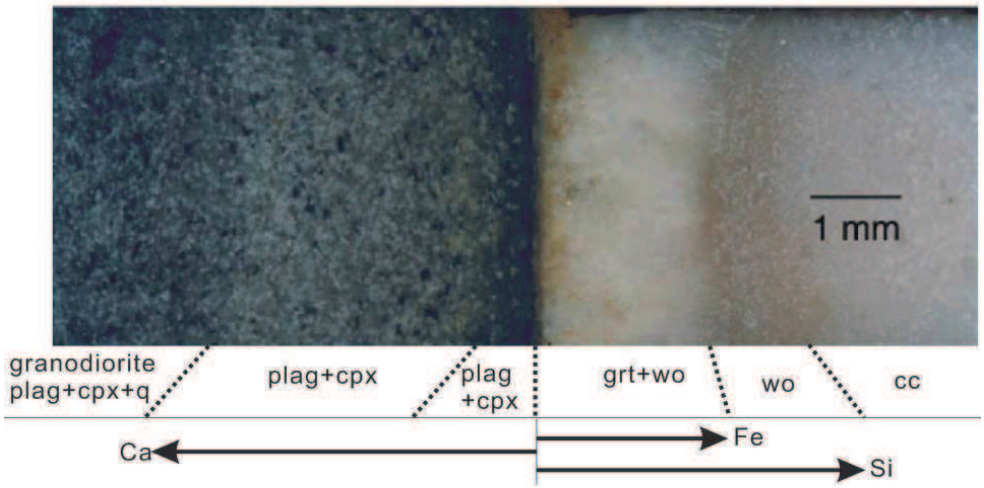

B

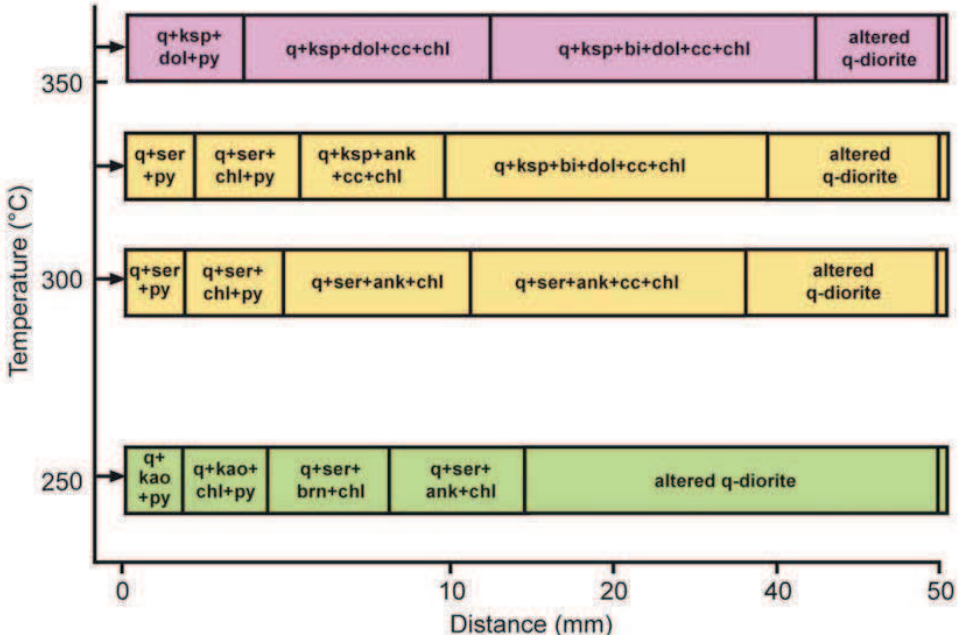

Fig. 1-12: (A) Zonation in an experimental skarn formed at the contact between granodiorite and limestone at 600°C, Pfluid = 0.1 GPa (X_{CO2} = 0.07); (B) Experimental formation of carbonate metasomatic zones in a column of comminuted quartz diorite as a function of temperature.

$P_{H2O+CO2}$ = 100 MPa, X_{CO2} = 0.1, log (mKCl/mHCl) =3.0, mKCl = 1.0, total S= 10^{-2} – 2.1^{-2} M, excess quartz, t = 336 hr. Scale of first 10 mm doubled for clarity. plag=plagioclase, cpx=clinopyroxene, grt=garnet, wo=wollastonite, cal=calcite, q=quartz, ksp=k-feldspar, dol=dolomite, c=calcite, chl=chlorite, bi=biotite, py=pyrite, ser=sericite (Zharikov and Zaraisky, 2003).

1.2.9 Skarn genetic models

Several models have been proposed to the skarnization process. The following section mainly discusses the two prevailing models.

1.2.9.1 Metasomatic model

In its broadest sense, it is a process of mass and chemical transport and reaction between adjacent lithologies. It seems that all skarn forming processes involved fluids. Fluids enriched in Si, Fe, Al and Mg were mainly derived from the magma. These fluids would dissolve the carbonated and convert them into skarn. This process is known as part of metasomatism. According to experimental result, as well as field observation, the metasomatic process could effectively concentrate economic elements (Liang, 2000). For a long time, skarn are also called contact metasomatic rock because they develop in/near the contact zone between acid-basic- intrusions and carbonate rocks (Fig. 1-13). High temperature magma will produce a temperature gradient toward the relatively cooler sediment wall rock; exsolved fluids from the magma during its emplacement could cause extensive reactions and results in the deposition of metals.

Skarn can be subdivided into exoskarn and endoskarn depending on whether the metasomatic assemblage is internal or external to the intruding pluton. Exoskarns occur at and outside the granite which produced them, and are alterations of wall rocks. Endoskarns, including greisens, form within the pluton, usually late in the intrusive emplacement and consist of cross-cutting stockworks, cooling joints and around the margins and uppermost sections of the granite itself.

The diversity of different metals found in skarns is controlled by different compositions, f_{O2}, and even different tectonic context of the igneous intrusions. Another criterion, skarns could be classified into magnesian and calcic, to describe

the dominant composition of the protolith and resulting skarn minerals. These terms can be used combined. Most of large, economically viable skarn deposits are associated with calcic exoskarns (Robb, 2005). Even though there are different metal associations in skarn deposits, the processes by which these deposits form are similar: First of all, magma and/or hot fluid emplacement, and then the extensive metasomatic reactions between the intrusions and the wall rocks.

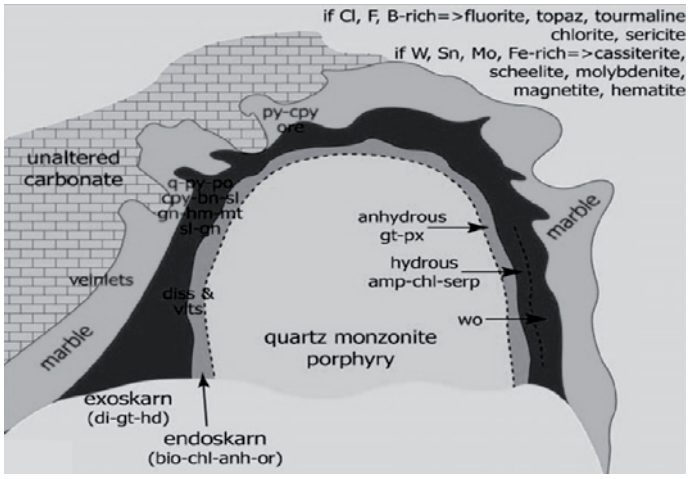

Fig. 1-13: A cartoon indicating metasomatic model for skarn formation (download from internet).

1.2.9.2 Magmatic hydrothermal model

An alternative is the magmatic hydrothermal model. This model is not new but not much mentioned. In 1953, in order to explain vein-like skarn, a skarn-type liquid/melt had been proposed (Абдулла Алиев Х. М.(translated by Xu, 1953). The author believed that the skarn-type liquid/melt was different from the metasomatic-type. In recent years, this point was reviewed and confirmed, mostly basing on melt inclusion and petrologic observation (Lin and Xu, 1989; Wu and Chang, 1998; Fulignati et al., 2001; Zhao et al., 2003; Zhao et al., 2003). The mainly difference between the metasomatic and magmatic hydrothermal model is that the magmatic hydrothermal model has extremely high temperature mineral assemblage, such as garnet-pyroxene formed at about 900-1000°C. This temperature range is not long belonging to the scope of metasomatism. In this temperature range, all has

become melt or liquid state (Lin and Xu, 1989). When the temperature decline, some Ca-silicate melt could crystallize into the skarn mineral assemblage. Fulignati et al. (2001) indicated that the high temperature skarns represent the magma chamber–carbonate wall-rock interface. The skarnization process results from the crystallization of a Ca silicate melt or from the consolidation of a cryptoexplosion breccia (Lin and Xu, 1989). Wu and Chang (1998) divided high temperature magmatic skarn forming process into two stages:

1) Stage of crystallization of Ca-silicate minerals. In this stage, mainly euhedral/subhedral crystals form with obvious accumulation features and often holes. Clinopyroxene is generally earlier than garnet. Early clinopyroxene is diopside, accompanied by magnetite and andradite; later clinopyroxene are mainly salite with small amount of aegirine composition. Early garnet is homogeneous andradite; the later are mainly strong anisotropic grandite, such as Tongling skarn Fe deposit (Fig. 1-14).
2) Stage of alkali aluminum silicate and carbonate minerals crystallization. Later alkali aluminum silicate minerals, potassium feldspar and/or sodium oligoclase (An =11% ~ 13%) and calcite and anhydrite, etc. would crystallize from the melt. They infill gap or crack. This mineral assemblage do not overprint on the primary stage, these minerals do not altered diopside and grandite, and especially, the gross alkali feldspar and calcite containing diopside/garnet/sphene/apatite inclusion indicate that it is rather a later crystallization.

According to literatures, the following features of magmatic skarns could be extracted:

(1) most magmatic skarns are associated with Fe+/-(Cu) deposits;
(2) all the magmatic skarns are proved by melt inclusions, most melt inclusions were found in the garnets and pyroxenes;
(3) some magmatic skarns occur in the form of vein-like;
(4) the early stages of magmatic skarns could be superimposed by later hydrous

stages;

The mechanism of the magmatic skarn forming process is not clear, however, the sediment assimilation of magma may provide some clues. Skarn xenoliths found in the large (70km*10km) picrite pluton leaded the previous researcher to conclude that the skarn are the products of dolomitic xenoliths to suffer high temperature contact-thermal metasomatism (Yu, 1985). After the study of skarns and cumulates formed at the contact between a magma chamber and its wall rocks, Gaeta et al. (2009) concluded that a 'skarn environment' can act as a source of CaO-rich silicate melts. In certain conditions, this CaO-rich silicate melts could crystallize into special mineral assemblage, such as garnet and pyroxene (Wu and Chang, 1998). This CaO-rich silicate melts could be come from the assimilation of sediment wall rocks. In addition, experimental study of limestone assimilation by hydrated basaltic magmas under the physical conditions of 1050–1150°C in temperature and 0.1–500 MPa in pressure shows that desilicated and alkali-rich magmas could be generated by assimilation of sedimentary carbonates, and the desilicated trends are negatively correlated to the increase of the limestone assimilation (Iacono Marziano et al., 2008).

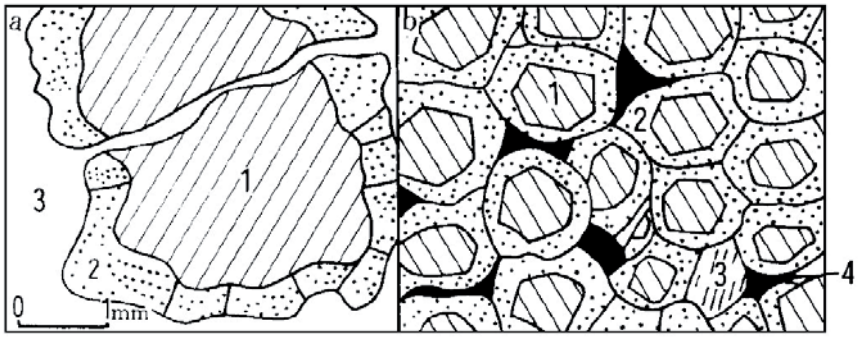

Fig. 1-14: Sketch of garnet growth and adcumulate from Tongling skarn iron deposit (Wu and Chang, 1998).

a. Peritectic massive sulphide ore aggregates andradite and grandite growth boundary: 1-andradite (homogeneous) aggregates; 2-strong un-homogeneous andradite grow boundary; 3-sulfide.

b. Garnet adcumulate:1-Automorphic andradite; 2-Non-homogeneous grandite growth boundary; 3-K-feldspar; 4-sulfide.

1.3 Skarn-related ore deposits (SROD)

1.3.1 Intrusion composition and tectonic setting of SROD

As a general rule: (1) Fe and Au SROD tend to be associated with intrusions of mafic to intermediate compositions (low silica, iron-rich, relatively primitive magmas); (2) Cu, Pb, Zn and W SROD are linked to calc-alkaline, magnetite-bearing, oxidized (I-type) granitic intrusions; (3) and Mo and Sn SROD are related to more differentiated granites that might be reduced (S-type). The igneous rocks associated with skarn deposits range in composition from gabbro to high evolved granite. It seems that all the deposits subclasses are associated with subalkaline to alkalic calca-calklaline magmatism; and they show systematic geochemical variation from Au, Fe Cu, Zn-Pb, W to Sn deposits (Fig. 1-15) (Ray and Webster, 1991).

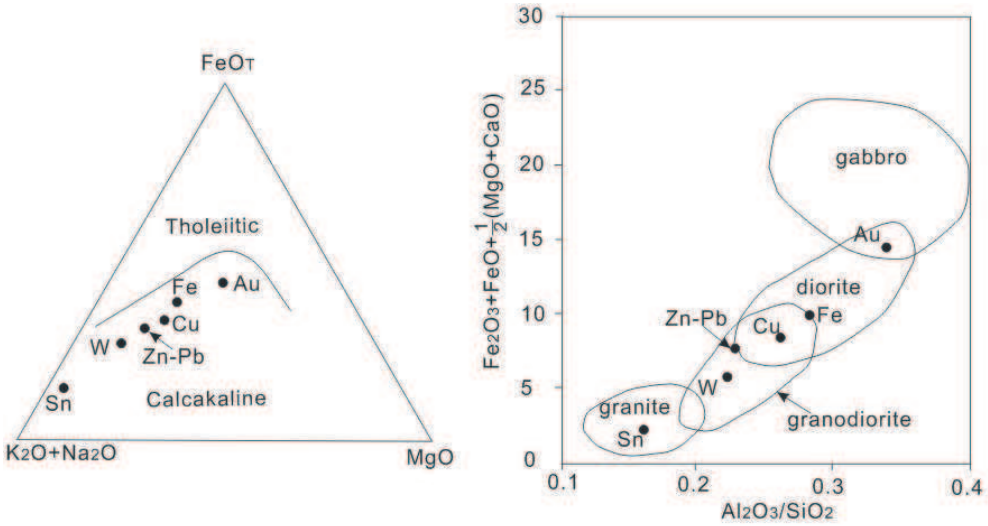

Fig. 1-15: AFM plot illustrating the calcalkaline affinities of the skarn-related intrusions to the left and principal oxide plot illustrating variable compositions of the skarn-related intrusions to the right (Ray and Webster, 1991).

Tectonic setting and magma petrogenesis maybe intimately linked, at first approximation, types of SROD might be favored by certain tectonic setting: Mo and Sn SROD would be favored by highly evolved crust in a post-subduction/collision

context, whereas large iron SROD would be most related to volcanic arc, close to the subduction zone (Ray and Webster, 1991; Kuscu et al., 2002). Towards the inner stable continental, protolith plutons are more SiO_2 in chemical composition and associated skarns are most likely rich in Mo or W-Mo with lesser Zn, Bi, Cu, and F. Many skarn are polymetallic, and with locally important Au and As occasionally. This transition from subduction zone to the inner part of the continental probably reflects the thickness, contamination, heat flux, composition of the crust. Because magmatism associated with shallow subduction angles may have more crustal interaction (Corbett and Leach, 1998). However, it is noteworthy that the presence of skarn does not necessarily indicate a particular geological setting or a particular protolith (Meinert, 1992). An idealized tectonic model for skarn formation is illustrated in Fig. 1-16. However, occurrence of SROD does not indicate certain geological back ground. It is noteworthy that there is very few Precambrian skarn and SROD which mostly formed during Phanerozoic times where plate tectonics and carbonate sedimentation occurred.

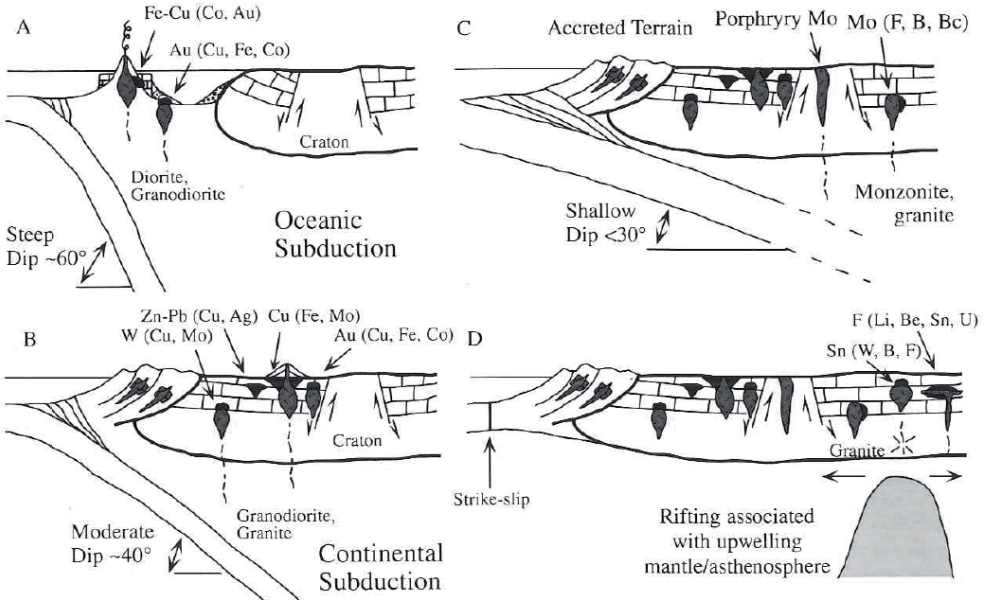

Fig. 1-16: Idealized tectonic setting models for SROD formation (after Meinert et al. 2005). (A) Oceanic subduction and back-arc basin environment. (B) Continental subduction environment with accreted oceanic terrane. (C) Transitional low-angle subduction environment. (D) Post-subduction, continental rifting or continental plume environments.

1.3.2 Calc-silicate/metal paragenesis

The mineralogical composition, such as refractory garnet and pyroxene, are informative to indicate skarn-related mineralization types. Garnet and pyroxene almost present in all skarn types and show marked compositional variability. Meinert (1992) indicated that the assemblage of manganiferous pyroxene and johannsenite is important criteria to identity zinc skarns. That the valence of iron could vary leads it to act as redox indicator. Systematic compositional plots reveal significant difference between different skarn related deposits (Fig. 1-17). These triangular plots showed that Fe skarns are preferable for Al-Fe^{3+} garnet and Mg-Fe^{2+} pyroxene; Cu, Zn, Au, and Mo skarns are similar with Fe skarn for the garnets, while the Sn and W skarn are trend to be with (Mn+Fe^{2+}) garnets. Cu, Mo, Sn, Au and Fe skarns are low in Mn for the pyroxene composition.

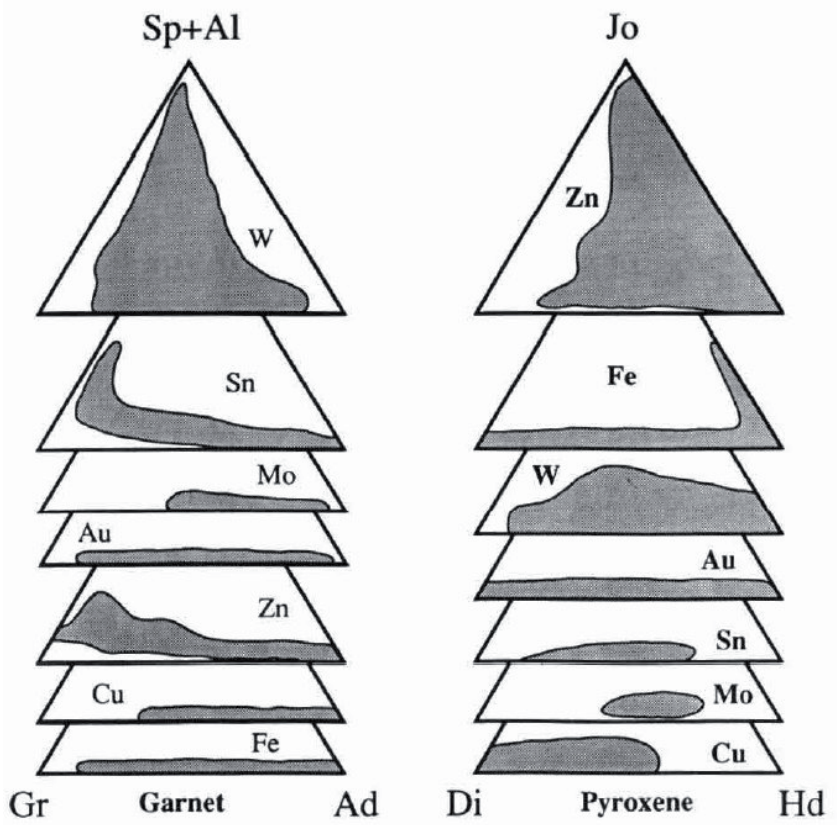

Fig. 1-17: Ternary plots of garnet and pyroxene compositions from major skarn types (Meinert, 1992). End members are: Ad=andradite, Gr=grossularite, Al=almandine, Sp=spessartine, Hd=hedenbergite, Di=diopside, Jo=johannsenite.

1.3.3 Giant Fe and Cu-Zn SROD

This section is to briefly introduce two famous types giant skarn deposits: Antamina porphyry skarn Cu-Zn deposit and Fe skarn deposit in the Andes Cordillera, Argentina and in Yangtze area, China. However, other skarn types deposit would share more or less common features. The aim is to provide a common outline of features of these types of deposits. These deposits are limited but representative.

1.3.3.1 Fe skarn deposits in Yangtze and the Andes Cordillera area

Except the massive sulfide deposits, the Fe skarn deposits are conspicuous in Yangtze area, China. According to Zhao (1989) who study hundreds of Fe skarn deposit in China, the occurrence of ore bodies of Fe SROD have some common features, such as (1) associated with small intrusion or along cupola/apex at the top of larger plutons; (2) the economic ore bodies mainly develop close to side of the sediment wall rocks, typically for iron skarn deposits; (3) the ore bodies are poor continuity. Besides, the top of the fold are favourable for ore bodies (Zhao et al., 1986).

The features of Fe skarn deposits in Andes Cordillera, Argentina have been summarized in other angle (Franchini et al., 2007). They concluded that the main features of the Fe skarns include: (1) association with mantle-derived middle Miocene (~15–11 Ma) diorite stocks and sills; (2) widespread alteration including epidote ± amphibole ± magnetite endoskarns, and zoned garnet (Grs:0–66; Adr:32.5–100) ± magnetite ± pyroxene (Di:24–50; Jo:2–9; Hd:74–41) exoskarns formed from oxidized, saline, high-temperature brines (530º–660ºC; 60–70wt.% NaCl equiv.); (3) and magnetite-hematite orebodies associated with quartz ± epidote ± calcite ± actinolite formed at lower temperatures (290º–436ºC) from saline fluids (32–50 wt.% NaCl equiv.) of magmatic origin.

1.3.3.2 Antamina Cu-Zn porphyry skarn deposits

The Antamina deposit was thought to be the largest Cu-Zn porphyry skarn deposit in the would which reserves 559 million tonnes with Cu 1.24% (Jebrak and Marcoux, 2008). It is located east of the Cordillera Blanca in northern Peru. It also yields zinc, silver, lead, molybdenum and bismuth mineralization. The ore is mined by open pit methods, and batch treated by ore type through a conventional grinding and flotation mill. Its formation is associated with mineralized porphyry copper plutons and contact metasomatism (Fig. 1-18).

Except the Antamina deposit, for this porphyry-skarn type Cu deposit, the early potassic alteration in porphyry correlates with the early oxidized prograde calcic exoskarn zoned, away from the contact, from andradite with salitic diopside to wollastonite to marble. Magnesian exoskarn after dolomite has prograde forsterite and diopside, retrograde tremolite, actinolite, talc, serpentine, phlogopite, chlorite and anhydrite. Magnetite may be present. Chalcopyrite and bornite replace marble relics in skarn, skarn itself, or fill fractures in skarn and adjacent hornfels. When mineralized porphyry directly borders exoskarn, the Cu-(Mo-Au) mineralization continues without interruption and large combined porphyry-skarn ore bodies result. Endoskarns are commonly Cu mineralized but large discrete ore bodies are uncommon. Convecting fluids causing sericitization in porphyry are responsible for skarn retrogradation, silicification, pyritization and argillization. Small amounts of sphalerite and galena may precipitate in the skarn at porphyry contact, but larger Zn-Pb deposits form in separate bodies outside the contact, still in skarn or in marble with or without jasperoid. In the Central mining district, New Mexico, the "giant", enriched Santa Rita (Chino) porphyry copper deposit borders on a "porphyry-Cu related skarn" with characteristic andradite-diopside association (Einaudi et al., 1981). This skarn is Cu dominant and mined together with the porphyry ores; sphalerite is minor, at marble contact.

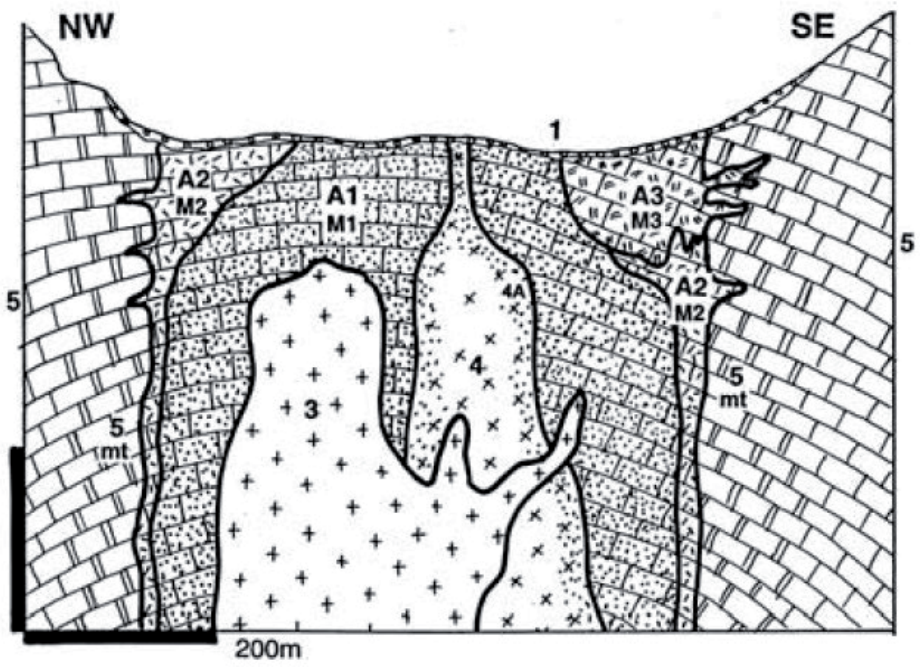

Fig. 1-18: Antamina Cu-Zn deposit, Peru. This is a "giant" Cu-Zn skarn in the exocontact of a quartz monzonite stock that hosts only a minor porphyry-style Cu mineralization. From LITHOTHEQUE No. 3201, modified after O'Connor (2000) recite from (Laznicka, 2010). 1. Q overburden; 2. Mi-Pl andesite dikes; 3. Mi3 intermineral & postmineral granodiorite; 4. Mi2 quartz monzonite porphyry; 4A. Endoskarn in porphyry; 5. Cr3 limestone, 5mt is marble near contact. A1, brown grossularite skarn, hosts chalcopyrite-dominated replacements; A2, green garnet skarn, hosts M2, mostly sphalerite. A3, wollastonite skarn, hosts bornite-rich ores.

In addition to single continuous Cu skarn-porphyry deposits like Mission (Fig. 1-19) or Twin Buttes in Arizona, porphyry and skarn often form separate orebodies yet this rarely follows from simple database entries and production statistics. Regardless, when carbonate wall rocks are present, mineralized Cu-porphyry is an excellent indicator of possible skarn presence, and vice-versa. There are hundreds of Cu-skarns without Cu porphyries, but most are small although. Those associated with phaneritic plutons are probably eroded to the "mesozonal" granite depths where porphyry copper deposits rarely form and, instead, mesothermal Cu (and Pb-Zn-Ag and Au) veins coexist. Alternatively, porphyry Cu deposits may still be discovered and there are several encouraging case histories where Cu skarns were long known and mined before porphyry coppers have been discovered (e.g. Grasberg Cu-Au porphyry in the Ertsberg Fe-Cu skarn group, Papua (Irian Jaya); Antapacay

porphyry in the Tintaya Cu skarn district, Peru; Cadia Hill Au-Cu porphyry in the Old Cadia Fe-Cu skarn field, New South Wales).

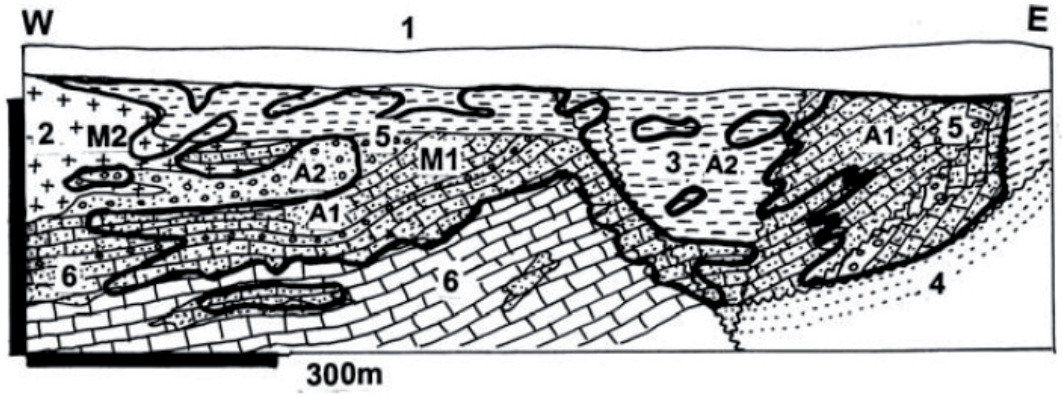

Fig. 1-19: Mission deposit, Pima (Tucson-south) district, where most Cu concentrate comes from exoskarn. From LITHOTHEQUE No. 534, modified after Kinnison (1966). M1 is pyrite, chalcopyrite > bornite ore in skarn, M2 is a fracture stockwork in porphyry and biotite hornfels (recite from Laznicka 2010). 1. T3-Q fanglomerate; 2. T1 quartz monzonite porphyry; 3. Cr arkose, shale; 4. Tr-Cr red beds; 5. Pz quartzite, shale; 6. Pz miogeoclinal carbonates; A1. Exoskarn and silicate marble; A2. K-silicates and sericite altered hornfels & intrusion.

1.3.4 A focus on skarn-related iron deposit

Here I would like to emphasize the iron skarn deposits because, in this thesis, the studied objects yield massive magnetite with skarn beyond their economic importance and scientific significance. Iron skarns deposits are of largest skarn deposit which have been mentioned above, and they often also enriched in Co, Ni, Cr, and Au (Meinert et al., 2005). Some of their key features that make these skarns conspicuous apart from those associated with more evolved magmas. These features could include: their association with intermediate to basic plutons, well develop endoskarn, widespread sodium metasomatism, and the absence of Sn and Pb etc. These features reflect the relatively primitive magmatism and higher metasomatic temperature. Iron skarn deposits principally consist of magnetite near the garnet zone. They could range up to 5000 million tones in size and grade up to 45 per cent iron (Laznicka, 2010). According to geochemistry of their hosting rocks, two type of iron skarn could be distinguished: calcic iron skarn and magnesian iron skarn hosted

respectively by limestone and dolostones. Calcic iron skarns are tending to be associated with intermediate to basic magma that intruded island arc volcano-sedimentary sequences. The deposits commonly exhibit widespread calcium metasomatism and may contain albite-scapolite alteration as well as sporadic geochemical enrichment in copper, cobalt, nickel, arsenic and gold (Ettlinger and Ray, 1989). Many of the calcic iron skarns have a strong stratigraphic control: such as skarns on Vancouver and Texada islands where they are commonly found where Jurassic gabbroic to granodioritic plutons intrude upper Triassic limestones of Quatsino Formation (Ray and Webster, 1991). Many iron skarn deposits are related to mafic magmatism, average SiO_2 is less then 60% (Fig. 1-20). Iron skarns are mined for their magnetite content and although minor amounts of Cu, Co, Ni, and Au may be present.

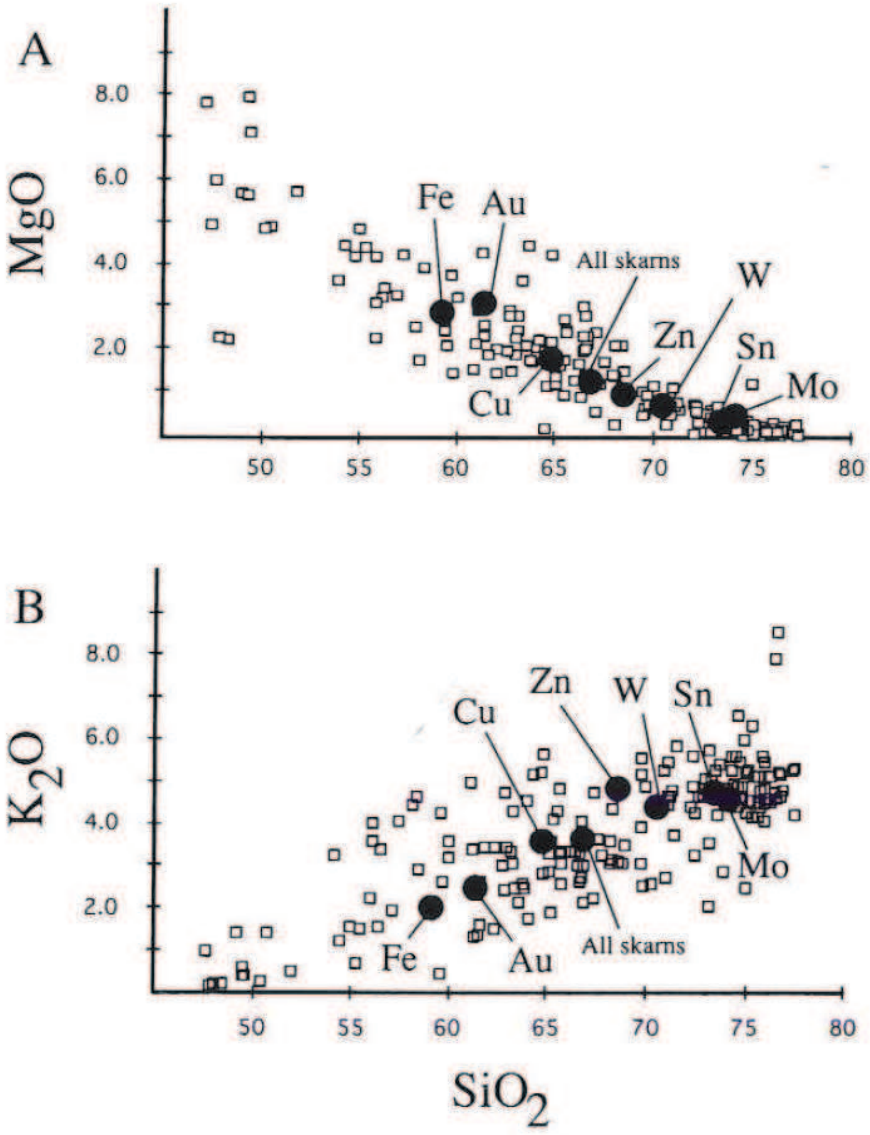

Fig. 1-20: Harker variation diagrams of (A) MgO and (B) K_2O vs. SiO_2, illustrating variation of major element abundances in plutonic rocks associated with the main skarn deposit types (after Meinert et al., 2005). Circle and square represent raw and mean data respectively.

Host wall rocks of calcic iron skarn include limestone, sandstone, volcanic rocks, graywacke, dolomite at contacts of mafic-ultramafic intrusions, as well as diorite. Whereas host wall rocks of magnesian iron skarn are typical dolostone or rocks with dolomitic composition. Wall-rock alteration of calcic iron skarns mostly involves extensive endoskarn development, which is characterized by albite, orthoclase, epidote, quartz, and scapolite. Magnesian iron endoskarn is relatively rare.

Iron skarn ore bodies are mostly spatially with or close to massive garnet. Some times they could form lentil bodies in limestone near the calc-silicate skarn zones (Koděr et al., 1998).

The morphology of ore bodies may be lenticular, lensoid and tabular. Some ore bodies may extend hundreds of meters to kilometers, such as Fe-Cu-Zn-Pb skarn in the Ocna de Fier-Dognecea orefield (Ciobanu and Cook, 2004). Thicknesses are quite various: tens to hundreds of meters. They could occur along faults and may contain polymetallic potential.

1.3.4.1 Features of the largest skarn-related iron deposits

Some of the largest iron deposits could share similarities. Musan and Kachar deposits were thought to be the two of the largest iron skarn deposit in the world which contained a reserve of 5200 Mt and 2000 Mt with an average grade of 50% and 45% Fe respectively (Koroteev et al., 1997; Meinert et al., 2005; Mao et al., 2011). According to some of the largest iron skarn deposits from the world (Musan magnetite deposit; Kachar magnetite deposit; Magnitogorsk magnetite deposit with reserve of 500 Mt graded 48% Fe; Sarbai magnetite deposit with reserve of 725 Mt graded 45% Fe; Sokolovsk magnetite deposit with reserve of 967Mt graded 41% Fe), they generally possess several similar characteristics:

1) The iron ore bodies are stacked thick lenses of massive magnetite gradational into "segregated ores" of densely disseminated magnetite;
2) The host rock rocks are related to volcanic sedimentary series;
3) All of them are near to or pass by deep faults;
4) They may associate with mafic/ultramafic magmatism.

1.3.4.2 Alkaline alteration

In iron skarn ore deposits, alkaline metasomatic alteration around the intrusion and aluminum silicate rocks is very common. As the result of alkaline metasomatic alteration, dark minerals often break down and it form light-colored rocks (Zhao et al., 1990). Light-colored rocks and mineralization are generally proportional to the altered intensity, therefore, the alkaline altered rocks are often served as one of the hallmarks of effective economic mineral exploring. It seems that for different silicate contents within the intrusion, alkaline metasomatic alteration is not the same: Na alterations mainly develop on the basic and intermediate magma; whereas K alterations develop on the rocks related to felsic magmatism (Xia, 2010).

Na metasomatism in skarn-type iron deposits of northern China, such as Daye iron deposit, extensively develop in the endoskarn. Intrusion rocks were mainly diorite, quartz diorite, monzonite and gabbro. Take the Daye iron skarn deposit as an example to illustrate the metasomatism, mineral assemblage and chemical variation (Zhao, 1990; Zhao et al., 2007; Xia, 2010; Zhang, 2010). The quartz diorite, which caused mineralization, was strongly albitized and scapolitized. Unaltered quartz diorite is gray, fine-grained. Hornblende and plagioclase grain can be clearly identified with the naked eye. After being albitized, rock color changes into light grey or pale grey. Granular structure is not clear. The boundary of minerals is hard to recognize. From normal quartz diorite to diopside-albitite change is a continuous gradient. Anorthite molecules in plagioclase gradually reduced and correspondingly the albite molecules increase. In addition, all hornblende has been altered by diopside. Rock chemical compositions change. After being albitized, Fe, K and Mg were taken out, whereas Na and Si were brought in. During this process Fe_2O_3 decrease rapidly, but FeO decrease slowly. With the progressively enforce of metasomatism, Na content increases, K content decreases, total (Na+K) is constant, about 9%. K taken by the fluid may become the major composition of iron-phlogopite. Such iron-phlogopite, which well developed around the deposit,

contains up to 7.54-9.7% K_2O.

K metasomatism in skarn-type iron deposits is common in the inner contact zone of granodiorite and granitoid. It is similar to Na metasomatism: K-feldspar would take place of plagioclase, primary K-feldspar, biotite and amphibole. According to mass balance calculations, Fe was taken from granodiorite during metasomatism and immigrated into altered zone (Liang and Qiao, 1991; Liang, 2000). The albite molecular content in metasomatic K-feldspar was very low or near zero. The level of albite molecular in K-feldspar seems depend on temperature. Because at high temperatures, K-feldspar and albite can be miscible in any ratio, but the ratio is limited at low temperatures. Magmatic K-feldspar in granite, because of its high temperature of formation, can accommodate Ab molecule in its structure at relatively high level, and metasomatic K-feldspar are metasomatic product at hydrothermal stage, being generated in a relatively low temperature, and thus Ab molecule content is also low.

1.3.4.3 Origin of iron

To the metasomatic model, altered reactions liberalised the iron to the fluid - the potential source for magnetite skarn (Koděr et al., 1998). The iron in the fluid is mainly in the form of halide complex ($FeCl_2$, $FeCl_3$, FeF_2, FeF_3) (Zhao et al., 1983). For some iron skarn deposits, Na metasomatism could effectively extract the iron into the fluid (Liang, 2000). While to the magmatic model, CaO-rich silicate melts or assimilation of sediment seems relate to the reason of iron concentration because the assimilation would efficiently change the liquidus of some minerals crystallization (Gaeta et al., 2009). Whatever, both the two models emphasize the fluid.

1.3.4.4 Association with mafic magmatism

Most of the time, when referring to mafic-ultramafic magmatic-related deposits, it may remind us the platinum-group element (PGE) and Ni-Cu potential. However, many of the world's iron ore deposits are associated with mafic-ultramafic magma, such as: Panzhihua Fe-Ti (Ganino et al., 2008; Pang et al., 2008) and iron skarn-type deposits in western British Columbia (Meinert, 1984). Mafic-ultramafic magmas could form in almost all tectonic environments. These rocks may intrude or extrude continental crust, either along well defined faults or rifts, such as continental flood basalt provinces: Emeishan basalt (Chung and Jahn, 1995; Gary et al., 2001), and the Great Dyke of Zimbabwe (Wilson and Prendergast, 2001). Mafic-ultramafic magma could be produced by partial melting of mantle material. Empirical statistics shows that ore deposits associated with mafic-ultramafic rocks appear as favorite host for: Fe, Ti, Ni, Co, Cr, V, Cu, Pt and Au among the others. That economic concentrations of magnetite occuring as massive has been hot debated for long time, such as Kiruna, Pea Ridge and Cerro Mercado, all of which are formed at a relative high temperature (>500° C). Many models have been proposed to explain the origin of these deposits. Two of them are popular: separation of an immiscible (Kolker, 1982) or sorting (Duchesne, 1999; Charlier et al., 2006) iron oxide magma from the parent felsic/mafic magma and those invoking a hydrothermal solution (Barton and Johnson, 1996; Borrok et al., 1998). Some researchers devoted to contamination of sediment also could cause concentration of iron. For example, in southwestern China, Panzhihua gabbroic intrusion host huge Fe–Ti–V oxide reserves at its base which associated with Emeishan flood basalts. The ore bodies are mostly concordant with the late-Proterozoic dolostones intruded. Petrological modeling showed that under normal conditions, Fe–Ti oxides crystallize at a late stage, after the crystallization of abundant olivine, clinopyroxene and plagioclase. It means that the ore bodies should neither occur at the base of the gabbroic intrusion nor concordant with dolostone. In order for titanomagnetite to separate efficiently to form the ore deposit, the Fe–Ti oxides containing magma should be fluxed by

CO_2-rich fluids (Ganino et al., 2008). About the immiscible model, geochemical inheritance could helps better understanding the ore-forming processes. Magma may inherit a surplus of potential ore forming trace elements because the source material from which it was derived was itself enriched in those components. The sorting model in its most general sense is the iron segregation process from the other minerals, invoking abundant hot water and/or gas. The contamination model probably involves in the Ca silicate melt and concentration of iron (Gaeta et al., 2009).

An other extensively study case is the Kiruna magnetite deposit, however mostly they associated with intermediate-felsic rocks. According to geological description, within the Kiruna ore body, skarn-banded ore lies directly beneath the apatite-banded ore (Parak, 1985). Therefore, it seems that Kiruna-type deposit has certain relation with skarn. Kiruna magnetite deposit is huge and serves 1-2% of iron to the world (Jebrak and Marcoux, 2008). This deposit, as well as this type deposits, has been controversial long time. Their ore bodies are directly next to the felsic pluton. The definition of Kiruna type deposits is loose, but characterized by low-Ti, massive magnetite, and apatite rich. Kiruna type deposits occur in many tectonic environment of the world. The ores are dominantly composed by magnetite, apatite, actinolite. The size of Kiruna-type deposits are various, from small dykes to hundred millions of tons of high-grade ore (Nystroem and Henriquez, 1994). The prevail opinion for its origin is magmatic (Weidner, 1982; Nystroem and Henriquez, 1995). However, some researchers argued that Kiruna ores are exhalative-sedimentary, precipitated as chemical sediments in a volcanic-marine environment (Parak, 1984). Several magnetite deposits which associate with skarns are classed as Kiruna type, such as Malmberget and Leveaniemi (the third largest in the world) deposits in Sweden (Parak, 1985). These deposits are hosted by schistous rocks and next to granitic plutons. These lead Parak (1985) to conclude these deposits may relate to skarnization. Hildebrand (1986) explicitly indicated that separation of iron phosphate and silicate melts by liquid immiscibility is not

supported by alteration and mineralogical study, and ascribed to a deuteric origin. However, magnetite texture features (Nystroem and Henriquez, 1994; Nystroem and Henriquez, 1995), petrology study (Mücke and Younessi, 1994) and geochemisty (Hou et al., 2010) displayed magmatic origin.

1.3.4.5 Differences and similarities with Iron-oxides Copper Gold deposits (IOCG) and other magnetite deposits

It is not long since iron oxide–copper–gold (IOCG) deposits are recognized as a distinct class deposit. But their huge reserves and moderate to high grades attract numerous attentions for explorations. IOCG comprise a wide spectrum of mineralization styles, and they are characterized by low-titanium, iron-rich rocks formed in extensional tectonic environments (Hitzman et al., 1992; Sillitoe, 2003; Groves et al., 2010). Famous IOCG deposits/district include: the Olympic Dam Cu-U-Au-Ag deposit, South Australia; the Wernecke Mountain breccias, Yukon; and the southeast Missouri iron ore district. Hitzman et al. (1992) proposed that 'Kiruna-type' (magnetite-apatite type) should be considered a subset of this larger class.

According to Hitzman et al. (1992), salient characteristics of this class of deposits are as follows: (1) Age. The majority of known deposits, particularly the larger examples, are found within Early to mid-Proterozoic host rocks (1.1–1.8 Ga); (2) Tectonic setting. The deposits are located in areas that were cratonic or continental margin environments during the late Lower to Middle Proterozoic, and in many cases there is a definite spatial and temporal association with extensional tectonics. Most of the districts occur along major structural zones, and many of the deposits are elongated parallel to regional or local structural trends. The host rocks may be igneous or sedimentary; many of the deposits occur within silicic to intermediate igneous rocks of anorogenic type. However, mineralization in many deposits is not easily related to igneous activity at the structural level of mineralization; (3)

Mineralogy. The ores are generally dominated by iron oxides, either magnetite or hematite. Magnetite is found at deeper levels than hematite. CO2, Ba, P, or F minerals are common and often abundant. The deposits contain anomalous to potentially economic concentrations of REEs, either in apatite, or in distinct REE mineral phases; (4) Alteration. The host rocks are generally intensely altered. The exact alteration mineralogy depends on host lithology and depth of formation, but there is a general trend from sodic alteration at deep levels, to potassic alteration at intermediate to shallow levels, to sericitic alteration and silicification at very shallow levels. In addition, the host rocks are locally intensely Fe-metasomatized.

Currently, IOCG deposits are still relatively loosely defined. Some iron skarn deposits are classed into IOCG deposits, because IOCG deposits may have skarn-like affinities (Groves et al., 2010). Many deposits discussed or listed by Groves et al. (2000) are described as having skarn alteration and are more generally accepted as skarn deposits. For example, the 700km long, NNE striking Valerianov trend in Urals, which includes the Sarbai, Sokolovsk and Kachar deposits, hosts huge magnetite bodies. These magnetite bodies are described as skarns because they have skarn affinity (Koroteev et al., 1997). The Kachar deposit has been reported reserves of two billion tonnes of ore, probably in the grades of 45% contained iron in magnetite. But recently it has been lumped together with the IOCG class (Herrington et al., 2005; Groves et al., 2010). IOCGs mostly occur within magmatic-driven crustal-scale hydrothermal systems. Statistically, they are a coherent group with a very limited range of Cu and Au grades and Cu/Au ratios. Compare to iron skarn, they have unexpected high Au (Fig. 1-21).

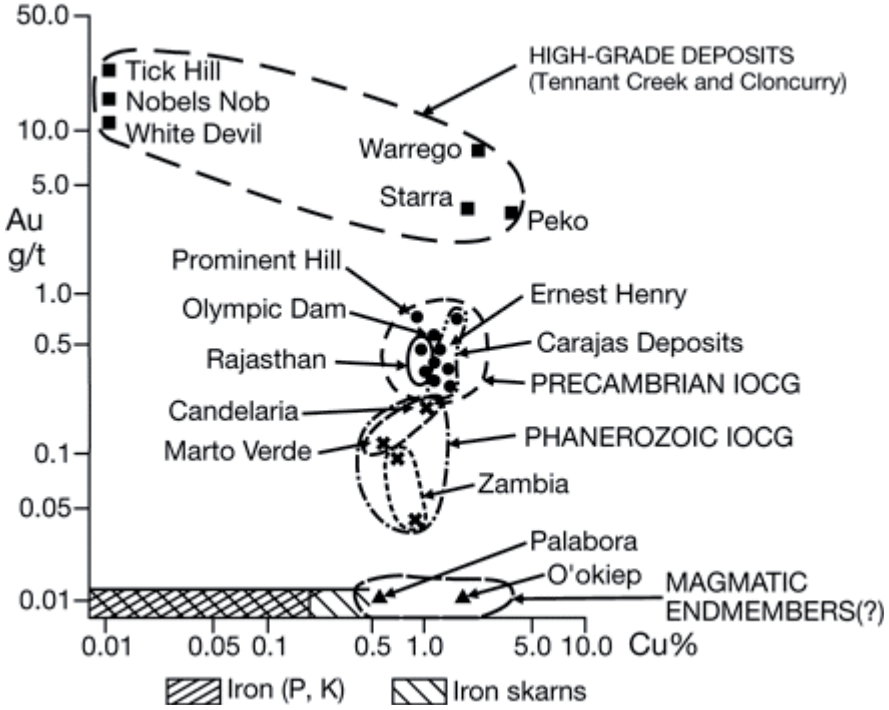

Fig. 1-21: Gold (g/t) versus copper (%) grades for IOCG deposits sensu stricto versus fields for iron oxide (P, F, REE) deposits and skarn deposits (Groves et al., 2010). Only deposits with greater than 100t resources are plotted. The high-grade Cu-Au or Au deposits from Tennant Creek and Cloncurry, Australia, commonly placed in the IOCG group. Note the lower copper and gold grades (closer to most porphyry-skarn Cu-Au deposits) of most of the Phanerozoic IOCG examples relative to the Precambrian examples and the low gold grades of Palabora and O'okiep. Also note that the upper limit in terms of gold for iron oxide-P-F deposits is poorly documented.

1.4 Problems: Major scientific questions on skarns and skarn-related iron deposits

The existence of extensive skarn attracts people's attention. Even the formation of skarn has been studied for long time, there are two aspects are overdue:

(1) The skarn forming processes which related to mafic magmatism. The heart of this issue is how the reactive fluid circulates and gives birth to mineral assemblage; how was their emplacements; in addition, the separating mechanisms of iron from the magma and how the assimilation process contributes the skarn forming are poorly understood;

(2) Geodynamic signification for iron mineralization associated with skarn in Tianshan orogenic belt.

Due to the importance of magnetite mineralization in the Chinese eastern Tianshan orogenic belt during late Paleozoic and early Mesozoic, the thesis takes the iron deposits of this area as the research object. Generally acknowledged dynamic model for the Eastern Tianshan is that it was formed progressive accretion of different blocks or terrain, arcs and accretionary complexes onto the southern margin of Siberia during the Paleozoic (Wang et al., 2010; Charvet et al., 2011). In this region, the iron deposits are hosted by: Precambrian metamorphosed volcanic sedimentary type (e.g.Tianhu iron deposit) (Jiang et al., 2002; Qin et al., 2003), Carboniferous volcanic sedimentary type (e. g. Wutongguo and Yamansu iron deposit), Permian gabbro-diabase type (e.g. Cihai iron deposit) (Xue et al., 2000; Zuo et al., 2004) and gabbro V-Ti-Fe type (e.g. Weiya V-Ti-Fe deposit) (Wang et al., 2006). These iron deposits are all invoking iron oxide, mainly magnetite, sometimes the magnetite occurs as massive ore bodies. The last three types involve mafic/ultramafic magmatism which will be emphasized in this thesis. The objective of this thesis was to investigate the skarn formation, tracing the metasomatic fluid, its relation with magmatism, its interaction with $CaCO_3$ contained wall rocks, and the skarn related magnetite formation. Two magnetite deposits are selected as the research targets: Yamnasu magnetite deposit (32Mt with 51%TFe) and Cihai magnetite deposit (23Mt with 45.7% TFe), which are two of the biggest iron deposits in the eastern part of region (Yu et al., 1999; Mao et al., 2005). Studying the two deposits are important for mineral exploration, as well as to metallogenic mechanism of magnetite between the mafic magmatism and wall rocks. The overarching aim of this study is to make significant contributions to figure out the magnetite mineralization and skarnization processes for the mafic-ultramafic magma.

Chapter 2 Geodynamics and Metallogeny of eastern Tianshan orogenic belt

Résumé:

L'évolution géodynamique du Tianshan oriental est caractérisée par l'accrétion de différents terranes sur la marge méridionale du bloc sibérien. Le Tianshan oriental est composé de quatre unités tectoniques limitées par de grands accidents. On distingue ainsi, du Nord vers le Sud: l'arc de Danahu, la ceinture d'Aqishan – Yamansu, le domaine médian du Tianshan et la ceinture de Beishan. Dans ces quatre unités, les formations carbonifères sont généralement bien préservées. Dans les deux unités méridionales, les formations paléozoïques reposent sur un socle précambrien composé de métasédiments. Dans les quatre unités, le Paléozoïque est surmonté par des sédiments terrigènes datés de la fin du carbonifère. Ces venues indiquent le début de la collision continentale. Dans les terrains phanérozoïques, les formations de Yanansu et Xiaorequanzi encaissent des minéralisations à Fe-Cu.

La plupart des plutons connus dans cette région sont datés de la fin du paléozoïque, quelque uns du Trias. Ces intrusions développent une auréole métasomatique importante au contact des calcaires.

Plusieurs phases métallogéniques ont été distinguées dans le Tianshan oriental: (1) 360-320 Ma, lors d'un stade de subduction, on a formation de minéralisations associées à des skarns et la mise en place de porphyres cuprifères. (2) 300-280 Ma, dans un contexte de collision, se forment quelques gîtes aurifères et skarns. (3) 280-245 Ma, lors d'un stade d'extension post-collision, on a formation des gisements à Cu-Ni magmatique et de minéralisations épithermales aurifères. La plupart de ces gisements sont localisés le long de la zone décrochante de Kangguer. (4) 245-220

Ma, un stade d'extension intracontinentale est marqué par la mise en place de skarns à W – Mo et par les minéralisations orthomagmatiques à Fe-V-Ti comme celle de Weiya.

Abstract:

The eastern Tianshan is characterized by progressive accretion of different blocks onto the southern margin of Siberia including: continental slivers, arcs and accretionary complexes. As defined in this thesis, the eastern Tianshan is composed by four tectonic units which are delineated by large faults: the northernmost belt (Dananhu arc belt), northern belt (Aqishan-Yamansu belt), Middle Tianshan terrane and the southern belt (Beishan belt). A literature survey on strata of this region displayed that the four belts generally preserve Carboniferous strata of which the Middle Tianshan terrane and Beishan orogenic belt have Precambrian metasedimentary basement; all of them turned into terrigenous deposit in the end of Carboniferous indicating the beginning of continental collision. Among the phanerozoic strata, the Yamansu Formation and Xiaorequanzi Formation are known as holding Fe-Cu ore bodies.

Many plutons in this region were known as late Paleozoic and a few of them may form during Triassic. These plutons intruded the sedimentary rock and caused extensive metasomatism where limestone occurred mostly. The mineralization processes in Eastern Tianshan are multiple periods: (1) 360-320Ma subduction-island arc stage: this stage mainly contain skarn related deposits, as well as porphyry Cu; (2) 300-280Ma collisional accretionary stage: this stage yield some gold deposits and skarn; (3) 280-245Ma post collisional extension strike-slip stage: numerous mafic-ultramafic Cu-Ni deposits with epithermal gold. Mostly these deposits distributed along the Kangguer shearing zone; (4) 245-220Ma intracontinental extensional stage: this stage yield W-Mo skarn and Fe-V-Ti orthomagmatic deposits, such as Weiya deposit. Four major deposit types were reviewed in this chapter: mafic/ultramafic intrusion related Cu-Ni-(V-Ti) deposits, gold mineralization, porphyry Cu and skarn related ore deposits.

Herein, the eastern Tianshan (tian = sky, celestial, shan = mountain) is defined as that part of the Tianshan mountain range (Fig. 2-1A). It locates to the East of Urumqi-Kuerle highway and is bounded to the north by the Tuha basin, which is thought to be a part of the Junggar block (Ma et al., 1997; Charvet et al., 2007), to the south by the Tarim block and to the east by the southern Mongolian fold belt. According to the definition, it consists of four terranes: the Dananhu island arc to the northmost and Aqishan-Yamansu belt (also called Jeuloutage orogenic belt) to the north, middle Tianshan terrane in the centre and late Paleozoic Beishan rift belt to the south, as well as part of South Tianshan terrane and Kuluketage terrane to the South-West (Fig. 2-2). These domains are separated by several crustal scale faults, namely Kangguer, Aqikekuduke-shaquanzi and Hongluihe faults (Xiao et al., 2004; Xiao et al., 2004; Gu et al., 2006; Gu et al., 2007; Pirajno, 2010; Xiao et al., 2010; Charvet et al., 2011). Some of these faults were considered as sutures, such as Kangguer fault with strike-slip shearing affinity (Xiao et al., 2010; Mao et al., 2011). The eastern Tianshan is a remote serious desertification Gobi area (Fig. 2-1B) located in eastern Xinjiang, northwestern China. It is a typical example of accretion and collisional orogen (Charvet et al., 2011).

A

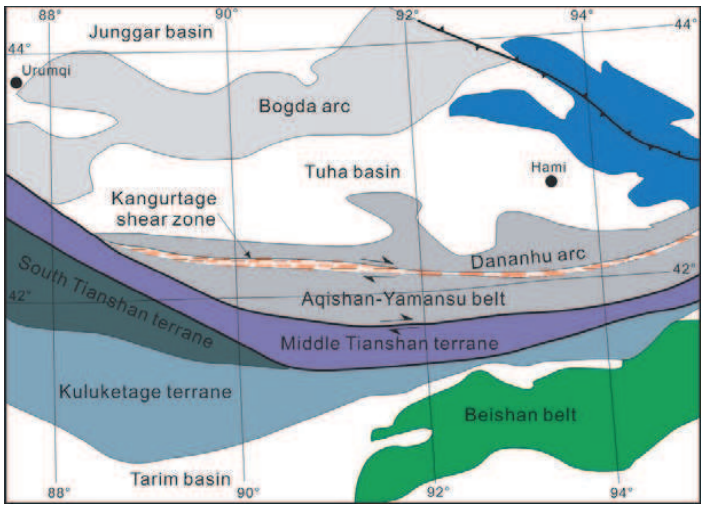

B

Fig. 2-1: (A) Schematic geological map showing the eastern Tianshan belt; (B) Eastern Tianshan gobi. Picture shows a serious desertification phenomenon. Very dry in this region, the average annual amount of water are less than 200 ml.

Early Chinese geologists considered the Tianshan as a geosyncline that formed on the northern boundary of the Tarim (Ren et al., 1980). There is a growing acceptance that the Tianshan orogenic belt was formed in late Paleozoic (Clive F, 1974; Burtman, 1975; Coleman, 1989) and it plays very important role in understanding the tectonic evolution of Paleozoic Eurasia or the Altaid tectonic collage (Sengor et al., 1993). The tectonic evolution of eastern Tianshan has been hot debated. Recently, the model of progressive accretion and collision are generally accepted. To the end of Carboniferous, collage was thought to be completed (Laurent-Charvet et al., 2002; Wang et al., 2009; Han et al., 2010; Wang et al., 2010; Charvet et al., 2011). It means there were not any more oceans between the micro-continentals in this region. During the Permian, all the units already amalgamated experienced a major crustal

scale dextral strikie-slip shearing in the whole Tianshan area, in order to accommodate the opposite motion of Siberia and Tarim cratons (Shu et al., 1999; Chen et al., 2005). Within eastern Tianshan, many mafic/ultramafic and felsic plutons, even A-type granite, are temporally and spatially associated with crustal scale strike-slip faults (Pirajno, 2010).

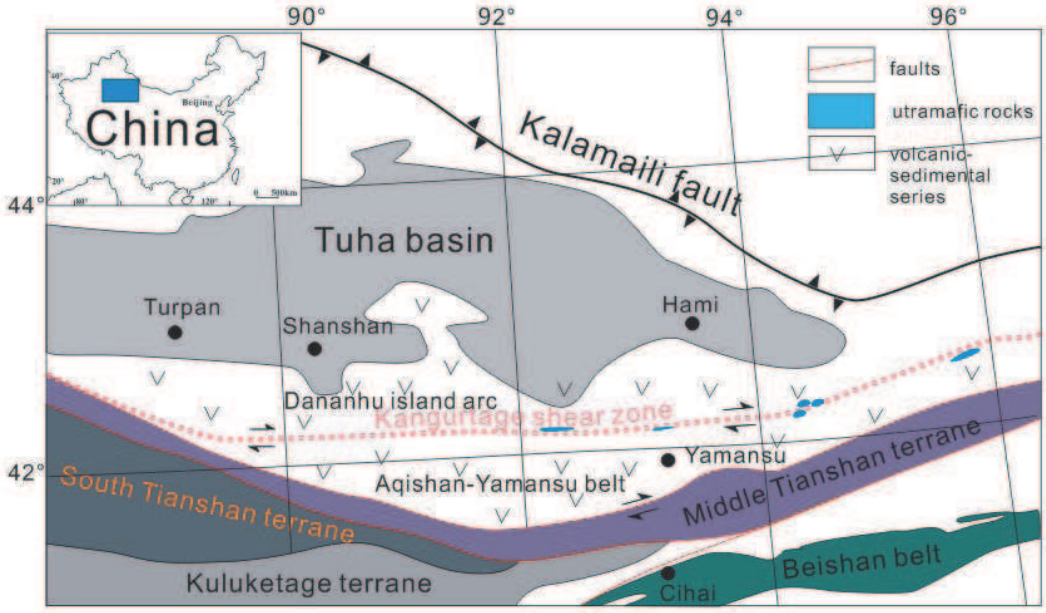

Fig. 2-2: Simplified map showing tectonic units and main faults of the eastern Tianshan, modified from Li (2004) and Gu et al. (2006). Major ultramafic intrusions associated with Cu-Ni deposits are added.

2.1 Tectonic units

Tectonically, the eastern Tianshan defined in this memoir could be divided four terrains: Dananhu island arc belt, Aqishan-Yamansu belt, Middle Tianshan terrane and Beishan Permian rift (Fig. 2-2). The present boundary between them are typically marked by strike-slip crustal scale shear zone, from the North to South, they are Kangguer, Main Tianshan Shear Zone (also called Aqikekuduke-Shaquanzi zone) (Laurent-Charvet et al., 2002) and Honluihe fault (Gu et al., 2006).

2.1.1 The Northernmost belt (Dananhu island arc belt)

Dananhu island arc belt is characterized by wild exposed arc affinity rocks and two

porphyry Cu deposits (Tuwu and Yandong). Four lithostratigraphic formation associations have been recognized based on detailed geological mapping in this belt: the Lower Carboniferous Xiaorequanzi Formation consisting mainly of volcanic rocks, the Upper Carboniferous Dikan'er Formation composed of clastic rocks intercalated with carbonate, the Upper Carboniferous Qi'eshan Formation comprising volcanic rocks, and the Upper Carboniferous Qishan Formation of clastic and carbonate rocks (Zhang et al., 2010). This formation association, their geochemistry of volcanic rocks, their fossils and spatial relationship together with previously published geochronological data suggest that the previously-thought Dananhu arc is actually made of arc volcanic rocks, back arc basin sediments and remnant oceanic basin sediments. From plutonism point of view, this belt probably had always been continental margin environment since late Devonien time because granites of arc affinity have been found (Song et al., 2002).

2.1.2 Northern belt (Aqishan-Yamansu belt)

The Aqishan-Yamansu belt is an important component of the eastern Tianshan, but it is also the most controversial belt. It is separated by the Kangguer strike-slip shear zone to the North and the Aqikekuduke-shaquanzi fault to the South (Fig. 2-2).

About the tectonic context of the Aqishan-Yamansu belt has been hot debated for long time. In this belt, large area of calc-alkaline magma developed and their geochemical affinity, as well as mineral compositional analysis, leading the some researchers to identify an arc (Ma et al., 1997; Hou et al., 2006; Wu et al., 2006; Zou et al., 2006; Hou et al., 2007). But in the other side, some researchers devoted to a rift model basing on tectonic geochemical analysis, metal assemblage, stratigraphic columns and volcanic rock (Xia et al., 2004; Mao et al., 2005). Large granitic plutons well develop within this belt. In addition, this belt comprises a 5 km thick section of Lower Carboniferous Yamansu Formation bimodal volcanic rocks, middle Carboniferous flysch of the Shaquanzi Formation, and Upper Carboniferous clastic

rocks, andesitic tuff, and intercalated carbonate of the Tugutublak Formation. Overlying unconformable Permian shallow marine and terrestrial clastic rocks were intercalated with bimodal volcanic rocks and carbonates (Wartes et al., 2002).

2.1.3 Middle Tianshan terrane (MTT)

MTT is characterized by a Proterozoic basement composed of gneiss, amphibolites and marbles (XBGMR, 1993; Hu et al., 1998; Hu et al., 2000; Liu et al., 2004; LI et al., 2007; Lei et al., 2011), some Lower Paleozoic granitic gneisses and metasandstone including Ordovician-Silurian volcanic-arc rocks, Silurian flysch, subduction-related Silurian-Early Devonian plutonic rocks, and post-orogenic Late Devonian granites. A major feature is that the angular unconformity of Lower Carboniferous conglomeratic molasse, which clearly overlies various older rocks (Charvet et al., 2011). MTT was thought to be part of the Tarim craton according to zircon chronology and Hf isotopic study (Lei et al., 2011).

2.1.4 Southern belt (Beishan orogen)

Beishan orogen situates in the Southern part of the eastern Tianshan as defined at the beginning. This belt was largely thought of as an early Paleozoic orogen, which evolved into a continental rift in the late Paleozoic (He et al., 2002; Xu et al., 2008; Xu et al., 2009). This belt consists of several arcs and ophiolitic melanges, and its youngest strata involved in the deformation of this region are Permian (Xiao et al., 2010). Distributions of mafic/ultramafic dykes and plutons with rift affinity are observed within this region (Zuo et al., 2003; Liu et al., 2006; Zhao et al., 2006). Mafic-ultramafic rocks and coeval acidic igneous rocks form a bimodal igneous series (Su et al., 2011), indicating the Beishan region was a late Paleozoic rift. Volcanics possess continental rift features (Jiang et al., 2006; Qin et al., 2011). From the view of volcanic sedimentary series, the formation and evolution the rift had been reported (Zhou et al., 2000). It reported that more than 90 deposits or mineralization points have been found, of which 6 deposits are middle to large class

(Cheng et al., 2008).

2.1.5 Northern shearing Zone (Kangguer shearing zone)

The Kangguer shearing zone is located between the northernmost belt (Dananhu island arc belt) and the Northern belt (Aqishan-Yamansu belt). It is a crustal scale dextre strike-slip shearing zone of Permian time (Chen et al., 2005; Wang et al., 2005) and famous for its syntectonic orthomagmatic Cu-Ni deposits and hydrothermal Au (Mao et al., 2005; Mao et al., 2008). This E-W-trending shear zone is composed of a series of mylonitized rocks that display well developed S-C fabrics, stretching lineation and rotational porphyroclasts. Some researchers held the opinions that it was a ophiolitic suture because numerous of mafic-ultramafic plutons distributed along this shearing zone (Cao, 1997; Li et al., 2005). Whereas some studies argued against this opinion and ascribe the emplacement of mafic-ultramafic intrusions to syntectonic emplacement, such as Huangshandong pluton (Fig. 2-5) (Chen et al., 2005).

The “suture” holders mainly derived from: (1) The geophysical data show significant difference between Dananhu island arc belt and the Aqishan-Yamansu belt which is coincide with all geological observations (Zhang et al.; Liang et al., 2001); (2) mafic/ultramafic intrusions occurred in this shearing zone. However, the opposite group ascribed the mafic/ultramafic intrusions to syntectonic plutons, and there were not obvious evidence for ocean floor, neither supported by structure study (Branquet et al., 2012) nor geochemical study (Zhou et al., 2004).

Although different opinions on its affinity, that Kangguer shearing zone marking the boundary between Dananhu island arc belt and the Aqishan-Yamansu belt is generally acknowledged (Li, 2004; Charvet et al., 2011).

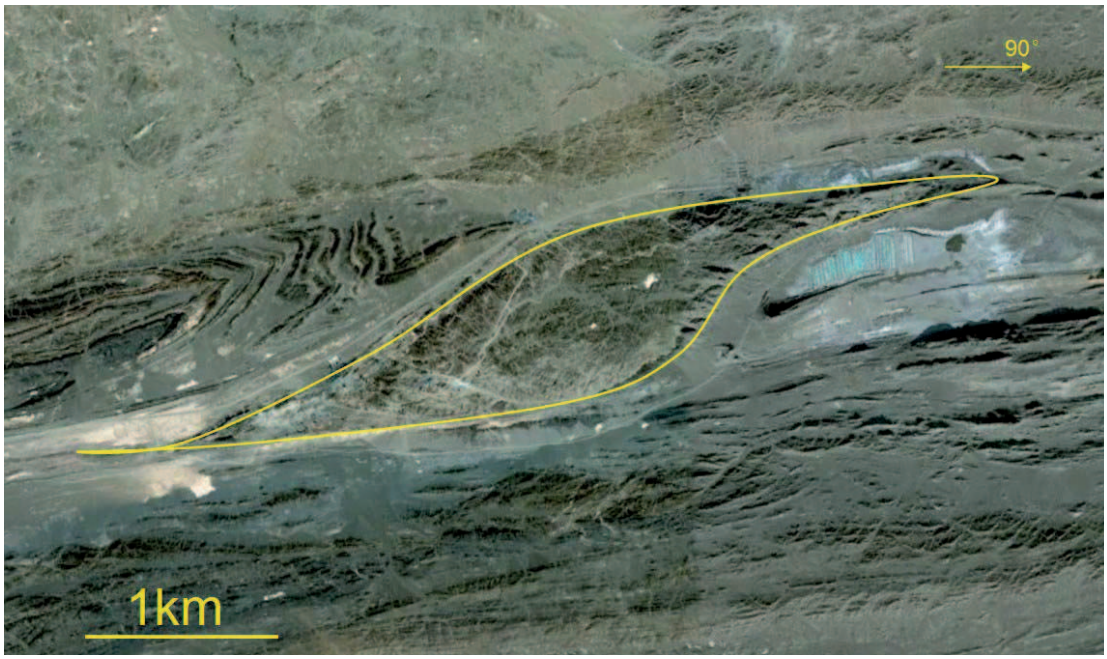

Fig. 2-5: Satellite image from Google EarthTM of the Huangshan Ni-Cu ore field which is emphasized in yellow line. The dextral shearing lineations around the pluton are clearly exposed.

2.2 Strata

The proportion of strata cropping-out in the five units mentioned above is different. However, the Permian and the Carboniferous seem occurred in all units. The Carboniferous was mainly composed by marine or shallow marine sediment which was unconformably overlain the Permian terrigenous sequence (Wartes et al., 2002).

2.2.1 Northernmost belt (Dananhu island arc belt)

Exposed strata are mainly composed by:

(1) Middle Ordovician Kekeshayi Formation: spilite keratophyre;

(2) Upper Ordovician Daluihe Formation: marine basic and felsic volcanites;

(3) Middle Silurian Baishanbao Formation: marine volcanites and clastic rocks;

(4) Lower Devonian Dananhu Formation: marine basic and felsic volcanic rocks, intercalated volcanic clastic rocks;

(5) Middle Devonian Tousuquan Formation: marine basic volcanic rocks and

intercalated clastic rocks;

(6) Upper Devonian Kangguertager Formation: paralic sedimentary clastic volcanic rocks ;

(7) Lower Carboniferous Xiaorequanzi Formation: bimodal volcanic rocks;

(8) Lower Carboniferous Wutongwozi Formation: bimodal volcanic rocks;

(9) Upper Carboniferous Dikaner Formation: terrigenous clastic rocks ;

(10) Permian: terrigenous clastic rocks and intercalated small amount of volcanic rocks;

(11) Triassic and Jurassic: terrigenous clastic rocks.

This sediment series was little metamorphic. From this sediment series, we can see that this belt was dominated by marine sedimentary before Carboniferous. Late Devonian and early Carboniferous were transition period. Since late Carboniferous, it had entered terrigenous sedimentary series.

Located in the southern margin of Dananhu arc, Tuwu and Yandong porphyry Cu deposits have been exploited for years. Four lithostratigraphic Formations nearby in the Carboniferous Dananhu arc belt, which may reflect its forming geological context of the ore forming, are recognized (Fig. 2-6) (Zhang et al., 2010). Details are as following:

(1) the Lower Carboniferous Xiaorequanzi Formation consisting mainly of volcanic rocks;

(2) the Upper Carboniferous Dikaner Formation composed of clastic rocks intercalated with carbonate;

(3) the Upper Carboniferous Qieshan Formation comprising volcanic rocks.

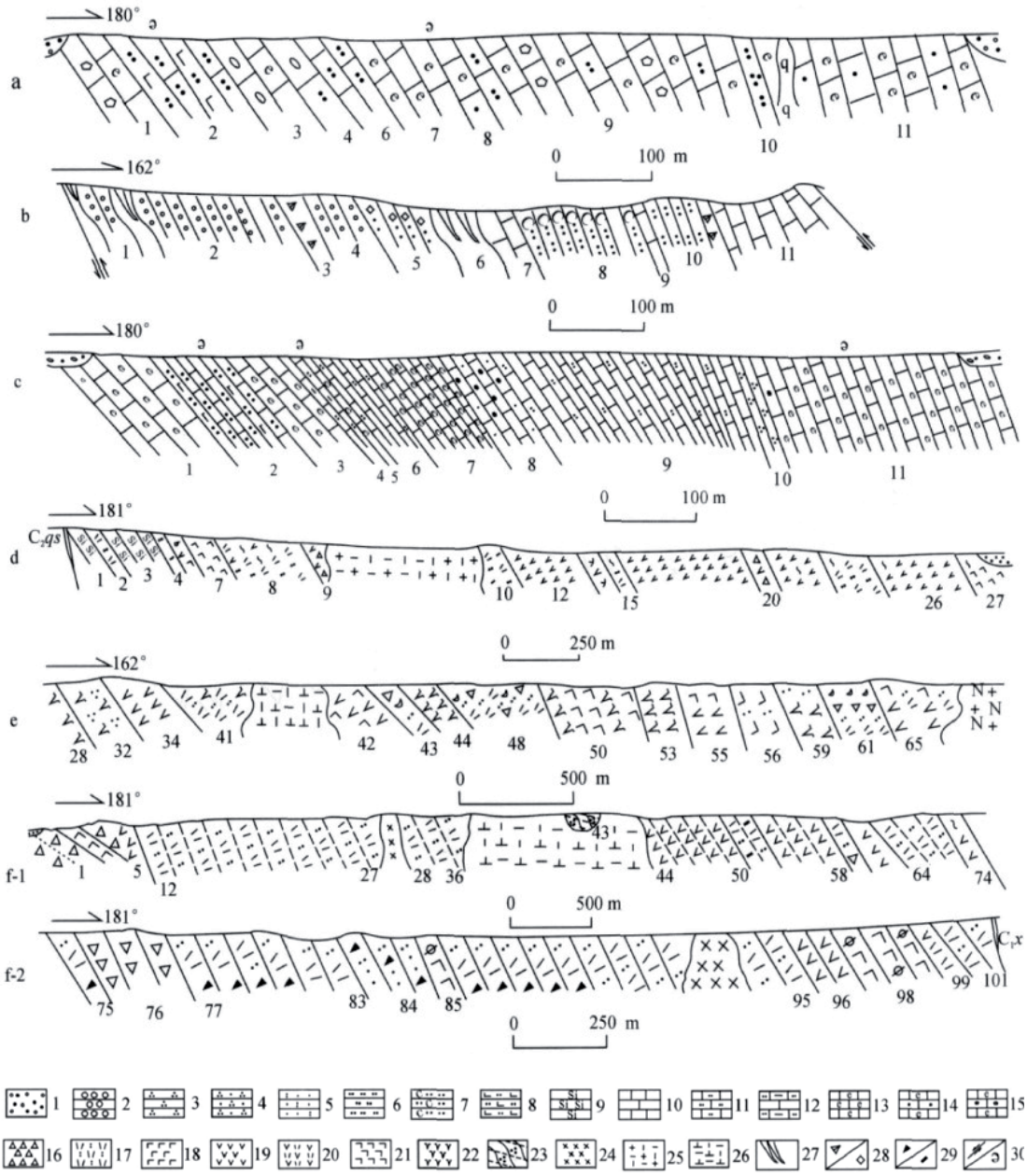

Fig. 2-6: Geological section of Carboniferous strata in Dananhu arc (Zhang et al., 2010). a: section of Dikaner fm; b: section of of Dikaner fm; c: section of Qishan fm; d: section of Xiaorequanzi fm; e: section of Xiaorequanzi fm; f: section of Qieshan fm. 1. Quaternary; 2. conglomerate; 3. sandstone; 4. quartz sandstone; 5. tuffaceous sandstone; 6. siltstone; 7. Carboniferous siltstone; 8. calcareous siltstone ; 9. chert; 10. limestone; 11. silty limestone; 12. argillaceous silty limestone; 13. bioclastic limestone; 14. bioclastic calcirudite; 15. bioclastic micrite; 16. volcanic breccia; 17. tuff; 18. basalt; 19. andesite; 20. dacite; 21. spilite; 22. albitophyre; 23. quartz hornstone; 24. gabbro; 25. granite; 26. quartz diorite; 27. quartz vein; 28. cataclastic/carbonation; 29. debris/ vitric; 30. fault/fossil position.

2.2.2 Northern belt (Aqishan-Yamansu belt)

In this belt, all strata before Carboniferous were poorly exposed. From early Carboniferous to early Permian, it has similar sediment series with the northernmost belt (Dananhu belt). Carboniferous island arc sedimentary very well developed covering most of the area of this belt. Island arc sedimentary massively develop leading previous study to call it "Carboniferous Aqishan-Yamansu island arc belt". Generally, most sedimentary series formed in shallow to the marine environment in Carboniferous. Details are as following:

(1) Lower Carboniferous Xiaorequanzi Formation (C1X): This formation develops better in the Western part. It mainly composed by andesite, quartz andesite, volcanic breccia, tuff, rhyolite, trachyte, basalt in the lower part with small amount of lava rock and clastic rocks in the upper part. Contains fossile: produetus sp., Spiriferineertus, S.aff, kasks, Avoniasp.

(2) Lower Carboniferous Yamansu Formation (C1y): Mainly develop in the Yamansu region and composed by thick calc alkaline—alkaline—acidic volcanic rocks and clastic-carbonate rocks. Flysch was observed, about 5000m thick. This formation could be subdivided into 5 parts (Han, 2003): (A) Coarse-grained sandstone, pebbly coarse-grained feldspathic sandstone complex, mainly composed of gray, gray pebbly coarse-grained feldspar greywacke, tuffaceous coarse-grained sandstone, silicified fine-grained crystalline limestone, with angle gravel plagioclase rhyolitic crystal tuff, silty mudstone, siliceous rocks; (B) Sandstone, conglomerate, crystallized limestone, mostly gray, dark gray; (C) Feldspar clastic sandstone in coarse-grained; (D) Clastic rocks and andesite; (E) Calc-alkaline volcanic clastic rocks. Mainly by the acidic detritus, quartz trachyte tuff, rhyolite, rhyolite dacite, tuff, crystalline limestone, dolomitic marble.

(3) Middle Carboniferous Shaquanzi Formation (C2S): mainly composed by flysch. From low to top, the lithology is conglomerate, sandstone, siltstone, mudstone and limestone. Contain fossile: Profusulina Sp., Fusiella Sp., Ozawainella Sp.,

Lithostrotionella sp. Pseudostaffella sp., Eostaffella sp. Yamansu Formation and Shaquanzi Formation is discordant.

(4) Middle Carboniferous Tugutubulake Formation (C2S): It discordantly covers over the Shaquanzi Formation (C2S). It is composed by calc conglomerate, tuffaceous sandstone, andesitic tuff breccia, andesitic tuff with limestone lenses.

(5) Lower Permian Aqikebulake Formation (P1a): It is composed by paralic sedimentary clastic rocks with some basic- felsic- volcanic rocks.

2.2.3 Middle Tianshan terrane (MTT)

In this belt, Precambrian sediment series were observed. Carboniferous sedimentary is also identified, but no well documented.

(1) Mesoproterozoic Xingxingxia group: it is set of low greenschist facies – ampibolite facies metamorphic rocks. The protoliths were flysch and clastic-carbonate rocks (Hu et al., 1986). Xingxingxia group is about 2400m thick in Xingxingxia region and composed by migmatite, gneiss, marble. Whereas it is up to 4000m thick in Kumishi;

(2) Mesoproterozoic Kawebulake group: It is concordant with Xingxingxia group and composed by marble, schist, quartzite, dolostone, gneiss, metasandstone.

2.2.4 Southern belt (Beishan orogen)

Diverse strata in this belt are better preserved. TTG (Trondhjemite, Tonalite, Granodiorite) which represent crust growth in Archean time was also reported in this belt (Zhou et al., 2000; Yang et al., 2006). Proterozoic is mainly composed by greenschist ampibolite facies metamorphic rocks which formed the metamorphic basement. Sedimentary series changed from marine facies (Sinian end early Paleozoic) to paralic sedimentary clastic facies (late Paleozoic) and terrigenous facies (late Paleozoic).

(1) Lower Proterozoic: metamorphic clastic rocks;

(2) Lower Mesoproterozoic: quartzite, slate and marble;

(3) Upper Mesoproterozoic: marble and clastic rocks;

(4) Sinian and early Paleozoic: siliceous limestone, terrigenous clastic rocks;

(5) Lower Devonian: missing;

(6) Middle Devonian: flysch and thick basalt. The basalt was about 1600m thick.

(7) Upper Devonian: dacite and acidic tuff. It is discordant covering the Middle Devonian;

(8) Carboniferous: It reaches about 10000m thick. The Lower Carboniferous is mainly composed by limestone, sandstone and shale. Lower Carboniferous discordantly covered the early Paleozoic. Middle Carboniferous is composed by spilite-keratophyre, terrigenous clastic rocks, limestone. Upper Carboniferous is composed by basic volcanic rocks, carbonate rocks and clastic rocks;

(9) Permian: Lower Permian contained pillow lava, spilite, keratophyre, tuff, sandstone, limestone; Upper Permian contained marine clastic rocks and limestone.

(10) Mesozoic and Cenozoic: mainly composed by lacustrine, alluvial facies and swamp sediment containing sandstone, conglomerate, shale and limestone.

2.2.5 Summary of the strata

The four belts generally preserve Carboniferous strata overlain unconformably by Permian (Fig. 2-7). MTT belt and Beishan orogen belt have Precambrian metasedimentary basement. All of them turned into terrigenous deposit in the end of Carboniferous indicating continental collision. Among the phanerozoic strata, the Yamansu Formation and Xiaorequanzi Formation are known as holding Fe-Cu ore bodies.

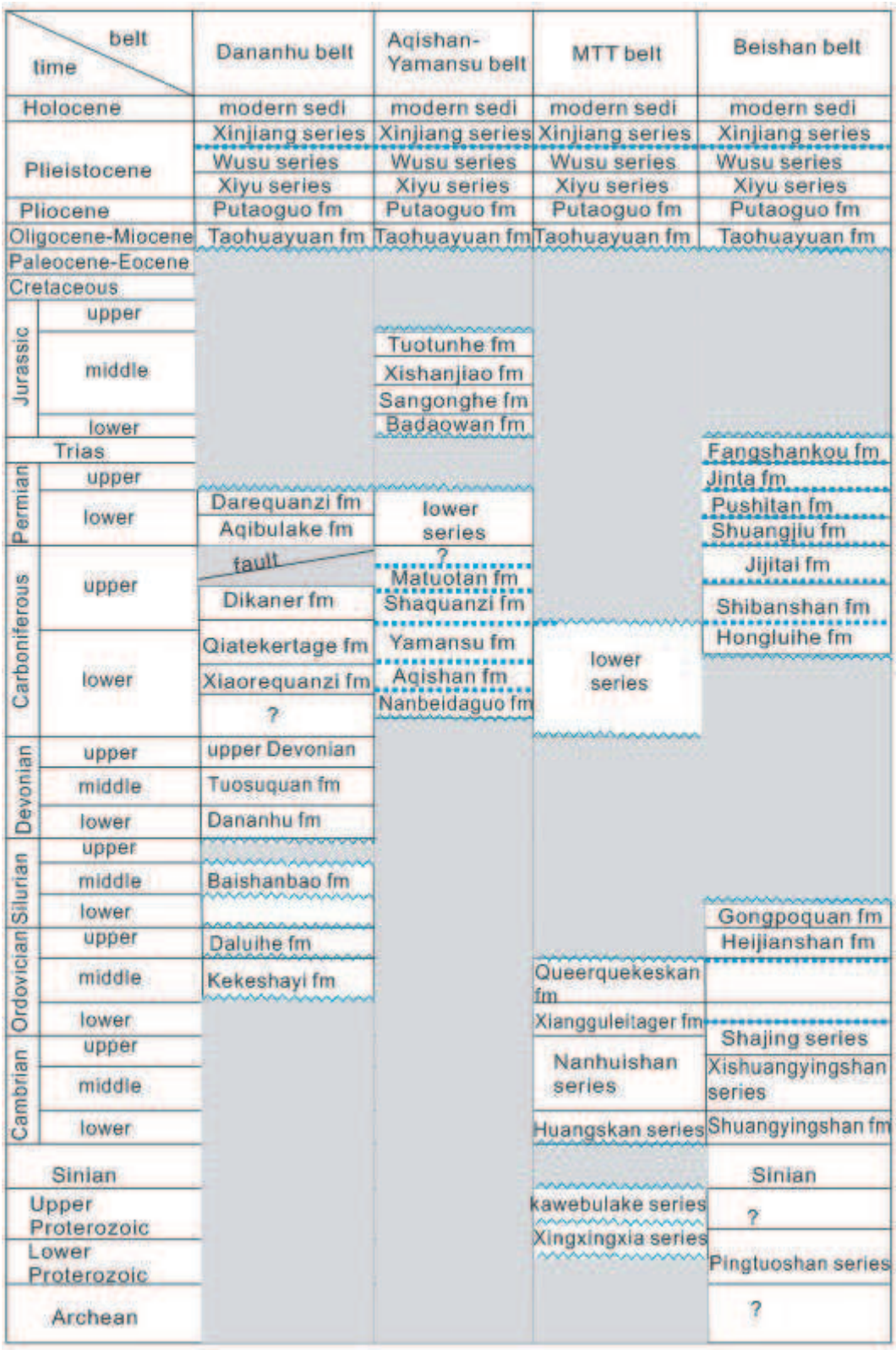

Fig. 2-7: Stratigraphic comparison of the Eastern Tianshan units (XBGMR, 1993; Han, 2002). Dotted lines mark the para-unconformity, wave lines mark angular unconformity.

2.3 Magmatism

The eastern Tianshan, even the whole CAOB, is characterized by large distribution of Paleozoic and Mesozoic magmatism, including granitic intrusions, basatic to rhyolitic valcanics, as well as mafic/ultramafic intrusions (Fig. 2-8). This magmatism recorded the tectonic evolutions. Numerous of granitic plutons show arc affinity in this belt (Wu et al., 2006). In addition, most Sr-Nd isotope data indicated that the magmatism of eastern Tianshan contains juvenile materials, including younger lower crust. This result led to the suggestion that the eastern Tianshan suffered Phanerozoic crustal growth

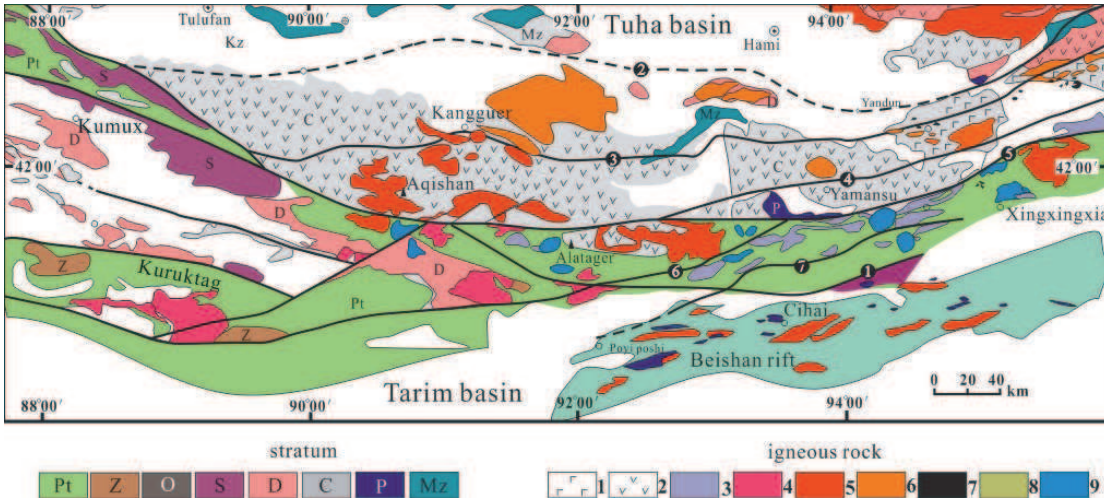

Fig.2-8: Schematic geological map of Eastern Tianshan Mountain (modify from Gu et al., 2005)
stratum: Pt-Proterozoic, Z-Sinian, O-Ordovician, S-Silurian, D-Devonian, C-Carboniferous, P-Permian, Mz-Mesozoic; igneous rock: 1-basic volcanic rock, 2- intermediate and quartz-feldspathic rock， 3- Precambrian gneissose granite，4-caledonian granodiorite and biotite granite, 5- Early and middle Hercynian quartz granodiorite, granodiorite, biotite granite, 6-Late Hercynian granodiorite, biotite granite, muscovite granite, 7- Late Hercynian mafic-ultramafic rock, 8- Late Hercynian alkali granite, 9- Indosinian granodiorite, biotite granite.
Fault: 1- Hongluihe fault; 2-Dikaner-qincheng fault; 3-Kangguer shearing fault; 4-Yamansu fault; 5- Aqikekuduke-shaquanzi fault; 6-Loubupo-weiya fault; 7-Xingxingxia fault.

2.3.1 Granitic plutons

Compared to mafic/ultramafic intrusions, granitic plutons are conspicuous. Most of the granites are associated with arc and have calc alkaline affinity. Likewise, these

granites could classed into I type and S type (Yuan et al., 2010). Some studies reveal that many of the post collisional granitic intrusions are A-type anorogenic granites that formed in an intra-plate extensional setting (Zhou et al., 2006; Pirajno, 2010). The Paleozoic granitic plutons have a wide range of compositions and roughly show a temporal evolution from calc-alkaline, alkaline to peralkaline series (Jahn et al., 2000; Wang et al., 2009). According to Gu et al. (2006), granite formation after major continental collision in the eastern Tianshan Mountains can be divided into three stages: the compression-extension transition stage (310-285Ma), the post-collision extension stage (285-250Ma) and the intra-plate stage (250-208Ma). These granites mainly contribute to the growth of the crust of eastern Tianshan (Gu et al., 2006).

2.3.2 Mafic-ultramafic plutons

Mafic/ultramafic intrusions are formed mainly in Permian, the post collisional stage. Some of them contain economic metals, such as Huangshandong, Huangshan, Xiangshan, Hulu, Tulaergen and Haibaotan (Zhou et al., 2004; Li et al., 2006; Li et al., 2007; Sun et al., 2007). Petrological and geochemical characteristics of these mafic-ultramafic plutons indicated that they are derived from depleted mantle and contaminated by crustal materials (Zhou et al., 2004). They are commonly found along strike-slip zones. These intrusions share similar features, for example funnel shaped, concentric zonation, small size and many host magmatic sulfide deposits (Mao et al., 2005; Li et al., 2007; Sun et al., 2008).

2.3.3 Volcanite

There are two volcanic belt in eastern Tianshan defined at the beginning, Dananhu island arc belt and Aqishan-Yamansu belt (Fig. 2-2). It seems little disputed for Dananhu island arc belt which is marked by huge calc-alkaline basatic volcanics. Whereas in Aqishan-Yamansu belt, basatic volcanics are companied by rhyolitic valcanics. It led some researchers to conclude that they composed bimodal valcanics

(Xia et al., 2004; Mao et al., 2005). In other term, Aqishan-Yamansu belt may be a rift during Carboniferous.

2.3.4 Chronology of magmatism

Magmatism of eastern Tianshan mostly associated with arc calc alkaline in early Paleozoic time. Carboniferous was a transition period and Permian was large scale strike-slip shearing time. These tectonic evolutions should correspond to magmatism. Late Paleozoic is a peak of magmatism indicating fast crustal growth (Table 2-1) (Gu et al., 2006). Dating research on the volcanic rocks are relative rare comparing to plutons. The data on volcanic dating being cited in Table 2-1 is from the Tuwu area where Tuwu porphyry Cu deposit occurs. Besides, A-type granite or alkaline rocks are rare in the four belts mentioned above. Permian alkaline granite is reported from Harlik Mountians to the North of Tuha basin (Wang et al., 2009).

Table 2-1: Chronology of magmatism in Eastern Tianshan

	northernmost belt (Dananhu belt)	Northern belt (Aqishan-Ya mansu belt)	MTT	Southern belt (Beishan orogenic belt)
Precambrian			Tianhudong gneissic granite: calc-alkaline, 707Ma (Rb-Sr) (Zhang et al., 2004) 696Ma (Rb-Sr) (Gu et al., 1990) Pingdingshan granite: 913Ma (Rb-Sr) (Gu et al., 1990) Xingxingxia granodiorite : 1218-1216Ma (zircon U-Pb) 1142Ma (Sm-Nd) (Liu et al., 2004) Xingxingxia granodiorite :809Ma, 1400Ma, 1750Ma (inherited zircon U-Pb) (Lei et al., 2011) Shalongdong granite : 470Ma (Rb-Sr) (Gu et al., 1990)	
Early Paleozoic				
later Paleozoic	Tuwu basic volcanites: 322Ma, rhyorite 319Ma (zircon U-Pb) (Li et al., 2004) Xianshuiquan gneissic granite : 367Ma (zircon U-Pb) (Tang et al., 2007)	Hongyuetan granite :328Ma (zircon U-Pb) (Wu et al., 2006)	Xingxingxia granodiorite : arc 424Ma (Lei et al., 2011) Baluntai mylonitized granite : arc, 405-416Ma (zircon U-Pb) (Yang et al., 2006) Gangou granitoids : arc 428Ma (zircon U-Pb) (Shi et al., 2007) Alatager granite : 320Ma (unpublished data) Sanchakuo granitic porphyry (contain Cu): 278Ma (Li et al., 2004)	Hongshishan gabbro 322Ma, rhyolite 279Ma, diorite 280Ma, troctolite 286Ma (Su et al., 2011) Luodong gabbro (associated with orthomagmatic Cu-Ni) 284Ma (Su et al., 2011) Cihai diabase: 268Ma (Rb-Sr) (Xue et al., 2000) Xuanwoling gabbro 261Ma (zircon U-Pb) (Su et al., 2011) Poyi gabbro and Poshi gabbro: 271-284Ma (Su et al., 2011)
Mesozoic			Weiya gabbro, quartz syenite, diorite porphyrite and fine-grained granite are 236 Ma, 246Ma, 233Ma and 237Ma, respectively (zircon U-Pb SHRIMP) (Zhang et al., 2005)	

2.4 Tectonic evolution of eastern Tianshan

2.4.1 Welding of the Central Asia Orogenic Belt (CAOB)

CAOB is huge comparing to the linear, narrow Circum-Pacific and Tethyan orogens. It is more than 5000km long, and its forming mechanism has attracted lots of researchers. But the question is still hot debated and going on. It has alternatively

termed the “Altaids orogenic belt” or “Central Asian Fold Belt”. An earlier model advocated by Sengor et al. (1993) suggested that the CAOB is a one arc system (the Kipchak-Tuva-Mongol arc) that developed by arc roll-back (Fig. 2-3 A and B). This model was modified by Yakubchuk et al. (2005), who suggested that the arc system comprised multiple chains of arc-backarc assemblages rather than one single arc system (Fig. 2-3 C). With the development of precise dating technology, geochemistry, as well as field observation, more and more different ophiolites suture has been found (Xiao et al., 2004; Wang et al., 2008; Xiao et al., 2008; Wang et al., 2010). According to the single-arc model (Sengor et al., 1993), seaward migration of the magmatic arc (or arc roll-back) was supposed to be a continuous process, and hence any ophiolite in the region would have to be dismembered in fragments obducted onto the Siberian Craton rather than representing discrete suture zones. Sengor et al. (1993) has explicitly denounced that those ophiolites in the CAOB mislead some conclusions. However, as pointed out by Buchan et al. (Buchan et al., 2001), the Bayankhongor ophiolite belt in Central Mongonlia is 300km long and 20km wide is not mixed with other rock units as is usually the case in accretionary complexes. This argues against ophiolites in CAOB as discrete fragments and supports the punctuated accretion. More importantly, the ophiolites in the CAOB often separate arcs that are distinct in terms of lithologies and geological histories (Windley et al., 2007). This also argues against their being formed in one arc-system. Besides, the single-arc model cannot explain the presence of fragments of oceanic plateau that are accreted on the CAOB.

A

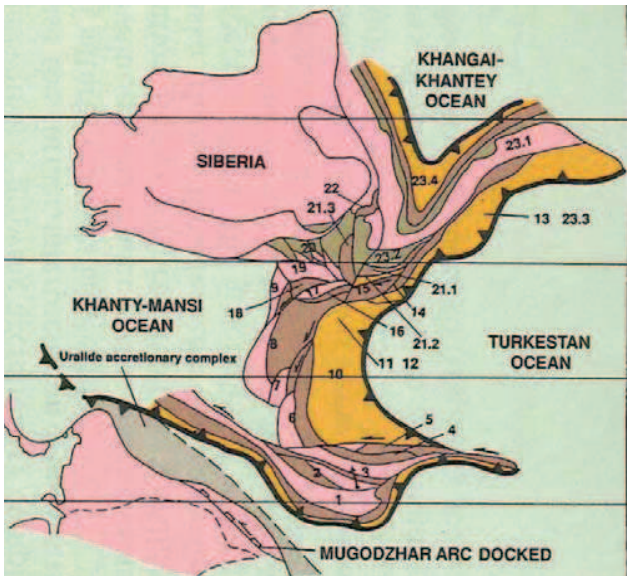

B

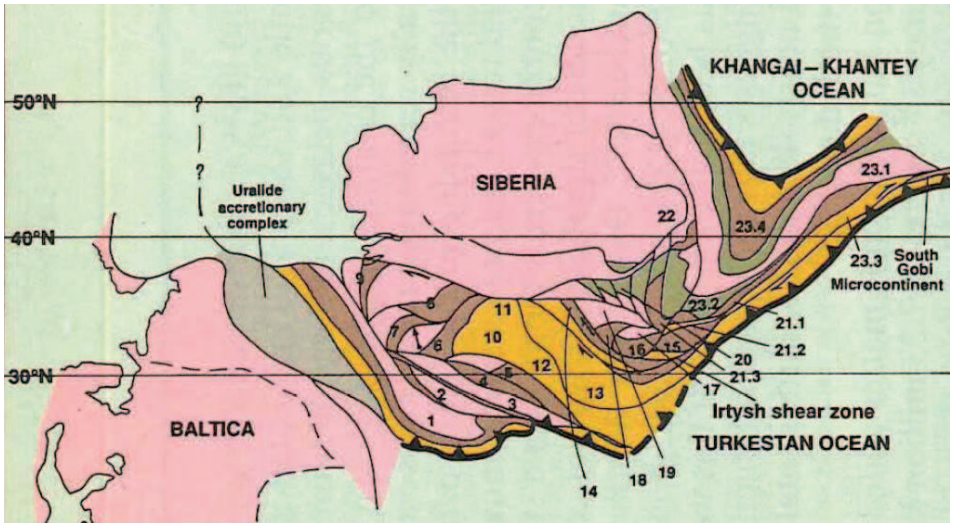

C

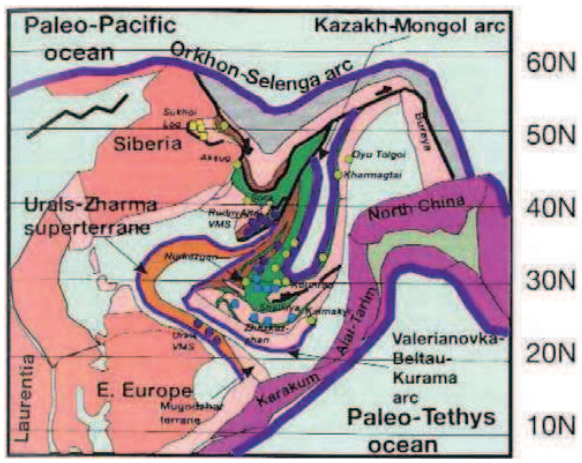

Numbers in (A) and (B) : 1.Valerianov Chatkal; 2. Baykonur Beshtash; 3. Chu-Terskey; 4. Sarytum; 5. Atasu Mointy; 6. Tengiz;7. Kalmyk; 8. Yerementau Chingiz Tarbagatai; 9. Ishim; 10. Junggaro Balkhash; 11. Zharma Saur; 12. Tar Muromtsev; 13. Surgut; 14. Kolyvan Rudny; 15. Gorny Altay; 16. Anuy Chuya; 17. Barnaul; 18. Salair; 19. Tomsk; 20. Batenev; (21.1) Kharkhirin sensu stricto; (21.2) Delyun Sagsai; (21.3) Western Sayan; 22. Oka-Jedinsk; (23.1) Tuva Mongol; (23.2) Ozernaya; (23.3) South Mongolian; (23.4) Khangai Khantey; 24. South Gobi; 25.Nurol; 26.Nadim.

Fig. 2-3: Reconstruction of CAOB. (A) and (B) Early Carboniferous 332-318Ma and Late Carboniferous 318-303Ma (Sengor et al., 1993). (C) By 340Ma, Laurentia, Siberia and Eastern Europe reassembled into a single continent (Yakubchuk et al., 2005).

The most accepted model suggests that the CAOB formed as a result of progressive accretion of different micro-continents, arcs and other tectonic units onto the southern margin of Siberia (Fig. 2-4) (Windley et al., 2007; Wang et al., 2010; Charvet et al., 2011).

Amount the numerous literatures supporting this model, the most compelling evidences derived from field evidence, paleomagnetism and paleofloral data, as well as dating and magmatism. Paleomagnetism data (Li et al., 1999) shows that Junggar plate remained a single microplate in Early Paleozoic, it combined with Kazakhstan plate in Late Paleozoic and formed the Kazakhstan-Junggar plate; Tarim plate was still one part of Gondwanaland before Sinian, it graduately separated from Gondwana in Early Paleozoic and shifted northward rapidly, It first collided with Junggar plate in the early stage of Late Paleozoic and became a accretionary wedge of Southern Laurasia. This progressive accretion is supported by magmatism, for example the geochemical data reveal an important crustal growth in continental scale during the Paleozoic time (Jahn, 2004).

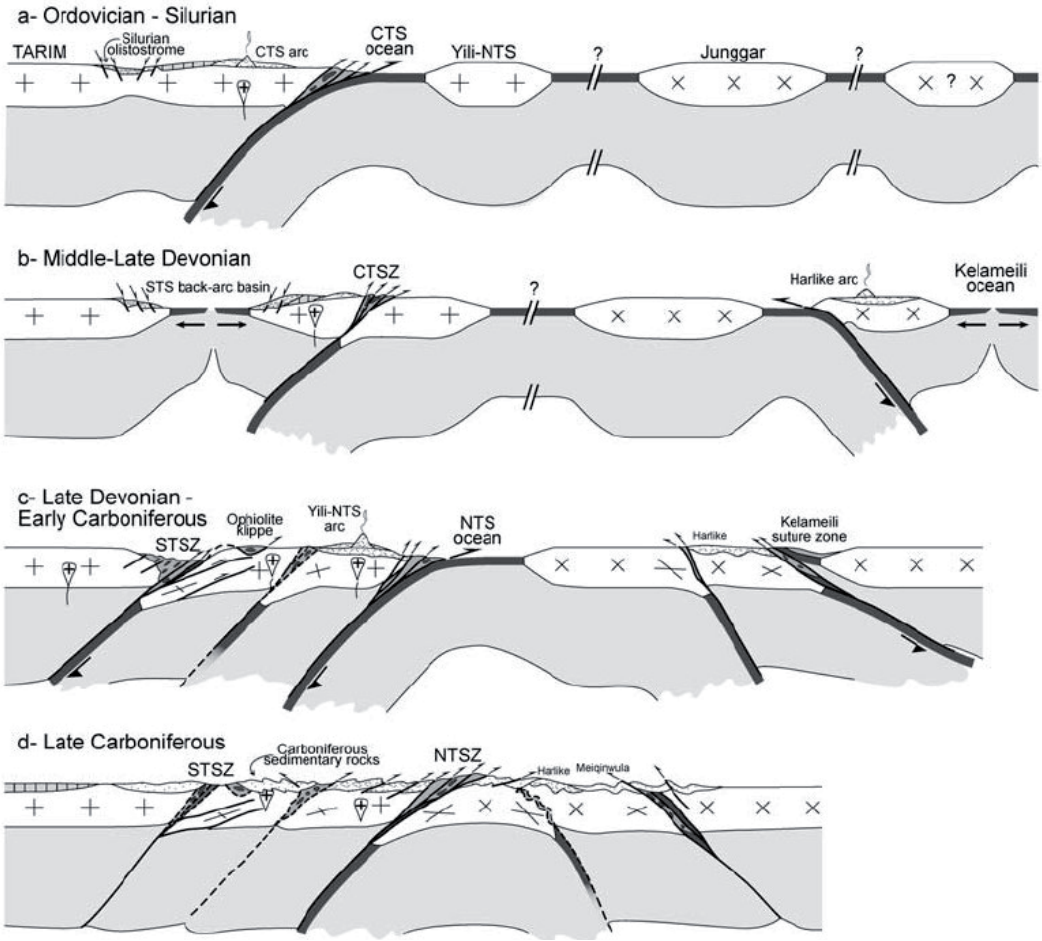

Fig. 2-4: Schematic geodynamic evolutionary model of Eastern Tianshan which is part of the CAOB (Charvet et al., 2007). CTS: Centre Tianshan; NTS: North Tianshan; CTSZ: Central Tianshan Suture Zone; NTSZ: North Tianshan Suture Zone.

2.4.2 Welding of the eastern Tianshan

Eastern Tianshan is part of CAOB and play important role in understanding its welding. Paleomagnetism data shows that Tarim plate still was one part of Gondwanaland before Sinian, it graduately separated from Gondwana in Early Paleozoic and shifted northward rapidly. It first collided with Junggar plate in the early stage of Late Paleozoic and became a accretionary wedge of Southern Laurasia (Li et al., 1999). Windley et al. (1990) suggested that the South Tianshan and Central Tianshan terranes collided with the Tarim Block during Late Devonian to Early Carboniferous. Xiao et al. (2004) and Charvet et al. (2011) proposed a more detail model in the Eastern Tianshan indicating the subduction direction and

reducing the collision age range. However, there are differences between the two groups. MTT ocean S-dipping subducted beneath the MTT and caused the MTT arc during Ordovician-Early Devonian (Charvet et al., 2011), whereas some study show that Devonian to Early Carboniferous, N-dipping subduction took place beneath the Dananhu-Harlik arc, giving rise to the Harlik arc and Dananhu arc are separated by the Tuha basin; In the Early to Mid-Carboniferous, the arc magmatism migrated southwards, leading the formation of Yamansu arc and MTT arc (Ma et al., 1997; Xiao et al., 2004; Gu et al., 2006; Wu et al., 2006); In the latest Carboniferous to Early Permian, all the continental blocks were amalgamated. Intracontinental wrenching then began (Xiao et al., 2008; Pirajno, 2010; Charvet et al., 2011). It was sinistral in the Mongolian Fold Belt, and dextral in Tianshan, where it was accompanied by opening of pull-apart basins, alkaline magmatism, and red molasse deposition. This huge strike-slip event accommodated an opposite motion of Siberia and Tarim (Levashova et al., 2003). Paleomagnetic data suggest that Yili-NTS and Junggar moved eastward with respect to Siberia, along the sinistral Erqishi fault system, with a displacement of 670±320 km from Late Carboniferous to Late Permian, and 820±370 km after the Permian; their eastward motion relative to Tarim reached 1160±380 km during the Permian (Wang et al., 2007).

In 2009, an international field excursion and workshop were organized to conduct a common observation and discussion on the tectonic evolution of the Chinese Tianshan. After that meeting, 25 researchers jointly published their main achievements, including acknowledged geological features, controversial and remaining scientific problems, and discussion of a tentative geodynamic model (Wang et al., 2010). Four issues are generally accepted: (1) Three main sutures zones: namely, central Tianshan suture zone, North Tianshan suture zone and South Tianshan suture zone; (2) Several continental blocks or microcontinents are involved in the orogen. They are Precambrian Tarim block, Central Tianshan block and Kazakh-Yili north Tianshan block; (3) Two continental magmatic arcs represented by volcanic, volcaniclastic and pyroclastic rocks, calc-alkaline plutons

are recognized; (4) Permain dextral strike slip faulting is a major tectonic event.

2.5 Mineralization in the eastern Tianshan

Eastern Tianshan has become one of the most important areas for mineral exploration because its abundance of metallic mineral deposits, such as Fe, Cu, Au, Ni, Mn etc. Three main types of ore deposits are well recognized: Permian orthomagmatic Cu-Ni-(V-Ti) deposits, quartz vein Au and Fe-(Cu) skarn ore deposits. Moreover, porphyry Cu and hydrothermal Cu mineralization occurrences, which maybe are related to arc, are being exploited. Currently, 1502 deposits or mineralized points have been reported in the Eastern Tianshan, of which significant deposits from Eastern Tianshan have been mapped (Fig. 2-9) (Mao et al., 2005; Wang et al., 2006; Sun et al., 2007; Cheng et al., 2008; Mao et al., 2008).

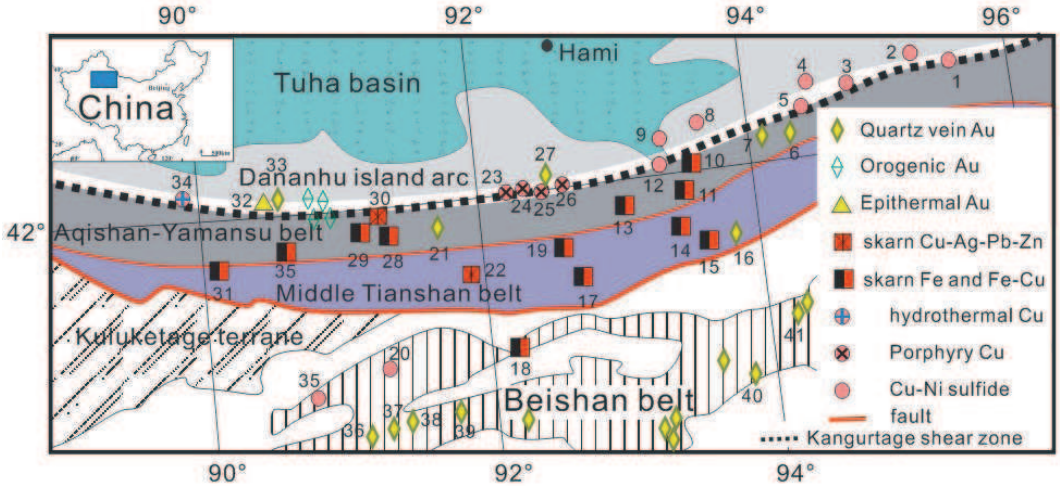

Fig. 2-9: Major ore distribution in Eastern Tianshan, NW China. Modify from Mao et al. 2005 , Wang et al. 2006, Sun et al. 2007; Cheng et al. 2008. Numbers inside: 1 Jingerquan, 2 Tulaergen, 3 Xianshuiquan, 4 Hulu, 5 Mati, 6 Dishui, 7 Baiganhu, 8 Huangshan and Huangshandong, 9 Xiangshan, 10 Shuangfengshan, 11 Heifengshan, 12 Tudun, 13 Yamansu, 14 M1406, 15 Tianhu, 16 Jingwozi, 17 Kumutage (also called Shalong), 18 Cihai, 19 Alatage, 20 Poyi Poshi, 21 Jiabaishan, 22 Lubaishan, 23 Yandong, 24 Tuwu, 25 Linglong, 26 Chihu, 27 Longxi, 28 Chilongfeng, 29 Aqishan, 30 Weiquan, 31 Hongyuntan, 32 Shiyingtan, 33 Kangguer, 34 Xiaorequanzi, 35 Luodong, 36 Baishitan, 37 Daqingshan, 38 Hongshijing, 39 Bayiquan, 40 Shijinbo, 41 Jiaobishan . There are still several orogenic Au deposit proposed by Mao et al.(2005).

Metallogenic peaks include Precambrian, Devonian, Carboniferous and Permian

(Wang et al., 2006). Among these deposits, iron deposits are characterized by their distribution spanning tectonic units with close and consecutive metallogenic ages (Jiang et al., 2002; Qin et al., 2002). Orthomagmatic Cu-Ni-(V-Ti) deposits seems to only associate with the Permian large scale strike-slip dextral shearing because they temporally and spatially appear in or near the shear zone except the Poyi-poshi Cu-Ni deposit. Some ore forming ages and tonnage are as following:

(1) Orthomagmatic Cu-Ni-(V-Ti) deposits: Tulaergen, reservation of Ni: 109600t, Cu: 60000t, Co: 10000t (San et al., 2007); Xiangshan, Ni and Cu bearing pentlandite Re-Os age 298±7.1Ma (Li et al., 2006); Huangshandong, Re-Os dating of Cu-Ni sulfide ores 282±20Ma (Mao et al., 2002) and zircon SHRIMP 274±3Ma (Han et al., 2004); Hulu Re-Os dating of Cu-Ni sulfide ores 283±13Ma (Chen et al., 2005); Poyi-poshi 271-284Ma (Su et al., 2011).

(2) Fe-(Cu) skarn: Yamansu, wall rock of ore bodies Rb-Sr 344±16Ma (Lu et al., 1996);

(3) Quartz vein gold: Kangguer, Sm-Nd and Rb-Sr gave 290.4±7Ma and 282.3±5Ma respectively (Ji et al., 1999). It reserve 10t Au with a grade of 7g/t (Rui et al., 2002); Xitan, reserve 6.4t Au with a grade of 5-10g/t (Rui et al., 2002);

(4) Epithermal gold: Shiyingtan, fluid inclusion in the quartz associated with ore, Rb-Sr 244-288Ma (Li et al., 1998).

2.5.1 Geochronological synthesis of mineralization

The mineralization processes in Eastern Tianshan are multiple periods. Zhang et al. (2008) subdivided them into four stages:

(1) 360-320Ma subduction-island arc stage: this stage mainly contain skarn related deposits, as well as porphyry Cu;

(2) 300-280Ma collisional accretionary stage: this stage yield some gold deposits and skarn;

(3) 280-245Ma post collisional extension strike-slip stage: numerous mafic-ultramafic Cu-Ni deposits with epithermal gold. Mostly these deposits

distributed along the Kangguer shearing zone;

(4) 245-220Ma intracontinental extensional stage: this stage yield W-Mo skarn and Fe-V-Ti orthomagmatic deposits, such as Weiya deposit.

These stages roughly coincide with granitic magmatism proposed by Gu et al. (2006).

Four main types of deposits developed in this region, including lithology, metallogeny, age etc, would be addressed in the following text.

2.5.2 Mafic-ultramafic intrusion related Cu-Ni-(V)-(Ti) deposits

Numerous of Permian mafic and ultramafic intrusions occur along the E-W-trending Kangguer shear zone for a length of about 270 km. These intrusions are thought to be syntectonic (Laurent-Charvet et al., 2002; Wang et al., 2008). Some of the intrusions host the orthomagmatic Cu-Ni-(V)-(Ti) sulfide deposits. These sulfide deposits related to mafic/ultramafic intrusions have attracted much exploring attention because of their large reservation. Mafic-ultramafic complexes are also the focus of numerous scientific studies. Many of these mafic-ultramafic complexes share common features as following:

(1) Relatively small size (mostly less than 10 km2). It seems that the smaller size the bigger probability of hosting economic mineralization;

(2) Occur in/along shearing zone;

(3) Around the pluton, lineation and foliation are quite clear, whereas inside of the pluton is not observed. But most of them show “S” shape in plane and funnel shape in profile. However, Branquet et al. (2012) reported that foliated diorite was observed;

(4) It seems that they are structurally controlled by regional ENE-SWS trending crustal scale faults;

(5) They generally possessed several geochemical characteristics, such as rich in volatiles as exemplified by the presence of amphibole or biotite; contaminated

by crustal materials (Gu et al., 1995; Zhou et al., 2004; Sun et al., 2007); V-Ti-magnetite and Cu-Ni-sulfide coexist (Wang et al., 2006). They seems associated with high MgO content magma (Zhou et al., 2004)

(6) The mafic plutons intruded the wall rocks and caused metasomatic hornfels (Gu et al., 2007), even some skarn was observed (Branquet et al., 2012);

However, the intrusions could be classified into single-phase intrusions and multiple-phase intrusions. Single-phase intrusions are typically represented by the ore-bearing Tulaergen intrusion. The Tulaergen deposit contains Ni 109600t, Cu 60000t, Co 10000t (San et al., 2007) which probably is the largest one in eastern Tianshan. This intrusion comprises amphibole pyroxenite, amphibole-bearing dunite, lherzolite, Olivine-websterite and to a lesser extent gabbro, all in transitional contact with each other (Sun et al., 2007). The Ni-Cu ore deposit is mainly hosted in the amphibole-bearing dunite and lherzolite, and consists of mainly massive to disseminated sulfides. Multi-phase intrusions are typically represented by the Huangshan intrusions, which have been much studied (Gu et al., 1995; Zhou et al., 2004; Zhang et al., 2011). The Huangshan intrusions comprise the Huangshanxi and Huangshandong bodies. The Huangshanxi body is elongated in shape and is about 3 km2 in area. The Huangshandong intrusion is lens-shaped, and is about 2.8 km2 in area, again characteristically small in size. The magmatic sulfide ores occur in stratiform disseminated and semi-massive forms in the footwall of the ultramafic units and also as stratabound disseminated ores in the mafic-ultramafic units. An interesting feature of the ore deposits in the Huangshan intrusions is that the majority of the sulfide ores is found at the contact between different phases of intrusions.

Wang et al. (2008) classified mafic-ultramafic related deposits into Cu-Ni type, V-Ti magnetite type, magnetite-(Co) type and Cu-Ni-V-Ti-Fe type according to their element association. They thought these deposits are chemically related and ascribed to post collisional environment. These mafic-ultramafic related deposits range more

then 35Ma (Wang et al., 2008; Zhang et al., 2008) which is quite different from mantle plume related deposits, such as Panzhihua V-Ti-magnetite deposit in SW china. This opinion is against to the ones who thought these orthomagmatic Cu-Ni deposits are associated with mantle plume activity (Mao et al., 2008). The later ones hold the mantle plume related opinion because mafic-ultramafic intrusions share similar features to Alaskan type complexes (Pirajno et al., 2008). The former ones argue against the mantle plume related opinion because: (1) The metallogenic ages are mainly between 260Ma and 300Ma, unlike mineralization from a mantle plume; (2) Compared with related deposits of the Emeishan mantle plume，the North Xinjiang series has a similar ore-forming element assemblage but has preferably developed Cu-Ni sulfide deposits rather than vanadic titanomagnetite deposits; (3) Geochemical features reflect a course where the magma source deepens and thermal interface moves down，energy gradually exhausts，and neo-continental crust forming in the post collision stage tends to stabilize.

2.5.3 Gold mineralization

The eastern Tianshan show two favourable east-west trending belts for formation of lode gold deposits: the Northern belt (Kangguer belt) and the Southern belt (Beishan belt).

2.5.3.1 Northern gold belt (Kangguer belt)

The main gold deposits in this belt include Kanggur, Shiyingtan (also called Xitan), Matoutan, Dadonggou, Xiaojianshan and Jinwozi. It is mainly hosted in Lower Carboniferous volcanic rocks, and controlled by ductile shear zones and syn-tectonic intrusions (Ji et al., 1997; Zhang et al., 2000). These Au deposits could be subdevised into: epithermal type, quartz vein types and replacement type (Mao et al., 2005).

2.5.3.1.1 Epithermal gold

Calderas, craters, diatremes and related faults play an important role in controlling most epithermal gold (Qin et al., 2002; Yang et al., 2009), such as Shiyingtan which contains approximately 10 tons Au, with an average grade of 15 g/t Au; silver grades are about 7 g/t (Pirajno et al., 1997). These epithermal gold deposits were placed into post collisional extension stage dated to be 280-245Ma (Zhang et al., 2008) based on geochronological data and regional geological evidence. This stage is coincided with the regional shearing and emplacement of mafic-ultramafic plutons. Gold deposits are mainly hosted by volcanic and sub-volcanic rocks of calc-alkaline affinity and dominated by basalt-andesite-dacite-rhyolite suites, and associated pyroclastic rocks. Altered mineral assemblages are dominated by two series: adularia–chalcedony–sericite and alunite–kaolinite–quartz (chalcedony). Associated minerals correspondent to the ore include: free gold (usually found interstitial to grain boundaries), electrum, pyrite, chalcopyrite, arsenopyrite, various sulfosalts of Ag and As, and some selenides (Ag_2Se) and chlorides (Ag_2Cl).

Kangguer gold deposit occurs in the Kangguer shear zone and classed into the epithermal type (Pirajno et al., 1997). However, it was controlled by the shearing (Gong et al., 2004; Wang et al., 2006), so, some researchers classified it into orogenic gold (Mao et al., 2005). Approximately 100 to 300 m wide hydrothermal alteration zones surround the orebodies, which can be divided into three zones. An inner zone of altered mafic rocks, part of the orebodies themselves, consists of quartz, chlorite, pyrite, chalcopyrite and magnetite; a middle zone comprises a pyrite-bearing phyllic and/or a sericitic alteration assemblage; and distal alteration is characterized by a sericite-chlorite assemblage. Vertically, the zoning consists of Au-Ag-As ores in the upper 170–200 m and Cu-Pb-Zn ores below this depth.

Almost all gold occurs as native gold, with minor electrum and gold-bearing tellurides. The main mineralization stage of the Kanggur gold deposit formed at 290

to 282 Ma, and the late stage quartz-carbonate veins at 254Ma (Li et al., 1998).

2.5.3.1.2 Quartz vein gold

Quartz vein Au deposits developed mainly in the eastern part of the studied area, including Jiabaishan (or Xifengshan), Baiganhu, Chihu and Longxi, are all worked by small-scale mines and have reserves ranging from <1 to 3 tons Au, although grades typically average 10–15g/t (Ji et al., 1996; Wang et al., 2006). These deposits occur in the Northernmost belt (Dananhu island arc), the Northern belt (Aqishan-Yamansu rift belt), such as Baiganhu, and the Kanggur shear zone. Mineralization is composed of sulfide-bearing quartz veins dominated by pyrite and arsenopyrite, with minor chalcopyrite, tetrahedrite, galena, and sphalerite. Generally gold grades are higher with elevated sulfide content. The host rocks are mostly granitic stocks, although some veins cut the volcanic and sedimentary rocks. The width of wall-rock alteration is proportional to the thickness of the ore veins. The main alteration types are silicification and sericitization. The mineralization is dominantly controlled by a set of NNE- to NE-trending tensile fractures (Mao et al., 2005). About the age of these gold deposits, it is still uncertain. However, these gold deposits probably relate to crustal shearing in Permian time.

2.5.3.1.3 Orogenic gold

In previous study, vein gold in the greenschist facies rock was thought to be mesothermal gold deposits. Recently, this type could be generated in a wide range of temperature (150-740°C) and depth (up to 15-20km). It is quite different from the classication proposed by Lindgren (1933). Many research result shows that these deposits have similar element assemblage, fluid and associate with orogeny (Kerrich and Cassidy, 1994; Goldfarb et al., 1998; Groves et al., 1998). Currently, orogenic gold deposits refer to those generated in the compreesional/transprssional environments, including pat of vein, mesothermal, part of Precambrian,

turbidite-hosted, slaty hosted, greenschist hosted and shear zone hosted gold. Typically, there is a strong structural control of the gold deposits and orebodies. Some gold deposits, such as Kangguer and Shiyingtang, are classed into orogenic gold in Eastern Tianshan previously studied by Rui et al (2002). The ore zones of these deposits include magnetite- and sulfide-rich auriferous quartz veins and massive lenses, as well as barren quartz-carbonate or carbonate veins. Sulphide-rich quartz veins occur either as large vein swarms or as fine stockworks in highly altered volcanic rock. The quartz-carbonate and carbonate veins formed during the second stage contain sparse pyrite, but no gold. Copper, lead and zinc are also highly anomalous in the ores.

2.5.3.2 Southern gold belt (Beishan belt)

This belt is characterized by numerous Au mineralizaion with some Cu-Ni, Fe, W and Mn deposits (Fig. 2-7). Major gold deposits include Baishitan, Daqingshan, Hongshijing, Bayiquan, Shijinbo, Jiaobishan. However, they are all in low grade, about 5g/t. Hosted rocks are composed by metabasalt, phyllitized tuffaceous sandstone and andesite. The ore minerals include Pyrite, magnetite, marcasite, ilmenite, chalcopyrite, hematite, cuprite, bornite, vallerite, pyrrhotite, galena, sphalerite, arsenopyrite, limonite, free gold and silver; gangue minerals are mainly quartz, biotite, sericite, chlorite, epidote, muscovite and garnet. Ore structure is sparse disseminated, vein and veinlet. Wall-rock alterations are dominated by silicification, carbonation, chloritized, epidotization, sericitized etc. But, low degree in geological research and exploration led to the difficulty of identifying these gold types.

2.5.3.3 Geochronology of major gold deposits

As described above, the Shiyingtan and Xifengshan are epithermal gold and quartz vein gold respectively. Kangguer gold deposit may belong to the orogenic type.

These deposits play important role in the local economy. Understand their metallogenic age could help the future exploration. Several geochronological studies of gold deposits are listed in Table 2-2. Although these gold deposits are classed into different types, they have similar metallogenic age. Coincidently, these ages are very concordant with crustal shearing. This is the reason that Rui et al. (2002) thought orogenic gold deposits are widely spread in Eastern Tianshan.

Table 2-2: Chronology study of gold deposits in Eastern Tianshan.

simple position	lithology	age	method
Kangguer	rhyolite	300±13Ma	Rb-Sr isochron
Kangguer	rhyolite	299Ma	zircon U-Pb
Kangguer	andesite	>300±13Ma	under the rhyolite
Kangguer	mylonite	>290Ma	hosted rock of ore bodies is mylonite.Some hosted rocks are surround by ore bodies. The ore bodies are dated to be 292Ma and 282Ma by Sm-Nd and Rb-Sr isochron.
Kangguer	quartz porphyry	282±16Ma	Rb-Sr isochron
Kangguer	inclusions in mineralized quartz	282±5Ma	Rb-Sr isochron
Kangguer	magnetite and pyrite	290±7Ma	Sm-Nd isochron
Kangguer	tonalite	248±1Ma	Rb-Sr isochron
Kangguer	tonalite	275Ma	zircon U-Pb
Kangguer	quartz vein	258±21Ma	Rb-Sr isochron
Kangguer	quartz vein	254±7Ma	Rb-Sr isochron
Xifengshan	andesite	>300Ma	granodiorite that intruded the andesite is dated to be 283Ma by Rb-Sr isochron. In addition, the underlying yield significant fossil of lowwer Carbonifeous
Xifengshan	granodioritic porphyry	284±13Ma	Rb-Sr isochron
Xifengshan	Inclusions in mineralized quartz	272±3Ma	Rb-Sr isochron
Shiyingtan	metaandesite	>393Ma	the tonalite that intruded into the andesite is 293Ma basing on Rb-Sr isochrn
Shiyingtan	tonalite	293±1Ma	Rb-Sr isochron
Shiyingtan	tonalite	287±3Ma	zircon U-Pb
Shiyingtan	ore quartz vein	288±7Ma	Rb-Sr isochron
Shiyingtan	granitic porphyry	266±3Ma	Rb-Sr isochron
Shiyingtan	rhyolite	256±13Ma	Rb-Sr isochron
Shiyingtan	cryptoexplosive breccia	261±7Ma	Rb-Sr isochron
Shiyingtan	quartz vein	244±9Ma	Rb-Sr isochron

2.5.4 Porphyry Cu deposits

Porphyry copper deposits are characterized by large tonnage and low grade bulk mineable deposit, related to porphyritic intrusions, stockwork and breccia-hosted ore, large volumes of hydrothermal alteration and supergene enrichment (Cooke et al., 2005). The known porphyry copper deposits are associated with arc calc alkaline magmatism, such as western South and North America and Southeast Asia. The largest porphyry Cu deposit is in Chile. Almost all mines exploiting large porphyry deposits produce from open pits. There are several mineralized porphyry occurrences in eastern Tianshan, including: Tuwu, Yandong, Chihu, Linglong and Sanchakou (Qin et al., 2003; Mao et al., 2005). These porphyry Cu deposits are close in space in the Dananhu island arc belt (Fig. 2-7) and mostly buried in the sand. They possess common features:

(1) Hypogene veinlets and disseminations are dominated by chalcopyrite and pyrite, with local bornite, covellite, and molybdenite.

(2) The gangue minerals are dominated by quartz and sericite, with minor chlorite, kaolinite, epidote, K-feldspar, biotite, and carbonate probably caused by later epithermal alteration (Ren et al., 2002; Li et al., 2006).

(3) Porphyry and associated copper mineralization are early Carboniferous in age (Rui et al., 2002). For Tuwu and Yandong porphyry Cu doposits, the porphyry plutons are monzonite and diorite porphyry. The porphyry plutons intruded into volcanic sediment series thought to be Carboniferous (Hou et al., 2005). Geochemical research displayed that the mineralized porphyry had characteristics of adakitic rock (Zhang et al., 2004).

2.5.5 Skarns in eastern Tianshan

Skarn deposits are very common in the eastern Tianshan and play an important role in economic resource. They can be subdivided into Fe(-Cu) and Cu-Ag-Pb-Zn types.

2.5.5.1 Iron skarn deposits

The Fe-(Cu) skarn deposits have been recognized since the 1970s, but some researchers suggest that they are oxidized VHMS-type deposits because the mineralization is stratiformly hosted Lower Carboniferous volcanic marine facies rocks and the ore occur as massive (e.g. Qin et al., 2002). Iron-rich magnetite skarn deposits are predominant, including Yamansu, Bailingshan, Heijianshan, Chilongfeng, Hongyuntan, Aqishan, Heilongfeng, Shuangfengshan, Cihai and Shaquanzi.

However, these iron skarn deposits distributed spanning tectonic units with close and consecutive metallogenic ages (Jiang et al., 2002; Qin et al., 2002), they are mainly occur within a 400 km long by 15 km wide corridor of the Northern belt (Aqishan-Yamansu belt). The skarn minerals consist: grossular-andradite, diopside-hedenbergite, vesuvianite, and wollastonite. Mostly, prograde skarn assemblage was locally replaced by actinolite, chlorite, epidote, sericite, and calcite during retrograde alteration. Ore minerals include: magnetite, hematite, pyrite, chalcopyrite and pyrrhotite.

2.5.5.2 Cu-Ag-Pb-Zn skarn deposits

Another type of skarn yield Cu with minor Ag-Pb-Zn is observed in this region (Mao et al., 2005). They are distributed in the Yamansu-Aqishan belt. These occurrences are newly recognized from following-up of geochemical anomalies in 2000 by the XJBGMR. These deposits include: Weiquan, Shuangqing, Heiyingshan and Lubaishan. The Weiquan deposit is the largest of these skarns. Hosted rocks mostly are Carboniferous intercalated limestone. Skarn is composed by andradite, diopside, vesuvianite, and epidote, whereas the retrograde assemblage is dominated by actinolite, chlorite, and fluorite. Ore minerals include: chalcopyrite, bornite, magnetite, pyrite, sphalerite, galena, argentite and molybdenite.

Chapter 3 Yamansu magnetite deposit

Résumé:

Le gisement à magnétite de Yamansu est localisé dans la ceinture de Aquishan-Yamansu. Cette ceinture est composée pour l'essentiel de volcanites et calcaires carbonifères et d'intrusions granitiques. Le district de Yamansu (15 km de long sur 2 km de large) est localisé dans la zone décrochante de Yamansu. Ce district comprend six amas minéralisés, celui de Yamansu, situé à l'extrémité orientale du district, est le plus important. Plus précisément, le district de Yamansu est situé sur le flanc sud d'un anticlinal orienté E-W. Il est limité vers le Sud par une faille qui contrôle le développement d'un bassin permien. Tous les amas de magnétite de ce district sont exploités pour la magnétite. Ils présentent par ailleurs de faible quantité de pyrite et de chalcopyrite. Les corps à magnétite de Yamansu sont encaissés dans un skarn à grenat, stratoïde, d'une puissance de l'ordre de 50 m, développé aux dépens de calcaire et de basalte.

Les grenats, qui sont la phase dominante du stade prograde, présentent une zonalité complexe: (i) au cœur des grains, la composition est proche du pôle andradite; (ii) ce cœur est entouré d'une couronne de calcite recelant quelques inclusions de magnétite; (iii) la bordure est constituée d'une solution solide andradite – grossulaire dont la composition évolue de 25% de grossulaire dans la partie interne à 45% de grossulaire en périphérie. Cette zonalité suggère que ces grenats se forment en trois stades, sous des conditions décroissantes de fO_2. Le second stade correspond à un changement de composition du fluide probablement appauvri en Si et/ou avec une fO_2 n'autorisant pas la formation d'andradite. Le dépôt de la magnétite massive d'intérêt économique suit la formation de ces grenats à zonalité complexe. Une dernière génération de grenat, de composition identique à celle des bordures des grenats à zonalité complexe, remplie des fractures sécantes sur la magnétite et

correspond à une phase de déformation fragile postérieure au dépôt des corps minéralisés. Finalement, les grenats de Yamansu ont enregistré des circulations de fluides à composition chimique contrastée comme on peut en observer en environnement hydrothermal.

Les skarns à grenat et les corps à magnétite présentent une allure stratoïde et sont encaissés dans les calcaires et les basaltes. L'ensemble pend vers le Sud avec un angle de 60°. Pour mieux comprendre la formation de ces objets, une étude magnétique (ASM et Paléomagnétisme) a été menée sur les skarns et les basaltes. Les données paléomagnétiques montrent que deux composantes peuvent être isolées: une composante primaire et une composante correspondant à une remagnétisation. La composante primaire, suggère, que lors de leur formation, les basaltes et les skarns étaient en position horizontale. L'étude ASM confirme ce résultat: la plupart des linéations et foliations magnétiques sont horizontales. Cinq des 22 sites étudiés montrent un degré d'anisotropie élevé, supérieur à 20%, suggérant une remobilisation tectonique postérieure à l'emplacement des basaltes. Finalement l'étude du magnétisme des roches suggère que le basalte ait intrudé horizontalement les calcaires et que le skarn s'est formé alors que l'encaissant était lui aussi dans cette position.

Le calcul du bilan de masse de la skarnification du basalte montre que ce processus nécessite un apport en fer. Un tel fluide pourrait également être à l'origine des corps à magnétite.

Un modèle génétique à quatre stage est finalement proposé:

(1) Stade de chevauchement à vergence vers le Nord. Une telle déformation a déjà été reconnue (Wang et al. 2010; Charvet et al. 2011). Elle est accompagnée selon Wu et al. 2006 d'un magmatisme calco-alcalin.

(2) Mise en place du basalte. Le basalte a été injecté probablement à la faveur d'une faille préexistante. Une partie du basalte s'épanche en surface, une autre est

injectée horizontalement dans les calcaires. Cette partie correspond aux basaltes recelant des blocs de calcaire.

(3) Circulation d'un fluide riche en fer à l'origine de la skarnification des basaltes et contribuant à la formation des corps à magnétite. Basculement et circulation d'un fluide felsique à l'origine des paragenèses borées (tourmaline, axinite) reconnues dans les skarns.

Abstract:

Yamansu magnetite deposit (YMD) is located in the Aqishan-Yamansu arc belt which was dominated by Carboniferous volcanites, limestone and large granite plutons. Locally, the Yamansu ore field is located in a shearing zone so-called Yamansu shearing zone which is about 15km for length and 2km for width. Except YMD, the Yamansu ore field contain more than 6 ore bodies of which YMD is the biggest in the easternmost part of the mined area. Precisely, the Yamansu ore field is located in the southern flank of an anticline broadly oriented E-W. To the South of the ore field, the Yamansu shearing zone was bordered by a fault that controlled the development of a Permian basin. All deposits located in this shearing zone are mined for magnetite with minor pyrite and chalcopyrite. Basing on petrology, mineralogy and geology study, YMD would be ascribed to a skarn-type deposit. The magnetite ore of YMD is mainly hosted by a ~50m thick stratiform garnet skarn located within limestone and basaltic formations.

The garnets which dominated the prograde stage of skarnization in YMD are original. Textural observations and chemical analyses of garnet enable the recognition of complex zoning: (i) in the core of the grain, the composition is close to end-member andradite; (ii) this core is surrounded by a zone with inclusions of calcite and a few crystals of magnetite; (iii) the border is an andradite-grossular solid-solution, which displays broad compositional variations from 25 mol% early to the 45 mol% late grossular. This zoning suggests that garnet form through three stages of precipitation under decreasing fO_2. The second stage records a change in the chemical composition of the fluid possibly depleted in Si, and/or with a fO_2 value not suitable for andradite formation. The massive economic magnetite stage follows the deposition of these complex garnet grains. The latest garnets, whose composition is similar to that of the complex grain rims, infill fractures related to a late brittle deformation. Thus, garnets from Yamansu magnetite deposit record

episodic flow of fluid with contrasted chemical composition which was typically controlled by hydrothermal environment.

Both the massive garnet skarn and ore bodies are actually sandwich-like in the limestone and basalt. They are south dipping, with angle about 60°. In order to track the fluid path where iron-rich fluid circulated and responded for the formation of skarn, paleomagnetism and AMS method (Anisotropy of Magnetic Susceptibility) have been applied. For the paleomagnetic data from massive garnet skarn and basalt, two components could be distinguished: the primary and the remagnetized. The primary component indicates that initial occurrence of basalt was horizontal, as well as the garnet skarns. AMS results are concordant with paleomagnetic data, of which most magnetic lineations (K1) and foliations are horizontal. 5 sites out of 22 sites (23%) show anisotropy degree (Pj) higher than 20% indicates it suffered tectonic event after basalt's emplacement. Overall, these data support that, initially, the basalt shallowly intruded into limestone horizontally, coincidentally, the skarn was formed horizontally too.

Whether there is a causal relationship between the basalt and the skarn is not clear, however fragments of marble fell into the altered basalt caused by magmatic stopping suggest the basalt was not totally concretionary when intruding into the limestone. Mass balance calculation showed that the basalt was probably accompanied by iron rich fluid responding the massive magnetite deposited.

A four-step-metallogenic model has been proposed:

(1) North-verging thrusting and folding stage; However, in Yamansu area, the limestone was little deformed basing on morphology of ripple plane. This stage was commonly recognized (Wang et al. 2010; Charvet et al. 2011) and was companied by calc-alkaline magmatism (Wu et al. 2006);

(2) Emplacement of basalt. The basalt injected, probably along a pre-existing fault; Part of the basalt erupted to the surface, and part of them horizontally injected

into the limestone layer where clasts of limestone were observed;

(3) Iron fluid injected and caused extensive skarnization. Part of the basalt was altered into skarn and contributed to the massive magnetite ore shoots formation. The circulation of CO_2 probably enforced the metasomatism;

(4) Rotation and felsic fluid contribution.

3.1 Introduction

Yamansu magnetite deposit (YMD) (Fig. 3-1) is located in the Aqishan-Yamansu arc belt (Ma et al., 1997; Hou et al., 2006; Wu et al., 2006; Zou et al., 2006; Hou et al., 2007) which was dominated by Carboniferous volcanites, limestone and large granite plutons. Sometimes, this belt was thought to be a rift according to geochemical data and bimodal volcanic rocks (Xia et al., 2004; Mao et al., 2005). Locally, the Yamansu ore field is located in a shearing zone so-called Yamansu shearing zone. As defined by Gu et al. (2006), the Yamansu shearing zone extended more then one hundred kilometres. Herein, for simplify the concept and facilitate the following discussion, Yamansu shearing zone is defined as that part of the whole shearing zone, about 15km for length and 2km for width (see the geological map of Fig. 3-2 and Fig. 3-3). It is in the southern part of an anticline.

Fig. 3-1: Bird-eye view of the Yamansu open pit. As a general role, the rock in dark rose is garnet skarn; in black is mineralized bodies; in white is marble.

Except YMD, the Yamansu ore field contain more than 6 ore bodies of which YMD is the biggest one in the easternmost part of the mined area. Precisely, the Yamansu

ore field is located in the southern flank of an anticline broadly oriented E-W. In this southern flank, the magnetite ore is mainly hosted by a garnet skarn located within limestone and basaltic formations; to the South, the Yamansu shearing zone was bordered by a fault that controlled the development of a Permian basin (Fig. 3-2 and Fig. 3-3). All deposits located in this shearing zone are mined for magnetite with minor pyrite and chalcopyrite.

YMD was mined in open pit, now turn into underground exploitation. YMD is operated by the BAOSTEEL Company and contains a reservation of 32 Mt with an average grade of 51% Fe, and 20,000 t with a mean of 0.06% Cu (Mao et al., 2005). Other companies mined the other ore bodies to the west which are next to the Yamansu open pit and there is not precise data on the reservation. During the mining process, both reserves of iron and copper were increased, but exact amounts have not been reported.

A

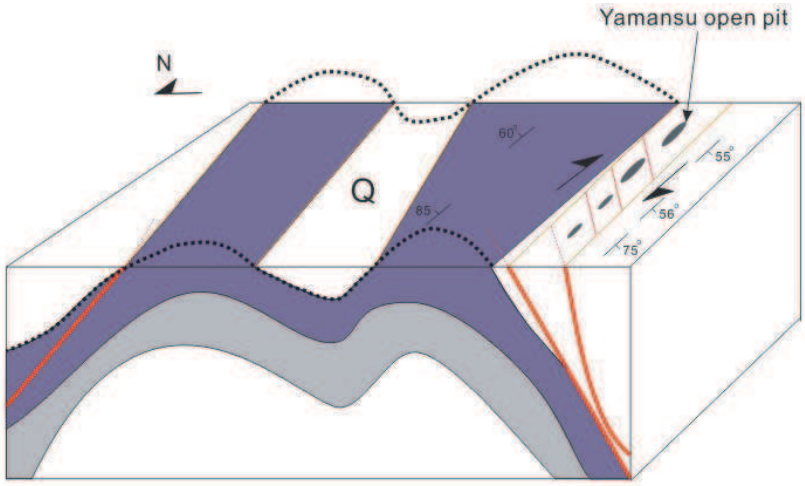

B

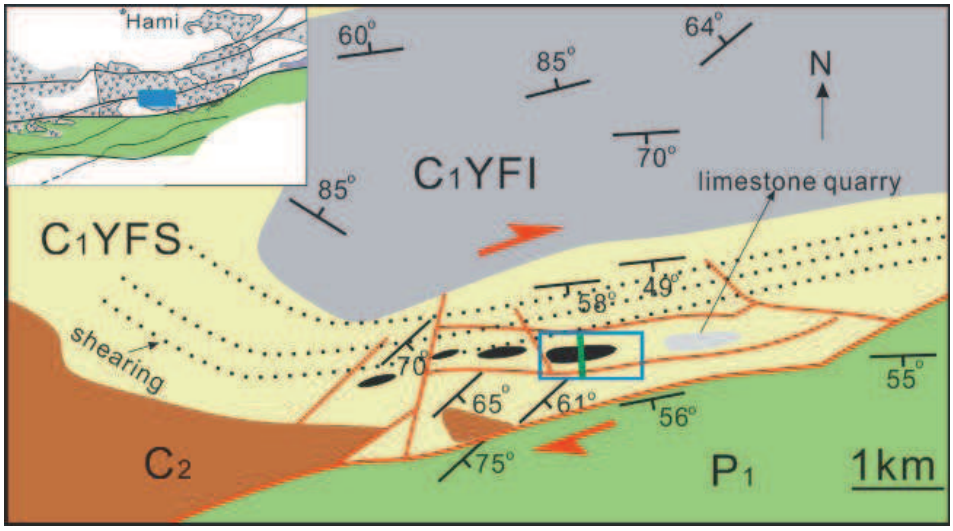

Fig. 3-2: Geological schematic map of Yamansu region. (A) A schematic map shows the anticline and the position of Yamansu deposit locating in the shearing zone; (B) A structural geological map shows the faults marked in red, the magnetite ores and strata. The Yamansu open pit is indicated by the blue rectangle. In this blue rectangle, the green line indicates the position of the profile of Figure 3-14. C1YFS- Lower Carboniferous Yamansu upper Formation, C1YFI- Lower Carboniferous Yamansu lower Formation, C2- Upper Carboniferous, P1- Lower Permian. Dotted lines indicate the shear zone trace. The inset rectangle shows part of the Central and Northern Tianshan, south of Hami city and the position of the Yamansu region along crusted-scale Permian shear zone (Zhang and Ding, 1984).

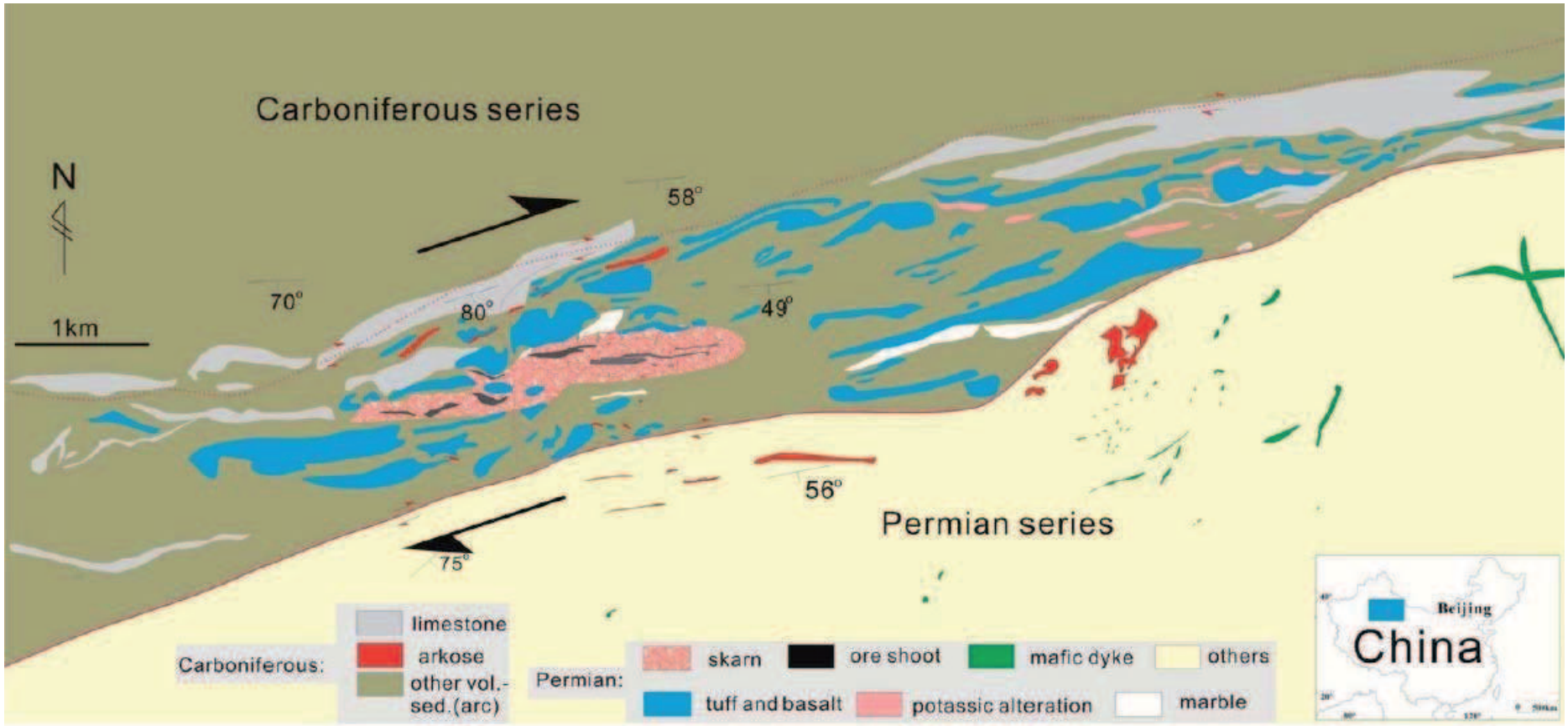

Fig. 3-3: Geological map of the Yamansu ore field in the E-W trending shearing zone. The others lithology in Permian are mainly graywack, with some siltstone.

3.1.1 Previous studies on YMD

3.1.1.1 Strata

In the Yamansu area, formations are mainly Lower Carboniferous called Yamansu formation. It occupies four fifths of the total area. Lower Permian strata unconformably overlay it. From the old to the new, the sequence is following (Fig. 3-4):

(1) Yamansu formation (Lower Carboniferous formation): it was mainly composed by tuff, basalt and limestone. It contains lots of fossils, such as Crinoids (Fig. 3-14B).

(2) Lower Permian Hongluihe formation: mainly exposed in the Southern part of the Yamansu region. It is fault contact with the Lower Carboniferous Yamansu formation (unconformably contact in the whole region between Carboniferous and Permian (Wartes et al., 2002)). It is composed by sandstone, graywacke and siltstone indicating the beginning of terrestrial deposits.

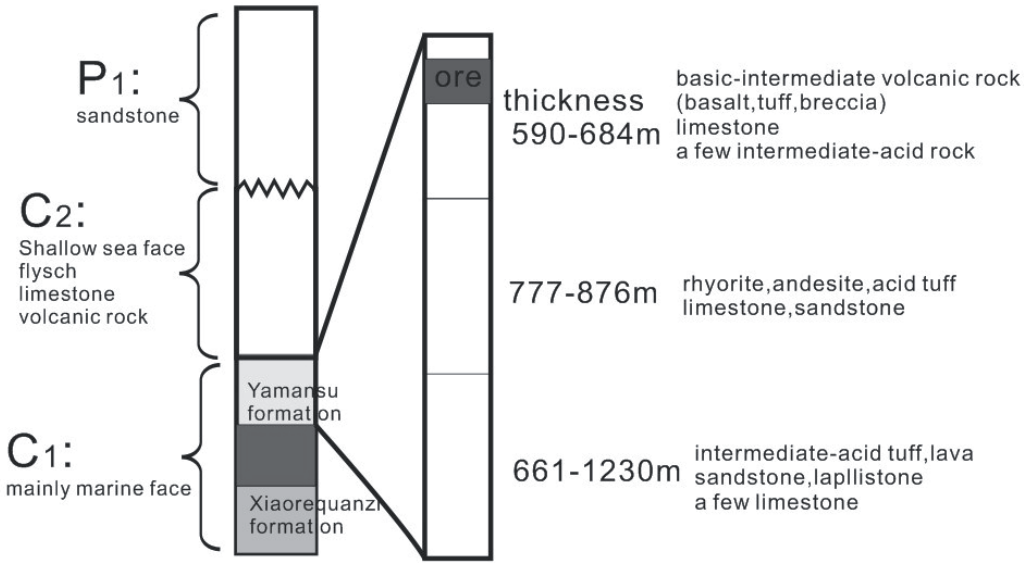

Fig. 3-4: Schematic stratigraphic column from the Aqishan-Yamansu arc belt.

3.1.1.2 Geophysical characteristics

In the Yamansu ore field, both magnetic and gravity work has been done in 1960s in order to investigate the magnetite ores, but both magnetic and gravity maps were not found by the author. However, the paper text was preserved by the Baosteel Company which reported that the gravity Bouguer anomaly clearly shows YMD and its peripheral strata. The whole west-east trending Bouguer anomaly belt is 18.5km long and 2km width (Baosteel-Company, 1977). The YMD is located in the centre of this anomaly belt. The gravity Bouguer anomaly is caused by combined geological factors in three levels: first level, the intensity of 1.5mgal background which is caused by the medium density of volcanic strata; second level, the intensity 3 mgal, maybe caused by the garnet skarn; the sharp third level is up to 4.5mgal, caused by the known iron ore. Strata are south tilting, which result in steep and mild gravity anomaly occurrence in the north and south respectively. It seems that gravity anomalies in this area are strictly controlled by the strata and the shearing zone. The gravity anomalies area is bigger than the magnetic anomalies area, but they have a good positive relation. High magnetic anomalies could be caused by magnetite bodies.

3.1.1.3 Isotopic data

Isotopic data are emphasized because they are useful for indicating metal source. Pyrite is common in Yamansu deposit. 5 samples of S isotopic results show that they (δ34S) vary from +0.05—+2.90‰, average 1.95‰ (Lu et al., 1995), and slightly higher but close to chondrite or primitive mantle (Chaussidon et al., 1989; Chaussidon and Lorand, 1990). The average $\delta^{32}S/\delta^{34}S$ is 22.177 which is also close to mantle. These data are concentrated. Two $\delta^{18}O$ value (4.92‰ and 5.25‰) from the massive magnetite and one $\delta^{18}O$ value (8.31‰) from calcite, which occurred in massive magnetite (Lu et al., 1995; He, 2007) show that the magnetite probably derived from dip source and suffer epithermal process indicated by Rye (1993).

Here, attention should be pay that different origin for the pyrite and magnetite could not be excluded.

3.1.1.4 Metallogeny

As to the metallogeny for YMD, 2 mainly models have been proposed: early workers mainly advocated a volcanic host metamorphic sedimentary (VHMS) origin (Baosteel-Company, 1977; Lu et al., 1995; Lu et al., 1996; Qin et al., 2003; Wang, 2005); Although Mao et al. (2005) and Liang (2000) questioned this and ascribed ore genesis to pluton contact metamorphic processes: a skarn model. The former ones believe that iron precipited from submarine volcanic fluid, which may derive from deep source in Carboniferous. They hold the VHMS model largely based on the wall rock of basalt which was altered by the skarn. The basalt was called "spilite", which normally formed when basaltic lava reacts with seawater, or from hydrothermal alteration when seawater circulates through hot volcanic rocks (Price et al., 2005). A summary of literatures supporting the VHMS opinions are as follows:

(1) the ore shoots are massive and the occurrence is stratiform, no mafic/andesitic pluton in the Yamansu shearing zone;
(2) the contact between ore bodies and the marble is straight and net, non alteration;
(3) there are relics of basalt (spilite) in the skarn; albite is primary mineral in the basalt. So, the basalt is rich on Na leading previous researcher thought the deposit originate from the Na rich volcanic hydrothermal process (Ding, 1990; Wang, 2005).
(4) the grain size of magnetite is small;
(5) the content of Mn, V and P in the magnetite is relative high reflecting sediment origin;
(6) the $^{32}S/^{34}S$ value is close to upper mantle.

However, some of these proof mentioned above seems to be farfetched to support the VHMS origin. Besides, the ore forming process was thought to be associated

with spilite and keratophyre (Lui and Chen, 1979). Whereas garnet growth in host rocks is massively developed, as well as the retrograde phase, leading the later one hold the opinion that there is a mafic pluton beneath the ore bodies causing the skarnization (Mao et al., 2005).

3.1.1.5 Ages

The age of the wall rock (limestone) is unequivocal because characteristic fossils were found in the limestone. This limestone was thought to be early Carboniferous (Baosteel-Company, 1977; XBGMR, 1993). The mineralization age is still in debate. Lu et al. (1996) gave an Rb-Sr isochron age of 344±16Ma of the basalt which constituted the wall rock of the skarn with $^{87}Sr/^{86}Sr$ initial value of 0.7055±0.0001 (1996). Some researchers who hold the opinion of VHMS origin took it as mineralization age (Ding, 1990; Lu et al., 1995; Wang, 2005). This Carboniferous age seems to be unsubstantial because of lacking affected and directly dating method on the ore formation or related alteration.

The age of large scale strike slip fault in the eastern Tianshan region is emphasized here because the studied Yamansu ore field located in a shearing zone. This zone was part of strike slip faults. This shearing zone was generally thought to be active in Permian (Shu et al., 1999; Chen et al., 2005; Wang et al., 2010; Charvet et al., 2011).

3.1.2 Questions

According to the previous studies mentioned above, this chapter concerns the following problems:

- The mineral paragenesis and chemical composition, as well as alteration process of this deposit, which may serve to the metallogeny. In YMD, magmatism or hydrothermal process that could be the cause of the mineralizing process is still poorly understood;

- The attitude of ore shoots and skarn. The heart this problem concerns the relations between the strike slip shearing fault and ore forming time. The ore forming age is up in the air because of lacking directly dating method. Actually, the inclination of the ore shoots, skarn and foliation of shearing zone are dipping into the South. If only reason from this inclination, it seems that the ore shoots, skarn and the shearing are contemporary; but, if the attitude of the ore shoots and skarn were attested to be different from the fault at beginning. That could indicate the ore forming time was earlier then the shearing zone.

3.2 Research methods

In order to better understand the questions proposed above, field works as well as laboratory analysis have been done. The major works are listed in Table 3-1. A two-week mapping executed in the Yamansu shearing zone is emphasized. The mapping area is about 15km long and 2km width (Fig. 3-3). This dimension is comparable to gravity Bouguer anomaly in this shearing zone.

Table 3-1: Major works in Yamansu iron deposit

objects	content
field research time	1 days in 2008, participant: author and Wang Zhenyu; 7 days in 2009, participant: author, Luc BARBANSON, Yannick BRANQUET, Stanislas SIZARET, Bo WANG; 21 days in 2010, participant: author, Changzhi WU
work area	5 km2 in detail, 60 km2 sketchy
sample	about 40kg
thin section	210 sheets
zircon dating	23 points, cathodoluminescence images 10 sheets
Ar-Ar dating	4 samples of K-feldspar
electron microprobe	390 points
geochemical analysis	27 samples for major element; 27 samples for trace element
oriented cores	275 for Anisotropy of Magnetic Susceptibility; 20 for paleomagnetism analysis

3.3 Geology

The Yamansu ore field is characterized by more than 6 linearly distributed ore bodies which located within a narrow and long, E-W trench (Fig.3-3). This trench is called Yamansu shearing zone bordered by faults. It is dominated by limestone, tuff, basalt and arkose with minor lava. They are located along the boundary between superior Carboniferous volcanic sediment series of Yamansu Formation to the North and Permian terrestrial sandstone-shale-cherts series to the South. The basalts and arkose also became elongated in the ore field. Most of ore shoots and skarn dipped into south with angle about 60° according to observation in the Yamansu open pit and drill hole data. All of the ore shoots are parallel or subparallel to the strike slip shearing zone. Some of them are obviously wrecked by subordinated faults (Fig. 3-5).

Fig.3-5: Geological map of Yamansu open pit.

3.3.1 Outcrop morphology, faults and kinematic analysis

Yamansu shearing zone is nearly E-W trending, as well as the Yamansu ore field (Fig. 3-3). From the geological map, the morphology of outcrops, especially the basalt and arkose, is lineally distributed (Fig. 3-3). Some outcrops may reach a few kilometres and the length-width ratio maybe bigger than 10.

For the shearing zone, nearly vertical mylonitic foliation and sub-horizontal stretching lineation in the limestone define its strike-slip feature. Kinematic indicators, such as pressure showdown, subsidiary structure, morphology of the ore shoots suggest that it was a dextral strike-slip ductile shear zone oriented in a nearly E-W direction.

In the Yamansu open pit, there are two prevailing groups of the faults (Fig. 3-6A). The plane of first group is parallel to the ore bodies and the limestone formation (the right photo of Fig. 3-6A). Its attitude is about 160°∠75°. While the other one is mostly NE-SW trending and tilt angle is either to the West or to the East with subvertical angle. Steroplots are done to better understand the kinematics of these two groups (Fig. 3-6B and C). Lineation (stretching and mineral lineation) measurements also show two groups (Fig. 3-6B): (1) E-W with slightly low to middle angle; (2) SW dipping with slightly higher angle. Fault planes also show two groups (Fig. 3-6C) which strictly corresponds to lineations. These faults seem to be brittle. The second group lineation probably associated with the regional dextral strike-slip caused by book shelf structure. Subaltern N-S compressive thrusting, which probably corresponds to the second group lineation, was observed in the limestone (Fig. 3-7D).

A

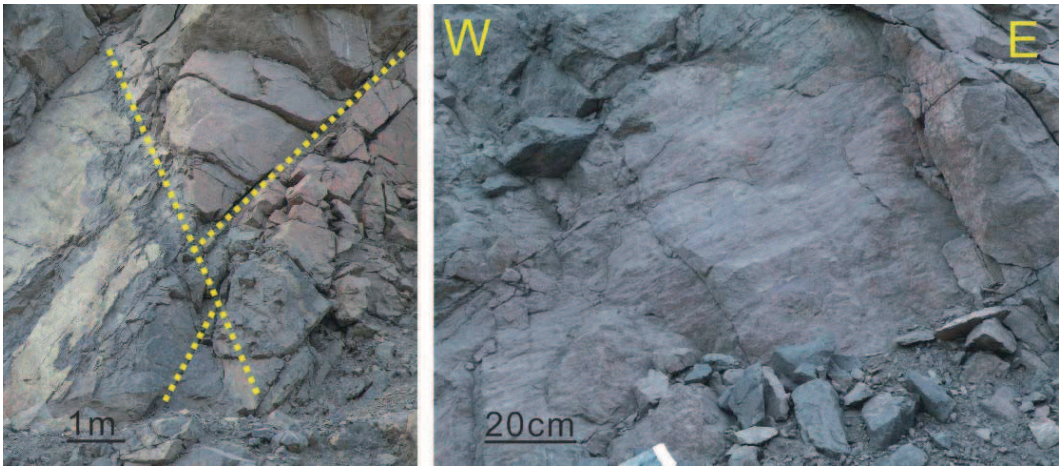

B C

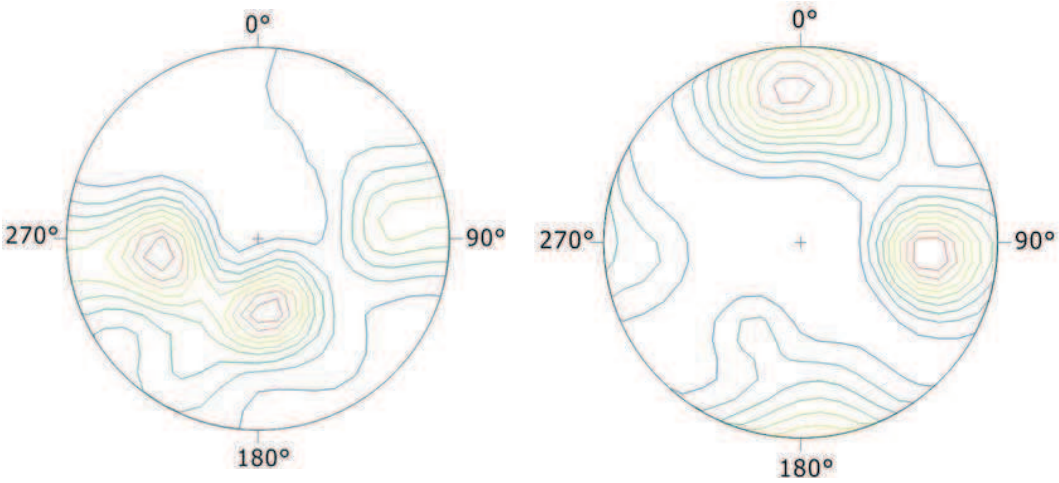

Fig. 3-6: Faults and stereo plots. (A) Conjugation faults to the left and fault plane to the right; (B) Lineation stereographic plots, 350 measurement points; (C) Foliation stereographic plots, 301 measurement points. Measurements are in the Yamansu open pit. Stereographic plots are Schmidt equal lower hemisphere projection.

In addition to fault planes and streaks in the open pit, pressure shadow, fractures, foliation and lineation developed in the limestone are well informative. According to field and lab microscope observations, two kinematic patterns could be distinguished.

1. Firstly, NW-SE compressive shortens (Fig. 3-7). These shortenings are progressive. At the beginning, cracking filled by later calcite was produced by

NW-SE compressive squeeze. Cracking was parallel to principal stress (Fig. 3-7B). With the development of compressive shortenings, principal stress rotated according to observations in the field. Because the sectrix curve of the conjugate is not parallel to the cracking. Therefore, the angle between the sectrix curve of the conjugate and the long axe of the cracking was the rotation angle (Fig. 3-7C). And then, Conjugate strike-slip occurs. This stage only developed in the northern side of the open pit, at a certain distance from the Yamansu open pit. It means that this stage is preserved a little far from the fault. Companying this compressive shortening, thrust probably occurred (Fig. 3-7C).

2. Secondly, dextral shearing (Fig. 3-7E). The photo illustrates that calcite indicates dextral shearing. Oriental samples are from the Yamansu open pit. It is very coincident that the Permian strike-slip shearing is dextral which leads to identify Yamansu fault is part of the regional dextral shearing (Shu et al., 1999; Pirajno, 2010).

Basing on the analysis above, Yamansu ore field suffered NW-SE compressive squeeze, companied by thrust, and then, it was wrecked by the Permian dextral shearing.

A

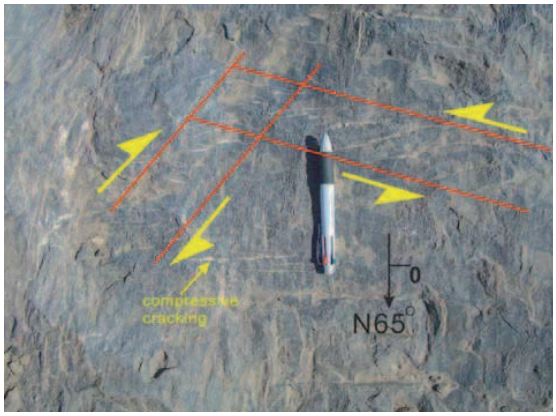

B

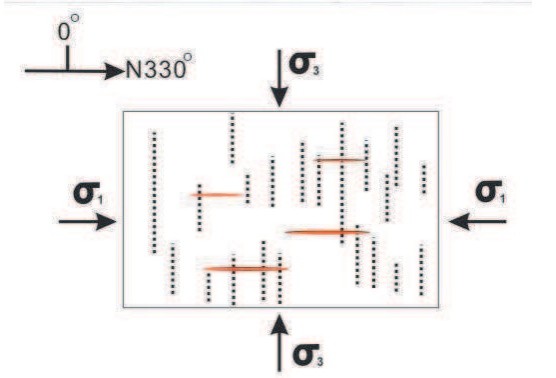

C

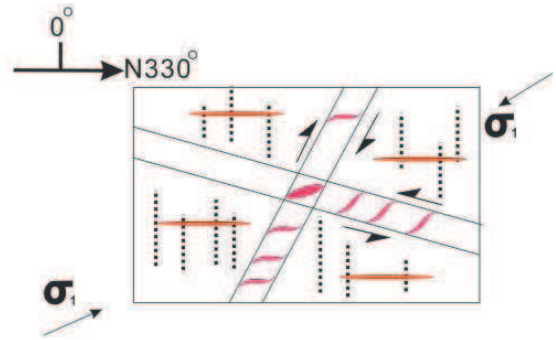

Fig. 3-7: Kinematic analysis. (A) N-S compressive shortens causing related conjugate fracturing system. (B) and (C) are explain models for fracturing systems. (B) Cracking filled by later calcite was produced by compressive squeeze. Cracking is parallel to principal stress. (C) With the progressive development of compressive shortens, in the studied case, principal stress (1) rotated about 30°. (D) Subaltern structure of N-S compressive shortens. New birth calcite indicating thrust in the Yamansu open pit. (E) Calcite indicating dextral shearing.

D

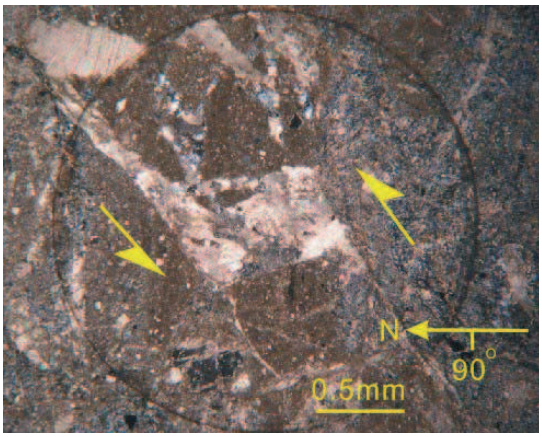

E

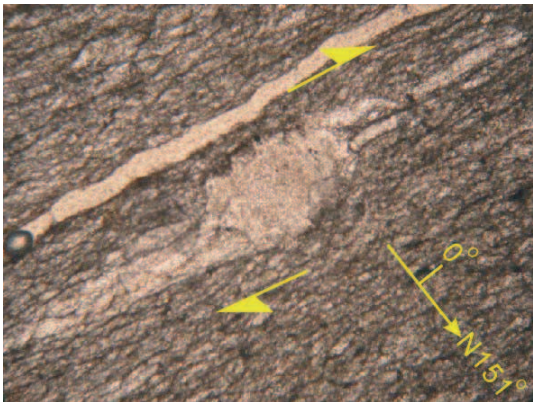

3.3.2 Arkose

3.3.2.1 Geology

The arkose is generally red or pale red, which is composed by clasts of K-feldspar, plagioclase, quartz, rock detritus, calcite and fine grained groundmass with minor disseminated pyrite (Fig. 3-8A). Some quartz showed overgrowth boundary. The size of K-feldspar, plagioclase and quartz vary, range from 50 to 500μm. Some rock clasts were observed. The contact between basalt which is the direct wall rock of skarn, and arkose is not clear because of weathering, probably gradual (Fig. 3-8B). Both the arkose and basalt were wrecked by later shearing and displayed long-strip shape (Fig. 3-3). This arkose also deposited in the Permian series.

A B

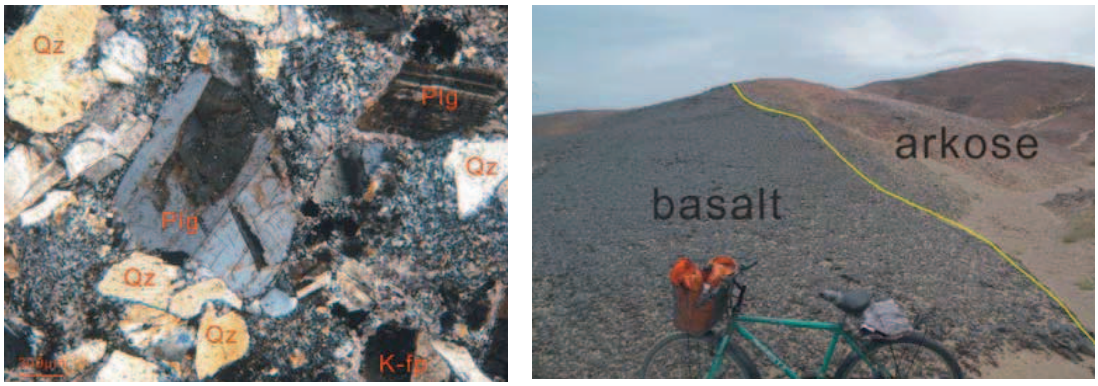

Fig 3-8: Photos showing arkose. (A) photomicrograph of arkose in transmitted crossed polarized light. Some quartz show overgrowth boundary; (B) contact outcrop between basalt and arkose.

3.3.2.2 Zircon dating

In the Yamansu ore field, arkose was involved in the shearing deformation. Therefore, the zircon from the arkose may give a lower limitation of the strike slip deformation.

Zircons for LA-ICP-MS U-Pb dating were separated from a sample of the Yamansu arkose (N41°52′35.9″, E93°52′51.9″). The zircon separation was carried out first by conventional magnetic and density techniques for the concentration of non-magnetic

heavy fractions. Representative zircon grains were then picked out under a binocular microscope. Then, the selected zircons were casted in an epoxy mount and polished down to half section. Morphology and internal structures were recorded in transmitted and reflected light and by cathodoluminescence (CL) images (Fig. 3-9) in order to guide LA-ICP-MS analysis.

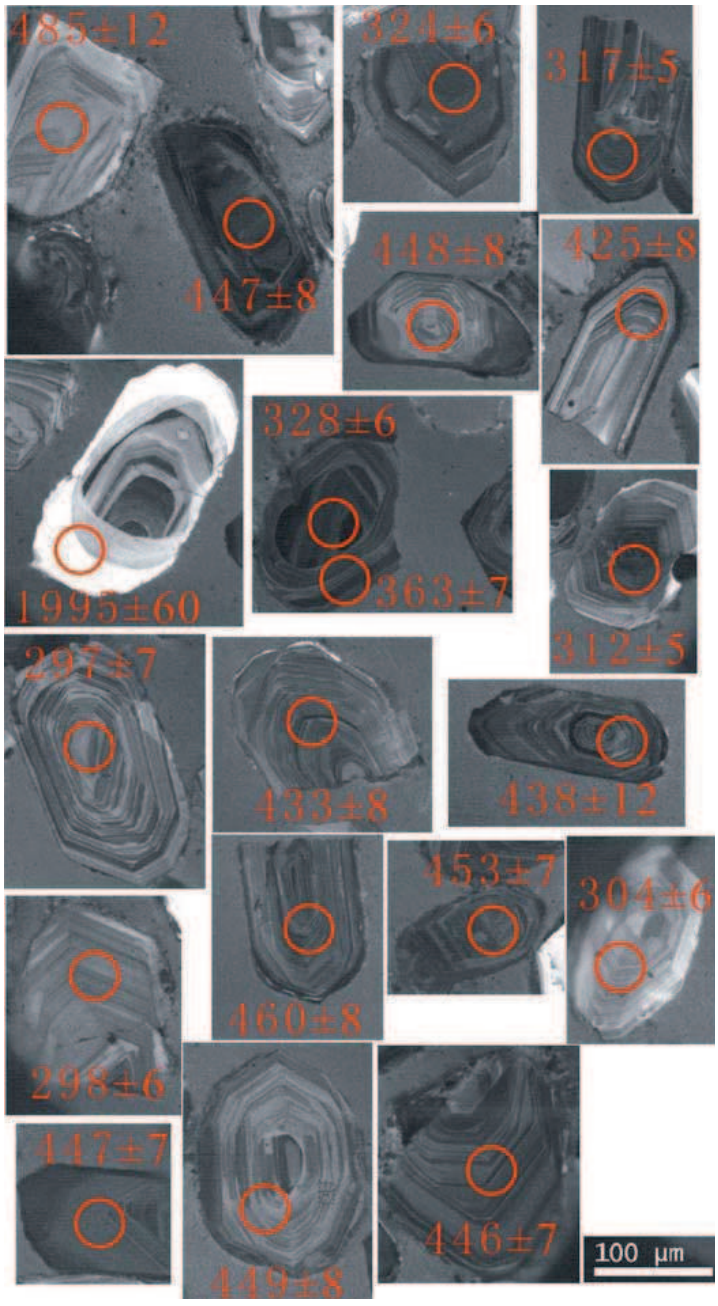

Fig. 3-9: Cathodoluminescence (CL) images and in-situ LA-ICP-MS U-Pb ages (in red) results of representative zircons from the Yamansu arkose.

CL imaging was carried out on a Gatan MonoCL3+ machine at the State Key Laboratory of Continental Dynamics, Northwest University, China. Zircon LA-ICP-MS U-Pb analyses were performed on an Agilent 7500 ICP-MS with a New Wave UP213mm laser ablation sampler at the State Key Laboratory for Mineral Deposits Research, Nanjing University. Each run comprises 10-12 sample analyses corrected by four GJ-1 zircon standards. Another well-determined reference zircon (Mud Tank) was also analyzed to control reproducibility and instrument stability. Spot diameter for Laser ablation is adjusted to 40μm. Detailed analytical procedures, precision and accuracy are the same as those described by Jackson et al. (2004). Analyses results were obtained by use of the GLITTER ver4.0 (Macquarue University), and age calculation and plotting of concordia diagrams were made by Isoplot program (ver 2.49) (Ludwig, 2001).

Zircon grains used for LA-ICP-MS U-Pb analyses are mostly euhedral, transparent to semi-transparent, light brown or colorless and generally 100 μm in length, have length/width ratio between 2:1 and 4:1. Most zircon grains show fine prismatic shape with abraded pyramids. The CL images indicate some inherited cores. Concentric oscillatory zoning is common in most crystals. A total of 24 analyses were conducted on 23 grains. One grain with an inherited core was analyzed at two spots (on the core and rim, respectively, Fig. 3-9. The results are listed in Table 3-2 and illustrated on a concordia diagram in Fig. 3-10. Zircons of this study are characteristic of magmatic origin and have magmatogenic oscillatory zones. Most analyses are concordant or nearly concordant within error and plotted on or near the concordia in the U-Pb Concordia diagram (Fig. 3-10A), although some analyses show weak loss of radiogenetic Pb. Despite that a lot of the zircon grains analysed look to be magmatic in morphology, they are actually inherited or xenocrystic and can only be discriminated by isotope ages.

Based on their ages and position along the concordia (Fig. 3-10A and B), the 24 analyses could be divided into 3 groups, however its limited data. $^{206}Pb/^{238}U$ ages

for younger zircons (<1000 Ma) are obtained with higher precision than those based on $^{207}Pb/^{206}Pb$ ratios due to the relatively lower abundance of ^{207}Pb in younger zircons, but $^{207}Pb/^{206}Pb$ ages for older zircons (>1000 Ma) are more precise than their $^{206}Pb/^{238}U$ ages, and thus we present $^{206}Pb/^{238}U$ ages for younger zircons (<1000 Ma) and $^{207}Pb/^{206}Pb$ ages for older zircons (>1000 Ma) in this chapter. The following is the three age groups:

1. Precambrian group: Tow analysis point (Fig. 3-10A) show Precambrian age that may inherited from the Middle Tianshan basement (Lei et al.; Liu et al., 2004).
2. Early Paleozoic group: The wide distributed rock of Paleozoic has been recognized (Mao et al., 2010). The result gives a peak age of 441±10Ma (95% confidence, MSWD=4.9) which maybe a mixed age because the peak is not very concentrate and limited data.
3. Late Paleozoic group: 7 clustered analyses of $^{206}Pb/^{238}U$ age gives an average age of 312±11Ma (95% confidence, MSWD = 4.0, Fig. 3-10C).

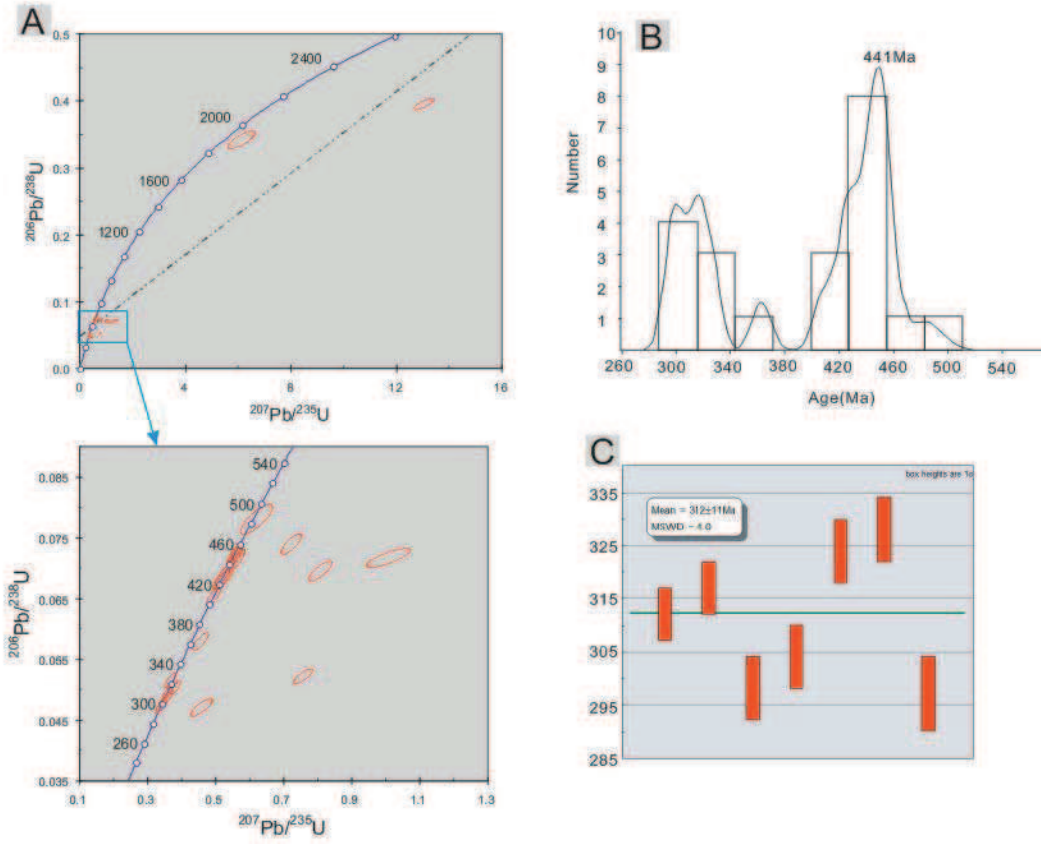

Fig. 3-10: U-Pb concordia diagram and weighted average age for zircons from the Yamansu arkose. A: U-Pb concordia diagram; B: U-Pb Concordia weighted average age diagram of Paleozoic, showing two peaks: 312Ma and 441Ma. C: Weighted average of the late Paleozoic group (312±11Ma).

The above distribution of zircon ages implies that the late Paleozoic weighted mean age of 312 ± 11 Ma can be interpreted to represent the latest sediment age of the Yamansu arkose. The shearing could not earlier than this age because the from the Fig. 3-3 we can see that the outcrop form of the arkose has high length-width ratio and located in the strike-slip zone. But it also indicated that, at about 312 Ma, continental arc probably approached its end and began to turn into intercontinental deformation.

Meanwhile, there are quite a lot of inherited/xenocrystic zircons in this arkose, which yielded Precambrian and early Paleozoic age. These ages of

inherited/xenocrystic zircons indicate that there are Precambrain source and early Paleozoic geothermal or tectonomagmatic events did occur during evolution of Yamansu arc/rift zone. The early Paleozoic group probably associated with closure of Paleo-Asian ocean (Hu et al., 2007).

3.3.3 Dykes

7 mafic dyke outcrops with N-S trending direction were observed in the open pit (Fig. 3-5 and Fig. 3-11A). These dykes cut the marble and basalt indicating later formation (Fig. 3-11A). In the eastern part of the Yamansu ore field, there are rather dyke swarms (Fig. 3-3). These dykes range 10-50cm in width in the Yamansu open pit. These dykes were dated to be Permian in age (Li et al., 2006; Ouyang et al., 2006). It is noteworthy that the contacts between the mafic dykes and marble are emphasized. Some of the contacts yield pyrite and garnet skarn (Fig. 3-11B) of which the garnet will be discussed in the paper of "garnet".

A B

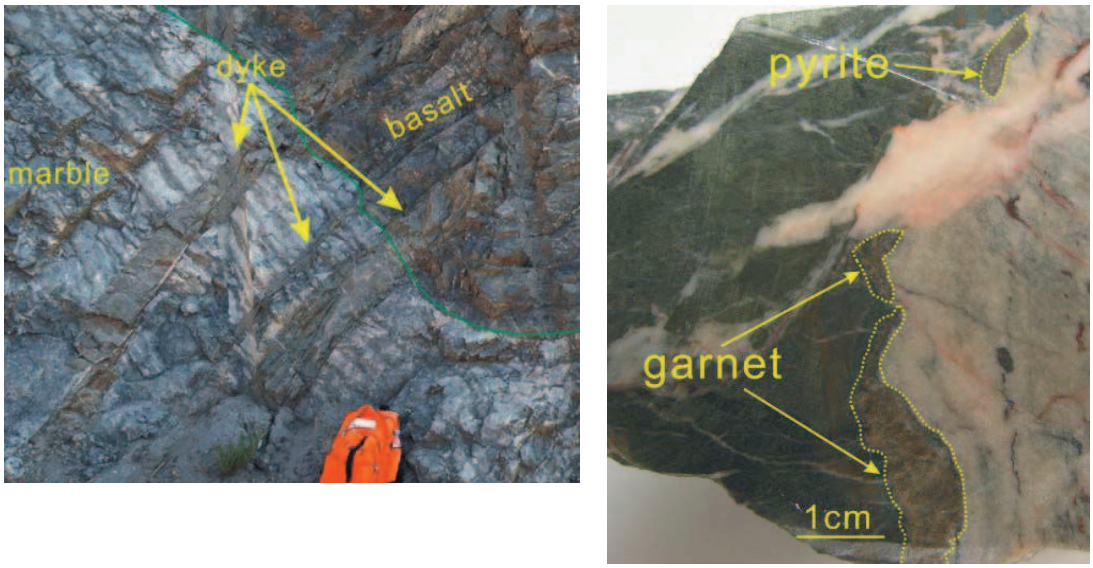

Fig. 3-11: Mafic dykes in Yamansu open pit. (A) Photo showing mafic dykes cut the marble and altered basalt. The green line marks the boundary between marble and altered basalt. (B) Photo showing mafic dyke cut the limestone and cause skarnization. The yellow circle emphasizes the pyrite and garnet. The pale green part to the left and while part to the right are altered mafic dyke and marble respectively. Sample is from Yamansu magnetite deposit, NW China.

3.4 Skarn

3.4.1 Wall rocks

During the study of the Yamansu skarn, two protholith should be involved: basalt and limestone which also act as the skarn wall rocks presently.

3.4.1.1 Basalt

The basalt wall rock is composed by plagioclase phenocryst, disseminated magnetite and fine grain groundmass, sometimes minor amount of hematite was observed (Fig. 3-12 A, B and C). Within basalts, we distinguished small size disseminated magnetites which likely are primary magmatic (Fig. 3-12C). These magnetite grains were about 20μm in size. Pyrite was devoid within this basalt. There are relics of basalt in the massive garnet skarn indicating transition from basalt into skarn (Fig. 3-12D). The sizes of these relics basalt vary, from a few centimetres to about 30cm. In this relic basalt, pyrite was observed.

Plagioclase phenocryst ranged 3-5mm in size. They were white in colour and subhedral to euhedral. The geochemical composition of plagioclase had been analyzed (Table 3-3) and the result displayed that they are albite.

A

B

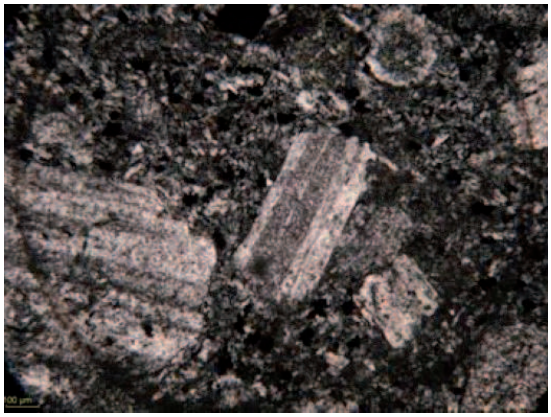

C

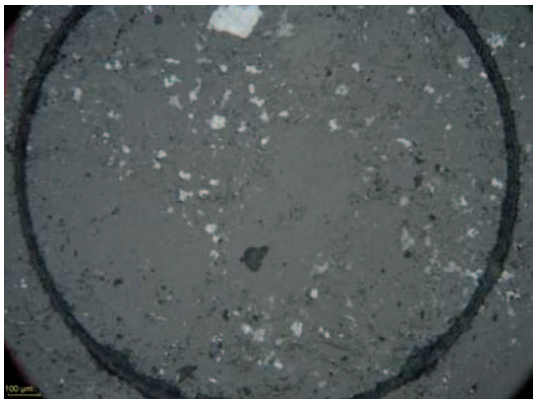

Fig. 3-12: Photographs of basalt from Yamansu magnetite deposit. (A) Hand specimen of basalt. Plagioclase phenocrysts are in white. (B) and (C) Photographs of basalt in plane-polarized light and reflected light from the same thin section, respectively. In the (B), the plagioclase shows multiple twins. In the (C), disseminated magnetite and hematite are observed in the fine grain groundmass, around the plagioclase phenocryst. (D) Photo showing relics of basalt in the massive garnet skarn. Relics of basalt are emphasized in dotted yellow lines; massive garnet skarn is in pale rose.

D

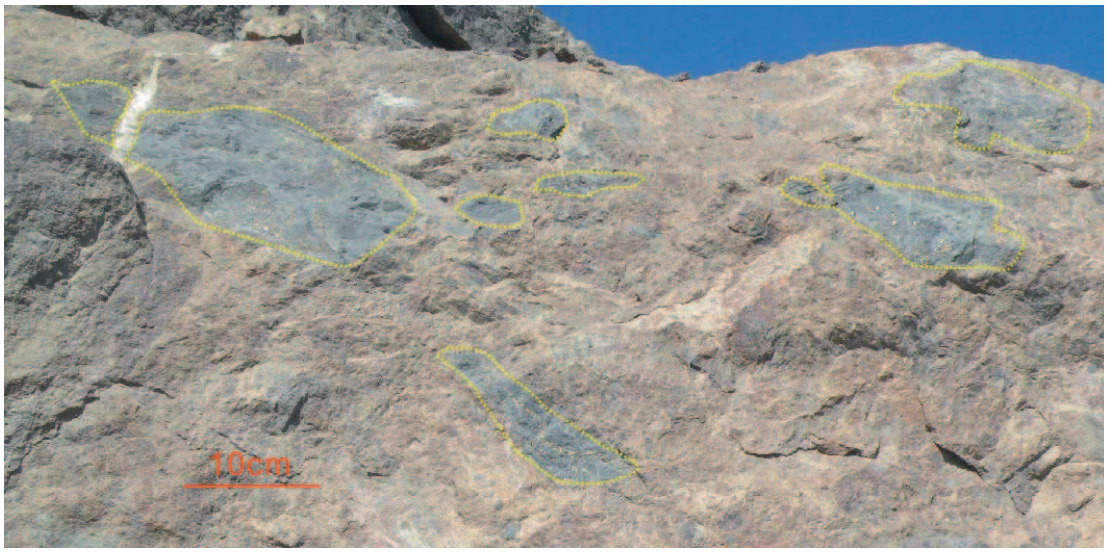

Fragments of marble within strongly altered basalt were observed in the gallery, about 200m underground, suggesting mafic magma stoping (Fig. 3-13). Around the fragments of marble, potassium metasomatic alteration developed leading the formation of K-feldspar. It is obvious that this basalt was later then the limestone.

Fig. 3-13: Clasts of marble within altered basalt suggesting mafic magma stoping. The photo was taken in the gallery, about 200m underground. Potassium metasomatic alteration developed leading the formation of K-feldspar (in the pale red part).

3.4.1.2 Limestone

In the Yamansu ore field, about one third proportions limestone has been changed into marble. They are fine in grain size (less then 1mm) and white to grey in colour; whereas the marble was composed by bigger grains of calcite and mostly pure white. The limestone wall rock was thought to be early Carboniferous because characteristic fossils were found inside (Baosteel-Company, 1977; XBGMR, 1993). The limestone wall rock is part of Yamansu formation formed in submarine

environment (Hou et al., 2007). Limestone mainly develops in the northern part along the Yamansu fault. It has well developed planar-linear fabric (Fig. 3-7) indicating dextre kinematic direction. Ripple plane of the limestone was observed in the Yamansu open pit (Fig. 3-14A). A limestone layer of about 30cm thickness containing fossils were found in the Yamansu open pit, in which crinoid and testacean are well developed (Fig. 3-14B).

A

B

Fig. 3-14: Limestone wall rock. (A) Limestone in the YMD open pit showing ripple plane (165°∠49°). (B) Fossile of crinoid found in the limestone in the open pit.

3.4.2 Skarn

Two distinct skarn groups could be identified: the prograde skarn (garnet-pyroxene) and retrograde skarn (epidote-chlorite-actinolite-tourmaline-feldspar). Garnet skarn, which contain magnetite and minor amount of pyroxene inside, was massively developed in YMD. Massive magnetite ore shoots located in the central; ore bodies are spatially associated with a 50 m thick stratoid garnet skarn, massive garnet skarn develops preferentially in the hanging wall (Fig. 3-15A). Garnets crystals generally occur as hexagonal shaped grains ranging in size from 1 to 6 mm; in the footwall, prograde stage minerals were extensively altered by calcite, epidote and chlorite.

Skarn zonation is well developing in the Yamansu open pit. The main fabric within the massive garnet skarn is a centimetre- to metre-scale, textural and mineralogical banding. This corresponds to alternation of coarse grained garnet rich ribbons with small-size green epidote and chlorite rich ribbons.

Rhythmic banding pattern composed by magnetite bands and garnet bands is observed at the top of the ore shoots (Fig. 3-15B).

Tourmaline – K-feldspar – epidote assemblage alteration, which normally associated with granitic plutonism, on the basalt is observed (Fig. 3-22A and 3-22B). This alteration seems quite different from the garnet – pyroxene – magnetite assemblage which seems being caused by the progressively advance fluid front (see section 3.4.3.1).

A

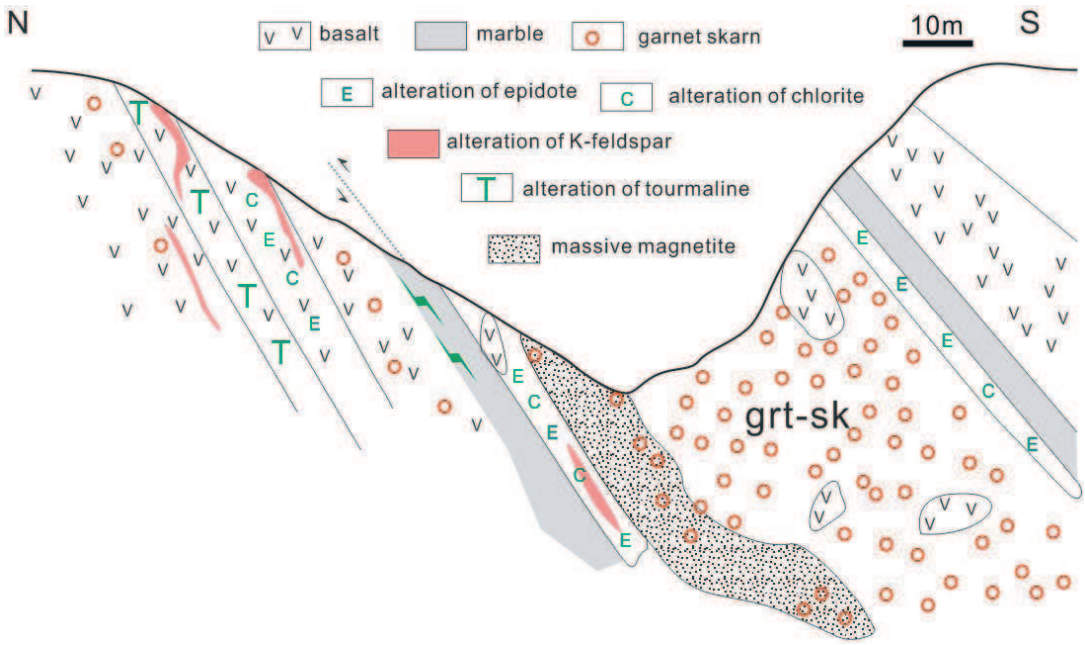

B

Fig. 3-15: Figures of (A) Cross section of Yamansu open pit. It shows the development of a massive garnet skarn around the magnetite ore body and the presence of basaltic relicts within the former formation. grt sk=garnet skarn; (B) Rhythmic banding of garnet and magnetite. Garnet is in pale yellow, magnetite is in black.

3.4.3 Ore shoots

The main ore mineral is magnetite, mostly the magnetite grains were euhedral and ranging mostly from 5-30μm in size. Massive magnetite bodies are of two types: (i) massive magnetite lobes replacing marble show a reactional front outlined by garnet growth (Fig. 3-16). The progression of the magnetite replacement front is marked by integration and growth of garnets within massive magnetite; (ii) massive magnetite lenses in the centre of Yamansu open pit which present a banding pattern composed by alternation of magnetite and garnets ribbons (Fig. 3-15B).

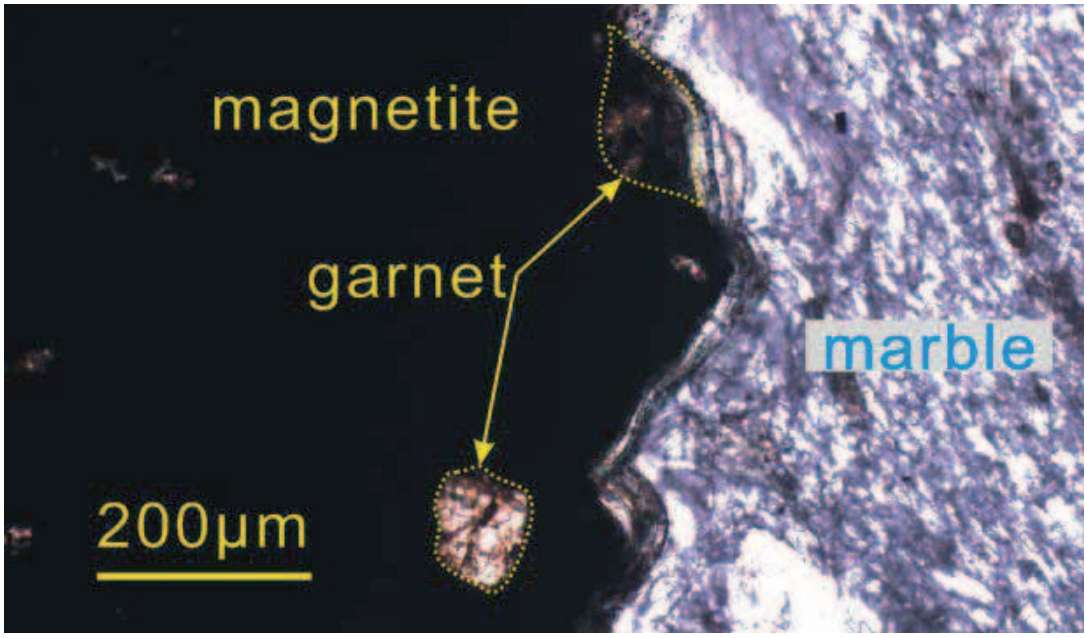

Fig. 3-16: Microphotograph of iron rich front. It display that this front progressively absorbs the calcite and gives birth to garnet grains, in transmitted plane polarised light. The magnetite is black to the left. The yellow dot lines outline the new birth garnet.

3.4.3 Skarn transitions

Skarn forming processes are elements immigration processes. Transitions from the wall rocks into skarns and the reactional fluid front into the skarn should be observed. These alterations or transitions argue its skarn-related metallogeny.

3.4.3.1 Transition from iron-rich-fluid to skarn

The transition from iron-rich-fluid to marble seems quite sharp (Fig. 3-17). The massive magnetite represents the iron rich fluid and the contact between magnetite and marble represents the reaction fronts (Meinert, 1992; Meinert et al., 2005). The progressively advancing reactional fronts were outlined by garnet grains, indicating that absorb the calcite and gave birth to the garnet (Fig. 3-16 and Fig. 3-17).

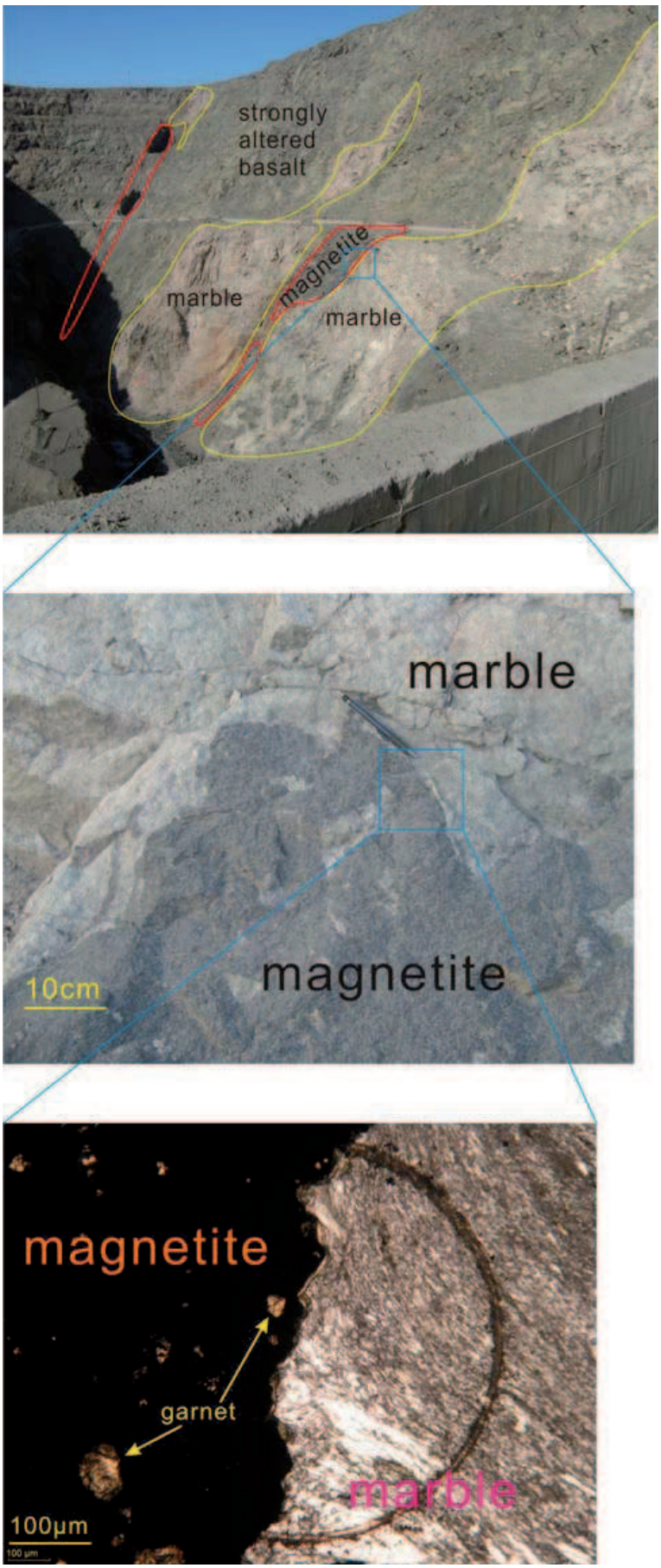

Fig. 3-17: Contact between massive ore shoots and marble. The topmost photo shows the spatial relation between marble, magnetite and altered basalt in the field; The middle photo shows the contact between marble and magnetite (magnetite and marble are in black and white, respectively). It is noteworthy that some clasts of marble in the massive magnetite; The base photo shows micro-structure between magnetite and marble (exoskarn) in transmitted plane polarised light. It shows magnetite replacement front within marbles. The advancing front yields to corrosive brecciation of marble.

Element distribution maps of transition from iron-rich-fluid into skarn from YMD showing contact between marble and magnetite are studied (Fig. 3-18). The progressively advancing front yields to corrosive brecciation of marble and produces garnets. The reaction fronts generally show low Ti content neither the marble nor the magnetite (Fig. 3-18A). These element distribution maps show contrast content of Al, Si, Ca and Fe between the marble side and magnetite side. The massive magnetite side contains obviously higher Al (Fig. 3-18B). One thing should be highly emphasized that the Si content seems significant higher in the slim zone between the magnetite side and the marble side (Fig. 3-18C) whereas the Fe is relatively low (Fig. 3-18 D). Because the earliest garnets were andradite ($Ca_3Fe_2[SiO_4]_3$) (see section 3.4.4.1.1).

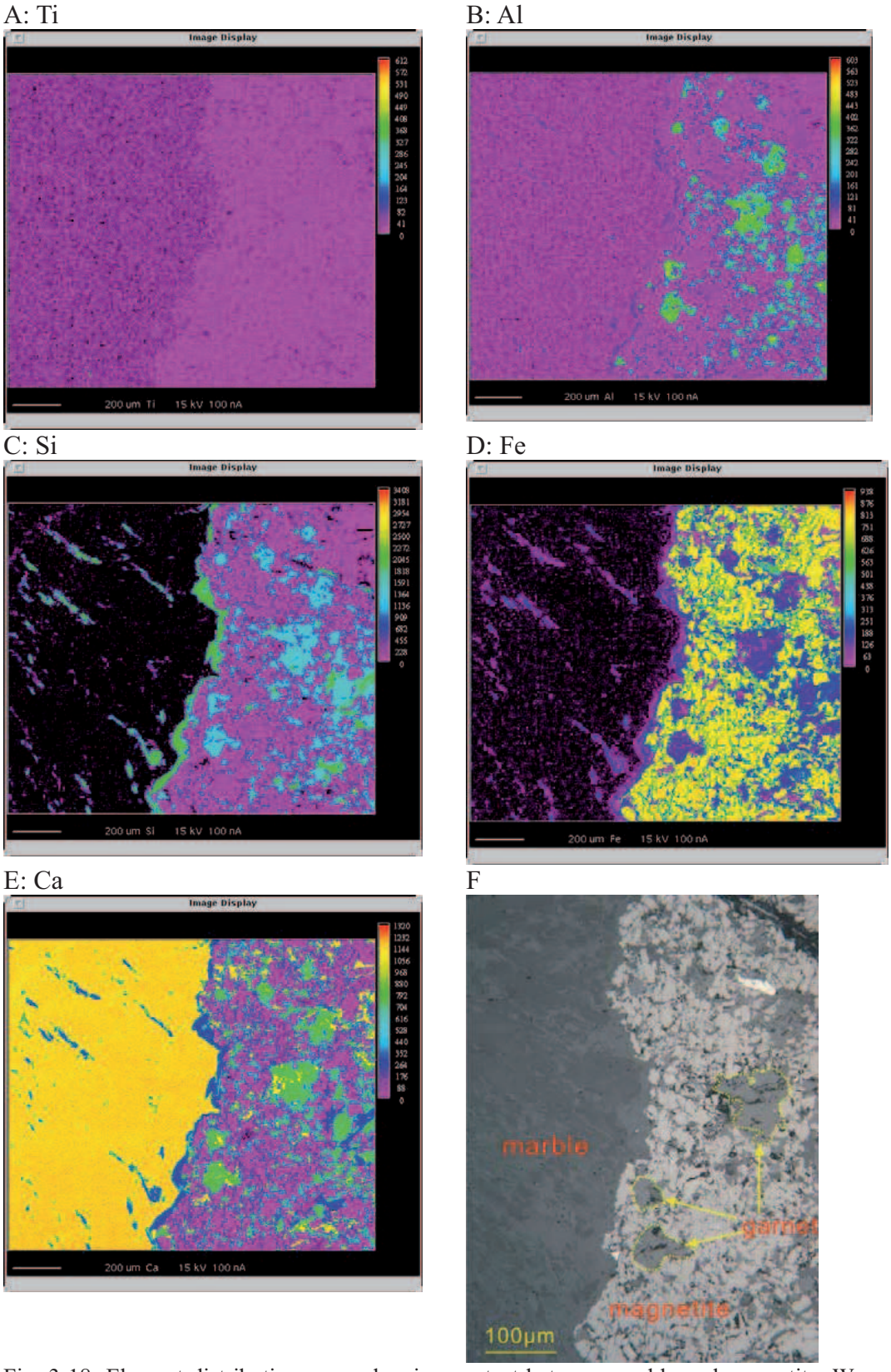

Fig. 3-18: Element distribution maps showing contact between marble and magnetite. Warmer color indicates higher content. The magnetite replacement front is digesting the marble. The advancing front yields to corrosive brecciation of marble. Yellow dot lines mark the garnet grain in (F), in reflected light.

3.4.3.2 Transition from basalt to skarn

The basalt acted as the wall rock of skarn. The transition from basalt to skarn has been partially described above (Fig. 3-12D and Fig. 3-16A).

Within the massive garnet ribbons, relics of basalt were observed. These basaltic clasts vary in size from a few to about 30 centimetres and show irregular rounded shapes with gradational and wavy boundaries. Sparse idiomorphic pyrites develop in the basaltic relics. In some places, far from massive garnet ribbon skarn and magnetite bodies, basalts are partially replaced by andradite growing in the groundmass, whereas the plagioclase is little replaced (Fig. 3-19A). They occur in isotopic and significant different to the grandite. And them the total basalt was replaced into skarn (Fig. 3-12D). All these observations support the replacement of basaltic protolith into garnet skarn. No relation is observed in altered basalts between massive magnetite and garnet growth.

A

B

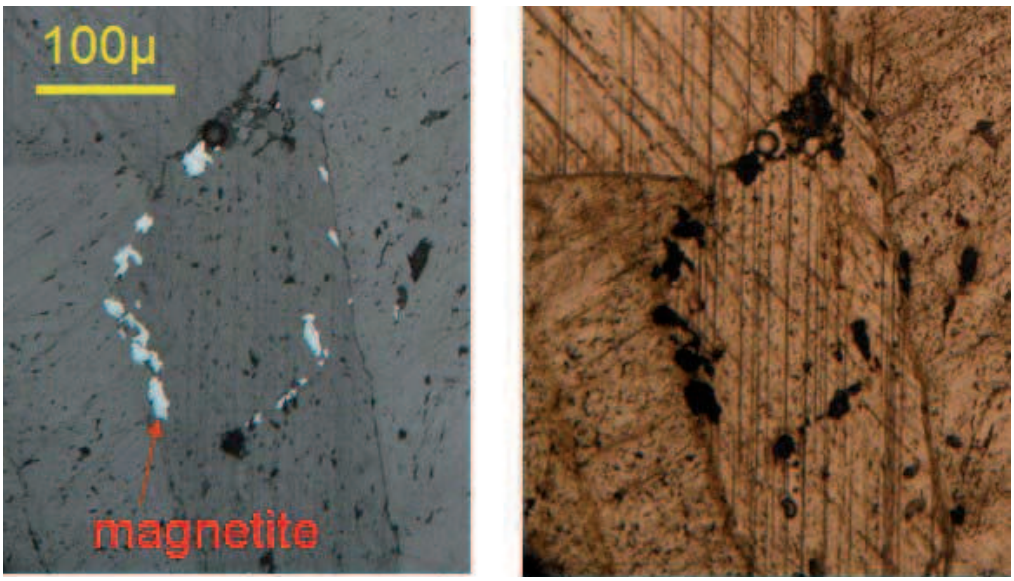

Fig. 3-19: Photos (A) showing andradite alteration of the basalt. Garnets are andradites in pink colour; Plagioclases are in white colour; Groundmass and disseminated magnetite are in black; (B) CO_2 rich fluid dissolved the garnet. The two photos are the same but in reflected light to the left and in transmitted light to the right.

3.4.3.2 Later altercation on skarn

The retrograde stage is dominated by epidote and chlorite (see the article of garnet in section 3.4.4.1.1). Fluid circulation in retrograde stage is evident in YMD. Late

fluid which was rich in CO_2 extensively altered the massive garnet skarn (Fig. 3-19B). In this figure (Fig. 3-19B), garnets totally disappear, and inclusions of magnetite which were altered into hematite were preserved. In this late stage, sulphides were observed, mostly pyrite and chalcopyrite (Fig. 3-27).

3.4.4 Skarn mineralogy

The prograde and retrograde stages of skarnization were dominated by garnet and epodite and chlorite, respectively (Fig. 3-20). Others numerous skarn minerals have been identified and replaced within the paragenetic evolution presented in Figure 3-20. The massive magnetite stage then occurred between the prograde and retrograde stages. The prograde skarn minerals were extensively altered by chlorite and epidote (Fig. 3-26 and Fig. 3-27). In addition, sulphides (pyrite and chalcopyrite) are observed crosscutting the massive magnetite, indicating their later deposition (Fig. 3-29).

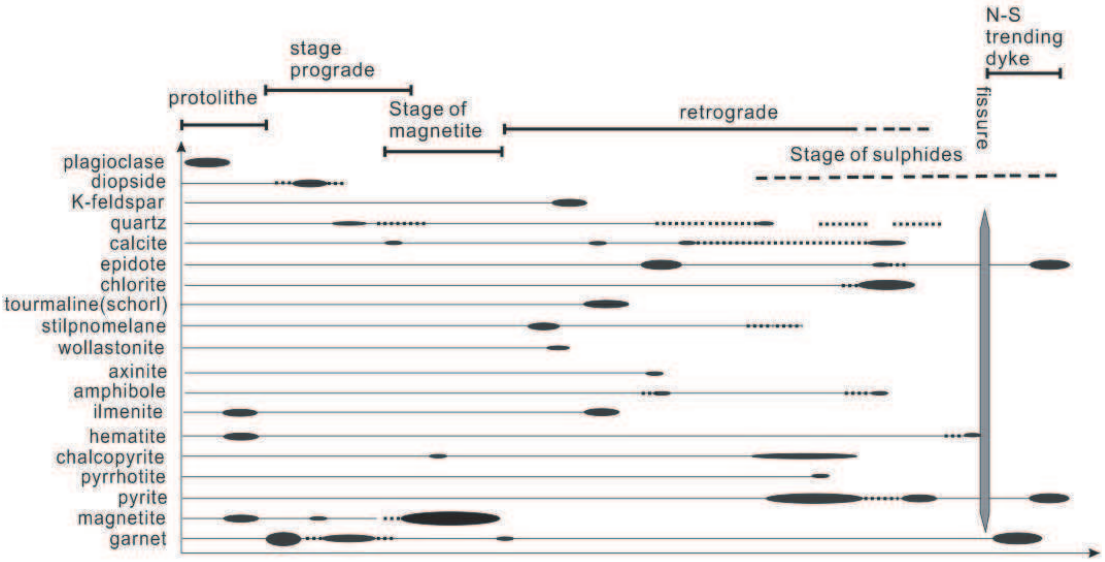

Fig. 3-20: Paragenetic sequence of the Yamansu iron deposit with temperature from chlorite geothermometers.

3.4.4.1 Prograde stage minerals

3.4.4.1.1 Garnet

Garnet was massive developed in YMD and they displayed a complex zoning which could give some information on the ore forming process.

ARTICLE

Early-stage evolution of garnets in the Yamansu magnetite deposit (East Tianshan orogenic belt): implication for metasomatic fluid composition and iron ore deposition

ABSTRACT

The Yamansu magnetite deposit is located in a shear zone with a composite planar-linear fabric, in NW China, Central Asia Orogenic Belt. Garnet associated with magnetite bodies is massively developed, leading previous works to identify a "skarn-type" iron deposit. Textural observations and chemical analyses of garnet enable the recognition of complex zoning: (i) in the core of the grain, the composition is close to end-member andradite; (ii) this core is surrounded by a zone with inclusions of calcite and a few crystals of magnetite; (iii) the border is an andradite-grossular solid-solution, which displays broad compositional variations from 25 mol% early to the 45 mol% late grossular. This zoning suggests that garnet form through three stages of precipitation under decreasing fO_2. The second stage records a change in the chemical composition of the fluid possibly depleted in Si, and/or with a fO_2 value not suitable for andradite formation. The massive economic magnetite stage follows the deposition of these complex garnet grains. The latest garnets, whose composition is similar to that of the complex grain rims, infill fractures related to a late brittle deformation. Thus, garnets from Yamansu magnetite deposit record episodic flow of fluid with contrasted chemical composition which was typically controlled by hydrothermal environment.

Keywords: garnet zonation, skarn iron deposit, massive magnetite, oxygen fugacity, Tianshan orogeny, Yamansu.

INTRODUCTION

Large variations in composition, from core to rim within a zoned crystal, reflect the chemical and physical changes of the medium where the crystal grew. Thus, analysis of intracrystalline zonation of metasomatic minerals may provide a more or less continuous record of the processes taking place during the evolution of metasomatism (Jamtveit and Hervig, 1994; Rollinson, 2003; Sabau et al., 2006). Garnet is a common mineral in skarns and also a refractory mineral that dominates the prograde metasomatic stage. Zonation is commonly used as a fluid probe which may indicate episodic flow of fluid during metasomatic processes. The garnet group is subdivided into several species that combine end-members which, as such, are relatively rare in nature. Garnet of near-end-member composition may occur in different skarn-type deposits, of which the Fe skarn garnet is characterized by a low content of Mn and high Al and Fe (Meinert, 1992). Zoned garnets in iron skarn deposit have been described as well, such as in the Beni Bou Ifrour deposit (Rhazi and Hayashi, 2002). However, calcite and magnetite crystal zonation found in the garnet grain were rare.

The studied garnets are representative of a large mineral paragenesis developed in a contact zone between carbonate sedimentary sequences and basaltic sills and dykes. This paper describes the complex early-stage evolution of garnets in the magmatic/hydrothermal environment of the Yamansu magnetite deposit (eastern Chinese Tianshan) and provides new insights into about the iron ore forming process.

GEOLOGICAL SETTING

The eastern Tianshan belt formed from welding of terranes and arcs in the late Paleozoic (Wang et al., 2010; Charvet et al., 2011). The boundaries between the different accreted terranes correspond to large crustal scale strike-slip faults. The

Late Paleozoic tectonic-metallogenic framework of the eastern Tianshan was mainly characterized by: (i) Carboniferous island arc and adakitic rocks formation (Zhang et al., 2004; Wu et al., 2006) and its subsequent metamorphism during collision; (ii) Permian wrenching associated with pull-apart like transtensional zones. During this evolution, tectonics combined with mafic-ultramafic and calc-alkaline magmatism were responsible for the formation of a major metallogenic province with ore deposits types as different as porphyry copper, epithermal gold and orogenic lode gold (Qin et al., 2002; Chen et al., 2003; Mao et al., 2005; Zhao et al., 2008). The large crustal-scale strike-slip faults were thought to be active in the Early Permian and were coeval with emplacement of mafic-ultramafic complexes bearing important Cu-Ni-(Fe)-(V) ore deposits (Shu et al., 1999; Laurent-Charvet et al., 2002; Chen et al., 2005; Pirajno, 2010). The Yamansu iron deposit is located along one of these strike-slip shear zones with dextral kinematics, called Yamansu fault (Fig. A-1a). A brittle segment of this shear zone separates (Fig. A-1a) (i) a northern part, including the iron deposit and composed by the Carboniferous Yamansu formations with a volcano-sedimentary lower sequence and an upper sequence characterized by thick limestone layers, from (ii) a southern part corresponding to a Permian basin, filled with conglomerate and chert series intercalated and/or intruded by diorites and andesites. Late Permian mafic N-S-trending vertical dykes cross-cut the two series (Li et al., 2006). The lack of a detailed paragenetic understanding leads to uncertain interpretations of existent radiometric ages. Thus, the formation age of the Yamansu deposit is still debated. The two prevailing views for the genesis of the Yamansu deposit are a syngenetic volcano-sedimentary exhalative model (Wang, 2005) or an epigenetic skarn-type model (Mao et al., 2005). As described below, our data are consistent and reinforce a model of skarn-related iron deposits.

The Yamansu ore field

The Yamansu ore field contains more than six lenticular ore bodies situated within a narrow, 5 km long, E-W-trending vertical shear zone. The Yamansu magnetite deposit, exploited in an open pit and an underground mine, is the easternmost and

biggest of these bodies (Fig. A-1a). The Yamansu magnetite deposit has been mined for more than 30 years. The two biggest ore shoots contain a reserve of 32 Mt with an average grade of 51% Fe, and 20,000 t of Cu with a mean grade of 0.06% Cu (Mao et al., 2005). The lithology in the shearing zone is dominated by limestone, tuff and basalt. The limestones are considered as Carboniferous in age on the basis of fossils (XBGMR, 1993). Along high strain zones, limestones have suffered boudinage. As a result, 10 to 100 metres long limestone lenses crop out along the Yamansu open pit. Some of them, which host the magnetite bodies, have recrystallized into nearly pure marble.

The ore bodies are spatially associated with a 50 m thick stratoid massive garnet skarn (Fig. A-1b). Mineralized bodies, skarn, basalt and the hosting limestone sequence are all south dipping with an angle of about 60°. They are located in the central part of the open pit. Skarn zonation is well developed, especially around the magnetite ore body (Fig. A-1b). The skarn zonation was clearly affected by Permian dextral wrenching and the ore shoots appear to have been deformed during this tectonic event. Two sets of faults are observable in the Yamansu open pit: NE-SW-trending and E-W-trending respectively. The last set is parallel to the trend of the ore bodies and shows a subtle thrusting component, while the first one displays a clear right-lateral strike-slip component and may be interpreted as second-order synthetic faults within a bulk E-W-trending regional wrenching.

Skarn textures and paragenesis

The main fabric within the massive garnet skarn is a centimetre- to metre-scale, textural and mineralogical banding. This corresponds to alternation of coarse-grained garnet-rich ribbons with small-size green epidote and chlorite rich ribbons. Within the massive garnet ribbons, relics of basalt were observed (Fig. A-2a). These basaltic clasts vary in size from a few to about 30cm and show irregular rounded shapes with gradational and wavy boundaries. Sparse idiomorphic pyrites develop in the basaltic relics. In some places, far from massive garnet ribbons and magnetite bodies, basalts are partially replaced by andradite growing in

the groundmass, whereas the plagioclase is little replaced (Fig. A-2b). All these observations support the idea of a replacement of basaltic protolith into garnet skarn. Within the massive garnet ribbons, garnet crystals generally occur as hexagonal shaped grains ranging in size from 1 to 6 mm. Most garnet grains display complex zoning generally characterized by three zones (Fig. A-2c, A-2d and A-5b): (i) in the centre of the grain, the andradite core is brown, isotropic, devoid of inclusions, and surrounded by (ii) a rim, 5 to 20µm thick, made of calcite and a few magnetite inclusions; (iii) the border, which is an andradite-grossular solid-solution (up to about 45 mol% grossular), mostly shows appreciable anomalous birefringence (oscillatory zoning) and sector twinning (Fig. A-2d). The border generally contains numerous inclusions of gas, liquid and daughter minerals (Fig. A-2c). Associated with garnet (andradite+grandite), minor amount of clinopyroxene (28 mol% diopside and 72 mol% hendenbegite) have been identified, all contributing to the prograde stage of the skarn. This prograde stage is mainly developed near the ore shoots in the centre of the Yamansu open pit (Fig. A-1b). Relations between massive magnetite and garnet are also very informative. Within basalts, we distinguished small size disseminated magnetite which likely is primary magmatic. No relation is observed in altered basalts between massive magnetite and garnet growth. Massive magnetite bodies are of two types: (i) massive magnetite lobes replacing marble show a reaction front outlined by garnet growth (Fig. A-2e), the progression of the magnetite replacement front is marked by integration and growth of garnet within massive magnetite; (ii) massive magnetite lenses in the centre of Yamansu open pit present a banding pattern composed by alternation of magnetite and garnets ribbons (Fig. A-2f). It is noteworthy that veinlets filled with grandite (grossular mol content varying between 40-45%, and anomalous birefringence) are observed crosscutting both massive magnetite and garnet skarn (Fig. A-2g). These grandite fillings share similar characters with the borders of zoned garnets described above.

The prograde skarn minerals were extensively altered into chlorite and epidote (Fig. A-3a). In addition, sulphides (pyrite and chalcopyrite) are observed crosscutting the massive magnetite, indicating their later deposition (Fig. A-3b).

The massive magnetite stage then occurred between the prograde and retrograde stages (Fig. A-4).

Finally, a last generation of garnet (Fig. A-3c) has been recognized along contacts between the NS-trending Permian mafic dykes and marbles.

Numerous other minerals have been identified and replaced within the paragenetic evolution presented in Fig. A-4.

MINERAL CHEMISTRY AND FORMATION TEMPERATURE

Prograde stage

In the Yamansu magnetite deposit, Si, Al, Ti, Fe, Mn, Mg, Ca, K, Na, P, F and Cl have been analysed in garnet, pyroxene and chlorite with an electron microprobe CAMECA SX50 using the PAP correction, 20 kV accelerating voltage, 15nA sample current and different counting time according to the analysed elements (10s for Si, Al, Ti, Fe, Mn, Mg, Ca, K, Na; 20s for P, F and Cl). Analyses were done in the common laboratory of BRGM-CNRS-University Orleans France. All Fe in the analyses is expressed as Fe2+. Only the analyses significant at a threshold of 5% have been considered. Representative data for a single garnet are listed in Table A-1. Structural formulae are calculated on the basis of 8 cations, $Fe^{3+} = 2 - (Al^{3+})^{VI} - Ti^{4+}$ and $Fe^{2+} = Fe(total) - Fe^{3+}$. The structural formulae of garnet show that in the core of the grain, the composition is close to theoretical andradite while the border shows andradite-grossular solid solution (Fig. A-5a). This is consistent with the observations done under the microscope. The cores generally contain about 3 wt% less SiO_2 (Table A-1) than the borders. Figure A-5c shows that Si, Ca, Fe display contrasting contents in the cores and the borders, whereas Ti and Al show fluctuations. As a whole, the borders contain higher Fe^{2+}, Ti, Al, (Mn+Mg) and Ca than the cores (Fig. A-5d).

The average pyroxene composition of five analyses is: 51.9 wt% SiO_2; 8.4 wt% FeO; 0.1 wt% MnO; 11.7 wt% MgO; 24.1 wt% CaO; 1.2 wt% Al_2O_3; 0.4 wt% Na_2O and the corresponding structural formula is: $(Ca_{0.99}Na_{0.01})^{VI}(Mg_{0.67}Fe_{0.27}Al_{0.05})^{VI}(Si_{1.99}Al_{0.01})^{IV}O_6$. It is not suitable to use the

garnet-clinopyroxene Fe^{2+}–Mg geothermometer (Råheim and Green, 1974; Krogh, 2000), because of the low content of Mg and too much Fe^{3+} in the garnet. However, according to the salinity of fluid inclusions in calcite (Lu et al., 1996) and calculated possible stability limits of stilpnomelane (Miyano and Klein, 1989) which altered garnet in the Yamansu deposit (see paragenesis Fig. A-4), it seems that the formation temperature of garnet was above 500°C.

Retrograde stage

As indicated in the paragenetic table (Fig. A-4), the retrograde stage is dominated by epidote and chlorite. The chlorite thermometer (Cathelineau and Nieva, 1985) shows a temperature of 280°C during the retrograde epidote-chlorite-pyrite stage.

DISSCUSSION

The data presented above and the observed textures are clearly diagnostic of metasomatic replacement of basalts and limestones. Moreover, at least part of the skarnization process was triggered by the massive magnetite deposition (Fig. A-2e) which was itself controlled by pervasive flow of iron-rich very hot brines. A literature survey and an analysis of published chemical data on iron-skarn-type garnet displayed a clear negative correlation between Ca and Fe^{2+}, and relatively low Mn (Verkaeren and Bartholome, 1979; Xu and Lin, 2000; Rhazi and Hayashi, 2002). The studied garnets of Yamansu deposit are not exceptional and they display relative high content of Ca and only minor contents of Mn^{2+} and ferrous end member. These features are characteristic of the calcic magnetite skarn deposits as defined by (Einaudi et al., 1981). Comparing to the magmatic garnets, such as the garnets from granitoid rock, generally show lower Ca, higher Fe^{2+} and variational Mn (Allan and Clarke, 1981; Wright and Haxel, 1982; Kebede et al., 2001; Dahlquist et al., 2007; René and Stelling, 2007). Consequently, we argue that metasomatism was achieved dominantly by fluid circulation rather than diffusive processes only.

Kinetics of garnet growth

The growth history of the euhedral zoned garnets in the investigated skarn can be traced in terms of a three-stage process from the centre to the border.

1. First, cores of andradite precipited with a near-end-member composition. In this stage, the percolating fluids were rich in oxidized iron. The SiO_2/Fe_2O_3 ratio and the FeO content in the fluid control the hedenbergite/andradite ratio (Deer et al., 1982), which is very low at Yamansu. This is consistent with the low SiO_2 content of the Yamansu protoliths, mainly composed by basalt and limestone. That could be the reason for the scarcity of Ca-rich pyroxene in the skarn. Also, it implies that during this stage, fO_2 was relatively high.
2. During the second stage, calcite and a few magnetite crystals were deposited. This event has to be related to the input of a fluid rich in CO_2 and depleted in SiO_2. In fact if SiO_2 was brought in, andradite would have formed. The transition from Ca3Fe2Si3O12 (andradite), where the iron is present as Fe^{3+}, to magnetite, where part of the iron is divalent could be linked to a decrease in fO_2. According to Gustafson (1974), such a transition may occur between 10-15 bar (at 800°C) and 10-32 bar (at 400°C) for fO_2 at 2 kbar Pfluid. An alternative explanation might be linked to excess of CO_2 in the fluid and the following reaction:

   $Ca_3Fe_2Si_3O_{12}$ (andradite) + $3CO_2$

   → $3SiO_2+3CaCO_3+ (1/2)Fe_3O_4 \downarrow + (1/4)Fe_2O_3 \downarrow + (1/8)O_2$

   The increase in fO_2 could be related to the decarbonation of limestone during the skarn formation process.
3. During the third stage, the rim formed. It is andradite-grossular solid-solution with up to 45 mol% grossular component. The compositional shifts in garnet are generally interpreted to reflect sudden changes in the parameters controlling its growth (Jamtveit and Andersen, 1992). Liou (Liou, 1973) suggested that, in the andradite-grossular solid solution, as fO_2 decreases, the grossular component increases. In our case, this process may involve the input of Al and consumption of magnetite, as follows:

$3SiO_2+3CaCO_3+(1/3)Fe_3O_4+(1/2)Al_2O_3+(1/12)O_2$

$\rightarrow[Ca_3Fe_{(1/3)}][Fe_{(2/3)}Al]Si_3O_{12}+3CO_2$

These grandite rims show distinct oscillatory zones and sector twinning (Fig. A-2d and Fig. A-5b). Various hypotheses have been put forward to explain the origin of such phenomena (Kingma and Downs, 1989; Garcia-Casco et al., 2002; Shtukenberg et al., 2002). Shtukenberg et al. (Shtukenberg et al., 2002; Shtukenberg et al., 2005) ascribed it to Al/Fe ratio in octahedral cation, whereas Holten et al. (Holten et al., 2000) emphasized on nonlinear local dynamics. These oscillatory zones are probably associated with hydrothermal environments (Jamtveit, 1991; Jamtveit et al., 1993).

Hydrothermal process

The evolution from andradite to grandite is compatible with the replacement sequence of basalts. As demonstrated by observations (Fig. A-2b), the primary replacement of basalts initiated with the growth of isotropic brown andradite within the fine grained groundmass of the basalt. At this stage, most of the magmatic plagioclases seem to be little altered according to the shape of plagioclase and relations between garnet and plagioclase (Fig. A-2b). Subsequent decomposition of plagioclase liberated Al into the fluids inducing grandite rim crystallisation (Fig. A-5d). Concomitantly, Ti, Fe^{2+} and (Mn+Mg) are enriched in the fluids, explaining the higher contents observed in the garnet rim (Fig. A-5c, d). In addition, the grandite rims contain higher SiO_2, up to about 3 wt% (Table A-1).

However, the transition from andradite to grandite observed in the Yamansu skarn is opposite to the evolution with decreasing temperature in the $Ca_3Al_2Si_3O_{12}$-$Ca_3Fe_2Si_3O_{12}$-CO_2 eutectoid system (Shoji et al., 1985; Rubin and Kyle, 1988). Moreover, the grandite composition is very sensitive to variations in temperature, pH, fO_2 and salinity of the hydrothermal solution (Jamtveit et al., 1995). Therefore, it seems that the observed chemical evolution was mainly controlled by the local composition and the variation of fO_2 of the fluid rather than by temperature or pressure. It may indicate a successive decrease of fO_2 during garnet growth which

is then effective from the prograde stage to the late retrograde stage.

This process is also supported by mass balance calculations. One poorly altered basalt sample and one massive garnet skarn sample were taken as original and final product of skarnization, respectively. The detailed treatment and the isocon fitting follow the method proposed by (Grant, 1986). The calculations give the mass-balance relation (Table A-2):

100g basalt + 14.1g CaO + 3.4g Fe_2O_3

= 107.4g massive garnet skarn + 4.8g Al_2O_3 +2.1g K_2O + 1.5g Na_2O

These calculations clearly indicate gains of CaO, Fe_2O_3 and a loss of Al_2O_3 of the basalt. We suggest that CaO might be leached from the limestone during decarbonation. External input of Fe_2O_3 is inferred to the flow of iron-rich hot brines responsible for massive magnetite deposition.

CONCLUSIONS

From the foregoing discussion, we postulate an early-stage evolution of the garnet in Yamansu magnetite deposit. The garnet grains display a complex zoning with a core of andraditic composition. Then, probably due to decreasing fO_2 and/or depletion of SiO_2 in the fluid, andradite stopped growing and a thin rim with calcite and magnetite inclusions precipitated. Continued fO_2 decrease and introduction of Al may have caused grandite formation at the border of the grains. The economic massive magnetite stage postdates the formation of these complex garnet grains. The latest garnets, whose composition is similar to that of the complex grain border, infilled fractures that were related to a late brittle deformation. Fluid composition, fO_2 and fCO_2 may play an important role for the shift in composition along the andradite-grossular series.

Acknowledgements

We specially thank the Baosteel Company for providing access to their mine and unpublished documents. The first author benefits a scholarship grant from the French Minister of Education and Research. This study was financially supported by

National Basic Research Program of People's Republic of China (2007CB411301), National Natural Science Foundation of China (No.40603008 and 40672040) and Geological Survey Project (1212011140056). Dr. J. Lui, Dr. Fernando Corfu, Dr. Ane Engvik and Dr. Christian Chopin are acknowledged for stimulating discussions and constructive comments.

References.

Figures:

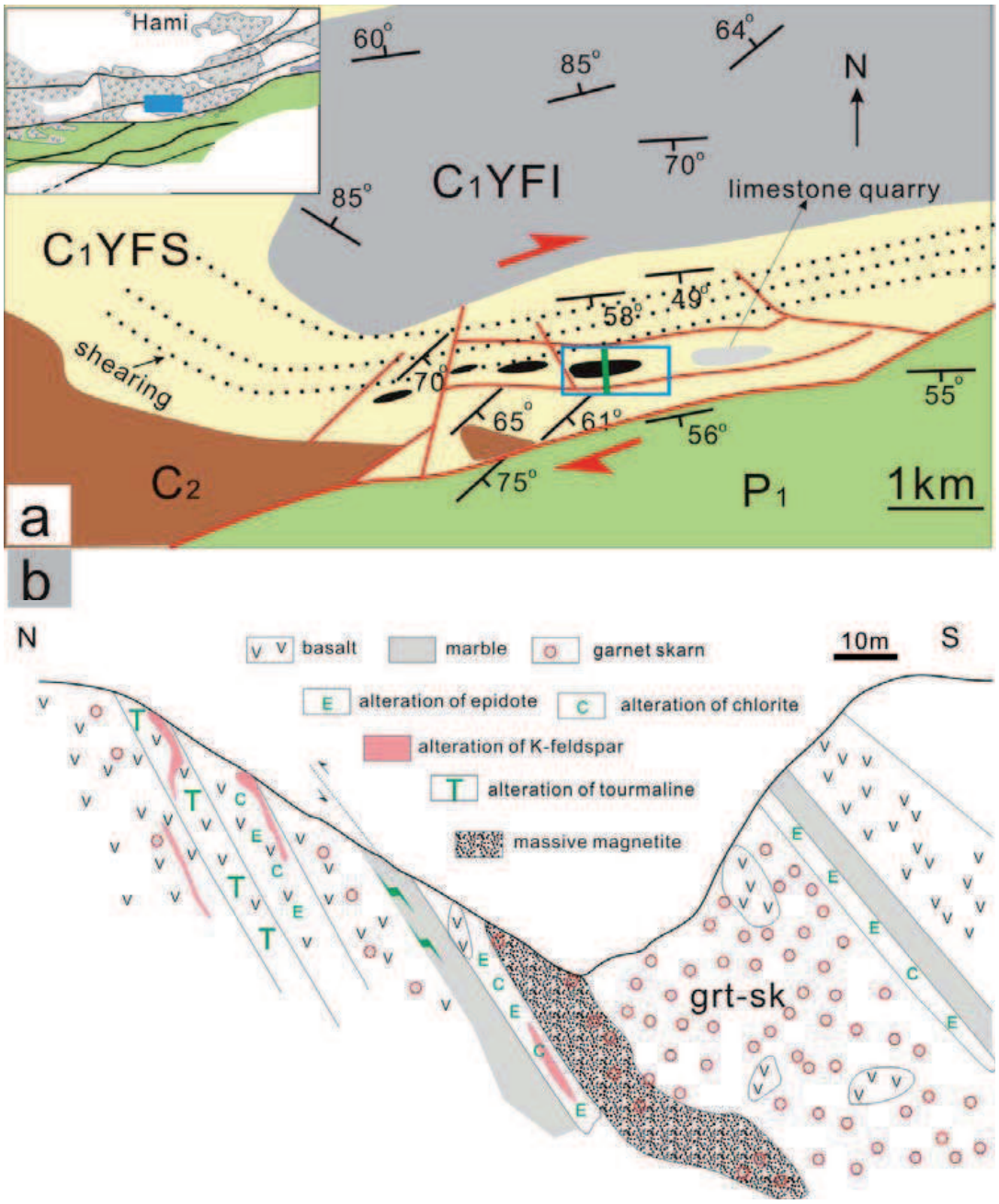

Fig. A-1. Maps and cross section of the Yamansu iron deposit. (a) Sketch illustrating the structure of the Yamansu ore field in the eastern Tianshan orogenic belt. The Yamansu open pit is indicated by the blue rectangle where the green line indicates the position of profile. C_1YFS- Lower Carboniferous Yamansu upper Formation, C_1YFI- Lower Carboniferous Yamansu lower Formation, C_2- Upper Carboniferous, P_1- Lower Permian. Dotted lines indicate the shear zone trace. The inset shows part of Central and Northern Tianshan, south of Hami city and the position of the Yamansu region along crustal-scale Permian shear zones. (b) Profile of the Yamansu iron deposit. It shows the development of a massive garnet skarn above the stratoid magnetite ore body. Note the presence of basalt relics within the garnet skarn formation.

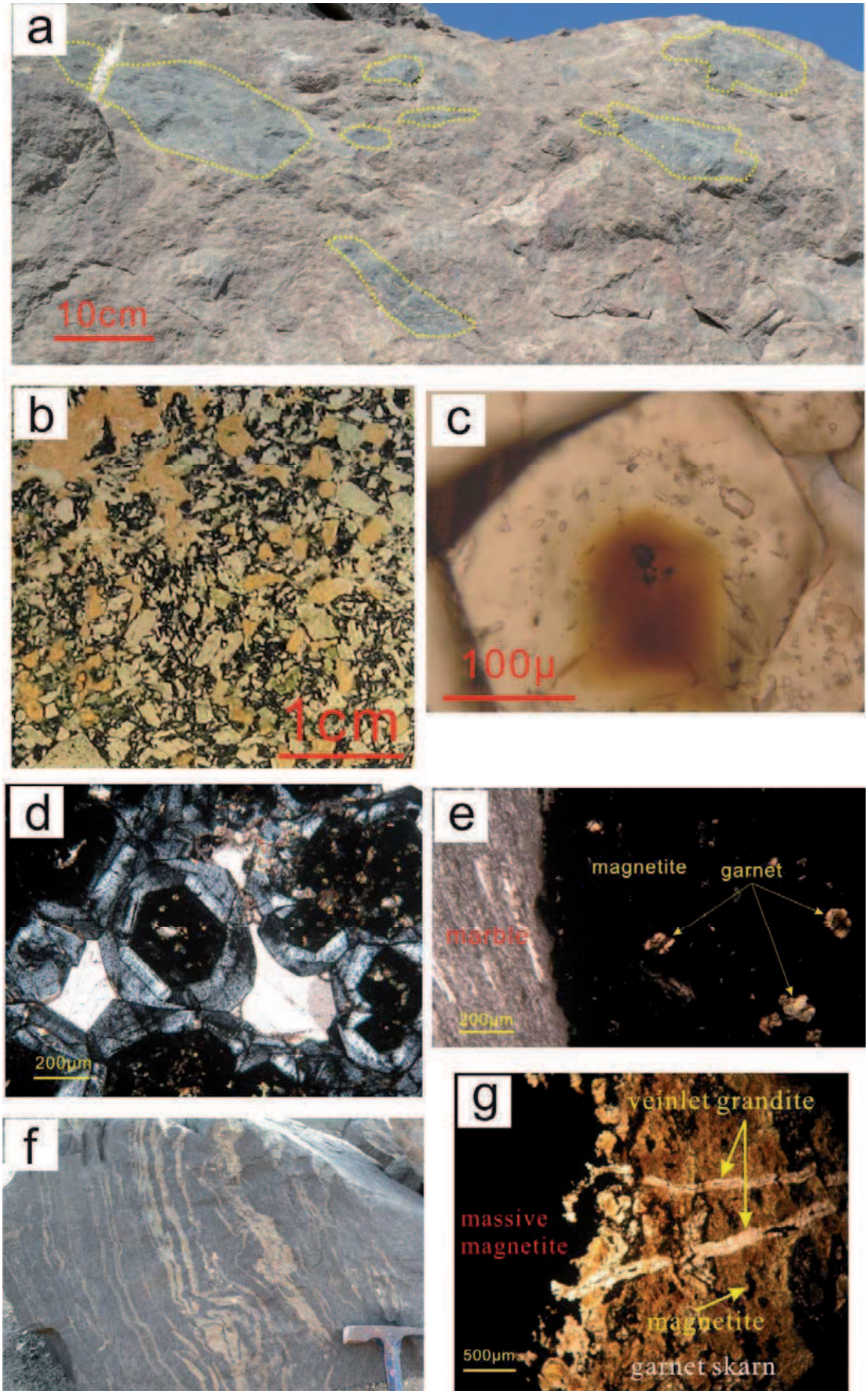

Fig. A-2. Outcrops and photomicrographs of the prograde and massive magnetite stages. (a)

Relics of basalt (emphasized by dotted yellow lines) in massive garnet skarn (pale rose). (b) Andradite alteration of basalt. Garnet is andradites in pink colour; plagioclases are in white colour; fine grain groundmass and disseminated magnetite are in black; (c) Microphotograph showing the andradite core and grandite rim. The rim contains numerous inclusions (gas, liquid and daughter minerals), in transmitted plane polarised light. (d) Andradite cores show isotropic and the grandite borders appreciable anomalous birefringence (oscillatory zoning) and sector twinning (transmitted crossed polarised light). (e) Photomicrograph of iron-rich front at the contact magnetite mineralization-limestone. This front is outlined by garnet (in transmitted plane polarised light). (f) Rhythmic banding of garnet and magnetite. Garnet is in pale yellow, magnetite in black. (g) Veinlets infill with grandite cutting across massive magnetite (black part on the left) and massive garnet skarn (brown and yellow zone on the right). Sparse magnetite appears in the massive garnet skarn (transmitted plane polarised light).

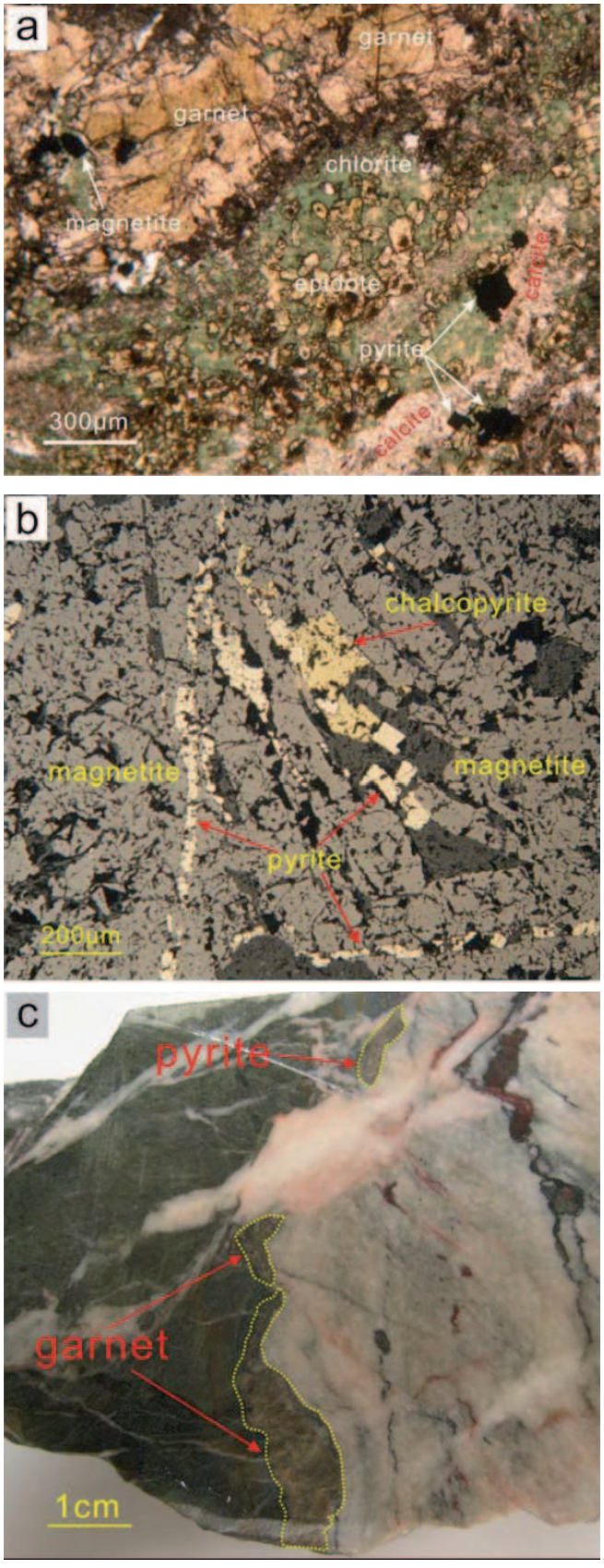

Fig. A-3. Retrograde and late stages (a) Retrograde minerals altered the garnet (in transmitted plane polarised light). (b) Late pyrite and chalcopyrite cutting the massive magnetite. Pyrite is in yellow, magnetite is in deep gray, in reflected plane polarised light. (c) Mafic dyke cutting the limestone with a band of garnet, mostly andradite in composition at the contact between dyke and host rock. The yellow circle emphasizes the pyrite and garnet. The pale green part on the left and white part on the right are altered mafic dyke and marble, respectively.

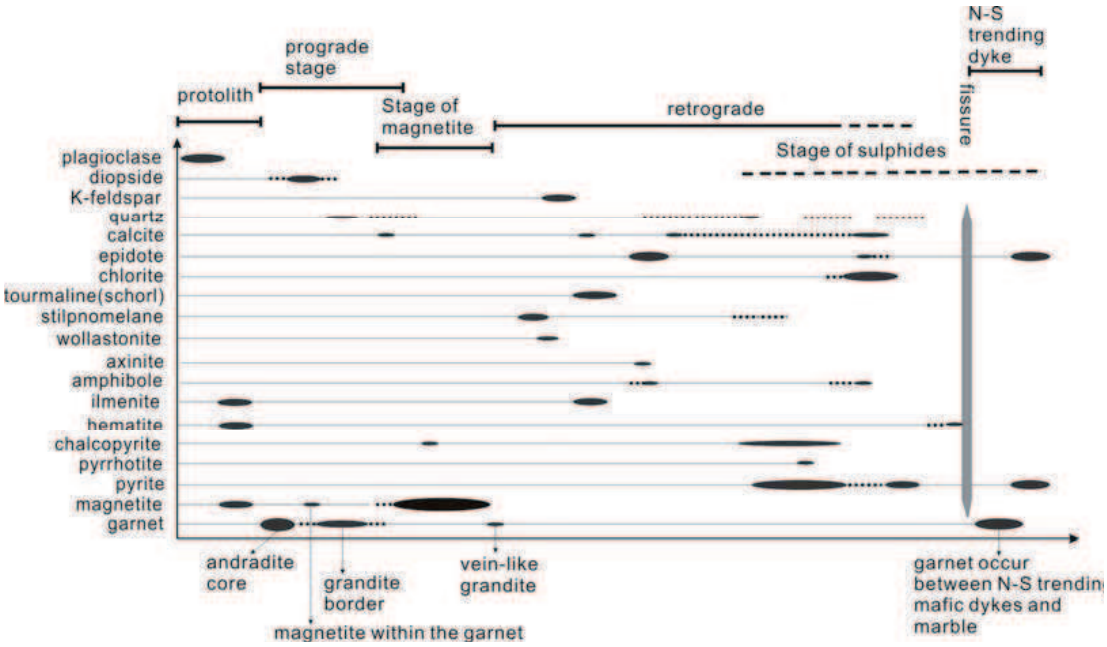

Fig. A-4. Paragenetic sequence from the Yamansu magnetite deposit, eastern Tianshan, China.

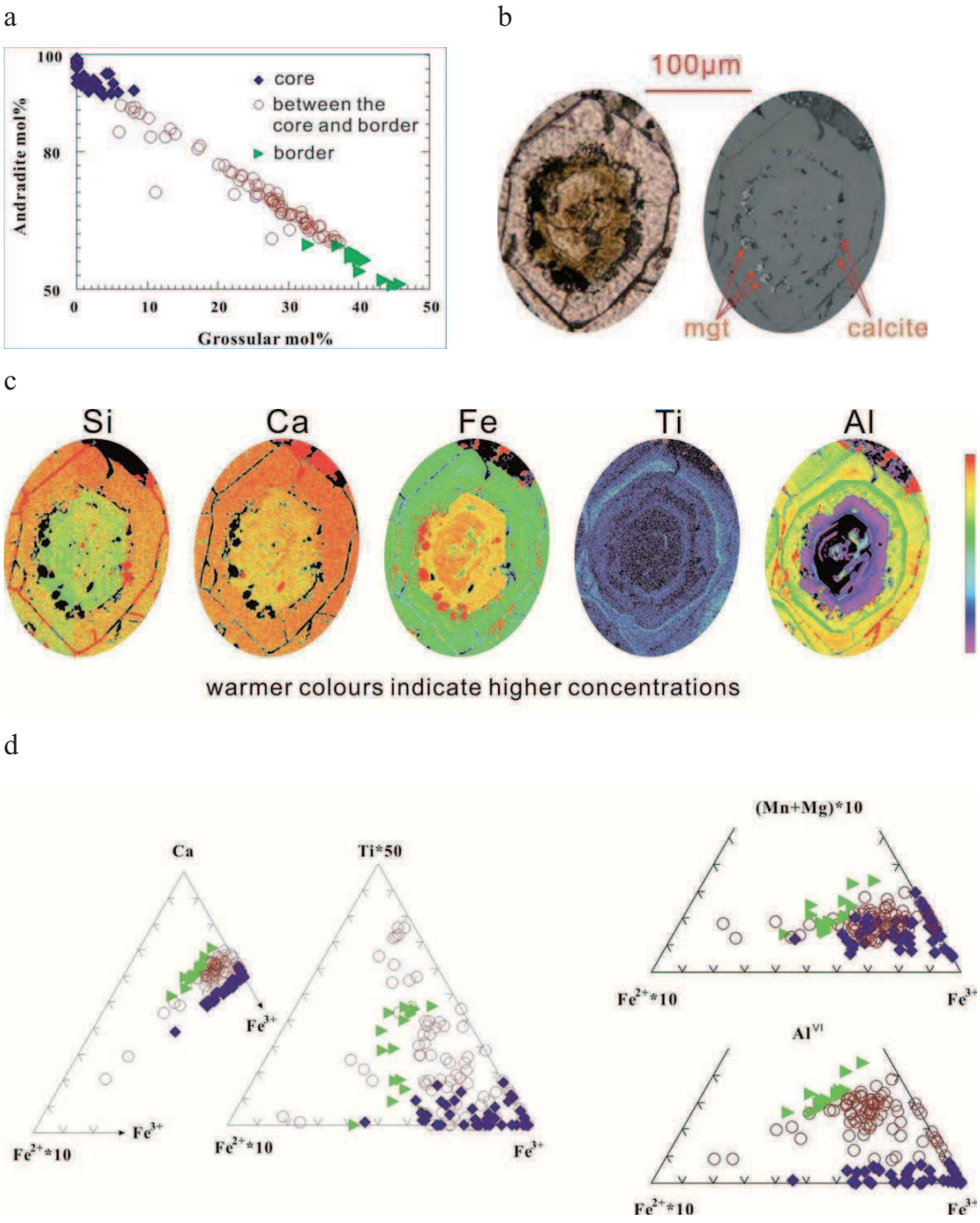

Fig. A-5. (a) Electron microprobe analyses showing the compositional variations of garnet from andradite core to grandite border. (b) Euhedral garnet from the massive garnet skarn: left and right in transmitted and reflected plane polarised light, respectively, mgt for magnetite. (c) Element distribution maps of the euhedral garnet shown in b. (d) Chemical composition of garnets (in cation per formula unit). See (a) for symbols legend.

TABLE A-1. REPRESENTATIVE CHEMICAL ANALYSES OF A SINGLE GARNET CRYSTAL FROM THE MASSIVE GARNET SKARN

	Recalculated analyses											
	core					border						
SiO_2	34.22	34.79	34.45	34.00	34.14	36.39	36.85	37.05	36.85	36.88	36.13	36.67
Al_2O_3	0.55	1.66	0.86	0.94	3.04	8.44	8.48	8.57	7.60	8.63	8.00	7.71
Fe_2O_3	30.89	29.32	31.40	31.07	27.86	20.14	19.25	19.54	19.83	19.58	19.96	20.21
TiO_2	0.00	0.02	0.02	0.04	0.00	0.37	0.94	1.36	1.44	0.51	1.45	0.79
CaO	31.81	32.47	32.48	32.36	31.92	34.29	33.84	33.68	34.02	33.61	33.53	33.25
FeO	1.12	0.00	1.45	1.42	0.55	0.30	0.63	1.25	0.42	0.96	0.57	0.84
MnO	0.34	0.30	0.39	0.33	0.50	0.46	0.38	0.49	0.34	0.35	0.44	0.48
MgO	0.08	0.21	0.06	0.04	0.09	0.08	0.09	0.13	0.00	0.12	0.15	0.14
Sum	99.01	98.78	101.09	100.20	98.11	101.26	100.45	102.07	100.49	100.64	100.23	100.08
	Structural formula											
Si	2.94	2.96	2.91	2.90	2.91	2.95	2.97	2.95	2.98	2.97	2.93	2.98
Al(IV)	0.06	0.04	0.09	0.10	0.09	0.05	0.03	0.05	0.02	0.03	0.07	0.02
Al(VI)	0.00	0.12	0.00	0.00	0.21	0.75	0.78	0.75	0.71	0.78	0.69	0.72
Fe^{3+}	2.00	1.87	2.00	2.00	1.79	1.21	1.17	1.17	1.21	1.18	1.22	1.24
Ti	0.00	0.00	0.00	0.00	0.00	0.04	0.06	0.08	0.09	0.03	0.09	0.05
Ca	2.93	2.95	2.94	2.96	2.91	2.94	2.92	2.87	2.95	2.90	2.91	2.89
Fe^{2+}	0.08	0.00	0.10	0.10	0.04	0.02	0.04	0.08	0.03	0.06	0.04	0.06
Mn	0.02	0.02	0.03	0.02	0.04	0.03	0.03	0.03	0.02	0.02	0.03	0.03
Mg	0.01	0.03	0.01	0.00	0.01	0.01	0.01	0.01	0.00	0.01	0.02	0.02
Andradite	100	94	100	100	89	63	61	63	65	61	65	64
Grossular	0	5	0	0	8	35	36	33	34	36	32	32

Chemical composition variations, from border to core, within a single euhedral crystal of garnet as shown in fig. 5b. From top to bottom: recalculated chemical analysis (wt%), structural formulae and mol% of andradite and grossular. The calculus used to distribute total Fe between Fe^{3+} and Fe^{2+} is given in the text.

TABLE A-2. GEOCHEMICAL COMPOSITIONS OF BASALT, MASSIVE GARNET SKARN AND RELATED MASS BALANCE CALCULATIONS ACCORDING TO GRANT (1986).

samples	basalt Y159 wt%	skarn Y102 wt%	Δm_i (g) from Y159 to Y102
SiO_2	46.15	42.52	-0.55
TiO_2	0.85	0.58	-0.23
Al_2O_3	21.20	15.30	-4.79
MgO	4.10	3.39	-0.46
CaO	7.68	20.32	14.11
Fe_2O_3	5.22	8.07	3.43
FeO	3.72	3.64	0.18
MnO	0.55	0.34	-0.19
P_2O_5	0.09	0.11	0.03
Na_2O	1.78	0.23	-1.53
K_2O	4.38	2.10	-2.13
LOI	4.39	3.69	-0.43
Σ	100.11	100.29	
ρ	(g/cm^3)	2.82	
*f*v			0.9

Δm_i (in grams) gain or loss of elements during the transformation of basalt into massive skarn; positive value means gain, whereas negative value means loss. ρ=density; *f*v =volume fator.

3.4.4.1.2 Pyroxene

The nomenclature here, adopted to describe those clinopyroxene ($ABSi_2O_6$) which can be included in this studied hydrothermal system, use the classification of (Morimoto, 1988). Some details are different from the (Poldervaart and Hess, 1951), such as diopside could be subdivided into diopside and salite. Wollastonite ($CaSiO_3$) has similar chemical compositional spectrum to the pyroxene where magnesium and iron substitution for calcium ends with diopside and hedenbergite respectively. But it is structurally very different, with a third SiO_4 tetrahedron in the linked chain (Deer et al., 1992). So, the proportion of Ca plays an important role. According to the nomenclature, when the Ca (in mole fraction) content is more than 50%, it belongs to the wollastonite.

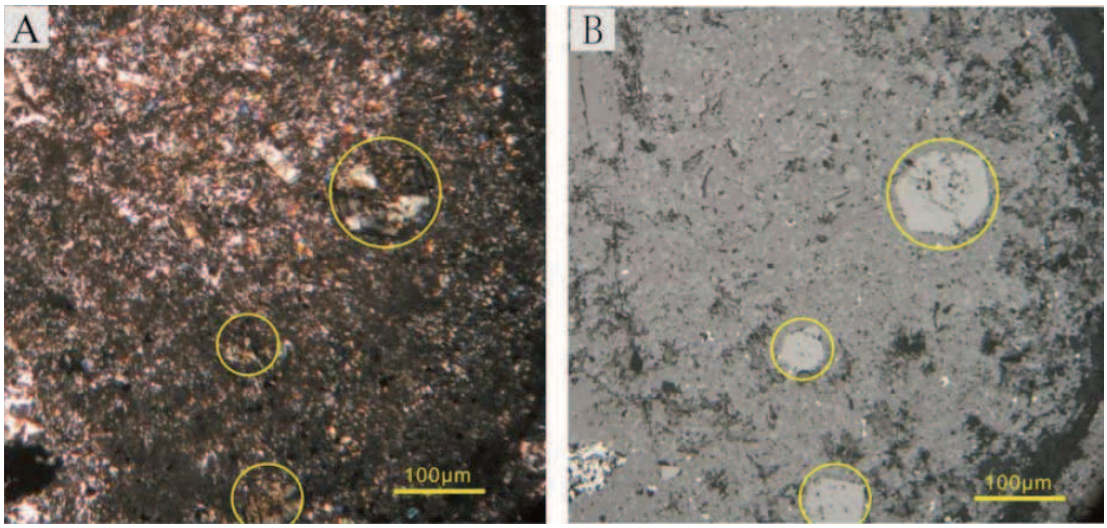

Fig. 3-21: Photographs of pyroxene. (A) and (B) are the some photo but in reflect light and transmitted plane polarised light respectively. Garnets are in the yellow circles. In the (B), pyroxenes are relatively small size but with high order colours.

In the studied case, the pyroxene commonly companies the garnet. It show relative high interference colours (Fig. 3-21). The EPMA composition of pyroxene is listed in Table 3-4. They show variation in composition. The grained pyroxene in Fig. 3-21 (A) and (B) illustrate are rather diopside. While the some radial pyroxene show the composition of augite. It is maybe because of alteration for the radial pyroxene

during retrograde stage. Both of them show moderate Fe+Mn+Mg and (Fe+Mn+Mg)/Ca.

3.4.4.1.3 Magnetite

In YMD, the magnetite occurs in the massive ore shoots (Fig. 3-16, 3-17), basalt (Fig. 3-12C) and even in the massive garnet skarn. Generally, these magnetites were in euhedral to subhedral crystal and relatively small, less than 0.1mm. EPMA analysis result, as well as structural formula, is list in Table 3-5. Because all Fe in the analyses by EPMA is expressed as Fe^{2+}. The structural formulae are calculated on the basis of 4 oxygen (equivalent to 8 electrovalency), $Fe^{3+} = 8 - Si^{4+} - Fe^{2+}(total) - Ca^{2+} - Al^{3+} - Mn^{2+} - Ti^{4+} - Mg^{2+}$; $Fe^{2+} = Fe(total) – Fe^{3+}$.

For these studied magnetites, Fe^{3+} showed clearly negative relation with respect to Si, whereas the Al and Ca were obscure (Fig. 3-22). The magnetite in the basalt was thought to be primary, however, they do not show significant difference to the hydrothermal magnetite, probably because of alteration.

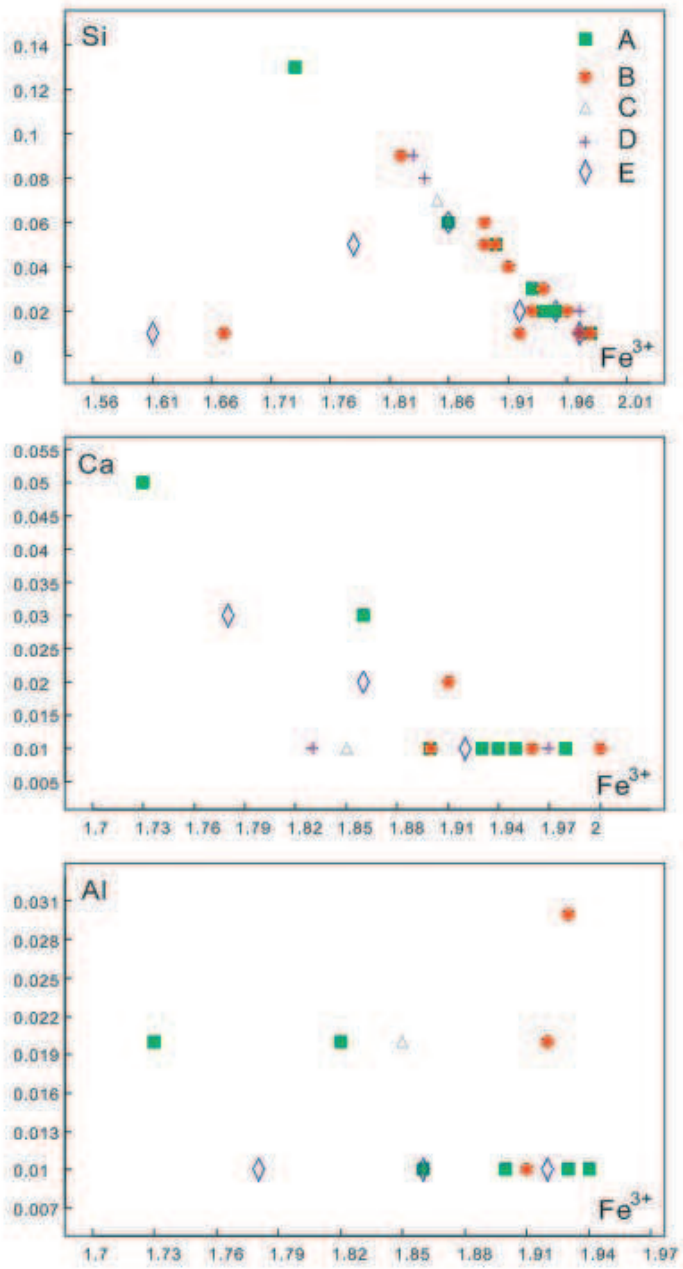

Fig. 3-22: Chemical composition of magnetite (in mole fraction of cation). A=massive magnetite; B=disseminated magnetite in the garnet skarn; C=disseminated magnetite with epidote; D=magnetite in basalt; E=magnetite in garnet.

3.4.4.2 Retrograde stage minerals

3.4.4.2.1 Stilpnomelane

In YMD, stilpnomelane occurred exclusively in the garnets (Fig. 3-23). Stilpnomelane is a phyllosilicate mineral of the mica group. Normally, it associated with banded iron formations, or as a metamorphic mineral associated with the

blueshist and greenschist facies. Stilpnomelane is rare in igneous rocks (Deer et al., 2009). It has been reported in skarn, such as Grythyttan skarn (Oen et al., 1986), as well as alteration haloes in shearing zone (Mapani and Wilson, 1998). In the Harhada iron deposit, Inner Mongolia, stilpnomelane is found with quartz, magnetite, siderite, minnesotaite, deerite and the Fe-V rich silicate erliannite (Feng et al., 1986). In addition, stilpnomelane is commonly reported from the banded iron formations, such as iron ore deposits of the central Hamersley Province (Thorne et al., 2009). It seems that stilpnomelane is formed usually in the low to middle pressure system with fluid circulation. The phase relations of A1- and Fe-bearing silicates in the system K_2O-FeO-MgO-Al_2O_3-SiO_2-H_2O-CO_2, in the presence of quartz and magnetite, are discussed by Miyano and Klein (1989). They indicated that the upper stability limit of stilpnomelane in iron-formations at about 430-470°C and 5-6 kilobars. In the studied case, the Yamansu stilpnomelane altered the garnets which probably formed at about 500°C. It was formed in a typical iron rich hydrothermal system and altered by later chlorite. Stilpnomelane will decompose to biotite and almandine at higher temperature and to zussmanite and chlorite at higher pressure (Miyano and Klein, 1989). Stilpnomelane occurs mainly within iron-, manganese-, and pyrite-ore deposits of volcanic-sedimentary origin, associated with crystalline series and preferred development of stilpnomelane in these formations may by explained by the particular chemical composition of the respective ores (Kräutner and Mede§an, 1969).

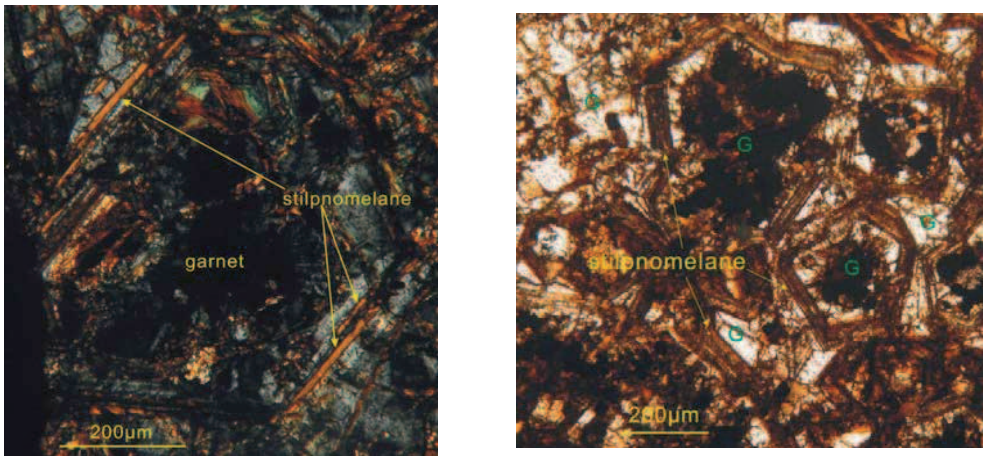

Fig. 3-23: Microphotograph of zoned alteration of stilpnomelane in garnet. They show that stilpnomelane is in brown yellow both in transmitted cross and plane polarised light, in the left and right respectively. G=garnet.

In the studied case, most of them show brown yellow color. Pleochroism ranges from brown to brown yellow. To confirm this mineral, EPMA (Table 3-6) and X-ray diffraction (XRD) analysis have been executed. Measurements of XRD were realized in ISTO. XRD experimental conditions are as following:

1. Grinding powder in agate mortar (mortar cleaned at Fontainebleau sand)
2. INEL diffractometer in transmission XRM3000
3. RX Tube Co anticathode
4. Monochromator before: Co Kalpha1
5. Lambda = 1.78897 Angstrom Kalpha1 Co
6. Sample in capillary diameter 0.3mm glass 050 Mark Hilgenberg Gmbh
7. INEL CPS 120 curve detector
8. acquisition 3-120 ° 2Theta
9. 0.03 ° resolution
10. Standard calibration 2Theta by NAC + direct beam from 0 to 90 °
11. Acquisition software: INEL Windif

XRD diagrams have peaks at 12.2A indicating either the sepiolite or stilpnomelane. The EPMA result shows that the chemical composition fits better to the stilpnomelane. Structural formula calculation has been done as well (Table 3-6).

3.4.4.2.2 K-feldspar

K-feldspar occurs in the retrograde stage and mostly associated with epidote and tourmaline (Fig. 3-24A). Sometimes, it is associated to chlorite which had been described by some researchers (Deer et al., 1997; Bird and Spieler, 2004). The EPMA analysis results of K-feldspar are listed in Table 3-7. K-feldspar altered the garnet in YMD, which was similar in iron skarn deposits, such as Beni Bou Ifrour deposit (Rhazi and Hayashi, 2002). During skarnization, K would notably enriched in the fluid and K metasomatic alteration in skarn-type iron deposits is common in the inner contact zone of both mafic and felsic intrusions (Zhao et al., 1984). Zhao et al. (1984) suggested that the amount of albite molecules contained in orthoclase mainly depends on the temperature of formation. That is because at high temperatures the components of orthoclase (Or) and albite (Ab) may be intermixed in arbitrary proportion; but at lower temperatures the intermiscibility is limited. However, in the studied case, it seems that there is another group of feldspar beyond the K-feldspar which hold only small amount of Na. This feldspar contain about 0.33-0.58 Na par unit (Table 3-7).

A

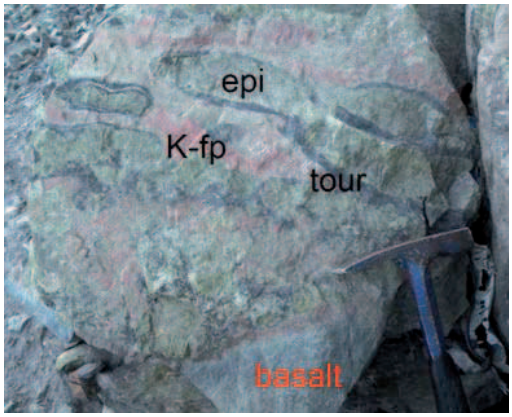

B

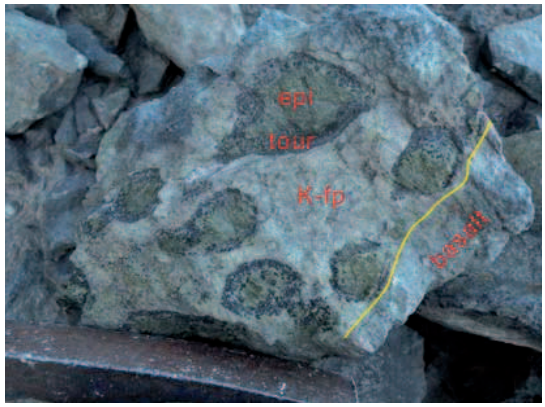

C

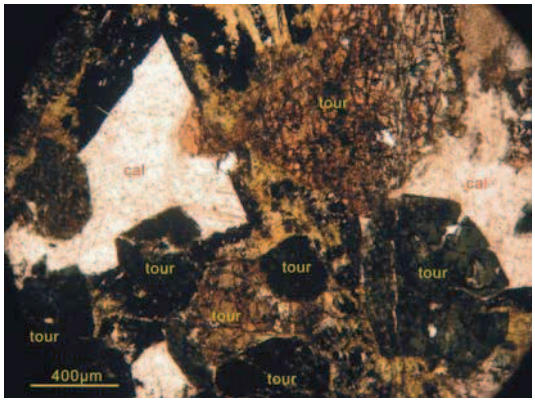

Fig. 3-24: Tourmaline nodules and K-feldspar photomicrographs.
(A) K-feldspar, epidote and tourmaline are on rose, green and black, respectively, whereas, (B) K-feldspar is white; (C) Photomicrographs of tourmaline in hydrothermal magnetite deposit in transmitted plane polarised light. tour=tourmaline; cal=calcite; K-fp=K-feldspar.

3.4.4.2.3 Tourmaline

In the studied case, tourmaline mainly develops in the hanging wall and next to the basalt (Fig. 3-15A). It occurs exclusively in nodules associated with epidote and K-feldspar (Fig. 3-24 A and B) which indicate connected with the separation of a late-stage boron-rich volatile fluid phase that probably exsolved from the crystallizing undersaturated magma (Balen and Broska, 2011). The tourmaline shows homogenous, no zonation (Fig. 3-24 C).

The structural formula of tourmaline could be written as following:

$$XY_3Z_6[T_6O_{18}][BO_3]_3V_3W$$

where:

X=Ca, Na, K and vacancy;

Y=Li, Mg^{2+}, Fe^{2+}, Mn^{2+}, Al^{3+}, Cr^{3+}, Fe^{3+};

Z= Mg^{2+}, Fe^{2+}, Al^{3+}, Fe^{3+}, V^{3+}, Cr^{3+}, Ti;

T=Si, Al;

V=OH;

W=OH, F, O.

EPMA analysis results have been listed in Table 3-8. The determination of structural formula requires the formulation of some hypotheses:

(1) Initially, we assume that the amount of boron is equal to 3 atoms per formula unit which makes possible the estimation of B2O3 in weight percent;

(2) 3 OH per formula unit in the site V. The amount of OH in site W will be deducted from the number of F atoms: OH (W) = 1 - F. this approach allows us to offer a reasonable anion V + W equal to 4*OH + F;

(3) The lack of occupation of the site Y is the lithium. In this case, in the site Y, Li = 3 - Σ cations;

(4) The maximum amount of Fe^{3+} in the Z site can be estimated by the following: Fe^{3+}(Z)=6-Al(Z); Fe^{2+} =Fe total- Fe^{3+}.

(5) Structural formulas were normalized on the basis of 24.5 cations (Manning, 1982). In absolute terms, a deviation from this charge would be observed if the valence of a cation was not properly estimated the site X or Z and/or if there was a substitution between O^{2-} and OH^{-}sites in the V and W. Thus, an excess of charge corresponds to a replacement of OH- by O^{2-} while a deficit correspond to the replacement of a divalent cation by a trivalent cation.

All of the Yamansu tourmalines are Ca rich, varieties (Ca/(Ca+Na)>0.4) with little F (usually <0.69%) and no significant K, Mn, or C1. The highest Fe values found were up to 14.06%. Average titanium is 0.24%. According to the X-site in tourmaline, which could be occupied by Na (and K), Ca and vacancy, the studied tourmaline located into the vacancy group and seems to be from the Fe3+-rich quartz-tourmaline rocks, calc-silicates and metapelites (Fig. 3-25) (Henry and Guidotti, 1985; Henry and Dutrow, 1992; Henry and Dutrow, 1996).

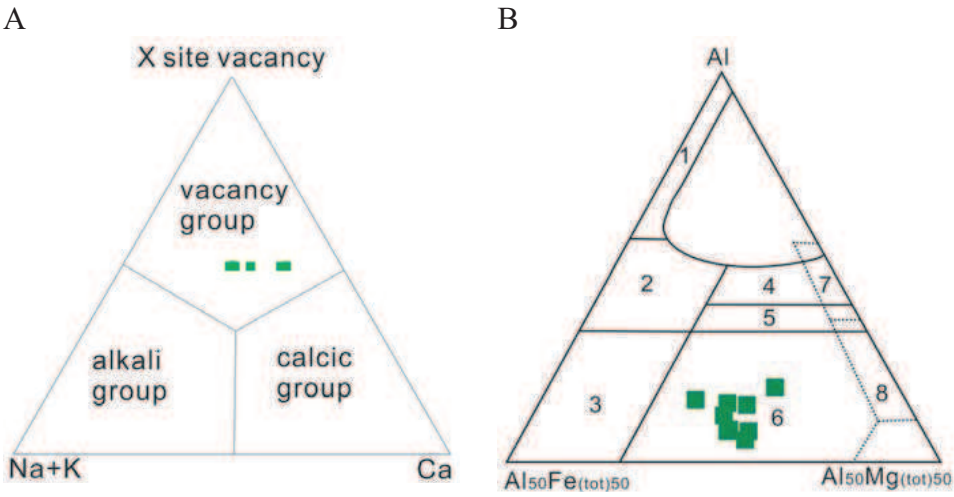

Fig. 3-25: The compositional ranges of tourmaline. (A) Na+K–Ca–X site vacancy; (B) Fe–Mg–Al: 1, Li-rich granitoids, pegmatites and aplites, 2, Li-poor granitoids, pegmatites and aplites, 3, hydrothermally-altered granitic rocks, 4, Metapelites and metapsammites (aluminous), 5, metapelites and metapsammites (Al-poor), 6, Fe3+-rich quartz-tourmaline rocks, calc-silicates and metapelites. 7, Low Ca ultramafics and 8, metacarbonates and metapyroxenites (after Henry and Dutrow 1992).

3.4.3.2.4 Axinite

Minor axinite in the massive garnet skarn was observed, which has a pale brownish colour but no detactable pleochroism. The related geochemical composition and structural formulae are showed in Table 3-9. These axinite are rich in Fe and Mg, relative poor in Mn.

3.4.3.2.5 Epidote

According the occurrence, two groups of epidote would be distinguished: (1) They associated with tourmaline and K-feldspar, altered the basalt. Mostly, these epidotes were embedded in tourmaline nodules (Fig. 3-24A and 3-24B). (2) Epidote is a common gangue mineral and is particularly associated with chlorite±calcite altering the prograde assemblage in YMD. For the second group, it favourably altered garnet

with relative bigger flake-like grain (Fig. 3-26A); when the epidote associated with chlorite±calcite, it is rather grained-like, it is round and smaller (Fig. 3-26B). However, for the chemical composition consideration, there is no significant difference between the two groups (Table 3-10). Both of the two groups contain high Fe^{3+} and very low Fe^{2+}. It seems that the fO_2 rose comparing to the grandite. The average structural formula of the epidote is

$(Ca_{1.97}Mn^{2+}_{0.02})^{VIII}[(Al^{3+}_{2.04}Fe^{3+}_{0.92}Mn^{3+}_{0.02})^{VI}][Si_{3.00}O_{12}]^{IV}[OH]$.

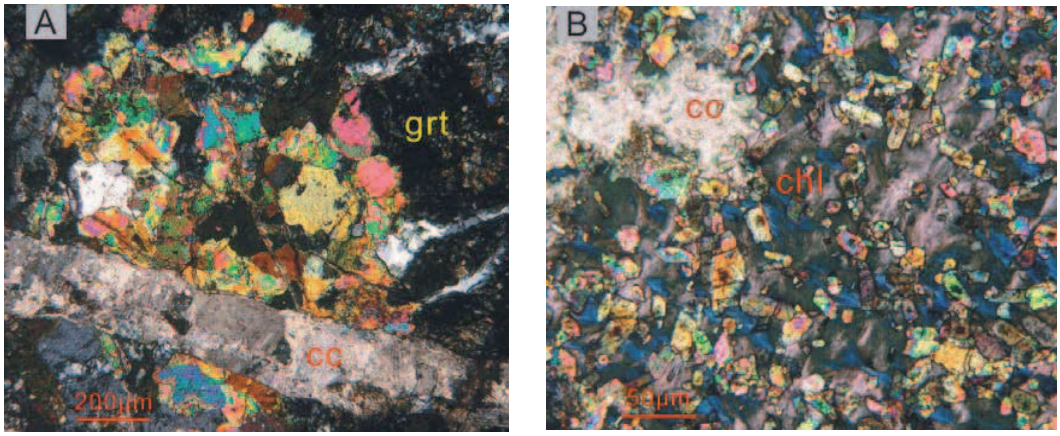

Fig. 3-26: Microphotographs of epidote. (A) epidote associated with tourmaline and K-feldspar; (B) flake-like (left) and (C) grainy (right) epidote from Yamansu skarn deposit. Both are in transmitted cross polarised light. On the right photo, the epidote is associated with chlorite and calcite in green and white respectively. grt=garnet; cc=calcite; chl=chlorite.

3.4.4.2.6 Chlorite

In the studied case, chlorite, commonly develops in the hanging wall and closed to the tourmaline zone and associated with calcite and epidote, altered the prograde stage minerals (Fig. 3-27). Chlorite constitutes a major hydrothermal alteration product in the calcite - chlorite - epidote zone. It shows a tendency to crystallize in radial aggregates or booklets. Chlorite is encountered also in veinlets and as vug fillings, with epidote and calcite.

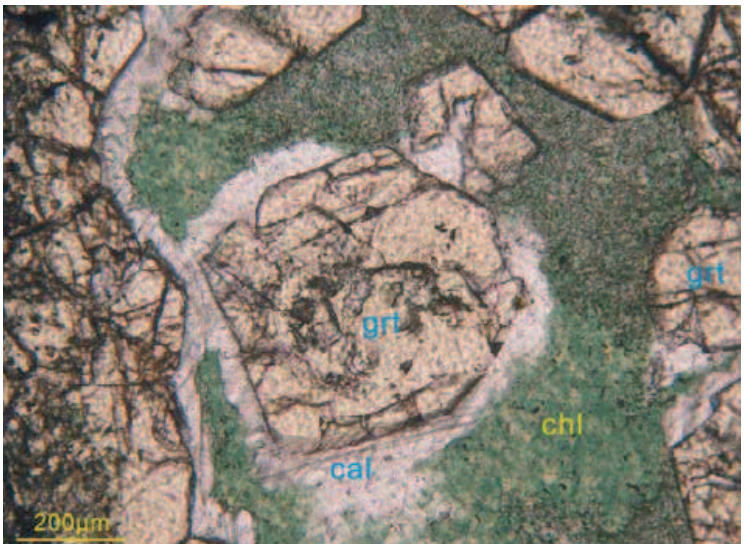

Fig. 3-27: Microphotograph showing chlorite and calcite alter the garnet. cal=calcite, chl=chlorite, grt=garnet.

Chlorite is useful for calculating the hydrothermal temperature. Its chemical composition is listed in Table 3-11. Because variations of site occupancy (mainly Al^{IV} and the octahedral occupancy (6- $A1^{VI}$ - (Mg + Fe^{2+})= VAC) are considered mainly as temperature dependent (Cathelineau and Nieva, 1985). The results are showed in Fig. 3-28. This geothermometer is dominantly basing on the Al^{IV} content in the tetrahedral site of chlorites. Other chemical changes, such as the variation in Fe and Mg contents, are partly influenced by temperature, but are strongly dependent on the geological environment, and consequently on the solution composition. About 15°C difference between the two calculation methods. The average temperature about 280°C for the formation of chlorite is preferred. The empirical relationships between chemical variables and temperature were calibrated from 150-300°C, but extrapolations at lower and higher temperatures seem possible for chlorites (Cathelineau, 1988).

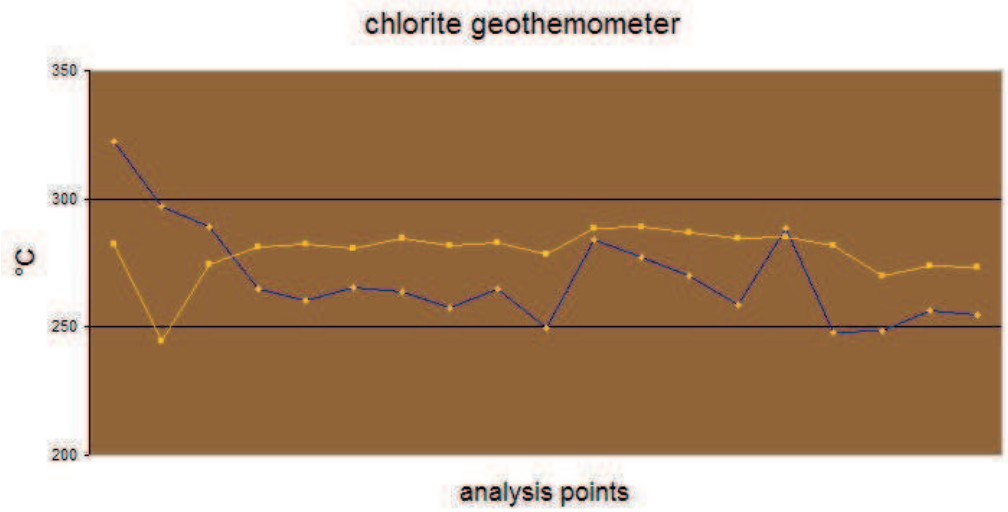

Fig. 3-28: Diagram showing temperature calculated from chlorite. The blue line is calculated on correlation between Aliv and temperature of formation of the chlorite; whereas the yellow line is from relation between vacancy=6-sum$^{(VI)}$ and temperature.

3.4.3.2.7 Sulphides

Sulphides dominated by pyrite and chalcopyrite show clear generations in the late stage. Pyrite shows three stage growths of which the second stage is very fine grain (Fig. 3-29A). The earliest stage of pyrite seems to be relatively high pressure because hydraulic fracturing rather then corrosion is observed (Fig. 3-29B). Mottled texture formed by randomly-oriented, needle-shaped aggregates of aligned pyrite crystals in an earlier pyrite matrix was observed (Fig. 3-29C). Chalcopyrite was associated with pyrite, either in the vein with calcite (Fig. 3-29D) and pyrite or occurs as inclusions in pyrite. According to observations in microscope, there seems a tendency that the later pyrite is, the more proportion of chalcopyrite.

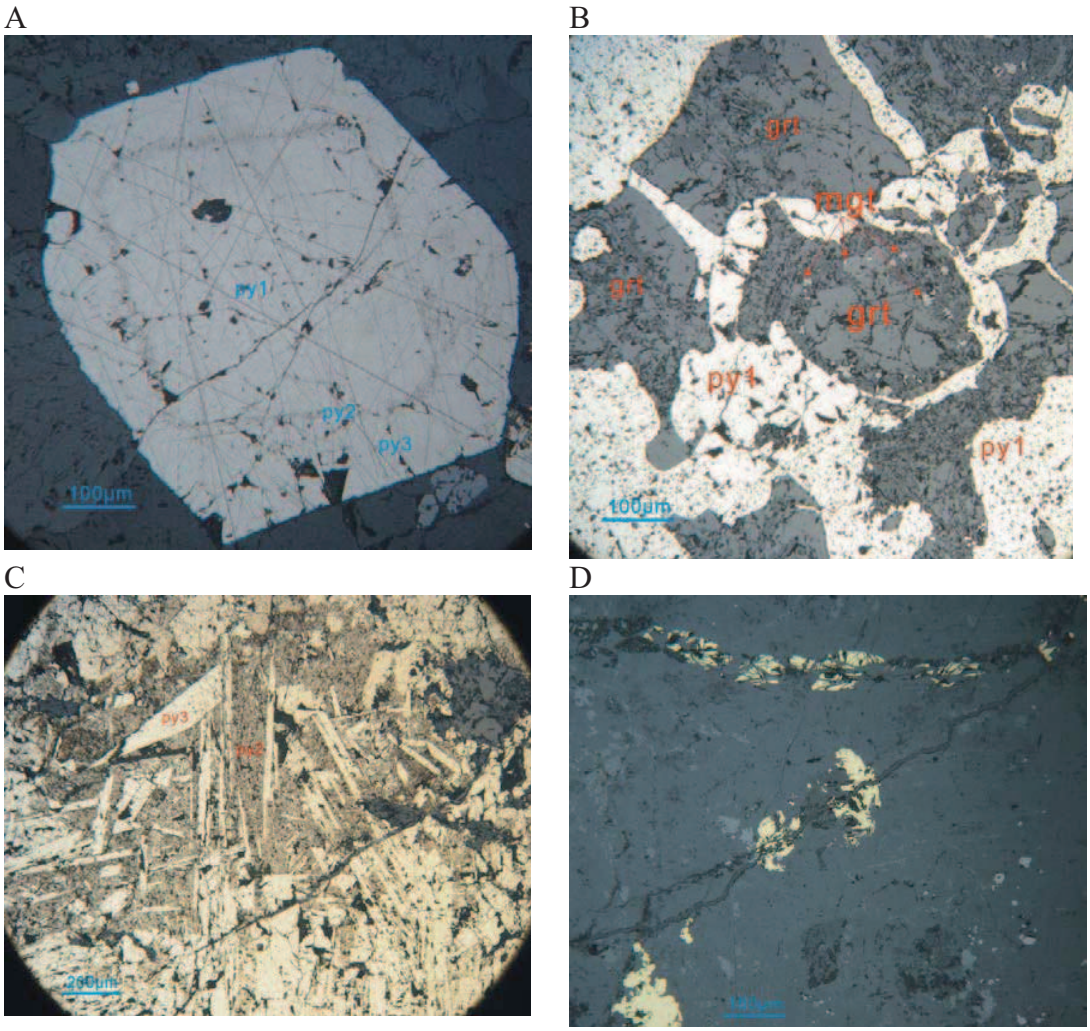

Fig. 3-29: Sulphides in the late retrograde stage skarn dominated by pyrite and chalcopyrite. (A) Three generations of pyrite; (B) Hydraulic fracturing showing iron rich fluid cracked the garnets. (C) Mottled texture formed by randomly-oriented, needle-shaped aggregates of aligned pyrite crystals in an eralier pyrite matrix. (D) Chalcopyrite in the vein, associated with pyrite and calcite. All micro photos in plane reflect light.

3.4.5 Dating on the K-feldspar-related stage

In order to better constrain the forming age of the skarn, four K-feldspar samples were selected for Ar-Ar dating. The step heating dating was executed in the $^{40}Ar/^{39}Ar$ geochronology laboratory at Department of Geosciences, National Taiwan University in a Varian-MAT VG1200 mass spectrometer equipped with a

double-vacuum Mo furnace and an all-metal extraction line. The mass spectrometer, furnace, and extraction line are all under computer control and fully automated. The crude result and related calculated parameters was listed in the Table 3-14. The four K-feldspar samples display similar results, about 246.8±2.0Ma, however errors were not given (Fig. 3-30).

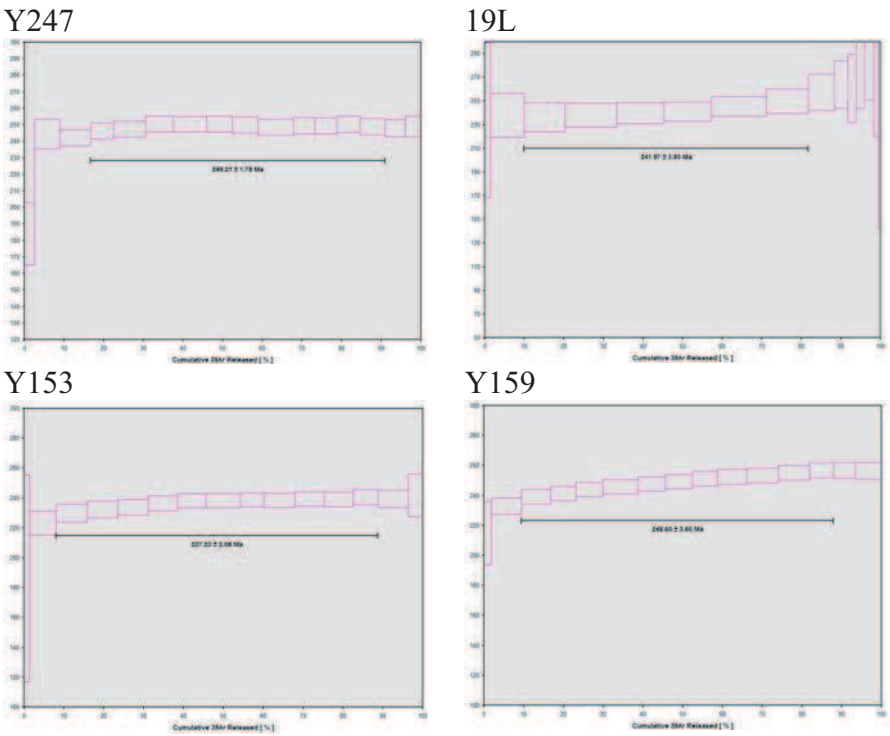

Fig. 3-30: Step heating Ar-Ar dating on four feldspar samples from YMD.

3.5 Geochemistry

Geochemical data of skarn and wall rocks may help to better characterize the immigration of elements and metallogenic environment. In addition to the major elements, trace elements also have analyzed.

3.5.1 Major and trace elements

26 representative samples of major and trace element data of different lithologies from the Yamansu ore field are presented in Table 3-12. Major element contents of

the rock were analyzed on a VF-320 X-ray fluorescence spectrometer (XRF) at the Modern Analysis Center, Nanjing University. Uncertainties for major elements are generally less than 2%. Trace element and rare earth element (REE) contents of the rock were analyzed on an ICP-MS (Finnigan MAT-Element 2) machine at the State Key Laboratory for Mineral Deposits Research, Nanjing University. Precisely weighted 50 mg sample powders were digested by a HF + HNO_3 mixture in Teflon bombs. An internal standard solution containing the single element Rh was used to monitor signal drift during counting. Analytical precision for most elements by ICP-MS is better than 5%. Detailed analytical procedure is documented in (Gao et al., 2003).

3.5.1.1 Basalt

4 samples of basalt including the altered basalt were analysed. The basalt contains low to medium SiO_2 (40.53 – 49.31 %), Al_2O_3 (12.96 – 21.2%) of which the low SiO_2 value and the highest Al_2O_3 value may be altered by skarnization because even for the specimen spare garnets would be seem in the basalt and K_2O (0.29 – 4.38%), Fe_2O_3 (8.94 – 9.58%), but these basalt show high CaO (6.94 – 15.94%) and MgO (4.01 – 6.33%). In general, major element characteristics of the rock indicate that the rocks are chemically calc-alkaline, however the sample Y133 ploted into the tholeitic series.

The REE patterns are relatively flat and no Eu depletion, combining the slight enrich of Sr (Fig. 3-31), indicating these basalts were come from low fractionated magmas, and during this process, there was no plagioclase crystallized. This result is accord with the observation of plagioclase phenocryst in the basalt. The lower HREE feature indicates that primitive magma for the basalt is likely to be generated at the deep levels, where the residual phases are dominated by garnets rather than plagioclase. The Yamansu basalt is generally enriched in large ion lithophile elements (LILEs), such as Cs (0.73-9.3ppm), Rb (3.89-192.77ppm), Sr

(62.39-483.07ppm), Ba (46.26-1570ppm), but depleted in typical high field strength elements (HFSEs), such as Ti (2358-6371ppm), Ta (0.09-0.22ppm), Y (11.28-22.33ppm). These features imply that the Yamansu basalt is of the arc affinity and the rutile maybe residue in magma chamber.

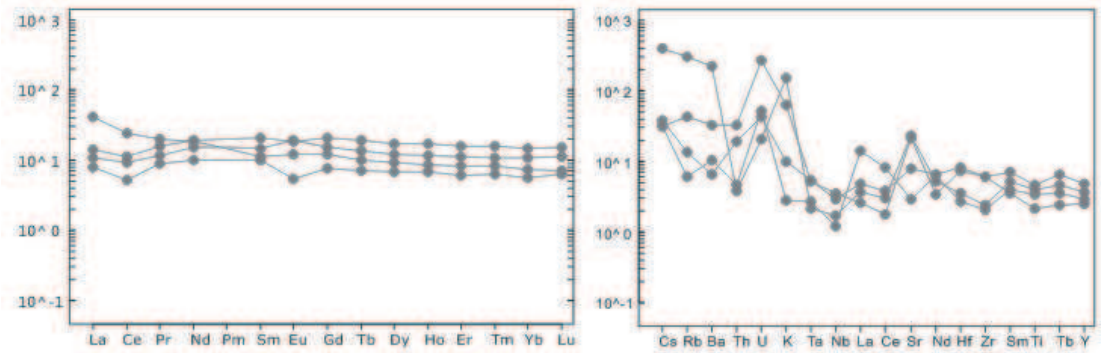

Fig 3-31: Trace elements normalized patterns of basalt. (A) Chondrite normalized REE distribution pattern and (B) Spidergram for Yamansu basalt. Normalization values are from Sun and McDonough (1989).

3.5.1.2 Limestone

The limestone generally shows impure, containing K_2O, Na_2O and Al_2O_3 etc corresponding to different colour of the limestone (Table 3-11). Probably affected by hydrothermal fluid, the Al_2O_3 content would up to 9.7%. As indicated in the garnet section, the Al probably comes from plagioclase of the basalt. Strong variations are found in SiO_2 and $CaCO_3$. These variations of major elements could be ascribed to external input, maybe also affected by fluid.

The behaviours of rare-earth elements (REE) in marine waters, sediments, and carbonate rocks have been studied in detail by many workers, such as (Piper, 1974; Murphy and Dymond, 1984). Ce anomaly, in marine sediments and carbonate rocks has proved to be an excellent indicator of depositional environments (Liu et al., 1988). Almost all limestone samples analyzed from the Yamansu Formation show a more or less negative cerium anomaly normalized to Post Archean Australian Shale

(PAAS) (Taylor and McClennan, 1985), indicating oxidation level was relatively high. The shale normalized REE patterns are slightly turn-up on the heavy side (Fig. 3-32). The spider diagram shows they are depleted in V, Rb, Cs, Zr, Nb, Hf etc. REE patterns and spider diagram suggest that detrital sediments present in the limestones were probably derived from felsic source rocks.

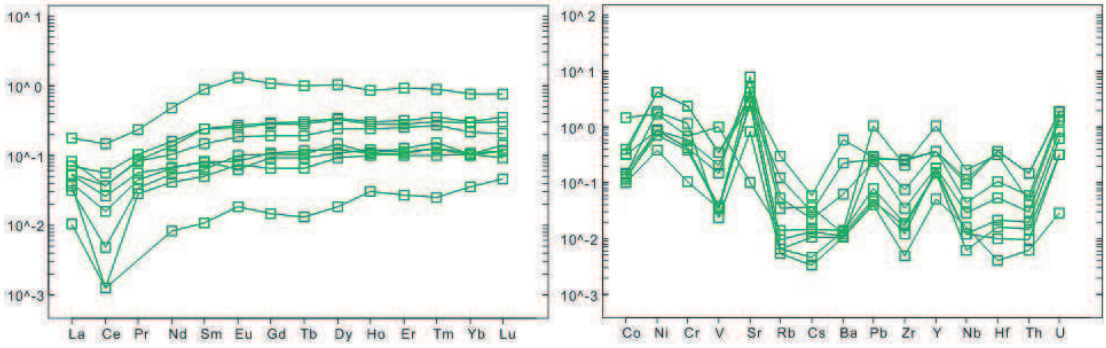

Fig. 3-32: Post-Archean Australian Shale (PAAS)-normalized REE and spider plots for the Yamansu limestones. PAAS normalization values from Taylor and McLennan (1985).

3.5.1.3 Skarn

The major elements of K_2O+Na_2O, Al_2O_3 and TiO_2 linearly increase, whereas the Fe_2O_3, and CaO decrease with the increase of SiO_2. Total REE content of skarn samples from YMD varies between 31.73ppm and 579.46ppm except the magnetite. Most skarns show relative low LREE/HREE ratio (Fig. 3-32) except the samples of Y102 epidote skarn and Y105 which altered garnet skarn. It is the two samples that contributed high total REE contents (Fig. 3-33). The samples of Y102 and Y105 show strong fractionation of LREE, while the HREEs are flat which behaviour as the others. It is maybe because these two samples were affected by felsic fluid. Most skarns have not Eu anomalies, however certain show slightly Eu positive anomalies, probably caused by relics of plagioclase. In the spider diagram, the skarns are generally enriched in LILEs, but depleted in Ta and Nb, probably inherited from the basalt.

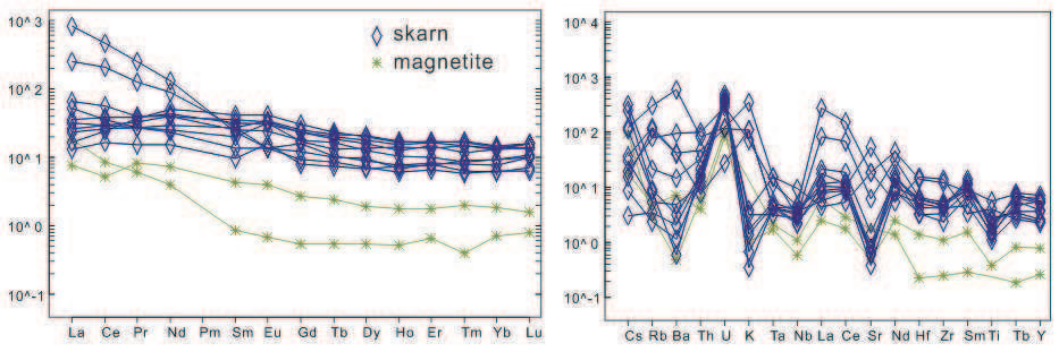

Fig. 3-33: Trace elements normalized patterns of skarn. (A) Chondrite normalized REE distribution pattern and (B) Spidergram for Yamansu basalt. Normalization values are from Sun and McDonough (1989).

3.5.3 Mass balance

In a study of metasomatically altered rocks, the immediate questions concern the nature of the original rock and the gains and losses of material necessary to produce the altered rock. By careful consideration of the field relations and petrology of an area, one maybe able to determine a "least-altered equivalent". This is probably the major step in unraveling the alteration process. Assuming that this has been done, one has to consider next the basis for determining the relative gains and losses that gave rise to the altered rock. In some cases the assumption of constant volume seems to work, in some, constant alumina, and in other cases, other components seem to have been relatively immobile.

In this study, mass balance was quantified during alteration. Major compositions of least altered rocks (two basalt samples, sample names are Y205 and Y159) and altered rock (one massive garnet skarn sample, sample name is Y102) are listed in Table 3-12 which are utilized in mass-balance calculations to estimate gains and losses of components in the samples. The calculations were made by the isocon method (Grant, 1986), which is a solution to the composition-volume relationships of Gresens' equations (Gresens, 1967).

3.5.3.1 Equations

Gresens' basic argument (Gresens 1967) is that some components are likely to have been immobile in the alteration process and that if these can be identified, they can be used to establish any volume change which has taken place. Gains or losses of other components can then be calculated assuming that the volume change is a factor common to the behavior of all components. That is, the alteration is pervasive, rather than confined to only part of the rock considered as in veins or alteration patches.

For the alteration of rock O to rock A, with possibly volume change, Gresens' basic formula is:

$$\Delta M_i = \left(f_v * \frac{\rho^A}{\rho^O} * C_i^A - C_i^O \right) * M_i^O$$

$$fv = \frac{M^A}{M^O} * \frac{\rho^O}{\rho^A} = \frac{V_A}{V_O}$$

M:mass; ΔM_i: gain or loss of mass of the chemical element i; f_v: volume factor, $fv = \frac{V_A}{V_O}$, where V_A and V_O are the volumes of respectively the altered rock and the initial rock; ρ: density; C_i: concentration of the chemical element i; O: unaltered (original) sample; A: altered (final) sample.

This equation is the basis for Gresens “Composition-Volume" diagrams as given in Gresens (1967). In this, for each component the relation between ΔM_i and a set of arbitrary values of f_v is shown, resulting in general in a set of intersecting straight lines. Where the lines for one or more components intersect $\Delta M_i = 0$, at or close to a common value of f_v this value is taken as the volume factor for the alteration. This implies that these components are relatively immobile in the alteration.

Changes in the amounts of mobile components are then read from the graph. These changes are commonly presented in terms of fictitious values of *v f* corresponding to zero compositional change, which maybe mathematically permissible but which unnecessarily obscure the real value of the method. A more direct method of applying Gresens' equation is as follows after (Grant, 1986). First note that Gresens' equation really relates to mass rather than to volume. The ratio of equivalent mass after (M^A) and before (M^O) alteration is:

$$\frac{M^A}{M^O} = \frac{V^A}{V^O} * \frac{\rho^A}{\rho^O} = f_V * \frac{\rho^A}{\rho^O}$$

$$M_i^A = M_i^O + \Delta M_i$$

so, we have

$$C_i^A = \frac{M^A}{M^O} * \left(C_i^O - \Delta C\right) \text{ and } \Delta M_i = \left(\frac{M^A}{M^O} * C_i^A - C_i^O\right) * M^O$$

$$\frac{M^A}{M^O} = \frac{V^A}{V^O} * \frac{\rho^A}{\rho^O} = f_V * \frac{\rho^A}{\rho^O}$$

$$\Delta M_i = M_i^A - M_i^O$$

$$\Delta M_i = \left(C_i^A \cdot \frac{\rho_A}{\rho_O} \cdot f_V - C_i^O\right) \cdot M_O \qquad (1)$$

For immobile elements ΔMi = 0 and equation (1) transforms in: $C_i^O = C_i^A \cdot \frac{\rho_A}{\rho_O} \cdot f_V$.

Then in a diagram C_i^O versus C_i^A immobile elements appear along a straight line, which slope pass through the origin. The value of f_v is deduced from measures of the slope, ρ_A and ρ_O. The gain or loss of element during the alteration is evaluated using equation (1).

For each component there is an equation of thisform, in which $\frac{M^A}{M^O}$ is constant. If we can identify in particular those (immobile) components for which $\Delta C_i = 0$, we can obtain this ratio by solving a set of simultaneous quations of the form:

$C_i^A = \frac{M^A}{M^O} * C_i^O$.

Plotting the analytical data ΔC_i^A against ΔC_i^O would help to identify those immobile components. The immobile components generate, through the origin, a straight line of slope $\frac{M^A}{M^O}$, which is the fundamental ratio of equivalent masses before and after alteration. This line, for which $\Delta C_i = 0$, may be called an "isocon," that is, "a line connecting points of equal geochemical concentration". It is readily determined by inspection, which involves the best fit of a straight line through a series of points.

Here, data for the major and trace components are proposed to plotted in the form of no rescaling, as weight percent of the oxides and ppm for the trace. It means that data are not scaled as shown in one diagram to generate the slope. Because the weight of components which are scaled may change the weight contributed to the slope.

3.5.3.2 Mass balance result

For the mass balance, the two least altered basalt (Y205 and Y159) samples and the garnet skarn (Y102) were taken as original and final, respectively. The detailed treatment of the calculations and the isocon fitting follows Grant (1986).

The calculations give the mass-balance relation referenced to 100g of basalt protolith for the garnet skarn, as following:

100g basalt + 14.1g CaO + 3.4g Fe_2O_3

= 107.4g skarn + 4.8g Al_2O_3 +2.1g K_2O + 1.5g Na_2O (from Y159)

and

100g basalt + 15.7g CaO + 2.8g Fe_2O_3 +2.1g K_2O

= 112g garnet skarn + 4.9g Na_2O + 2.5g MgO + 1.9g SiO_2 (from Y205)

Mass gains and losses of mobile major element oxides are calculated from such an isocon and reported in Table 3-13. The predominant changes are gains of CaO and a loss of Al_2O_3 in the basalt. This result suggests that CaO from the limestone is added to the basalt, whereas Al_2O_3 is leached out, during alteration.

3.6 Rock Magnetism study

Project of article

Initial geometry and strike-slip deformation of skarn related iron deposit: insights from paleomagnetic and AMS investigations (Yamansu deposit, eastern Tianshan, China)

Abstract: The eastern Tianshan has great economic potential with Fe-(Cu) skarn, Cu-Ni- and V-Ti othomagmatic deposits and orogenic Au lodes. In this province the timing relation between Fe-(Cu) skarn-related deposits and the deformation is poorly constrained. This study aims to give argument for the chronology between Fe-(Cu) skarn stage and large scale dextral strike-slip using paleomagnetism and AMS (Anisotropy of Magnetic Susceptibility) methods. The studied target is in the flank of an E-W striking anticline with a composite planar-linear shearing fabric. This flank contains more than 6 stratoid ore bodies located within a zone of several hundred meters wide and 5 km long. Among them, Yamansu magnetite deposit is the biggest one in the easternmost part. The ore bodies are spatially associated with a ~50m thick stratiform garnet skarn in the upper part of a Carboniferous limestone formation, leading previous study to identify a skarn-type deposit. Both the massive garnet skarn and ore bodies are actually sandwich-like in the limestone and basalt which acted as the protolith. They nearly W-E extend with angle about 60°. Magnetic mineralogy investigation showed that the magnetic remanence and susceptibility are carried by magnetite. For the paleomagnetic data from massive garnet skarn and basalt, two components could be distinguished: the lower and higher coercive ones. The former one presents an average direction of Dg = 9.7°, Ig = 58.9°, kg = 103.2, α_{95g} = 5.1° before bedding corrections, which is close to present Earth, and an average of Ds = 131.4°, Is = 66.1° in stratigraphic coordinates. The higher coercive ones show a mean direction of Dg = 136.8°, Ig = 15.6°, kg = 29.9, α_{95g} =10.3° in geographic coordinates, and Ds = 134.1°, Is = -27.9° in stratigraphic

coordinates. The direction from higher coercive components is compatible with the regional paleomagnetic data in late Carboniferous and Permian indicating that initial occurrence of basalt and the massive garnet skarn were horizontal. AMS results are concordant with paleomagnetic data, of which most magnetic foliations and lineations (K_1) (after bedding correction) are horizontal reflecting a horizontal fluid flow. Overall, these data support that the basalt horizontally intruded into limestone, the skarnization was then horizontally occurred. The iron-rich fluid probably ascended along a pre-existing fault and injected into the limestone and basalt, and then caused extensive skarnization and deposited the magnetite. The horizontal ore bodies, as well as the basalt and the skarns, were tilted by tectonic shearing events in Permian.

Key words: AMS, paleomagnetism, eastern Tianshan orogenic belt, skarn, basalt

1. Introduction

The eastern Tianshan is an important metallogenic province structured into four units (Fig. B-1): Dananhu arc belt, Kanguer shear zone, Aqishan-Yamansu belt and Middle Tianshan Terrane. These units have been formed by accretion-collision of arcs and microplates from Ordovician to Carboniferous (Charvet et al., 2011). At the end of the Carboniferous all the blocks were welded and structured by dextral shear during Permian due to relative displacement of the Jungar and Yili blocks (Wang et al., 2007). Today the boundaries of the different units are typically delineated by large strike-slip faults which accommodated the dextral movement between Tarim block and Siberian block.

Carboniferous and Permian are blooming periods for mineralizations in eastern Tianshan. Most of them are skarn-related iron deposits, porphyry Cu, orthomagmatic Cu-Ni and V-Ti, Orogenic Au and epithermal Au. With respect to tectonic evolution, four main metallogenic stages have been identified: (1) In the

early to mid-Carboniferous, magmatism related to the Dananhu arc generated magmatic intrusions (Zhang et al., 2004; Han et al., 2006), leading to formation of the porphyry Cu deposits (Yangdong and Tuwu porphyry Cu deposits). The magmatic front migrated southward to form the Aqishan-Yamansu arc in the late Carboniferous during the closure of the ancient Tianshan ocean (Ma et al., 1997; Hou et al., 2006; Wu et al., 2006; Zou et al., 2006; Hou et al., 2007); (2) Several mafic-ultramafic complexes were emplaced, resulting in world-class orthomagmatic Cu-Ni-Ti-V deposits during a post collisional period (280-245Ma) (Wang et al., 2008; Wang et al., 2009; Mao et al., 2011); (3) Gold lodes of the shear-zone-type are controlled by the Kangguer ductile shear zone, Permian dated, such as Kanguer and Shiyingtan Au deposits (Pirajno et al., 1997; Zhang et al., 2000; Wang et al., 2005; Zhang et al., 2008); (4) A finally Fe-V-Ti orthomagmatic deposit (Weiya deposit) during Triassic (Zhang et al., 2005). These mineralizations are successive in time and spanning the tectonic units in spatial.

In the eastern Tianshan, the deposits of the second stage are clearly formed during magmatic activity and Permian dextral shearing. The skarn-related Fe-(Cu) deposits in the Aqishan-Yamansu arc belt are supposed to have formed during Carboniferous before the Permian dextral shearing. This hypothesis is still questionable as tongue shaped granites are known to have develop contact metamorphism during early Permian (Wang et al., 2008; Branquet et al., 2012). The study of the deformation in the iron skarn-related deposit could offers new constrains to establish the metallogenic timing in the eastern Tianshan. The Yamansu magnetite deposit which is one of the most studied iron skarn in the eastern Tianshan province has been taken as target because: (1) it is located along a dextral strike-slip fault; (2) the age of the deposit is poorly constrained despite that it is hosted in Carboniferous limestone and basalt with an age of 344±16Ma given by Rb-Sr age isochron with $^{87}Sr/^{86}Sr$ initial value of 0.7055±0.0001 (Lu et al., 1995). To constrain the sequencing of iron skarn-related deposits and large scale strike-slip shearing, it is important to recognize if the basalt intruded/extruded prior or posterior to the major strike-slip fault. To answer this question, basalt and massive

garnet skarn associated to hydrothermal alternation have been sampled for a paleomagnetic and AMS studies. The AMS method has predominant advantage to trace deformations in banded iron deformation (Cifelli et al., 2004) and/or fluid circulation (Sizaret et al., 2006; Sizaret et al., 2006), due to essentially the sensitivity of magnetic minerals texture generated by orientation (Borradaile and Tarling, 1981; Hrouda, 1982).

2. Geological setting

The Aqishan-Yamansu arc belt suffered north-verging thrusting and folding in Carboniferous, expressed more ductilely in the Yamansu-Huangshan area, decreasing in intensity toward the west and north, but compatible with thin-skinned tectonics (Laurent-Charvet et al., 2002; Charvet et al., 2011). Yamansu magnetite deposit is located in the Aqishan-Yamansu arc belt. In the Yamansu deposit area, the limestone is considered as early Carboniferous in age according to characteristic fossils (Baosteel-Company, 1977; XBGMR, 1993).

In the Yamansu pit the limestone show ripple mark (165°∠49°) suggesting a sedimentary deposition in an infratidal environment. In the galleries, we observed xenoliths of limestone embedded in the basalt sill which was produced by magmatic stoping (Fig. B-3), the basalt was later than the limestone. The skarn and basalt are localized in the shear zone and may indicate that pre-existing faults or the strike slip fault could channelize ascension before basalt emplacement. In the southern, the Yamansu faults controlled a development of Permian basin (Branquet et al., 2012). Outcrops of grauwacks formations are elongate, parallel or sub-parallel to the shearing zone, and suggest tectonic accommodation during Permian. Finally in the Permian basin and within the pit of the Yamansu deposit, metre thick dykes cross cut skarn, Carboniferous limestone and Permian formations. These dykes have been dated Permian coeval with whole regional strike-slip shearing (Li et al., 2006).

3. Yamansu magnetite deposit (YMD)

The Yamansu ore field contains more than 6 regularly tabular ore bodies located along an E-W strike slip fault of 5 km in length, among them, YMD is the biggest one in the easternmost of this area (Fig. B-2a). The shearing was thought to be of Permian (Shu et al., 1999; Branquet et al., 2012). . YMD contains a reserve of 32 Mt with an average grade of 51% Fe, and 20,000 t of Cu with a mean grade of 0.06% Cu (Mao et al., 2005). The ore bodies are spatially associated with a ~50m thick stratoid garnet skarn, which are nearly W-E extending and south dipping, with an dipping angle about 60° (Figs. B-2b and B-2c). The ore bodies and skarns are actually interstratified within the Carboniferous limestones and the basalt sill.

3.1 Skarn texture and paragenesis

The main texture within the massive garnet skarn is a centimetre- to metre-scale banding of alternating coarse-grained garnet-rich ribbons with small-size green epidote and chlorite rich ribbons. Garnet crystals generally occur as hexagonal shaped grains ranging in size from 1 to 6 mm. Within the ribbons, relics of basalt were observed (Fig. B-4a). Relics vary in size from a few to about 30cm and show irregular rounded shapes with gradational and wavy boundaries and sparse idiomorphic pyrites develop in them. In some places, far from massive garnet ribbons and magnetite bodies, basalts are partially replaced by andradite growing in the groundmass, whereas the euhedral/subhedral plagioclase is still present (Fig. B-4b). All these observations support the idea of a replacement of basaltic protolith by garnet skarn.

Massive magnetite bodies are of two types: (i) massive magnetite lobes replacing marble with a reaction front outlined by garnet growth (Fig. B-4c), leading to integration of garnet within massive magnetite; (ii) massive magnetite lenses in the centre of Yamansu open pit with a banding pattern composed by alternating magnetite and garnets ribbons (Fig. B-4d).

The prograde skarn minerals dominated by andradite and grossular with minor

pyroxene is extensively altered by chlorite and epidote. Sulphides (pyrite and chalcopyrite) are observed crosscutting the massive magnetite, indicating their later deposition. A schematic paragenetic succession in the YMD is given (Fig. B-5).

According to the salinity of fluid inclusions in calcite (Lu et al., 1996) and calculated possibly stability limits of stilpnomelane (Miyano and Klein, 1989) which altered garnet in the YMD, it seems that the formation temperature of garnet was above 500°C. The chlorite thermometer (Cathelineau and Nieva, 1985; Vidal et al., 2005) gives a retrograde temperature of 280°C during the epidote-chlorite-pyrite stage (16 EMPA points).

3.2 Mass balance

In infiltrative skarn systems, especially those associated with sulphide and oxide mineralization, there are pronounced depletions in CO_2 and Ca coincident with increasing abundance of Si, Al, Fe, etc. In order to estimate the absolute amount of the gains and losses during metasomatism, the quantitative approach was applied to the garnet skarn in comparison with the poorly altered basalt. The detailed treatment and the isocon fitting follow the method proposed by Grant (1986). The calculations give the mass-balance relation (Table B-1):

100g basalt + 14.1g CaO + 3.4g Fe_2O_3

= 107.4g massive garnet skarn + 4.8g Al_2O_3 +2.1g K_2O + 1.5g Na_2O (1)

And

100g basalt + 15.7g CaO + 2.8g Fe_2O_3 +2.1g K_2O

= 112g garnet skarn + 4.9g Na_2O + 2.6g MgO + 1.9g SiO_2 (2)

These calculations clearly indicate gains of CaO, Fe_2O_3 and a loss of Al_2O_3 of the basalt. We suggest that CaO might be leached from the limestone during decarbonation. External input of Fe_2O_3 is inferred to the flow of iron-rich hot brines responsible for massive magnetite deposition.

3.3 Structure and deformation

In the Yamansu open pit, there are two dominant groups of faults. The fault

plane of the first group is subparallel to ore bodies and the ripple plane of limestone (165° ∠ 49°), while the other one is mostly NE-SW or NNE-SSW trending. Steroplots are done to better understand the kinematics (Fig. B-6a and B-6b). Lineation (stretching and mineral lineation) measurements also show two groups (Fig. B-6a): (1) E-W with slightly low to middle angle; (2) SW dipping with slightly deeper angle. Fault planes also show two groups (Fig. B-6b). These faults seem to be brittle. The first group lineation probably associated with the regional E-W dextral strike-slip caused by book shelf structure, whereas the second group may relate to thrust fault. Subaltern N-S compressive thrusting, which probably corresponds to the second group lineation, was observed in the limestone (Fig. B-6e).

To the north of the Yamansu open pit where limestone distributed, fractures and schistosity developed. According to field and microscope observations, two kinematic trajectories could be distinguished. Firstly, NW-SE shortenings (Figs. B-6c and B-6d). These shortenings are progressive. At the beginning, cracking filled by later calcite was produced by NW-SE compressive squeeze. Cracking was parallel to principal stress (step 1, Fig. B-6d). With the development of compressive shortenings, principal stress rotated according to observations in the field. Because the sectrix curve of the conjugate is not parallel to the cracking. Therefore, the angle between the sectrix curve of the conjugate and the long axe of the cracking was the rotation angle (step 2, Fig. B-6d). Conjugate strike-slip occurs (step 3). This stage only developed in the northern side of the open pit, at a certain distance from the Yamansu open pit. It means that this stage is preserved a little far from the fault. Companying this compressive shortening, thrust probably occurred. Secondly, dextral shearing (Fig. B-6f). The photo (Fig. B-6f) illustrates that calcite has experienced a dextral kinematic. Oriented samples are from the Yamansu open pit. This kinematics is coherent with the Permian strike-slip dextral shearing which leads several authors to consider that the Yamansu fault is part of the regional dextral shearing (Shu et al., 1999; Pirajno, 2010).

4. Paleomagnetic and magnetic fabric study

4.1 Sampling and measurement

275 cores from 24 sites have been sampled in the Yamansu open pit (Fig. B-2b) using a portable gasoline drill. Solar azimuth has been systematically measured for all samples to avoid the declination deviation caused by magnetite-rich basalt and magnetite ore bodies. The standard specimens of 2.5 cm in diameter and 2.2 cm in height have been prepared in laboratory.

All samples have been measured for the magnetic fabric study, and among these sites, 20 orientated cores have been taken for paleomagnetic studies from two sites separated by about 900m (Site 06 and Site 16 in Fig. B-2b). The lithology of these cores are classed in 6 groups, i.e., basalt, massive garnet skarn, ore shoot, retrograde stage skarn (epidote, chlorite, K-feldspar, tourmaline), marble and Permian dykes. Sites 06 and 16 are constituted by basalt with disseminated magnetite inside and massive garnet skarn, respectively.

Magnetic remanence measures and Alternative Field (AF) demagnetization were performed with Agico JR5A spinner magnetometer and Agico LDA-3 demagnetizer, respectively, in Institut des Sciences de la Terre d'Orléans, France. All specimens have been progressively demagnetized by about 10 steps from 0 to 50 mT. Corresponding remanent magnetic directions are calculated by principal component analysis (Kirschvink, 1980) and the average of these directions are calculated by Fisher statistics (Fisher, 1953).

The bulk magnetic susceptibility and AMS are measured with KLY-3S Kappabridge apparatus. The mean orientations of three principal ellipsoidal axes of AMS (K_1>K_2>K_3) for each site are computed with ANISOFT software using Jelinek's statistics (Jelinek, 1981). During the laboratory measurements, some samples show high magnetic susceptibility that saturated the magnetic measurements. In this case, the cores were re-cut into cubic specimens of 9mm and/or 6mm in length. However, smaller volume may increase the measure error for a single core, the specimen quantity of measurement mostly increases twice.

4.2 Magnetic mineralogy

In order to identify the magnetic remanence and susceptibility carriers, magnetic hysteresis measurements and thermomagnetic curves have been acquired by a translation inductometer within an electromagnet providing a field of up to 1 T of the paleomagnetic laboratory of Institut de Physique du Globe de Paris and an AGICO KLY3 Kappabridge-CS3 furnace apparatus of Laboratory of rock magnetism of Orleans University, respectively.

For all lithologies except marble, magnetic hysteresis measurements on five representative samples including the basalt, massive garnet skarn, ore shoot, retrograde stage skarn and Permian dykes reveal characteristics of ferromagnetic minerals (Figs. B-7a and B-7b). These samples containing relative high Hcr/Hc ratio (3.69-12.2) and low Mrs/Ms ratio (0.0347-0.14). The results have been projected on the Day Plot diagram showing the presence of multidomain magnetites with grain size bigger than 6μm, indicating that the magnetic fabrics are normal (Fig. B-9) (Dunlop, 2002). The thermomagnetic curves decrease during heating until 350°C and suggest the possible presence of maghemite or pyrrhotite, then the susceptibility show a sharp drop down at 580°C which concerns the Curie temperature of magnetite (Fig. B-7d). These results are consistent with microscopic observations in which magnetite grains were observed.

The hysteresis curve obtained from marble sample displays diamagnetic character (Fig. B-7c). Diamagnetic calcite with low iron content is known to have inverse fabric, i.e. the calcite <c> axes are parallel to K_3 axis (inverse fabric). Rochette (1988), Schmidt et al. (2006) and Essalhi et al. (2009) note that K_1, K_2 and K_3 are classified according to their algebraic values. Goniometric analysis confirm that the lower value K_3 is parallel to the <c> in YMD (Fig. B-8).

4.3 Paleomagnetic results

The progressive AF demagnetization reveals two distinct components of samples from the basalt and massive garnet skarn (Fig. B-10).

The first component isolated mostly from the massive garnet is totally cleaned

by less than 15 mT with a solo normal polarity. They are close to Present Earth Field (PEF) (the present dipolar geomagnetic field: D = 0°, I = 61°) in the geographic coordinates (before bedding corrections) (Fig. B-10a). Before the tilt correction, they displayed with an average of Dg = 9.7°, Ig = 58.9°, kg = 103.2, α_{95g} = 5.1° with n = 9. In stratigraphic coordinates (after bedding corrections), this average becomes Ds = 131.4°, Is = 66.1°, ks = 103.2 and α_{95s} = 5.1° (Table B-2 and Fig. B-11), which is incomparable with any paleomagnetic directions in surrounding areas since Late Paleozoic.

The second component displayed a solo reversal polarity with higher coercivity from 7 to 50 mT (Fig. B-10b). They present southeastward reversed directions in stratigraphic coordinates (Fig. B-12). Moreover, the directions from these reversal components show a relatively well grouped average with Dg = 136.8°, Ig = 15.6°, kg = 29.9, α_{95g} =10.3° and n = 8 in geographic coordinates, and Ds = 134.1°, Is = -27.9°, ks = 29.9 and α_{95s} = 10.3° in stratigraphic coordinates (Table B-2 and Fig. B-12). See the discussion for the origin of these reversal components.

4.4 Magnetic fabrics

The statistical results and associated parameters of these measurements are presented in Table B-3. The sites contained rich magnetite are of the skarn, the magnetite bodies and the facies with retrograde stage show obvious high bulk magnetic susceptibility (from $3.10*10^{-2}$ to $6.65*10^{-3}$ $SI*g^{-1}$), as well as basalt. The Permian dykes displayed relative low bulk susceptibility ($1.83*10^{-5}$ to $1.2*10^{-4}$ $SI*g^{-1}$) and the marble are diamagnetic.

Most of the samples have positive shape parameter (T) with a dominance of the magnetic foliation (Table B-3 and Fig. B-13a). This implies that the AMS foliation is statistically better defined than the lineation. The degree of anisotropy (P_J) is relatively low to moderate and increase with the susceptibility (Fig. B-13b).

Figure B-14 presents the AMS principal axes (K_1, K_2 and K_3) in lower equal area projection for each site with respect to the different lithology. Results of samples taken from basalt, magnetite bodies, skarn and retrograde stages are

presented after bedding correction using the stratigraphic plane measures (165°∠49°), marble and Permian dykes are still in the geographic system. Details of AMS characteristics are described in following:

(1) Three sites of basalt display horizontal magnetic lineation (K_1) and foliation with low anisotropy degrees (P_J values less than 1.2);

(2) Five sites of massive garnet skarn show also horizontal magnetic lineation and foliation. These horizontal lineations are well grouped in SW-NE direction. Two sites reveal high P_J values (Sites 15-1 and 04-2) and high susceptibility probably due to high content of magnetite (details are addressed in Section 5.2). One site displays vertical magnetic foliation (Site 17-1) with low P_J. Two sites seem ambiguous with intermediary angle of foliation but with horizontal lineation;

(3) Three sites of massive magnetite bodies display horizontal magnetic foliation with a SW-NE lineation. These three sites show lower P_J values. Another three sites of massive magnetite bodies N-S to NE-SW vertical foliation;

(4) The sites of retrograde stage show low P_J values and two of three sites present horizontal foliation, the remain one rather vertical;

(5) The two sites of marble show a vertical N80° foliation. The K_3 directions is about N350°;

(6) The AMS measured in the Permian dykes shows low anisotropy degree, clustered vertical lineation and variable shape parameters (Table B-3). In the case of Sample 04-1, the vertical foliation is dominant parallel to the dyke, and Site 14 has a shape parameter close to 0 and the magnetic foliation differs from the dyke orientation.

For most sites within the basalts, magnetite bodies, skarn and retrograde stage, the magnetic lineation (K_1) and magnetic foliation are horizontal or sub-horizontal and we do not observe relation between the anisotropy degree parameter and the position of the magnetic foliation.

5. Discussion

5.1 Initial geometric position

Sedimentary plane in the limestone indicates the initial sedimentary occurrence and is used for tilting the formation, however this occurrence varied a little depending on the locations. It is concordance or sub-concordance with the ore bodies and garnet skarn which are actually orientated in ~N165° with a dip angle of about 60° to the south (Fig. B-2c).

Paleomagnetic remanence carried by weak coercive and viscous magnetic minerals from 9 measured samples show recent remagnetisation close to PEF in geographic coordinates with single downward polarity (Fig. B-11). Moreover, its tilt corrected direction is not comparable with any directions from the Junggar Block or Tuha basin since Paleozoic (Li et al., 1999; Wang et al., 2007; Choulet et al., 2010).

The higher coercive components present solo reversal directions in stratigraphic coordinates. Though the fold test cannot be applicable to these directions because of monoclinal beddings, these solo reversal and relatively well-grouped directions are comparable with the Kiaman Reverse Superchron dated from 312 to 262 Ma (Merrill et al., 1996), similar to the rock age estimated at Late Paleozoic in the Tianshan region (Li et al., 1999). Furthermore, the corresponding positive and southeastward directions in geographic coordinates do not make any tectonic sense (Table B-2 and Fig. B-12). The magnetic remanence isolated from higher coercive component may be therefore considered as primary. Consequently, the basalt may be considered to more or less horizontally intrude in the limestone as sill before tilting caused by later strike-slip faulting. In the same way, the skarnization should have occurred before tilting. Though some precautions should be taken on this conclusion because of weak number of samples, the possible slightly inclined basalt bedding and the influence of secular variation, these results may be considered as qualitative ones.

5.2 Interpretation of magnetic fabrics: deformation vs. magmatic flow and fluid flow

After bedding correction, the horizontal fabrics of basalt with a low anisotropy degree could be interpreted to be primary and suggest a horizontal N-S magma flow forming sill intrusion. The skarn formation (i.e. massive garnet skarn, retrograde assemblage and magnetite bodies) show two principal types of magnetic fabrics, N-S vertical and horizontal with a SW-NE lineation. In these formations multi-domain magnetite is the main magnetic susceptibility carrier. It is known that in this case the degree of anisotropy (P_J) depends on the bulk susceptibility values (Km) (Fig. B-13b), and P_J with low (<1.1) to moderate (<1.2) values could be controlled by the magnetite content within samples rather than by deformation. This interpretation is consistent with the absence of correlation between the variations of the anisotropy degree and the two types of magnetic fabrics with vertical and horizontal foliation. The skarn magnetic fabrics are therefore interpreted as primary. Horizontal fabrics are similar to those displayed by basalt, and we should discuss if massive garnet skarn fabrics could be partly inherited. Mass balance calculation and higher value of bulk susceptibility in the massive garnet skarn comparing to the basalt suggest a re-precipitation of iron contained in the basalt into skarn magnetite. Therefore, in both skarn and massive magnetite the magnetite precipitated in metasomatic flows and should record the flow direction. We interpret the horizontal fabrics with NE-SW lineation as primary texture recording hydrothermal flow parallel to the boundaries of the sill and perpendicular to the Yamansu fault as they are proposed intuitively. The vertical NS foliations (such as Sites 17-1 in the garnet skarn and 12-2 in the magnetite ore body) with verticalised lineation could suggest the existence of N-S to NE-SW vertical hydrothermal flows in drains.

The AMS of marble is controlled by the orientation of the calcite <c> axes which are parallel to K_3 axis (inverse fabric; Figs. B-7c and B-8). This K_3 axis oriented in the direction close to 340- 350° could be interpreted as the result of the dextral shear. Several previous studies on natural samples show that low temperature (<300°C) shearing may produce a rotation of the <c> axis in the

opposite sense of the shearing as the twining of the calcite lead to parallelize the main strain σ_1 and the <c> axis [e.g. Turner et al., (1954); Wenk et al. (1987); Nadège (1997)]. Marble magnetic fabrics should have therefore formed during the dextral shearing.

The sites of dykes show a vertical lineation interpreted as recording of the vertical magma flow patterns. Previous studies have shown that mafic dykes mostly preserve a vertical K_1 orientation indicating magmatic flow (Craddock et al., 2008). Some studies reveal that the vertical-K_1-type dykes were formed in an extension and fast raise environment (Callot and Guichet, 2003; Cañón-Tapia and Herrero-Bervera, 2009), however imbrications have been observed in some cases (Tarling and Hrouda, 1993).

5.3 Mineralization model and conclusions

The general review on world skarn deposit proposed by Meinert et al. (2005) suggests a first simple genetic classification defining a continuum between metamorphic hornfels and metasomatic skarn. In the Yamansu Skarn, even if fluids produced by basalt should have contributed to deuteric alteration, the large amount of iron compared to basalt involved in the genetic process indicates a metasomatic dominant process with large flowing fluids. As discussed above for the basalt, a pre-existing fault probably has channelized deep ascending fluids. Therefore, the proposed model involves pre-existing fault that channelized basalt and metasomatic iron-rich fluid during the formation of the deposit (Fig. B-15). Then, the basalt and the skarn formation were tilted during the Permian dextral shear. The formation of the YMD could be described in 4 steps as following:

1. North-verging thrusting and folding stage (Fig. B-15a). This stage was commonly recognized (Wang et al., 2010; Charvet et al., 2011) and companied by calc-alkaline magmatism (Wu et al., 2006). In Yamansu area, the limestone is weakly deformed.
2. Emplacement of basalt (Fig. B-15b). The basalt injected, probably along a pre-existing fault E-W, flowed with a NS direction into the limestone and

formed weakly inclined sill;

3. Metasomatic fluids were channelized along the fault, flowed parallel to the sill with a N-S direction and produced the extensive skarnization and magnetite deposit (Fig. B-15c). The circulation of CO_2 come from the limestone probably enforced the metasomatism;
4. Permian dextral shearing tilted the formations to a positive flower structure could be the main reason for the actual basalt, skarn and ore shoot geometry (Fig. B-15d).

According to our studies of paleomagnetism and AMS a pre-existing fault should occur before the main Permian dextral shearing. This fault focalised magmatic activity and facilitated the emplacement of basalt sill and metasomatic flow that are responsible for the Yamansu deposit. The emplacement of basalt probably occurred in late Carboniferous or Early Permian before thrusting-folding and strike-slip developed.

Finally, it is worth to mention that this is the first time to use magnetic fabrics as textural arguments to identify flow direction in a skarn deposit. AMS method could be therefore considered as an efficient tool to improve our knowledge on flow circulation and front migration in metasomatic processes.

Acknowledgements

We specially thank Baosteel Company for providing access to their mine and unpublished documents. The first author benefits a scholarship grant from the French Minister of Education and Research. This study was financially supported by Chinese National 973 Project (2007CB411301), Geological Survey Project (1212011140056) and NNSFC (40603008, 40672040).

References.

Figures and tables in the article of section 3.6:

Table B-1. Geochemical composition of basalt, massive garnet skarn and related mass balance calculations according to Grant (1986).

samples	basalt wt%	Y159	Basalt Y205	skarn wt%	Y102	Δm_i (g) from Y205 to Y102	Δm_i (g) from Y159 to Y102
SiO_2		46.15	49.31		42.52	-1.90	-0.55
TiO_2		0.85	1.01		0.58	-0.36	-0.23
Al_2O_3		21.20	16.73		15.30	0.33	-4.79
MgO		4.10	6.33		3.39	-2.55	-0.46
CaO		7.68	6.94		20.32	15.72	14.11
Fe_2O_3		5.22	6.19		8.07	2.81	3.43
FeO		3.72	3.39		3.64	0.67	0.18
MnO		0.55	0.38		0.34	0.00	-0.19
P_2O_5		0.09	0.09		0.11	0.03	0.03
Na_2O		1.78	5.11		0.23	-4.85	-1.53
K_2O		4.38	0.29		2.10	2.05	-2.13
LOI		4.39	4.66		3.69	-0.55	-0.43
∑		100.11	100.43		100.29		
ρ (g/cm^3)		2.82	2.85		3.36		
f_V						0.947	0.9

Δm_i (in grams) gain or loss of elements during the transformation of basalt into massive skarn; positive value means gain, whereas negative value means loss. ρ=density; f_V =volume fator. Major element contents of the rock were analyzed on a VF-320 X-ray fluorescence spectrometer (XRF) at the Modern Analysis Center, Nanjing University. Uncertainties for major elements are generally less than 2%.

Table B-2: Paleomagnetic measurement results from Yamansu magnetite deposit.

	N	Dg	Ig	Ds	Is	ks	α95
Lower coercive and viscous remanence	9 (2 basalt ; 7 garnet skarn)	9.7°	58.9°	131.4°	66.1°	103.2	5.1°
High coercive remanence	8 (3 basalt ; 5 garnet skarn)	136.8°	15.6°	134.1°	-27.9°	29.9	10.3
Note that tilt correction is based on the ripple plane (165°∠49°) of limesonte. Paleomagnetic samples are from Sites 06 and 16 of basalt and massive garnet skarn lithology.							

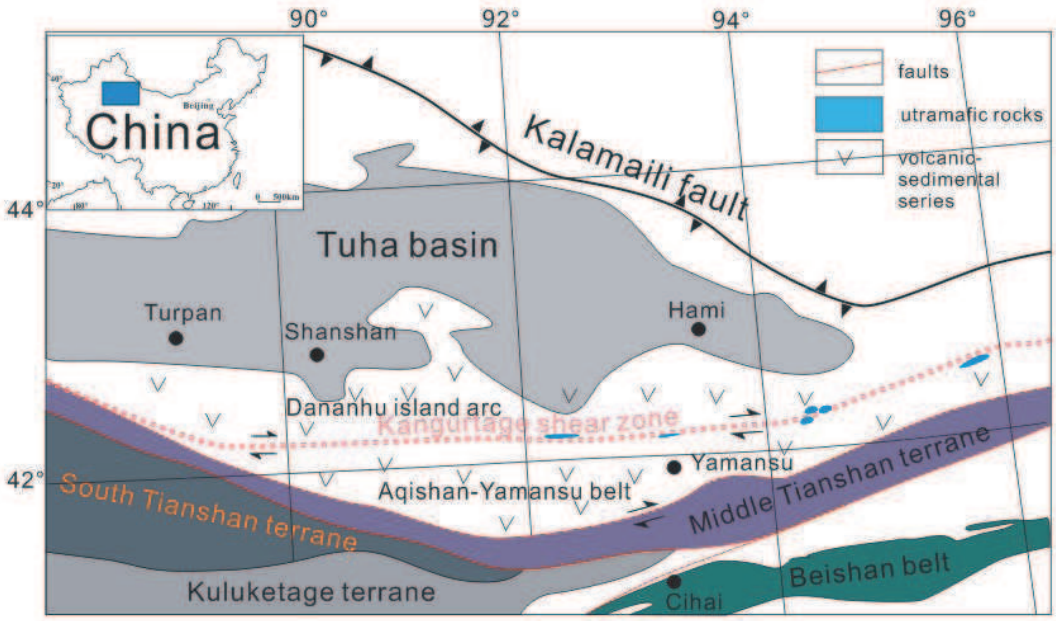

Fig. B-1: Simplified map showing the localization of the Yamansu iron skarn deposit and the main tectonic units of the eastern Tianshan [modified from Li (2004) and Gu et al. (2006)].

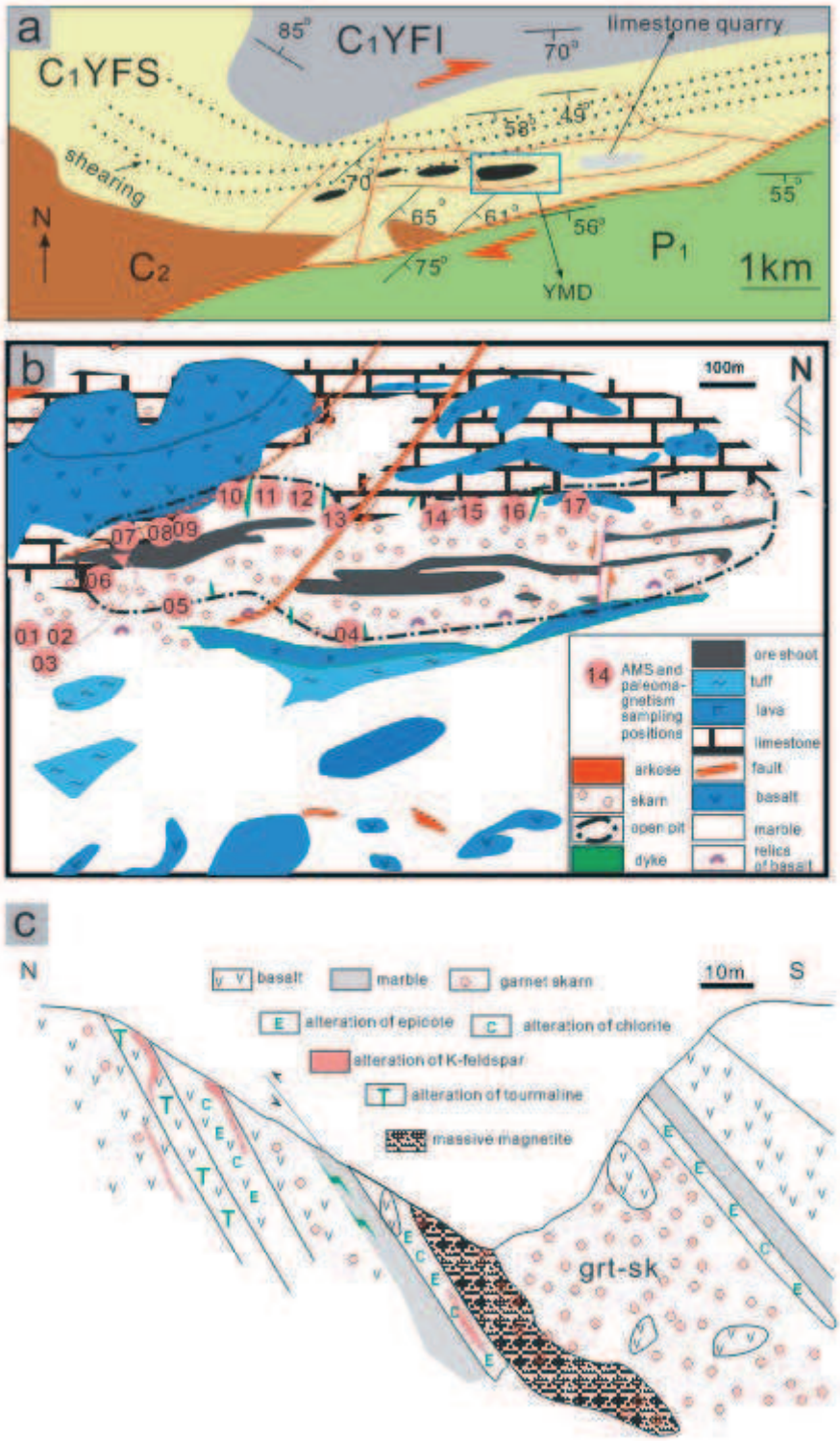

Fig. B-2: Maps and cross section presenting the Yamansu magnetite deposit. (a) Geological map of Yamansu ore field; (b) geological map of the pit of Yamansu; the samples name and positions used for AMS and paleomagnetic study are given in pink circle with numbers inside; (c) cross section of the Yamansu magnetite deposit showing the development of a massive garnet skarn above the stratoid magnetite ore body. Note the presence of basalt relics within the garnet skarn formation.

Fig. B-3: Marble fragments within strongly altered basalt, suggesting mafic magma stoping. The photo was taken in the gallery, about 200m underground. Reddish ribbons consist in K-feldspar occurrence due to the development of potassium metasomatism.

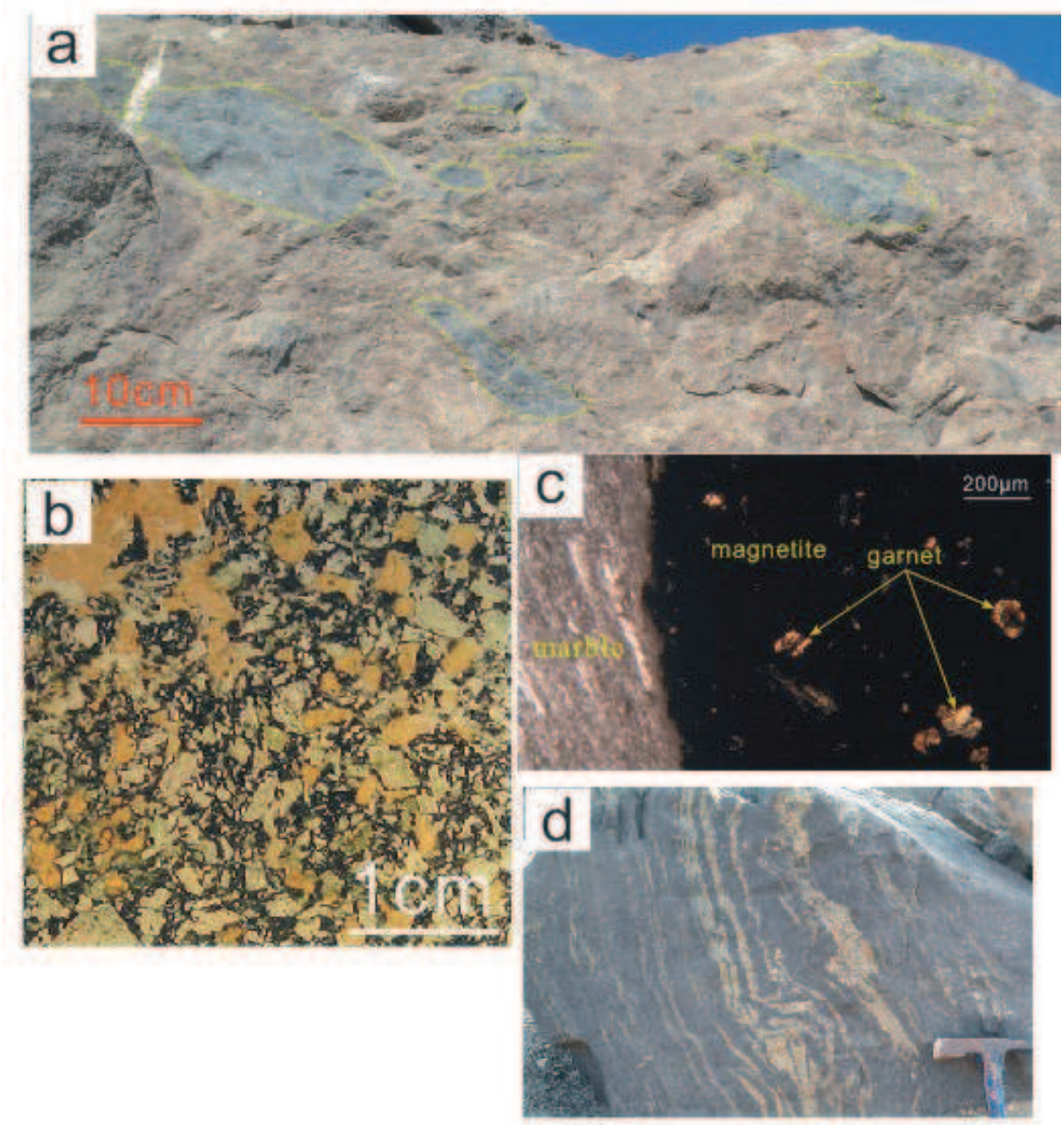

Fig. B-4: Texture and mineralogy of the prograde and massive magnetite stages. (a) Relics of basalt (emphasized by dotted yellow lines) in massive reddish garnet skarn. (b) Basalt with plagioclase (in white) altered by andradite (in pink). Groundmass and disseminated magnetite are in black; (c) Front developed along the contact between magnetite and marble, along this front garnet are develop and clearly visible here in transmitted plane polarised light. (d) Rhythmic banding of garnet (reddish) and magnetite (black).

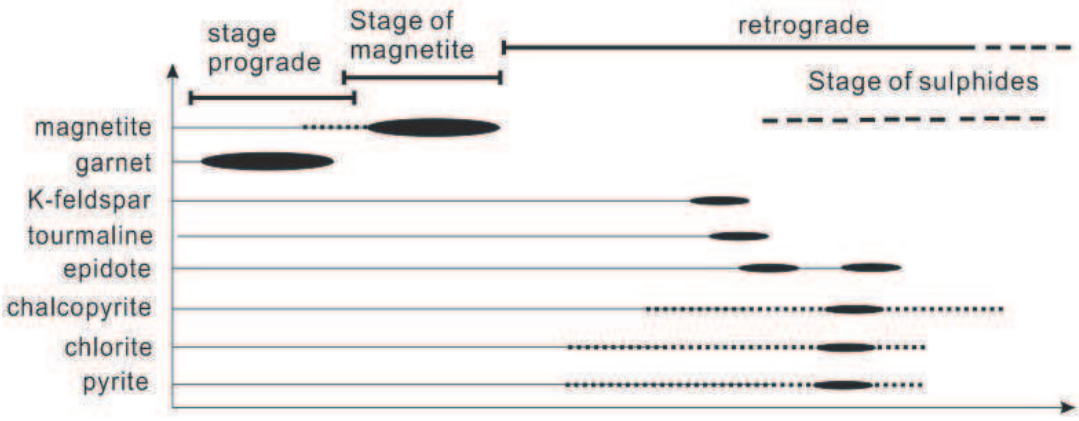

Fig. B-5: Simplified paragenetic succession of the Yamansu iron skarn.

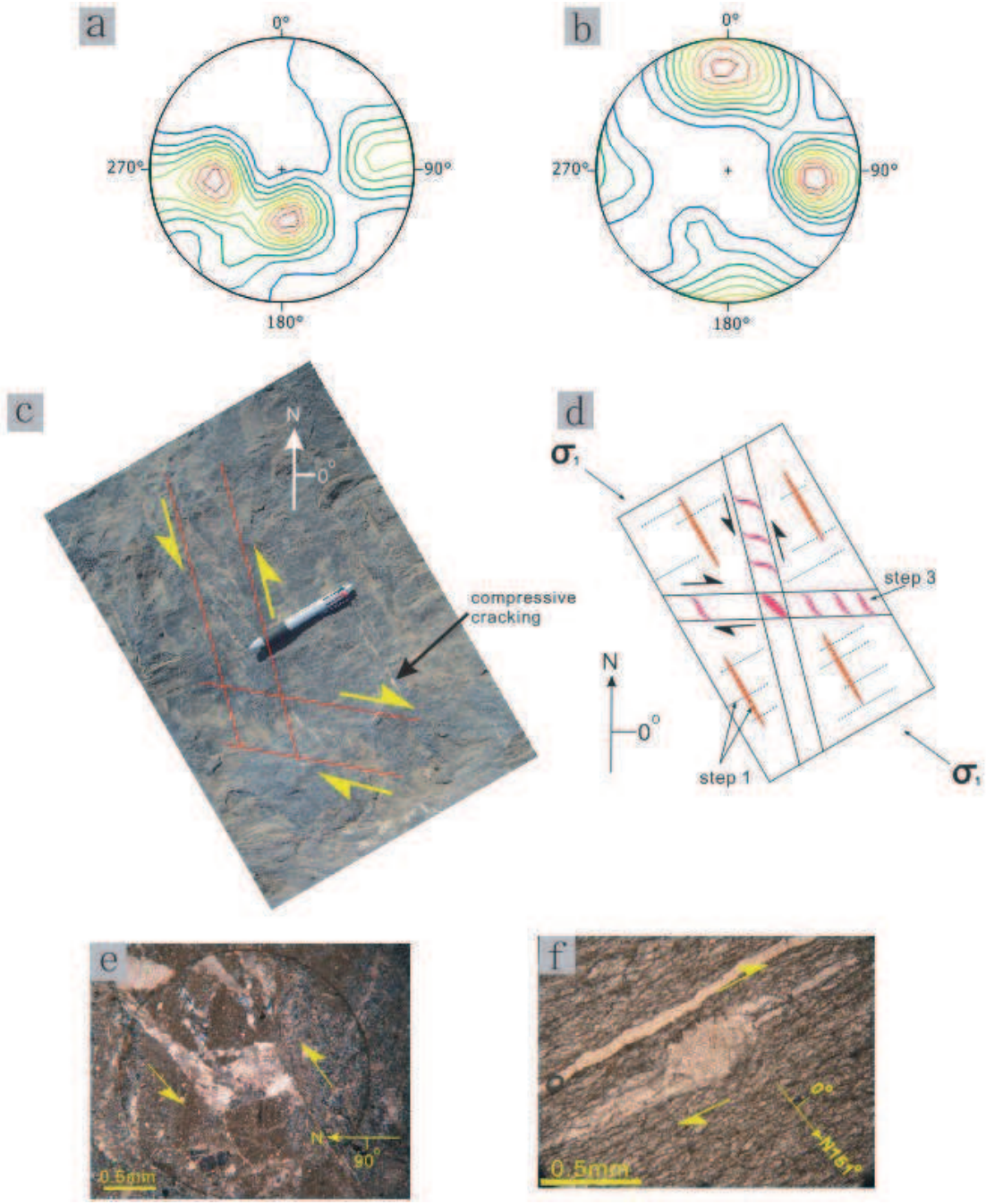

Fig. B-6 Stereographic projection plots (a and b), conjugation fracturing (c and d), thrust up (e) and dextral kinematic (f) microphotograph. (a) lineation stereographic plots of Schmidt equal angle lower hemisphere projection, 350 measurement points; (b) fault plane stereographic plots of Schmidt equal angle lower hemisphere projection, 301 measurement points; (c) NW-SE compressive shortens causing related conjugate fracturing system. Cracking filled by later recrystallized calcite was produced by compressive squeeze; (d) interpretative drawing of conjugate fracturing in (c); (e) subaltern structure of NW-SE compressive thrust up; (f) Calcite indicating dextral strike-slip.

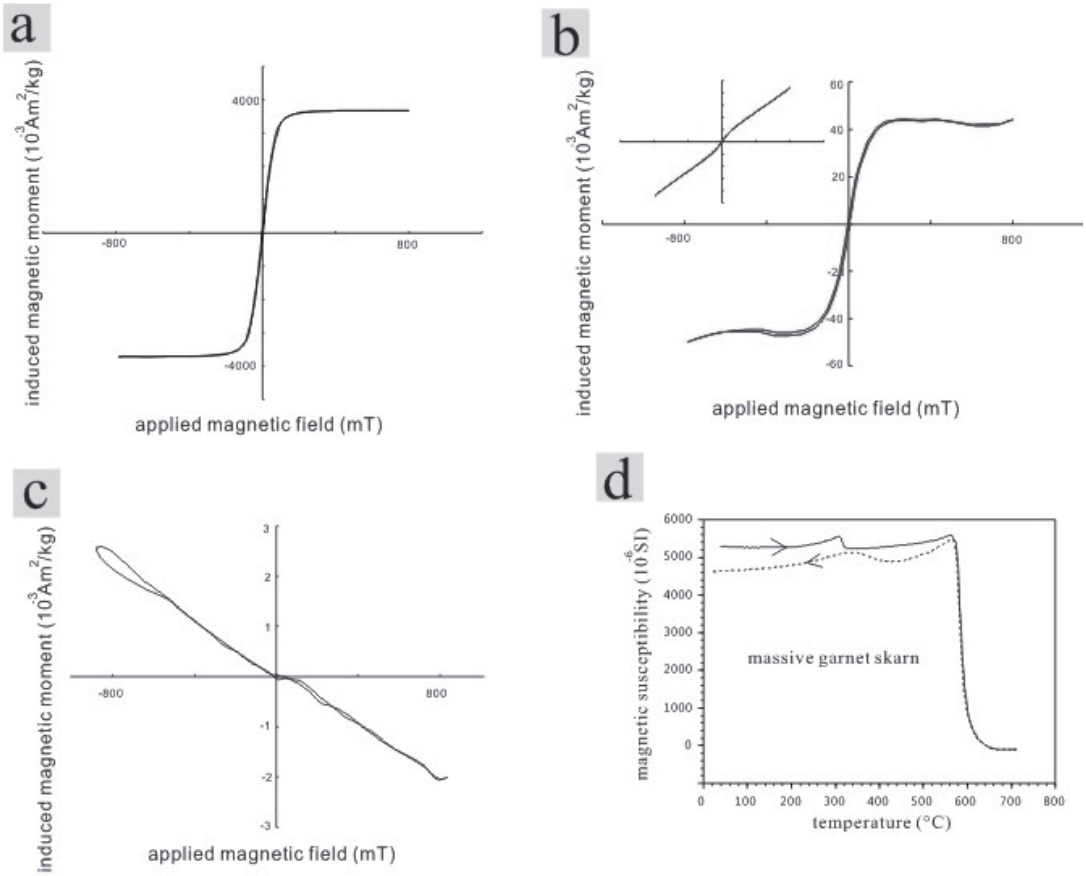

Fig. B-7 Magnetic analyses to identify the magnetic mineralogy. Hysteresis loops for : (a) basalt, (b) massive garnet skarn and (c) marble. (d) thermo-susceptibility curve measure for massive garnet skarn. The rapid decrease of magnetic susceptibility in (d) at about 580°C indicates the presence of magnetite. Solid (dotted) lines stand for heating (cooling) curves, respectively.

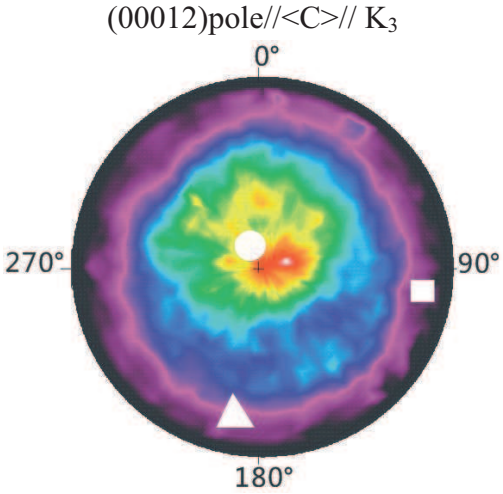

Fig. B-8: Analysis of the marble texture the stereogram give the lattice preferred orientation of the (00012) pole plane, i.e. the calcite <c> axis, the colour levels indicate the diffracted X-ray intensities. AMS measures are presented by square (K_1 magnetic lineation), triangle (K_2) and circles and (K_3 pole of magnetic foliation).

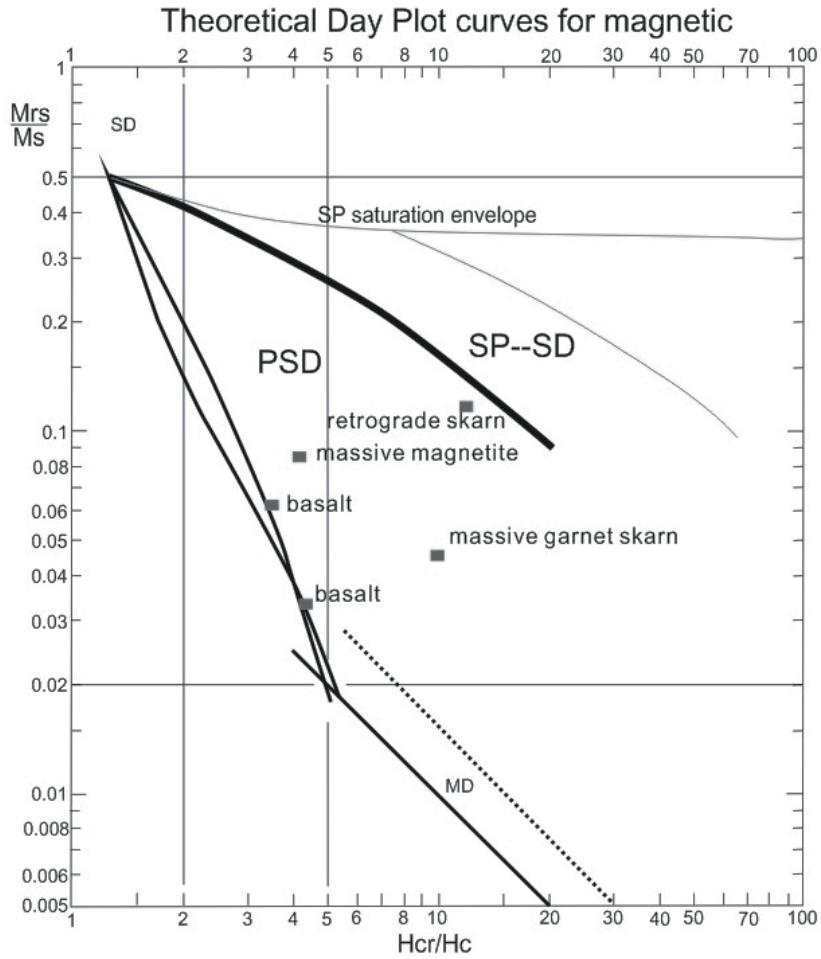

Fig. B-9 Mrs/Ms versus Hcr/Hc Day plot diagram modified after Dunlop (2002).

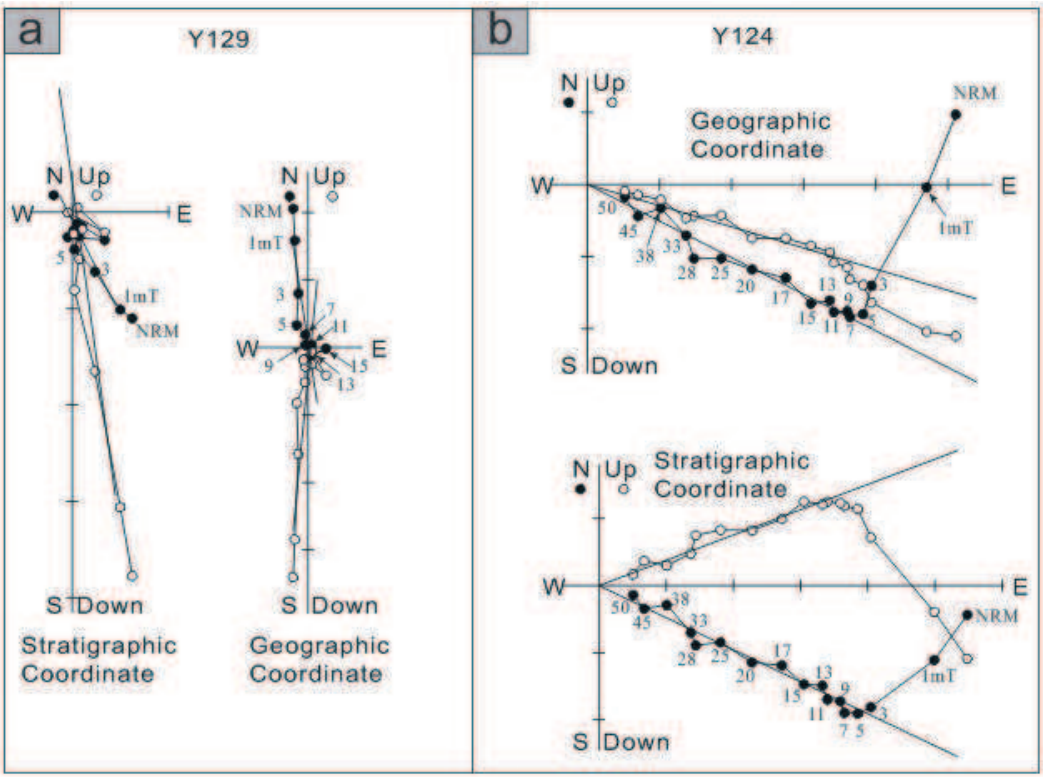

Fig. B-10 Paleomagnetic measurement results from Yamansu skarn deposit. Orthogonal projection of sample progressive AF demagnetization (Zijderveld, 1967) in geographic and stratigraphic coordinates. White and black circles represent vertical and horizontal plans, respectively. Numbers adjacent to data points indicate peak demagnetizing field in mT.

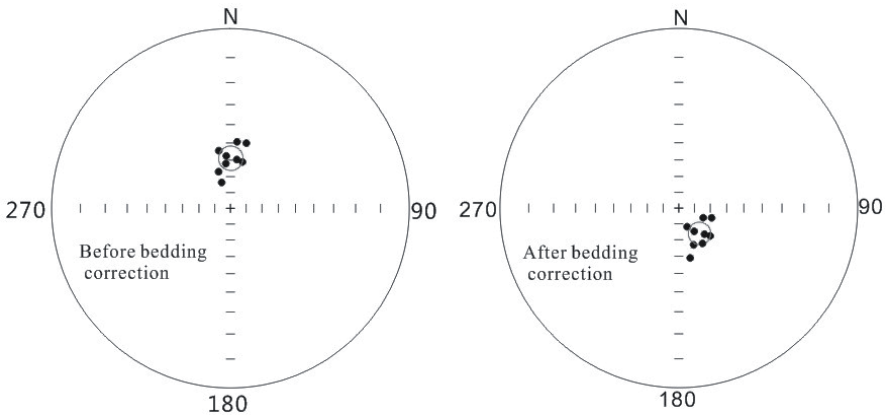

Fig. B-11 Equal-area stereoplots for weaker and viscous remanence which is close to present earth field.

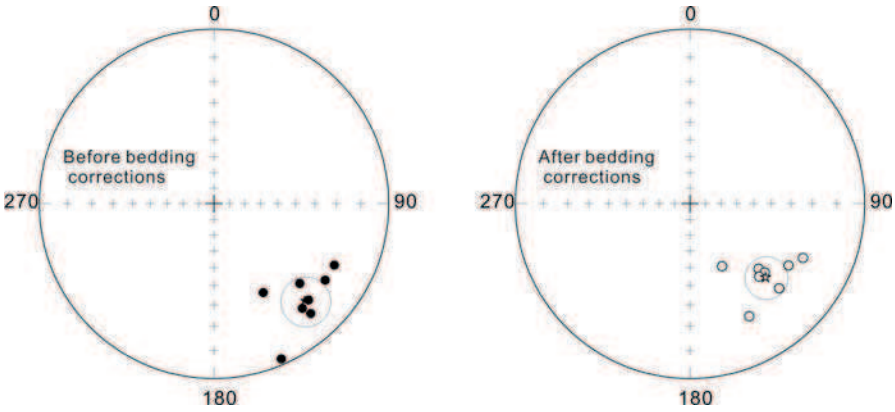

Fig. B-12 Equal-area stereoplots for hard remanence components. White (black) circles represent reversal (normal) polarities of mean direction. The left and right represent for geographic coordinates and stratigraphic corrected coordinates.

Table B-3: AMS statistic results and associated parameters

site	lithology	n	K_1				K_3				P_J	T	Km ($SI*g^{-1}$)
			D	I	$\alpha_{95\ max}$	$\alpha_{95\ min}$	D	I	$\alpha_{95\ max}$	$\alpha_{95\ min}$			
01-1	mgt	15	250.9	11.2	50.5	14.1	347.4	29.8	31.7	11.4	1.180	0.158	1.62E-02
01-2	mgt	18	254.8	3.5	37.4	7.7	346.6	27	31.1	8.3	1.081	0.363	3.10E-02
02	mgt	8	243.9	9.7	31.2	8.5	145.1	41.8	19.9	11.9	1.276	0.504	6.65E-03
03	mgt	17	225.5	33.4	52.6	19.3	318.7	4.9	23.5	12.3	1.128	0.204	1.18E-02
04-1	dyke	5	187.2	74.2	15.5	4.3	312.6	9.3	17	2.3	1.032	0.724	1.83E-05
04-2	basalt + grt	32	225.3	31.2	17	12.2	0.5	49.5	37.8	12.4	1.535	0.063	2.21E-02
05-1	grt	7	97.4	39.3	15.1	8.4	262.6	49.7	12.1	5.5	1.005	0.292	5.03E-05
05-2	basalt + grt	15	220.2	59.6	12.2	4.8	349.7	20.4	8.2	3.4	1.012	0.222	2.22E-05
06	grt	8	120.4	12.5	10	5.2	29.9	2.2	13.8	5.3	1.014	-0.379	1.33E-04
07	basalt	10	204	14.7	31.7	10.6	23.5	75.3	42.4	20	1.130	0.201	1.00E-03
08	rss	10	228.1	51.3	9.9	2.2	8.9	31.9	30.8	3.3	1.017	-0.150	2.33E-05
09-1	basalt	5	196.4	62.5	18.3	9.5	332.7	20.6	53.3	10.2	1.012	0.078	1.70E-05
09-2	rss	5	288.3	17.6	25	9.4	188.7	27.7	30	6	1.002	-0.194	2.90E-05
10	rss	7	107.4	23.3	20.2	4.6	346	50.5	17.6	6.7	1.119	0.571	8.54E-04
11	marble	9	73.6	11.9	8.8	4.2	339.5	19	7.5	3.4	1.130	-0.216	-2.38E-06
12-1	marble	6	80.6	2.6	14.4	6.2	350	13.3	14.3	11.1	1.591	0.352	-1.63E-07
12-2	mgt	16	2	25.1	14.2	8.9	99.7	16	12.1	9	1.141	-0.054	3.54E-02
13	grt	11	240.4	42.4	25.7	19.5	345.9	16.3	27.8	19.1	1.161	0.123	1.97E-02
14	dyke	7	192.7	81	10.7	5.8	53.2	6.9	16.2	5.7	1.025	0.002	1.20E-04
15-1	grt	9	222.8	24.7	12.7	12.4	347.7	51.2	17.3	10.2	1.229	0.388	1.16E-02
15-2	grt	21	91.9	19	18.2	14.5	341.5	45.4	25.8	14.1	1.199	0.154	1.51E-02
16	basalt	8	253	6.2	35.1	9.4	344.5	13.4	16.9	7.2	1.044	0.037	1.52E-04
17-1	basalt + grt	5	343.5	70.1	25.6	10.5	89.4	5.7	31.2	4.6	1.022	-0.110	8.60E-05
17-2	mgt	21	27.8	11.7	17.9	11.6	118.1	1.4	21.3	11.6	1.208	-0.300	3.08E-02

The results of AMS measurements from Yamansu open pit. n: number of specimens. K_1 magnetic lineation, K_3 pole of the magnetic foliation, D, I, α_{95min}, α_{95max} are declination, inclination, statistic confidence at 95% level. P_J: Corrected anisotropy degree, T: Anisotropy shape parameter (Jelinek, 1981), and Km: Mean bulk magnetic susceptibility ($SI*g^{-1}$); mgt: magnetite rich rock; grt: massive garnet skarn; rss: retrograde stage skarn dominated by epidote, chlorite, tourmaline and K-feldspar.

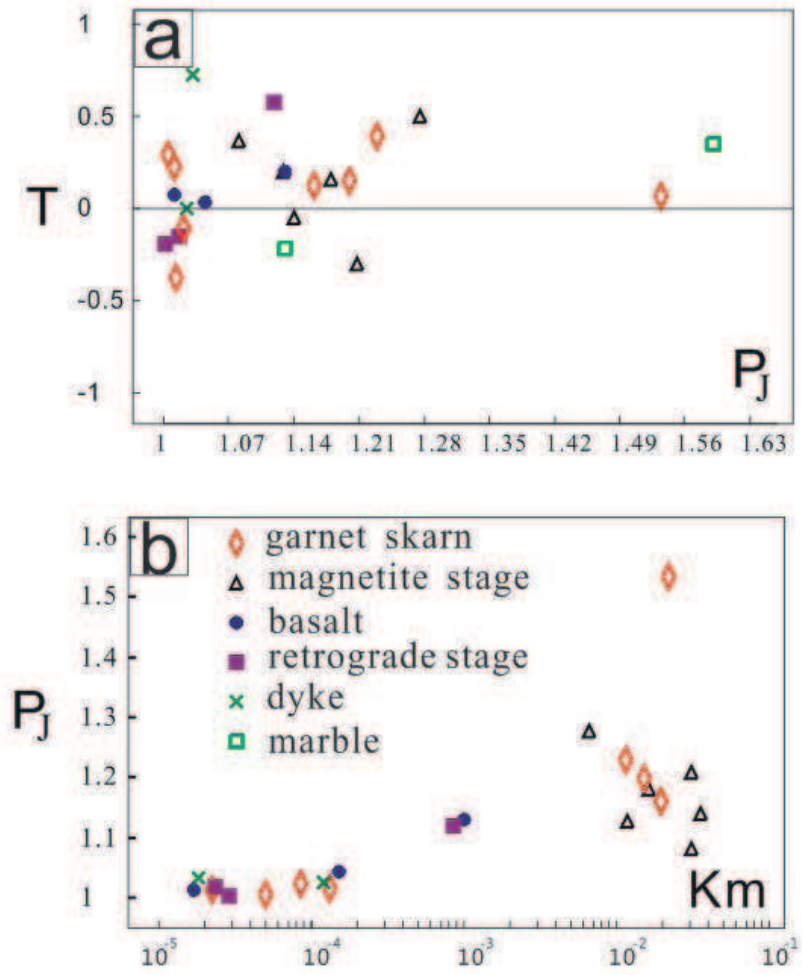

Fig. B-13: AMS scalar parameters for sites grouped by lithologies. (a): T shape parameter vs P_J corrected anisotropy degree and (b) P_J corrected anisotropy degree vs. Km mean bulk magnetic susceptibility in SI*g^{-1}.

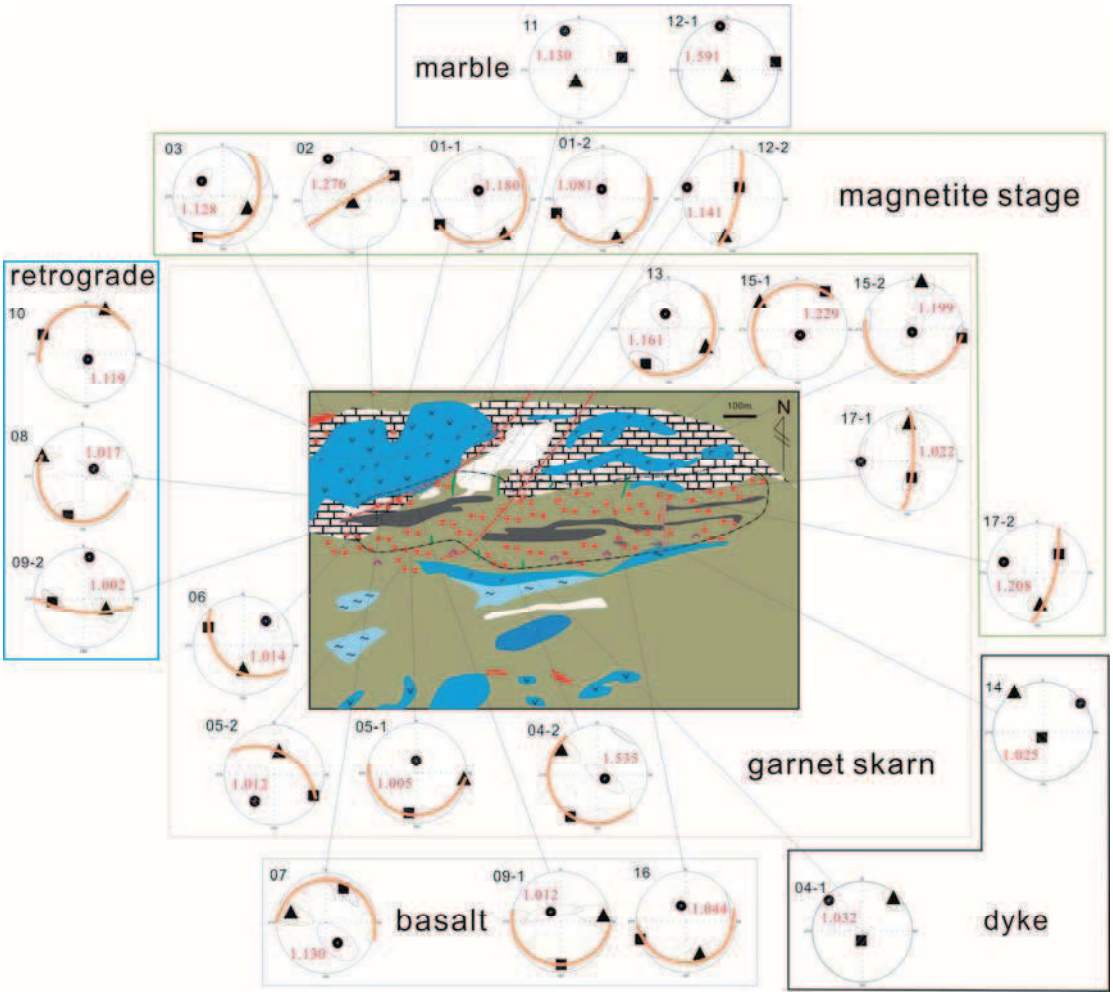

Fig. B-14: AMS results presented in lower equal-area projection stereoplot. Squares, triangle and circles stand for K_1 (magnetic lineation), K_2 and K_3 (pole of magnetic foliation), respectively. Confidence ellipses at 95% level are drawn around site-mean direction. All sites are tilt-corrected coordinates except the sites of dyke and marble. Tilt correction is based on stratification plane marked by the ripple marks in limestones (165°∠49°). P_J values are indicated in red and orange lines in stereoplots gives the magnetic foliation.

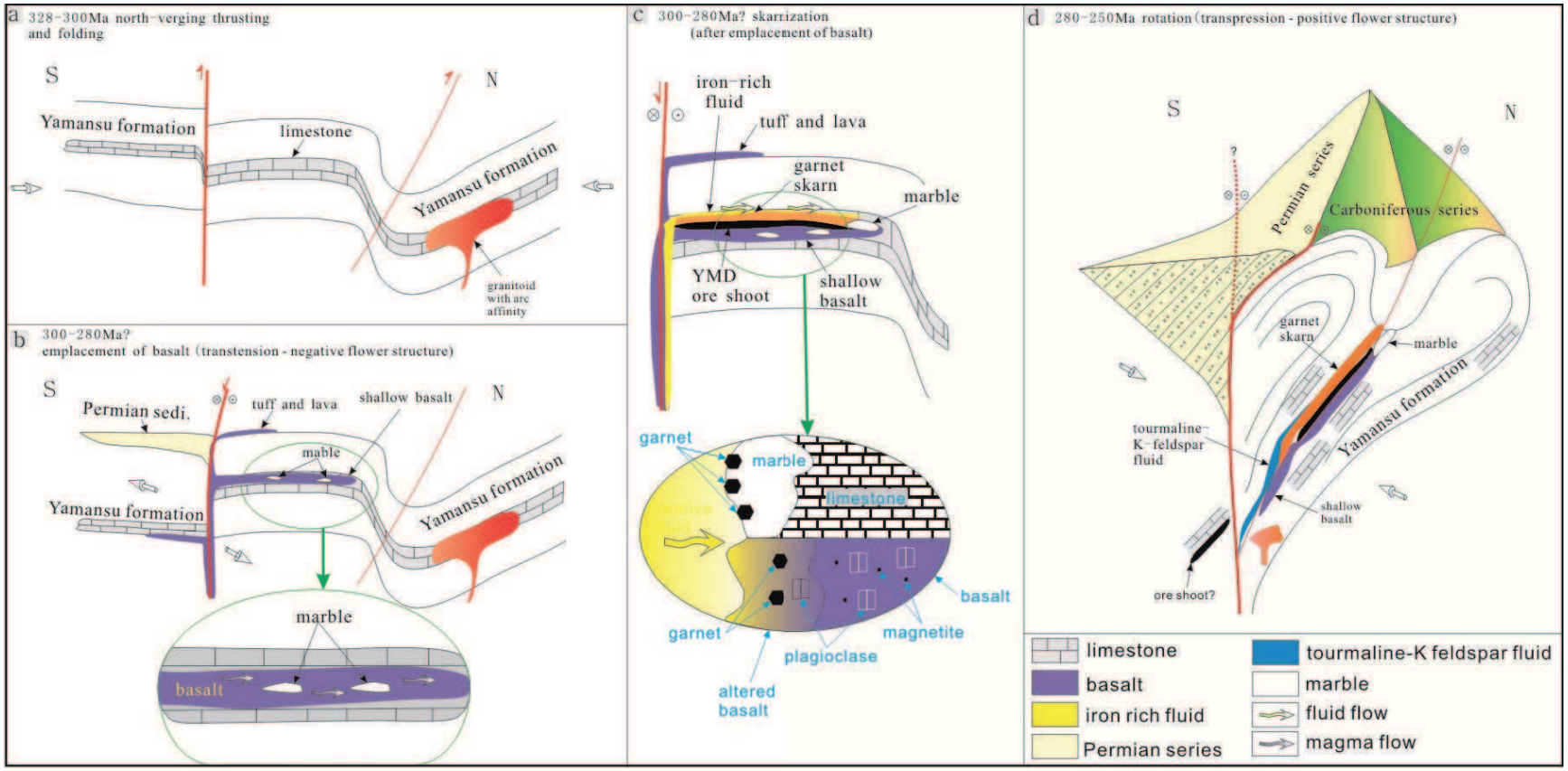

Fig. B-15: Hypothetical metallogenic model of the Yamansu iron deposit

3.7 Interpretation and discussion

3.7.1 Contribution for the massive magnetite ore shoots

When referring to massive magnetite ore shoots, the first thing should be the contribution for metals. In YMD, the iron mainly derived from two sources: the iron-rich fluid and the basalt. Iron rich fluid pumped into the basalt and limestone, which were approved directly by Fig. 3-16, Fig. 3-17, Fig. 3-18 and Fig. 3-12D. The Fig. 3-16 clearly showed that the magnetite replacement front within marbles and the advancing front yields to corrosive brecciation of marble to form garnet. A cartoon model was added (Fig. 3-34).

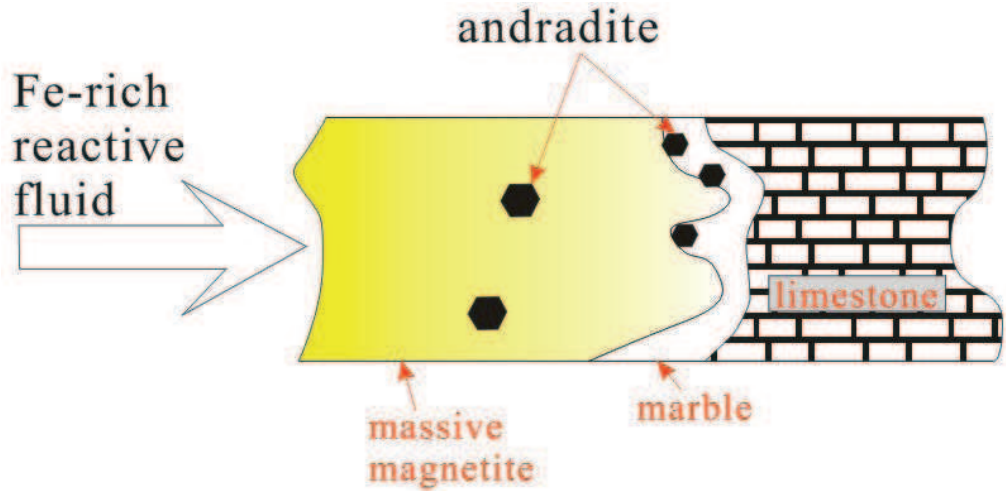

Fig. 3-34: Fe-rich reative fluid front progressively replaced the marble outlined by andradite growth. The formation of magnetite was hydrothermal.

Fragments of marble fell into the altered basalt, which were caused by magmatic stopping, indicated the basalt was probably shallowly intruded. The basalt contains magnetite (Fig. 3-11A, B and C). The basalt probably provides part of the iron for the massive magnetite ore shoots basing the following reasons:

1. Part of the basalt was change into garnet skarn (Fig. 3-11D, Fig. 3-14 and Fig. 3-15A). When the basalt was replaced into garnet skarn, iron was released;

2. This hypothesis was supported by mass balance calculation. If we assume the basalt have enough heat to product skarn when contact with limestone. The massive balance calculation result showed that the basalt did not hold enough iron to totally provide for the garnet skarn, nor the ore shoots. So, extra iron-rich fluid probably exists.

A schematic figure displayed the progressive replacement of basalt and formation of garnet, as following (Fig. 3-35):

(1) Spare andradite in the basalt beyond the reactive fluid front. In this stage, most andradite grown on the ground mass of the basalt, and it seems that the plagioclase was little altered (see section 3.4.4.1.1);

(2) Replacement of the basalt. The reacted fluid was relative rich on Fe and Al. The Al may contributed to the rim of the grandite, and the Fe may contributed to the massive magnetite ore shoots;

(3) Overgrowth of grantie-rim on andradite core.

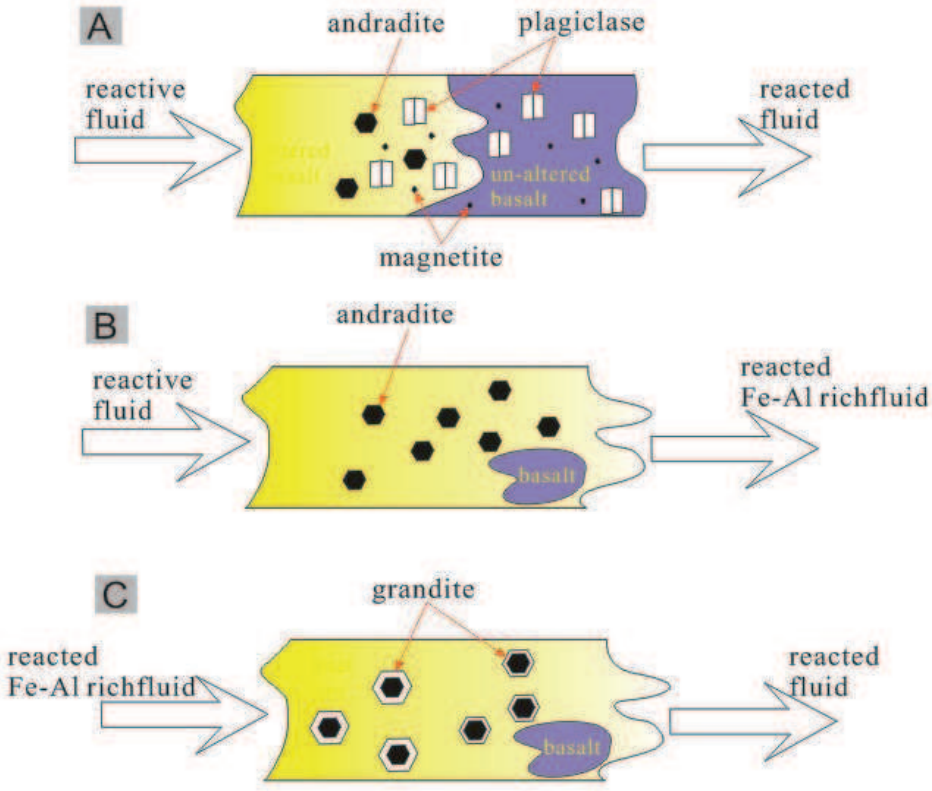

Fig. 3-35: Illustration of reaction front propagation and mineral zonation resulting from infiltration of reactive fluid. The magnetite was primary.

3.7.2 Felsic fluid contributions

The following reasons may lead to conclude that felsic fluid contributed to the skarn:

1. It was the iron-rich fluid that contributed to the formation of the ore shoots, not a granite pluton;
2. Tourmaline, axinite and K-feldspar assemblage present in the late stage of skarn, which altered the earlier skarn minerals (Fig. 3-22 and Fig. 3-24);
3. REE distribution patterns of two tourmaline-feldspar-containing samples showed irregular high content of LREE (Fig. 3-31);
4. Vein-like K-feldspar fluid injected the skarn and basalt (Fig. 3-36).

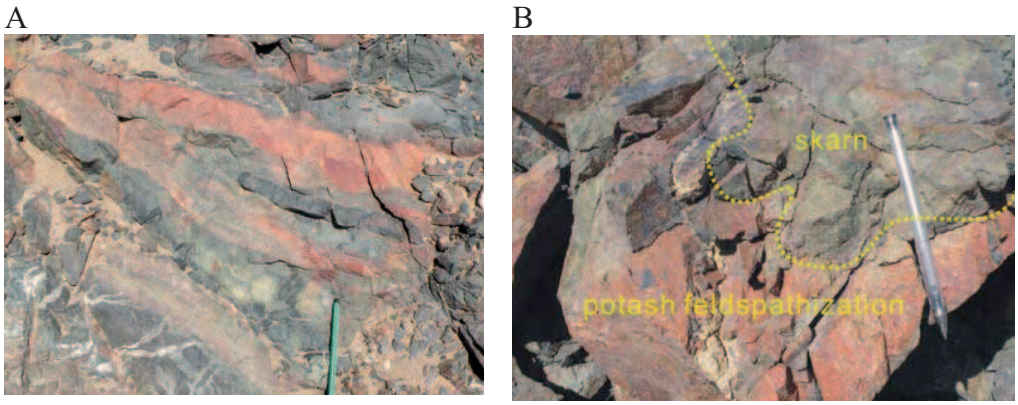

Fig. 3-36: Vein-like K-feldspar fluid injected the skarn and basalt. (A) red K-feldspar fluid injected black basalt; (B) K-feldspathization of skarn. It is noteworthy that the black phase and red phase in (A) are basalt and K-feldspar respectively.

Here, borosilicate is emphasized because it seems antipathetic in YMD. As showed above, the massive garnet skarn in YMD was caused by iron-rich fluid; significantly contrast to the felsic fluid (tourmaline-axinite-K-feldspar assemblage). Borosilicate is normally associated with granite intrusion and occurs almost exclusively in Sn±W skarn (Kwak, 1987; Meinert et al., 2005), is observed in the basalt of study target. Besides tourmaline, axinite is also observed in the YMD. As these two minerals are

rich in Boron, their associated skarns are often considered as granite related (London et al., 1996).

As to the origin of the Boron, the following analysis may provide some information. Boron is a widespread constituent of crustal rocks, being found in sedimentary, volcanic, plutonic and metamorphic environments. Boron can be considered as a quintessential crustal element (Anovitz and Grew, 1996). Some research demonstrate that the boron contents of extrusive silicic rocks are reportedly about ten times higher than in plutonic equivalents of the same gross magma type (London et al., 1996). The earth's upper continental crust contains average of 15 ppm B, whereas terrestrial sediments average about 100 ppm B, the values for pelagic marine clays are mostly 100 to 1000 ppm B (Leeman and Sisson, 1996). Tourmaline precipitation during diagenesis and burial metamorphism is common in politic assemblages and has been documented in shaly carbonates (Reynolds, 1965). Striking enrichment of pelitic and metavolcanic sequences is also seen in the formation of stratiform oceanic tourmalinites, e.g. Taylor and Slack (1984). Enrichment of evaporite sequences, especially those bearing volcanic detritus, is also seen in the production of danburite (London et al., 1996). Tourmaline concentrations in volcanic associated Cu-Co deposit are present within both felsic and mafic metavolcanic rocks (Slack, 1996). The later one is well documented in the Blackbird district of Idaho (Anderson, 1947; Lund et al., 2011).

3.7.3 Magnetite

3.7.3.1 Silicon in the magnetite

Substitution of Si in the magnetite structure has been debated for magnetite deposits, including skarns (Shiga, 1989; Westendorp et al., 1991; Shimazaki, 1998; Ciobanu and Cook, 2004). From figure 3-22, certain amount of Si occurs in the EPMA analysis result in the studied case. Based only on microprobe analyses silicon in

magnetite has been interpreted as substitution for Fe^{3+} in 4-fold coordination site by Westendorp et al. (1991). In another study of Si in magnetite, involving microprobe analyses and TEM observations, Newberry et al. (1982), conclude that Si in magnetite could be present as: (i) a $FeSiO_4$ component of a solid solution with magnetite, (ii) very small silicates inclusions and (iii) "unusual Si-rich domains of uncertain origin". Whatever the status of silicon in magnetite, the SiO_2 content in this mineral could be used as a criteria to discriminate magnetite of different origin (Dupuis and Beaudoin, 2011).

Magnetite from Fe-Cu skarn deposit of the Kamaishi mine, Iwate Prefecture, northeastern Japan contain up to 6.19 wt% SiO_2 (Shiga, 1989). The reported SiO_2 contents in magnetite are found only in hydrothermal environments, and it is suggested that fluid rich forming environments seem to be responsible for their formation.

3.7.3.2 Phosphorus content

Magnetite in Yamansu deposit occured in massive form which was similar to Kiruna-type deposits. As mentioned in the chapter 1, the definition of Kiruna type deposits is loose, but characterized by low-Ti, massive magnetite, and apatite rich (Romer et al., 1994; Borrok et al., 1998). Kiruna type deposits occur in many tectonic environment of the world. The ores are dominantly composed by magnetite, apatite, actinolite. The size of Kiruna-type deposits are various, from small dykes to hundred millions of tons of high-grade ore (Nystroem and Henriquez, 1994). The prevail opinion for its origin is magmatic (Weidner, 1982; Nystroem and Henriquez, 1995). In the studied case, P content has been also analysed, but their contents are under detectable limit of the microprobe. Yamansu deposit holds very low content of phosphorus in all the associated lithologies (see part 3.5). Chemically, Yamansu deposit is not a Kiruna-type.

3.7.3.3 Intercalated magnetite and garnet

Rhythmic banded garnet layer and magnetite layers were observed (Fig. 3-15B). With the rhythmic sequences, they commonly have thickness in the order of centimetre. Band boundaries could be ragged. This banded magnetite, intercalating garnet layers, is observed near the massive ore shoots. It seems that the intercalated band of garnet and magnetite was caused by rhythmic or fluctuant progress of the iron-rich fluid front (Fig. 3-16).

This banded texture of the magnetite and garnet is emphasized here. Banded structure could occur in a diverse geological environments and may consist of different mineral assemblages (Krug et al., 1996). This banded structure is also known as Liesegang phenomena. Using diffusion sources in gels, Liesegang (1913, recited from Krug et al. 1996) obtained bands and rings of precipitates. His experiments proved that rhythmic patterns could spontaneously develop in gels, without an inherited background, i.e., via self-organisation. Basing on modelling study, Jamtveit proposed similar conclusion for the chaotic zonation patterns in skarn garnets (Jamtveit, 1991). This banded structure is also interpreted by heritage structure (Cheilletz and Giuliani, 1988).

3.7.4 Constriction on the skarn forming time

The Yamansu limestone was deposited in early Carboniferous which is probably the earliest protolith related to the skarn in the Yamansu ore field. And then is the arkose which contained three group of age basing on U-Pb detrital zircons. The youngest group was dated to be about 312Ma. Direct proof, for the basalt later than the limestone, is that clasts of marble within strongly altered basalt (Fig. 3-13). The skarn altered the basalt indicating later forming. The N-S dykes, which associated with shearing, cut all the lithology mentioned above (Fig. 3-3; Fig. 3-5, and Fig. 3-11). In the end, tourmaline-K-feldspar fluid altered the earlier skarn minerals

which was dated to be about 250Ma by Ar-Ar K-feldspar dating. It indicated felsic magma fluid affection. Constrictions from paleomagnetic and AMS data showed the skarn, ore shoots and basalt were rotated by later tectonic event. So, a paragenesis could be followed (Fig. 3-37):

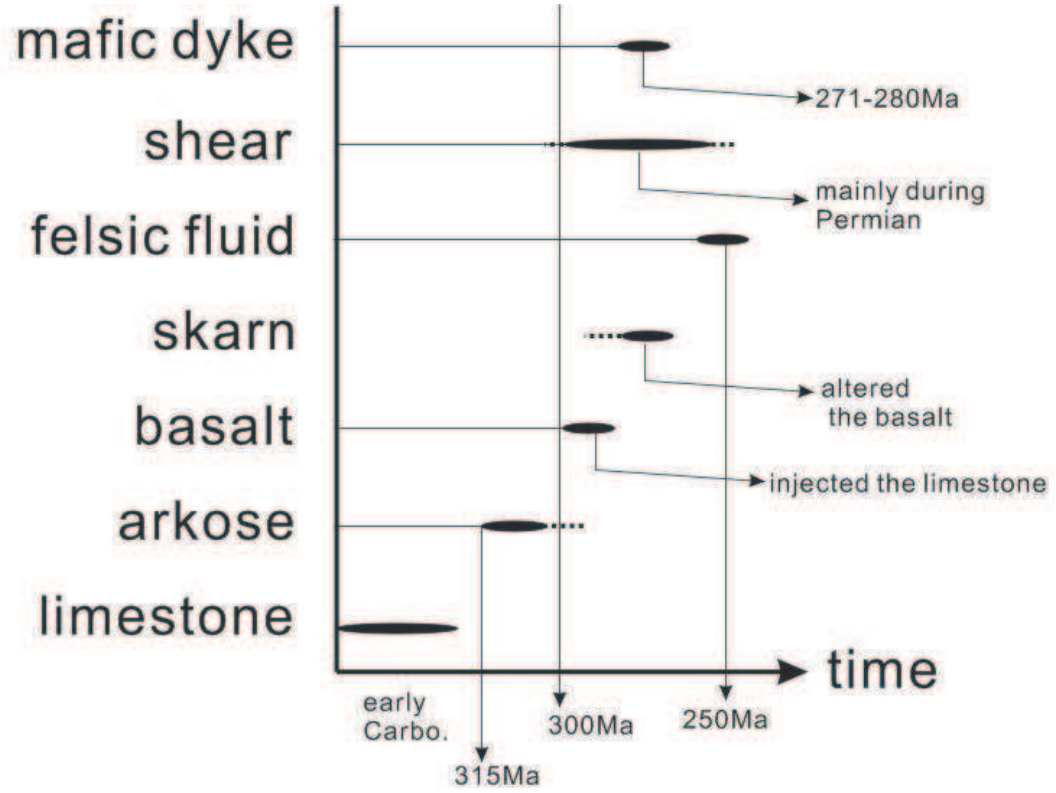

Fig. 3-37: Proposed paragenesis sequence. Note: limestone was early Carboniferous by fossils; detrital zircon in arkose displayed three group, the youngest group was dated to be 312Ma by U-Pb; fragement of marble in the basalt indicated the basalt was later then the limestone; skarn altered the basalt; felsic fluid (tourmaline-axinite-K-feldspar) altered the earlier skarn minerals and Ar-Ar K-feldspar dating showed 250Ma; shearing and mafic dykes were mainly Permian (Li et al., 2006).

3.7.5 Skarn forming model

Whether there is a causal relationship between the basalt and skarn is not clear, after all, the heat of basalt is very limited. However fragments of marble fell into the altered basalt caused by magmatic stopping suggest the basalt was hot when intruding into the limestone. Studies of drill cores from the Pasos Blancos area at El

Laco in the central Andes, northern Chile, give evidence of an intense and extensive subvolcanic contact-metasomatic process which contributed to the formation of iron ore bodies (Naranjo et al., 2010). This contact-metasomatic process resulted from shallow-level emplacement of very volatile-rich iron-oxide magma. However, in YMD, the basalt was probably accompanied by iron-rich fluid during its emplacement which correspond to the massive garnet skarnization. This hypothesis has been supported by mass balance result (see 3.5.3) and petrological observation (Fig. 3-16, Fig. 3-17 and Fig. 3-18). This magmatic stoping also suggested that the intrusion of the basalt would be later than some researcher thought (Ding, 1990; Lu et al., 1995; Wang, 2005). A proposed genetic model is given as following sequence (Fig. 3-33):

1. North-verging thrusting and folding stage. However, in Yamansu area, the limestone was little deformed basing on morphology of ripple plane. This stage was commonly recognized (Wang et al., 2010; Charvet et al., 2011) and was companied by calc-alkaline magmatism (Wu et al., 2006). Coevally, granitoid with arc affinity (Wu et al. 2006, 2011) presented and some of the caused metasomatism expressed by garnet-bearing skarn (Wu et al. 2011);
2. Emplacement of basalt. The basalt injected, probably along a pre-existing fault; Part of the basalt erupted to the surface, and part of them horizontally injected into the limestone layer where clasts of limestone were observed;
3. Iron fluid injected and caused extensive skarnization. Part of the basalt was altered into skarn and contributed to the massive magnetite ore shoots formation. The circulation of CO_2 probably enforced the metasomatism;
4. Rotation and felsic fluid contribution.

3.8 Conclusion

Through the above analysis, the conclusions are following:

1. YMD is not VMS, but the result of skarnization;

2. Contributions for the massive magnetite ore shoots derived from two parts: basalt and iron-rich fluid;
3. The prograde stage is dominated by garnet, with minor amount of pyroxene. The complex zoned garnet suggested three stage of its formation. According to the zonation of garnet, the fO_2 was getting lower and lower from the core to the border. Transferring from andradite to grandite, magnetite was deposited because of lacking silicon and/or fO_2 was not suitable. Whereas the whole skarnization process, fO_2 was fluctuant; the chlorite formed at about 280°C in the retrograde stage.
4. Detrital zircon in the arkose displayed three groups: Precambrian group; early Paleozoic group (441Ma); and the late Paleozoic group (312Ma). The youngest group gave the lower limit of its deposition;
5. Felsic fluid (tourmaline-axinite-K-feldspar) contributed to the later alteration, which was dated to be about 246Ma by Ar-Ar method;
6. Paleomagnetism and AMS data suggest that the basalt intruded initially into limestone horizontally, coincidentally, the skarn was formed horizontally too, as well as the ore bodies.

Chapter 4 Iron oxide-rich melt separation from mafic magma: the case study from Cihai skarn-related magnetite deposit, Eastern Tianshan, NW China

Project of article

Résumé:

Des concentrations économiques d'oxydes de fer, associées à des skarns, exprimées sous la forme d'amas massifs ou de lentilles sont connues dans le Tianshan oriental. Ces concentrations sont localisées dans les parties périphériques de grandes intrusions mafiques ou ultramafiques. Le gisement de Cihai est une de ces concentrations.

A Cihai, le minerai se présente sous la forme de filons composés de magnétite massive. Au microscope, des exsolutions de spinelle et d'ilménite apparaissent dans la partie interne des grains de magnétite, suggérant une origine magmatique pour ce type de corps minéralisé. Une comparaison entre les compositions chimiques des magnétites de Cihai et de Yamansu de skarn-type, montre que les premières sont plus riches en Al et Ti et plus pauvres en Si.

Une cartographie du gisement a permis de reconnaître cinq faciès: des skarns, les filons à magnétite massive, des métapélites, des dykes et un faciès noir. Ce faciès particulier apparaît noir en lumière transmise, polarisée et polarisée analysée, mais ne correspond pas à des phases métalliques. Les analyses chimiques ponctuelles et Raman ont montré que ce faciès est constitué d'albite, de pyroxène et de titanite. Les pyroxènes apparaissent corrodés par l'albite. L'ensemble de ces observations plaident en faveur d'une origine magmatique du faciès noir. Par ailleurs, du carbone a été détecté dans ce faciès lors des études au MEB et Raman. Le skarn est composé de magnétite, de pyroxène et de grenat. De nombreux clasts de skarn ont été observés tant dans les filons de magnétite massive que dans le faciès noir. Un modèle génétique est proposé dans lequel le faciès noir et la magnétite massive dériverait d'un même magma, la séparation entre ces deux phases étant probablement facilitée par l'introduction de CO_2.

Abstract:

Economic concentrations of Fe oxides, associated with skarn, occur as massive ore shoots and lenses in the peripheral part of a large mafic-ultramafic intrusions, Eastern Tianshan NW China. Cihai magnetite deposit is one of them. The Fe oxides are mostly magnetite with spinel and ilmenite exsolution in the inner part of grains indicating magmatic origin. Mapping was executed in Cihai magnetite deposit, and showed that it was mainly composed by five phases: skarn, massive magnetite ore shoots, metapelite and dyke swarm, as well as an original black phase. The black phase was light-tight and displayed isotropic comportment in transmitted light. Mineralogical chemistry and Raman studies showed that this black phase is composed by albite, pyroxene and titanite indicating magmatic, of which the pyroxene was corroded by albite. Skarn was dominated by magnetite, garnet and pyroxene. Numerous of skarn clasts are enclosed in the massive magnetite ore shoots and the black phase. Carbon was found in this black phase basing on SEM and Raman study. Geochemical data showed that the black phase and mafic-ultramafic rocks probably evolved from the same magma chamber and the black phase was assimilated. The high temperature iron oxide and black phase separation from magma silicates was thought to be related to introduction of CO_2-rich fluid occurring in the peripheral part of magma chamber.

Keywords iron oxide · skarn-related deposit · exsolution · melt immiscibility · assimilation · Tianshan · Beishan

Introduction

Magmatic Fe-Ti oxide ores are commonly ascribed to sorting of Fe oxide crystals from mafic magmas (Duchesne, 1999; Charlier et al., 2006; Pang et al., 2008) or accumulation of oxide melts that resulted from immiscible separation in mafic magmas (Lister, 1966; Kolker, 1982; Von Gruenewaldt, 1993). They mostly associated with mafic/ultramafic intrusions and, the magnetite grains, generally contain spinel-ilmenite exsolution and display curved boundaries against coexisting silicate minerals, such as the magnetite in Panzhihua (Pang *et al.*, 2008) and Bushveld (Von Gruenewaldt, 1993). However, magmatic magnetite ores associated with skarn-related iron deposits are not reported in the international literature.

Skarn is a metasomatic rock type (Liang, 2000; Zharikov and Zaraisky, 2003) defined by characterized mineral assemblage which dominated by calc-silicate minerals, such as garnet and Ca-rich pyroxene (Einaudi et al., 1981; Meinert et al., 2005). It mostly develops at the contact between magma bodies and carbonate wall rocks and in metamorphic environments. Liang (2000) conducted more than 6000 experiments on skarn formation and concluded that skarn could be formed in a variety of environment, including carbonate assimilation within magmas. Liang's result was confirmed by Iacono Marziano et al. (2008) who conducted an experimental study of limestone assimilation by hydrated basaltic magmas in the range 1050–1150°C, 0.1–500 MPa and the result showed that assimilation could lead to strongly silica-undersaturated melt which probably related to skarn formation. Melt and multiphase inclusions in skarn minerals with highly variable volume ratios have been considered as strong evidence for magma immiscibility (Zhang and Ling, 1993; Fulignati et al., 2001; Zhao et al., 2003). CO_2 has low solubility in the melt, and thus carbonate assimilation would cause three-phase (solid-melt-gas) process (Wenzel *et al.*, 2002). Some study demonstrate that a 'skarn

environment' can act as a source of CaO-rich silicate melts, and that the assimilation of these melts into the primitive magma is the main process responsible for magma contamination, rather than the direct ingestion of solid carbonate wall-rocks (Gaeta *et al.*, 2009). Moreover, changes in the chemical composition of magmas through assimilation of carbonated (formation of CaO-rich silicate melts and CO_2-rich fluid), is probably responsible for deposition of large economic Fe-Ti oxides ore (Ganino *et al.*, 2008).

The Cihai ore field, which includes three similar magnetite deposits (Cihai, Cinan and Cixi deposits) at the peripheral part of large mafic-ultramafic intrusion (Fig. C-1b), provides excellent examples for studying the interactions between carbonate assimilation in mafic magmas and skarn-related iron ore deposition. Indeed, at Cihai mine, the relative simply skarn mineral assemblage, the high temperature magnetite and the signature of sediment assimilation constitute optimal conditions to depict those interactions. Therefore, we emphasis on the biggest one: the Cihai magnetite deposit which is also the single one exploited in open pit.

The Cihai magnetite deposit (CMD): geological background and previous studies

The Cihai magnetite deposit (CMD) is located in the NEE-SWW trending Beishan orogenic segment of the Tianshan Mountains, North-Western China (Fig. C-1a). The Beishan orogenic segment is constituted by arcs and ophiolitic mélanges (early Paleozoic 462-412Ma by Guo et al., 2006) which were thrusted and overprinted by strike-slip faulting during Permian-Triassic times (Xiao *et al.*, 2010). The Beishan orogenic segment is thought to be a rift in Permian (Zuo and He, 1990; Zuo et al., 2003; Liu et al., 2006; Pirajno, 2010; Xiao et al., 2010). Permian molasse (Charvet et al., 2007) and bimodal series rocks about 280Ma (Su et al., 2011) are probably the main reasons leading to the rift affinity. It is nipped between Middle Tianshan

terrain to the North and Tarim craton to the South. The Beishan orogenic segment is one of the most important Ni-Cu-Fe and Au exploring district in China because more than 6 middle to large ore deposits have been found (Hu, 2007; Cheng et al., 2008) (Fig. C-1a).

The CMD is situated in a remote gobi-like area which was covered by 2 to 5m thick Quaternary sand. The discovery of CMD was due to the characterization of a strong magnetic anomaly (Fig. C-2c). In the ore field, host rocks are composed of Precambrian metasediments which outcrop in sparse localities (clastics and carbonates). The CMD contains a reserve of 23 Mt with an average grade of 45.7% Fe, and, according to geological report of the Baosteel Company, a certain amount of Co is present in the ore (Yu et al., 1999). The ore is mainly composed of massive magnetite. 73 lenticular ore bodies are recognized in the open pit. The biggest ore shoot is 535m long and 8.12 m thick. Most of them are 4.5 m thick (Fig. C- 2a, b).

At the earliest time, a skarn model was proposed for this deposit, mainly based on (1) the pyroxene-garnet assemblage which was altered by later hydrothermal minerals; (2) mafic intrusions and sediment rocks occurred in the mine, though directly contact between the two was not observed (Li, 1983). In recent years, multi-genesis model (subvolcanic - hydrothermal - alteration type or magma - differentiation - hydrothermal - alteration type) has become prevailing (Xue et al., 2000; Zuo et al., 2003; Wang et al., 2006; Tang et al., 2010), because (1) mistook the lithology of the direct ore wall rock; (2) geochemical study supported a magma differentiation process (Tang et al. 2010) which seems very farfetch to support the metallogeny; (3) Xue et al. (1999, 2000) explicitly indicated that the garnet-diopside assemblage is not in the domain of traditional skarn, and ascribed the garnet-diopside assemblage to a late subvolcanic altered stage. Liang (1991, 2000) conducted an metasomatic experimental study to simulated iron oxide concentration in CMD, and show that the garnet-diopside assemblage formed at 420-700°C and (270-700)*0.1MPa. He concluded that CMD was a skarn-type deposit (Liang and Qiao, 1991; Liang, 2000).

Mao et al. (2005) and Liang (1991, 2000) questioned this multi-genesis model and prefer to a skarn related model, because mainly drives on the "garnet-pyroxene-magnetite" mineral assemblage and a following hydrothermal alteration.

Xue et al. (2000) gave an Rb-Sr age of 268±7 Ma on the so-called ore wall rock "diabase". A similar single mineral K-Ar age of 260.3Ma was obtained on amphibole from the Cihai open pit (Zhang *et al.*, 1980), however the error was not given out and this age seems not quite reliable. These ages coincides with the large scale regional strike-slip deformation (Shu et al., 1999; Laurent-Charvet et al., 2002; Chen et al., 2005; Wang et al., 2009; Wang et al., 2010), as well as the large scale volcanic eruption (LIP) which may extend over an area of 250000km^2 (Jia, 1997; Chen et al., 2006; Zhou et al., 2009; Zhang et al., 2010) and the Permian A-type magmatism reported through the eastern Tianshan (Pirajno et al., 2008; Pirajno, 2010).

Lithology and petrology

All these metallogenic models are lacking of detailed lithological and petrological constraints. This part attends to fill this gap. Field (20 days) and petrography works allow us to investigate precisely lithologies and establish a new a new map of the open pit (Fig. C-2). The open pit provides excellent exposures which are lacking in the surrounding countryside covered by Quaternary sands. Particular attention was paid to the contact between the various lithologies and ore shoots.

The CMD presents five different rock types and lithologies: skarn, massive magnetite ores, metapelites, a mafic dyke swarm, and a cryptocrystalline black phase (Fig. C-2a and 2b).

From a broad point of view, the deposit is composed of skarns and metapelites crosscut by E-W-trending southward-dipping magnetite lentoid ore bodies and a sub-parallel mafic dyke swarm (Fig. C-3a). At some place, a late brittle deformation event associated with conjugate thrusting is responsible for a complicated spatial distribution of theses lithologies (Fig. C-3b). Crosscutting relationships between mafic dykes and ore bodies clearly indicate that mafic dykes postdate the ore formation (Fig. C-3c). It is noteworthy that no sedimentary carbonated rocks outcrop within the open pit, even though they are reported around the Cihai area.

Skarn

The maps elaborated during this study shows that the main part of host rocks within the CMD is constituted by skarns. This constitutes an important point, not recognized in previous studies (e.g. Tang et al. 2010). Skarns could be subdivided into two groups according to the proportion of garnet and pyroxene: pyroxene-rich skarn and garnet-pyroxene skarn.

(1) Pyroxene-rich skarn

This skarn contains about 90% pyroxene without garnet (Fig. C-4b, c). Recognizing this lithology is of major importance for metallogenic purposes because it is the main wall rock of ore shoots. This skarn is composed by pyroxene with small amount of apatite (about 5%) and magnetite (Fig. C-5a), however, sometimes, sparse garnet grains were observed in this lithology. The rocks present a typical granoblastic texture of metasomatic replacement and thus cannot be misinterpreted as a magmatic crystallized texture. Preview studies probably under estimated the proportion of pyroxene-rich skarn or confused it with mafic magmatic rocks (see our re-interpretation on Fig. C-1a). Contrary to the magmatic mafic rocks from dyke swarm, the pyroxene-rich skarn did not include plagioclase.

(2) Garnet-pyroxene skarn

This skarn is composed by garnet (about 40%), pyroxene (about 40%) and magnetite, with small amount of calcite (Fig. C-4a and 5b). They are brown to pale green coloured depending on the garnet/pyroxene ratio. This skarn commonly contain coarse grained garnets (10 mm max), small grained pyroxene and magnetite. Only small surface exposures of garnet-rich skarn were observed in the open pit. Nevertheless, according to the geological report of the Baosteel mining Company, this type of skarn is reported in drill cores.

(3) Late alteration

Late alteration is characterized by hydrous minerals (mainly amphibole and calcite), stockwork and sulphides. It seems that the paragenesis of these late alterations is quite close.

The late retrograde stage alteration is dominated by hydrous minerals, such as amphibole, biotite and chlorite, with small amount of epidote. Sulphides and big-size grained calcite were observed in this stage. Amphibole-biotite alteration is very common in the CMD, and is often associated with calcite in the retrograde stage (Figs.C-4b; C-5b, C-5c). It is characterised by coarse grained idiomorphic amphibole and calcite which seems adhere to fractures (Fig. C-4b). Chlorite altered almost earlier minerals and particularly garnets.

The prograde skarn is also affected by a stockwork. It is characterized by numerous small fractures, mainly filled with quartz and calcite. These fractures range from millimetre to centimetres in thickness. Two generations of vein could be distinguished (Fig. C-4c): i) a first generation of veins (vein 1), composed of calcite and euhedral coarse grains of quartz; ii) a second generation of reddish brown vein (vein 2) filled with rhombs of calcite, quartz and titanite. Within the vein 2, calcite pre-dates the quartz; and sparse iron oxides are intercalated between calcite crystals.

Calcite grains in vein 2 crystallized preferentially perpendicular to the walls of the vein. Their width increase from the wall to the centre part of the vein, suggesting a syntaxial filling. The vein 2 can also occur sporadically in mineralized bodies in the form of small patches or pockets. The rocks cut by the vein 1 and vein 2 include pyroxene-rich skarn, garnet-pyroxene skarn, metapelite, ore and the black phase.

In the CMD, observed sulphides are pyrite, chalcopyrite, marcasite, sphalerite and arsenopyrite. All the sulphides are found within fractures, cross cutting the skarn, ore shoots and black phase, indicating their later formation. The proportion of sphalerite and arsenopyrite among the others was very low. Sphalerite with micro-veinlets of pyrite occurs (Fig. C-6a) and pyrrhotite altered into "bird's eyes" structure and colloform pyrite was observed (Fig. C-6b). These structures suggest a low forming temperature during the sulphide stage. It seems that the sulphide stage was a little early than the stockwork because some sulphide was found in the breccias caused by stockwork (Fig. C-4c).

The metapelites

Metasedimentary formations exposed in this area are Sinian (Precambrian) and Cambrian in age for protoliths and are mainly composed of mica-quartz pelites, amphibole-bearing pelite, marbles and metadolostones. The metapelites in the CMD may derive from these formations. In those metapelites, minor amount of small pyroxenes were observed which suggest sedimentary transitional terms or alteration between pelites and carbonated rocks. Metapelites in the open pit contains a more diverse, siliceous metamorphic assemblage, suggesting either a shaley/pelite protolith or the introduction of silicon and other elements such as aluminium, iron, titanium or potassium, during metasomatism. The proportion of silicate minerals is highly variable in the metapelite: some samples contain up to 40% of minerals such as small grain pyroxene even though they are small size. Wollastonite was identified in this rock, but the most abundant silicate mineral is diopside whose percentage in

some cases exceeds others. Many of the meta-sedimentary rocks found in drill cores are banded (Fig. C-4d) at a centimetre scale, the banding being defined by variations in grain size or in the proportions of silicate minerals. The white stripes are mainly composed of calcite and quartz, and the dark stripes contain up to 80% of small (0.2 mm), euhedral grains of biotite. Minor opaque phases, such as pyrite and magnetite, are also present. The form and geometry of the concentric banding strongly resembles that described in sedimentary formation intruded by mafic dykes in this region by Wang and Li (1982).

The mafic dyke swarm

Mafic dyke swarm is high lighted here because it is very easy to confuse with pyroxene-rich skarn. Mafic dyke swarm is not the direct wall rocks of the ore shoots but cut them (Fig. C-3a and C-3c). According to microscopical observations, mafic dykes are composed by plagioclase, pyroxene and titanite with minor amphibole and biotite (Fig. C-5d). They are diabase in lithology which is very similar to that described by Tang et al. (2010).

Ore shoots

In the CMD open pit, it was very easy to recognize the ores because they were in black with higher density while the others were in green or pale green, or grey with less density. The ores mostly display a massive texture and occur in lens. The mineralization can also display disseminated or brecciated texture. Ore minerals are mainly magnetite, with small amount of hematite, ilmenite, pyrrhotite, pyrite, chalcopyrite, tetrahedrite and minor azurite. Most magnetite was subhedral or euhedral. However, ores can be distinguished into two types. In the first one, magnetite is companied by pyroxene and apatite (Fig. C-4e and Fig. C-6e), without garnet; in the second one, the ores include some garnet skarn clasts (Fig. C-4f).

The "black phase" in CMD

Black mushy cryptocrystalline phase, possibly relate to the ore formation in the CMD, has been recognized. There are no descriptions of this phase in previous studies. It looks like magnetite but is much less dense. In addition, like magnetite ore, this black phase includes rounded skarn clasts (Fig. C-4g). At some place, this black phase seems to "inject" the skarn following "fracture", with obvious replacement texture rather than open-space filling (Fig. C-4h).

At optical microscopy, it appears black and shows no interference color in transmitted both in plane or crossed polarized light (Fig. C-5e and C-5f). In reflected light, grey and low reflection minerals (pyroxene and small amount of titanite) were observed (Fig. C-4h, C-5g) and confirmed by EPMA and SEM. In this black phase, pyroxenes were altered (Fig. C-5g). The boundaries between the pyroxene and albite are golf curved (Fig. C-5h). In addition, SEM results also indicate prehnite. Moreover, between pyroxenes and titanites, the black and less reflected matrix presents a pure albite composition with electronic microprobe (Table C-5).

In order to distinguish whether the matrix with albite composition is a glassy or a crystallized meterial, Raman spectrometry has been carried out (Ramans spectrometer WITec Alpha500 RA, Centre de Biophysique Moleculaire, CNRS, Orléans, France). This Raman acquisition system allows large and fine scale compositional mapping (from a tens of micrometers to up than 10 cm) with a submicrometric resolution. It is an in-situ technique. The Raman spectrums explicitly indicate that they are crystalline albite (Fig. C-7a). In addition, from the Raman spectrum of the black matrix, we can see that, around the position 1587, there is a peak of C-C bond adding to the albite spectrogram (Fig. C-7a). SEM study was also executed on a Hitachi 4500 (Centre de Microscopie Electronique, Orleans University, France). This machine allows analysing light elements, such as carbon, with or without being metalized. The samples were metalization. The energy

spectrums show that there is carbon peak adding to the peaks of elements belonging to the albite one (Fig. C-7b), of which the samples are being metalized with gold. The existence of carbon micro-phase, probably, leads to its special optical characters.

Mineral texture and chemistry

Fig. C-8 illustrates a paragenetic sequence for the mineral assemblages and ore within the CMD. Mineral composition analyses were performed in the following conditions with an electron microprobe CAMECA SX50 using the PAP correction. Si, Al, Ti, Fe, Mn, Mg, Ca, K, Na, P, F and Cl have been analysed in garnet, pyroxene, albite and chlorite, 20 kV accelerating voltage, 15nA sample current and different counting time according to the analysed elements (10s for Si, Al, Ti, Fe, Mn, Mg, Ca, K, Na; 20s for P, F, and Cl). Si, Al, Ti, Fe, Mn, Mg, Ca, V, Cr, Ba, P, Zn, Ge, Ga and Co have been analysed in magnetite with 15kV accelerating voltage, 15nA sample current using the PAP correction and in 20s counting time. Analyses were performed in the common laboratory of BRGM-CNRS-University Orleans France. All Fe in the analyses is expressed as Fe^{2+}. Only the analyses significant at a threshold of 5% have been considered.

Pyroxene

Pyroxenes are calc rich which occur in the pyroxene-rich skarn, garnet-pyroxene skarn, black phase, massive ore shoots and mafic dyke swarm. The pyroxenes in the black phase are probably clasts of skarn because they are altered (Fig. C-5e, C-5f, C-5g and C-5h) and brecciated (Fig. C-4h). Clasts of garnet-pyroxene skarn in the black phase are observed (Fig. C-4g). The pyroxene in the massive ore shoots (Fig. C-4e) seems also to be clasts of skarn because magnetite grains are embedded in the pyroxene grains (Fig. C-6e). This texture also indicated the magnetite was later than the pyroxene. There are some features that could help to distinguish them (Table

C-1).

	pyroxene - rich skarn	garnet - pyroxene skarn	black phase	massive ore shoots	mafic dyke swarm
mineral assemblage	pyroxene, minor magnetite and apatite	pyroxene, garnet, magnetite	albite, pyroxene, titanite, pyrite, prehnite, amphibole	pyroxene, magnetite, apatite	pyroxene, plagioclase, sphene, minor apatite
size, shape and occurrence	small size, about 20μm; round; clustered; clear crystal boundary. granoblastic texture.	small size, about 20μm; round; clustered; clear crystal boundary; associated with garnet; granoblastic texture.	5μm-200μm, round; corrosion gulf; occur as clasts; they did not have clear boundary; from a broad view, pyroxene was most altered in the border.	5-50μm, sometimes embedded in the magnetite grains; corrosion gulf	about 50-100μm; angular, strip, platy; occur between the plagioclase. clear crystal boundary.

Table C-1: Pyroxenes incounted in different lithologies.

According to their chemical composition (Table C-2), it seems that the pyroxene in the black phase is somehow beyond the domain of pyroxene (Fig. C-9a and C-9b) because of too much calcium. Fe and Mg display linearly negative relation in pyroxene-rich skarn and garnet-pyroxene skarn (Fig. C-9b).

Garnet

Within the prograde garnet-pyroxene skarn, garnet content ranges from 40% to 70%. Garnets are mostly light brown colour. The grain size is highly variable, the largest one reaching 1.5 cm. They are euhedral (dodecahedron) or subhedral. Some garnets form aggregates and others are scattered. Garnets are altered by amphibole, biotite and chlorite during retrograde stage (Fig. C-5b). Garnets present intermediate composition between andradite and grossular (Table C-3 and Fig. C-9c). These features are characteristic of the iron skarn deposits as defined by Meinert (1992).

Magnetite

Magnetite is the constitutive mineral of massive ore bodies, and occurs also disseminated within the skarns. Magnetite frequently shows spinel-ilmenite exsolution, which mainly develop in the inner part of the magnetite grains, and displays curved boundaries against coexisting silicate minerals (Figs. C-6c, d), either in the pyroxene-rich skarn or in the garnet-pyroxene skarn. Some pyroxene grains are embedded in the magnetite with exsolutions and associated with apatite (Fig. C-6e). In the massive magnetite ores, magnetite grain boundaries meet generally at distinct triple junctions with ~120° interfacial angles (Fig. C-6f).

EPMA was carried out on magnetite. Co was reported in CMD, but in our study, the Co contain in the massive magnetite is out of detection limit of EPMA. Data were listed in Table C-4. The structural formulae are calculated on the basis of 4 oxygen (equivalent to 8 electrovalency), $Fe^{3+} = 8 - Si^{4+} - Fe^{2+}(total) - Ca^{2+} - Al^{3+} - Mn^{2+} - Ti^{4+} - Mg^{2+}$; $Fe^{2+} = Fe(total) - Fe^{3+}$. From the EPMA results, we can see that the magnetites are relative rich on Al, depleted on Si and Ti (Fig. C-10).

Albite within black phase

As described above, the black phase is mainly composed by albite (see Table C-5) and pyroxene clasts with minor amount of pyrite, titanite and apatite. Sometimes, the SEM spectre and EPMA result display certain K content probably caused by amphibole alteration.

Chlorite

Chlorite occurred in the late hydrothermal stage. In order to perform geothermometry calculation, composition of chlorite was analyzed (Table C-6).

Geothermobarometry

A literature survey and an analysis of published chemical data on assemblages containing coexisting garnet-clinopyroxene show that the calculated temperature results largely depend on the distribution coefficient K_D. But, in the studied case, it seems not suitable employing the garnet-clinopyroxene Fe^{2+}–Mg geothermometer (Saxena, 1979; Krogh, 1988), because of little content of Mg and too much Fe^{3+} in the garnet.

As mentioned above, the magnetite contains ilmenite and spinelle exsolution which could provide a temperature indicator. Numerous attempts have been made to model the exchange and oxidation reactions between magnetite$_{(ss)}$ and ilmenite$_{(ss)}$ (Powell and Powell, 1977; Spencer and Lindsley, 1981). Wu and Mason (1981) and Trestman-Matts et al. (1983) have shown that the octahedral valence ratio (Fe^{2+}/Fe^{3+}) for magnetite$_{(ss)}$ varies with temperature and composition (Wu and Mason, 1981; Trestman-Matts et al., 1983). An internally consistent solution model for magnetite$_{(ss)}$-ilmenite$_{(ss)}$ has been proposed via using linear programming (Andersen and Lindsley, 1988). They suggested that if Fe^{2+}, Fe^{3+} and Mn in ilmenite and ulvospinel component in magnetite are known in coexisting magnetite-ilmenite assemblage, the temperature could be calculated. But, in the studied case, the ilmenite exsolution in magnetite crystal is very small, ranging from 3 μm to less than 1μm. It seems difficult to analyse within EPMA. Combined with spinel exsolution in the magnetite, it probably could give constriction on their forming temperature.

According to variations of site occupancy (mainly $A1^{IV}$ and the octahedral occupancy (6- $A1^{(VI)}$- (Mg + Fe^{2+})= VAC)) which are considered mainly as temperature dependent (Cathelineau and Nieva, 1985), Chlorite geothermometry calculation result showed that: chlorite formed at about 280°C. This

geothermometer is dominantly basing on the Al^{IV} content in the tetrahedral site of chlorites. Other chemical changes, such as the variation in Fe and Mg contents, are partly influenced by temperature, but are strongly dependent on the geological environment, and consequently on the solution composition. The empirical relationships between chemical variables and temperature were calibrated from 150-300°C, but extrapolations at lower and higher temperatures seem possible for chlorites (Cathelineau, 1988).

Two types barometry seems could be used in CMD. (1) Single pyroxene geobarometer: Mercier proposed pressure could be estimated by any single pyroxene phase in equilibrium with a second pyroxene and either spinel or garnet basing on experimental data for the equilibrium reactions that characterize either the enstatite-diopside join or the Al-concentration in pyroxenes coexisting with an Al-rich phase are reduced to three or four thermodynamic constants, entropy, enthalpy, and change in volume (Mercier, 1976). Similarly, Nimis and Taylor executed experimental clinopyroxene synthesis at 850-1500°C and 0-60 kbar in the Ca-Mg-Si and Ca-Mg-Al-Si-Cr systems and in more complex lherzolitic systems (Nimis and Taylor, 2000). They indicated that the pressure is formulated as a function of temperature and clinopyroxene composition. (2) Clinopyroxene-garnet geobarometer: Mukhopadhyay proposed a relative simple geobarometric equation, however, he commented that high thermodynamic variance of garnet-clinopyroxene assemblage, experimental calibration of a geobarometer of garnet+clinopyroxene is virtually impossible unless composition of one of the phases is internally buffered (Mukhopadhyay, 1991). This equation is base on Al_2O_3 content of clinopyroxene and Ca-Mg ratio of the coexisting garnet. Although analysis of available volume data along binary joins of the ca-Mg-Fe garnets and across the Di-En-CaTs ternary clinopyroxenes yields a very comprehensive model for calculating the partial molar volumes of the various components in complex systems, the compositional variance cannot be reduced by attributing all nonidealities to the P- Z terms. Thus, the nonidealities are dealt with in terms of variations in P-T-X (composition). In that

event, the geobarometric equation reproduces the P of equilibration of the experimentally determined compositions of coexisting garnet and clinopyroxene at a given temperature within the reasonable uncertainty limit (a few kilobars) of the experimental values of P in the simple system $CaO-MgO-Al_2O_3-SiO_2$, as well as in more complex multicomponent systems.

In Mercier's equation (Mercier, 1976), he emphasized the possiblility of deriving fully any single analysis of a pyroxene provided (or assuming) an original equilibrium with a second pyroxene and an Al-phase (spinel or garnet). Although the paragenesis used should used also contain olivine (reaction given below), the equations might apply to some olivine-free assemblages, since no significant differences are found for estimates derived from peridotites and coexisting reequilibrated pyroxenites (recrystallized tectonites). In experiments, the enstatite/diopside join, at least, seems insensitive to the degree of Si saturation (Lindsley and Dixon, 1976). However, many pyroxenites still have magmatic textures and therefore the estimates derived from them cannot be representative of regional conditions.

However, the two methods mentioned above have one thing in common: the pressure calculation is largely depending on the temperature. Therefore, it seems difficult to calculate the pressure basing on the garnet-pyroxene assemblage.

Geochemistry

In order to better understand the relations of the lithologies mentioned above, geochemical analysis was executed. Major element contents of the rock were analyzed on a VF-320 X-ray fluorescence spectrometer (XRF) at the Modern Analysis Center, Nanjing University. Uncertainties for major elements are generally less than 2%. Trace elements and Rare Earth Elements (REE) contents of the rock

were analyzed on an ICP-MS (Finnigan MAT-Element2) machine at the State Key Laboratory for Mineral Deposits Research, Nanjing University. Precisely weighted 50 mg sample powders were digested by a HF + HNO_3 mixture in Teflon bombs. An internal standard solution containing the single element Rh was used to monitor signal drift during counting. Analytical precision for most elements by ICP-MS is better than 5%. Detailed analytical procedure is documented in Gao et al. (2003).

Major and trace element data for ten representative samples of the CMD are presented in Table C-7. Skarn, either the pyroxene skarn or the garnet-pyroxene skarn, contains high Fe_2O_3 (4.99-16.83%), FeO (7.42-15.81%) and CaO (15.22-26.67%); whereas low in alkaline, Al_2O_3 (6.9-10.34%) and TiO_2 (0.27-0.61%). The black phase displays relative high SiO_2 (56.11-50.77%) and Al_2O_3 (15.12-4.73%). For major elements, the black phase, mafic dyke swarm and the skarns display linear relations (Fig. C-11). A notable feature of the REE patterns is the Eu negative anomalies for the black phase; whereas others are positive or very weak negative (Fig. C-12). The skarns, black phase, mafic dykes and magnetite display similar spider diagram patterns (Fig. C-12) which are significantly depleted in Sr and certain large ion lithophile elements (Cs, Rb and Ba). Meanwhile, they are slightly depleted in Ta and Nd. For the black phase, it is relative rich in Cs, Rb and Ba. But it did not show Sr depletion.

Discussion

Hydrothermal VS magmatic magnetite

Argument n°1: To our knowledge, observation of spinel and ilmenite exsolutions within ore magnetite from iron skarn deposits has never been reported. In contrast, this feature, observed at the CMD (Figs. C-6c, C-6d, C-6e and C-6f), is very common in Fe-Ti ore deposits and more broadly in magmatic magnetite because the solid solution miscibility is different in different temperature. The studied spinel

exsolution in the magnetite of the CMD is composed by Fe and Al (± Si and Ti) according to SEM analysis. Therefore, it is rather hercynite in which probably part of the Al is replaced by Si or a result of melange. The equilibrium

$Fe_3Al_2Si_3O_{12}$(almandine)+$2Al_2SiO_5$(sillimanite) =

$3FeAl_2O_4$(hercynite)+$5SiO_2$(quartz)

has been calibrated with experiments (Bohlen et al., 1986; Shulters and Bohlen, 1989). It showed that this reaction occur when the temperature is above 800°C with corresponding pressure probably higher than 3.5kbar. The $Fe_3Al_2Si_3O_{12}$(almandine) could be in form of:

$$Fe_3Al_2Si_3O_{12}(almandine)+(1/2)O_2=Fe_3O_4+Al_2O_3+3SiO_2$$

The equilibrium listed above indicated that the separation of Fe (magnetite) and Al (hercynite) probably occur at the temperature higher than 800°C. However, Turnock and Eugster indicated that complete solid solution exists above 858°C (Turnock and Eugster, 1962).

Argument n°2: Chemical composition of magnetite of different types of deposits may help to distinguish different magnetite origin (Dupuis and Beaudoin, 2011). Theoretic chemical composition of magnetite is FeO:31.6%, Fe_2O_3:68.94%. Previous study results show that the magnetite can carry Ti, Al, Cr, V, Mg, Mn, Ca, Co, Ni, Sn, Cu, Zn, Ga, Se, Te, Ag and Au, of which most common components are TiO_2, Al_2O_3, MgO and MnO (Lin, 1982; Westendorp et al., 1991; Shimazaki, 1998). Magnetite is an inverse spinel. Based only on microprobe analyses, silicon in magnetite has been interpreted as substitution for Fe^{3+} in 4-fold coordination site by Westendorp et al. (1991). In another study of Si in magnetite, involving microprobe analyses and TEM observations, Newberry et al. (1982), conclude that Si in magnetite could be present as: (i) a Fe_2SiO_4 component of a solid solution with magnetite, (ii) very small silicates inclusions and (iii) "unusual Si-rich domains of uncertain origin". Magnetite from Fe-Cu skarn-type deposits of the Kamaishi mine, Iwate Prefecture, northeastern Japan contain up to 6.19 wt% SiO_2 which was also according to EPMA result (Shiga, 1989). In counterparts, the magmatic magnetite

seems to be very poor in Si, high in Mg and Al, such as Bushveld Fe-V-Ti-Cr-PGMs Complex (Von Gruenewaldt *et al.*, 1985) and Panzhihua Fe-(V-Ti) mafic-ultramafic intrusion (Pang *et al.*, 2008). In both magmatic ore deposits, Al_2O_3 and MgO contents in magnetite are up to 3 wt%.

Lin (1982) and Dupuis and Beaudoin (2011) realized a statistic compositional analysis on magnetite composition, and showed that:

1. TiO_2 and Al_2O_3 content were highest in magmatic magnetite and lowest in hydrothermal deposit;
2. MnO content was highest in sediment related magnetite containing deposit and lowest in magmatic deposit. This point is concordant with Einaudi et al. (1981);
3. The MgO content varied, largely depend on the hosting rocks;
4. SiO_2 content was highest in hydrothermal magnetite.

From Fig. C-10, we can see that four deposits distribute in significantly different regions. It is noteworthy that the analyses on the CMD magnetite prepensely avoid the exsolutions. Magnetite from the Yamansu skarn-type magnetite deposits illustrates high SiO_2 with appreciable amounts of CaO, but low in Al_2O_3, MgO. Magnetites with such unusual compositions are found only in hydrothermal environments (Shimazaki, 1998). For the magmatic magnetite, such as Weiya orthomagmatic Fe-V-Ti deposit in eastern Tianshan (Wang et al., 2008) and Panzhihua Fe-V-Ti deposit which related to plume (Pang et al., 2008), they show contrast different value to Yamansu skarn-type deposit: low SiO_2, relative high in Al_2O_3 and MgO (Fig. C-10). Magnetites from the CMD fall into the area which is relative rich in Al and depleted Ti and Si, which probably indicate that magnetites in CMD is neither a typical magmatic deposit which was only controlled by cooling, nor hydrothermal deposit, meanwhile, it verify its multiple genesis.

Chemical corrosion of the pyroxene in black phase

The black phase was composed by albite, pyroxene and titanite. Over 200 analyses

points were done in SEM, some result showed prehnite in chemical composition. The pyroxene occurred within the black phase probably is not contemporaneous with albite because of the following reasons:

1. Pyroxene was altered, probably by the albite. From a general view, the borders were corroded more than the cores. The pyroxene displayed irregular round shapes with gradational and wavy boundaries (Fig. C-5g and C-5h);
2. There are some pyroxene-rich skarn and garnet-pyroxene skarn clasts embedded in the black phase (Fig. C-5e and C-5f);
3. Titanite was observed in the black phase. This titanite had relative straight boundary (Fig. C-4h). The occurrence of titanite probably was at the cost of pyroxene. Reactions have been suggested for the origin of titanite (Xirouchakis et al., 2001; Xirouchakis et al., 2001; Harlov and Forster, 2002). They are based either on rehydration:

$$7CaFeSi_2O_6(\text{clinopyroxene})+3FeTiO_3(\text{ilmenite})+5SiO_2(\text{quartz})+2H_2O=$$
$$2Fe_5Ca_2Si_8O_{23}(OH)_2\ (\text{amphibole})+3CaTiSiO_5(\text{sphene})$$

or oxidation:

$$3CaFeSi_2O_6(\text{clinopyroxene})+3FeTiO_3(\text{ilmenite})+O_2=$$
$$3CaTiSiO_5(\text{sphene})+2Fe_3O_4(\text{magnetite})+3SiO_2(\text{quartz})$$

Both these two reactions involve clinopyroxene which is concord with the observation in microscopy. Two point of EPMA result show that the titanite contain about 2% Al_2O_3 (average SiO_2: 30.4%, FeO: 0.4%, F:0.5%, CaO: 29.0%, Al_2O_3: 2.2%, P_2O_5: 0.2%, TiO_2: 36.4%). So actually, the black phase was mainly composed by albite, and it probably was magmatic origin.

Assimilation

From a cartographic point of view, the three similar magnetite deposits known in the Cihai district are located at the contact between a large mafic intrusion and sediment (Fig. C-1b), suggesting they were geologically related. From a petrological point of view, the black phase embedded and altered the skarn clasts suggesting an

assimilation process which could occurred in the magma chamber (Amelin *et al.*, 1996), ascension (Gurenko et al., 2001; Neumann et al., 2002) or emplacement of the magma (Barbey *et al.*, 2001). The geochemical data may sideways constrict the assimilation as following:

(1) Major elements display linear relations between the black phase, mafic dyke swarm and the skarns (Fig. C-11). The black phase and the skarns displayed similar REE patterns in which the Eu content is contrasted between the black phase and the skarn. The spider diagrams hold similar information, however the black phase is rich on Rb, Ba and Sr (Fig. C-12). The high field strength elements (HFSE) ratio of Zr/Hf and Nb/Ta, which are sensitive to assimilation (Gill, 1981), display the black phase and the mafic dyke swarm were probably the result of assimilation of the mafic/ultramfic intrusions (Fig. C-13).

(2) In the CMD, the Ca rich pyroxene in the mafic dyke swarm (Fig. C-9a) are probably caused by the sediment assimilation of magma because sediment incorporation into magma could result in the favor of crystallization of Ca rich pyroxene and other phases (e.g. olivine, plagioclase) are consumed (Iacono Marziano et al., 2008).

(3) Wenzel et al. (2002) reported that Mg-skarns formed from silica-poor dolomitic xenoliths by interaction with the mafic magma of the Ioko-Dovyren intrusion. In his paper, he wrote that "rapid heating of dolomitic xenoliths by the mafic magma caused the decomposition of dolomite into calcite + periclase, releasing much CO_2. Further heating quantitatively melted the calcite. A periclase-rich restite was left behind after extraction of the low-density, low-viscosity calcite melt. The extracted calcite melt mixed with the surrounding mafic melt. This resulted in crystallization of olivine with CaO contents up to 1.67 wt%. A local decrease in the silica concentration stabilized $CaAl_2SiO_6$-rich clinopyroxene. Brucite/periclase-free forsterite–spinel skarns probably originated by crystallization from the mafic melt close to the xenoliths at elevated fO_2. The high fO_2 was caused by CO_2-rich fluids released during the decomposition of the xenoliths."(Wenzel *et al.*, 2002).

Melt immiscibility

In the CMD, the massive magnetite ore shoots and the black phase are magmatic origin according the above analysis. And it seems that they originated from the same magma chamber. Normally, the magmatic magnetite could be companied by the plagioclase, such as the Pangzhihua Fe-V-Ti deposit (Pang et al., 2008), however, in the CMD, the magnetite seems devoid of the plagioclase. It is possible that immiscible iron rich melt and silica rich melt occurred in basalt petrogenesis which was documented in the Skaergaard intrusion (Jakobsen et al., 2005). The segregation of these phases in the CMD probably associated with CO_2-rich fluids because previous study showed that CO_2-rich fluids, which released during decarbonatization of sedimentary floor rocks passed up through the magma, would cause fO_2 increases from the fayalite–magnetite–quartz buffer (FMQ) to FMQ+1.5 and lead economic concentration of magnetite to crystallize near the liquidus (Ganino *et al.*, 2008). A schematic model illustrates the formations of the CMD is proposed (Fig. C-14). In this model, the CO_2-rich fluids probably hold certain proportion of Al with contributed to the exsolution in magnetite because, from the Figure C-10, we can see that the magnetite in the CMD is relative rich in Al.

Conclusion

This paper concern about documenting the economic massive magnetite associated with skarn in the CMD. The texture and chemical composition of magnetite granis support that they are magmatic origin. The magnetite, skarn, mafic dyke swarm and black phase are genetic related, and the formation of massive magmatic magnetite ore shoots seems to be caused by circulation of CO_2-fluid derived from decarbonation of sediment.

Acknowledgements: We specially thank the Baosteel Company for providing access to their mine and unpublished documents. The first author benefits a

scholarship grant from the French Minister of Education and Research. We are grateful to Fatima LAGGOUN-DEFARGE and Nicolas BOST from ISTO for their contributions to the SEM and Raman analysis. This study was financially supported by the Geological Survey Project (1212011140056) and NNSFC (40603008, 40672040).

Figure caption

Fig. C-1 Simplified geological map of (a) the Beishan orogenic segment and its adjacent area (after Xiao et al. 2010, Cheng et al. 2008). Major magnetite deposits are indicated by red stars; The pillow basalt represent an early Paleozoic suture, dated to be 462-412Ma (Guo et al., 2006). Circles fill by green and yellow colour represent Cu-Ni and Au deposits. 1=Luodong, 2=Boshi, 3=Boyi, 4=Baishitan, 5=Daqingshan, 6=Hongshijing, 7=Bayiquan, 8=Shijinbo, 9=Jiaobishan. Skarn type deposits which although were not indicated in the map include: Bailingshan, Heijianshan, Chilongfeng, Hongyuntan, Aqishan, Heilongfeng, Shuangfengshan (Mao et al. 2005). (b) Geological map of Cihai ore field (after Yu et al. 1999; Tang et al. 2010). This map was re-interpreted. Tang et al. (2010) interpreted the skarn to be diabase. In order to mapping, trench and drill cores were executed, detail lithology description after the geological report edited by Yu et al. (1999), because of most of the area was covered by 2 to 5m thick Quaternary sand. The marble and schist were thought to be Precambrian (Yu et al., 1999). The numbers embedded in circles in (b) are: 1=olivine gabbro, 2=diabase, 3=troctolite, 4=basalt, 5=diabase, 6=diabase (Tang et al., 2010).

Fig. C-2 (a) Geological map of CMD open pit; (b) geological cross-section of the CMD. Ore bodies occurrences (some of them did not outcrop at the present topographic level of the pit) and geometries have been recognized through drill hole campaigns (courtesy of the Baosteel Company). This profile is the same as IVE profile in the geological report of the Baosteel Company; (c) Magnetic anomalies of CMD, the numbers indicate the magnetic field intensity (nT) (courtesy of the Baosteel Company).

Fig. C-3: (a) Mafic dyke swarm cutting the skarn and ore shoots; (b) Late brittle faulting affecting skarn, metasediments, ore bodies and mafic dyke swarm; (c) Mafic dyke cutting ore body.

Fig. C-4 Hand-specimen-scale characteristic textures of the CMD. (a) garnet-pyroxene skarn; (b) pyroxene-rich skarn altered by later amphibole-calcite assemblage; (c) later calcite-quartz veins crosscutting the pyroxene-rich skarn; (d) Banded metapelite; (e) massive magnetite including

clasts of pyroxene-rich skarn; (f) massive magnetite including clasts of garnet-pyroxene skarn. Note the ambiguous rounded shape of the clasts and the corrosion gulfs, all diagnostic of brecciation by chemical corrosion; (g) black phase brecciating the garnet-pyroxene skarn; (h) black phase "injected" the garnet-pyroxene skarn. The inset in (h) is a backscattered electron image indicating a titanite grain. It is noteworthy that the clasts of skarns in the massive magnetite and black phase in (f) and (g) respectively display ellipsoidal form which indicate replacement feature, neither the magnetite nor black phase skarnify.

Fig. C-5 Microphotographs and back-scattered electron image. (a) pyroxene-rich skarn with apatite inside, transmitted crossed polarized light; (b) garnet-pyroxene skarn, transmitted plane polarized light; (c) later calcite-quartz veinlets cross cutting pyroxene-rich skarn, transmitted crossed polarized light; (d) mafic dyke, transmitted crossed polarized light; (e) and (f) are black phase with skarn clasts in transmitted crossed and plane polarized light respectively; (g) black phase in reflected plane light. The boundaries of pyroxene are marked by dotted yellow line. Part of the pyroxene was altered. (h) back-scattered electron image of black phase showing irregular round shaped pyroxenes and titanites with gradational and wavy boundaries. ap=apatite; cpx=clinopyroxene; mgt=magnetite; grt=garnet ; pl=plagioclase; amp=amphibole; al-cpx=altered pyroxene; ab=albite.

Fig. C-6 Microphotographs and backscattered electron images. (a) sphalerite (grey) with microveinlets of pyrite (pale yellow), reflected plane light; (b) pyrrhotite altered into "bird's eyes" structure and colloform pyrite, and covellite at the rim, reflected plane light. (c) and (d) magnetite with spinel and ilmenite exsolution, backscattered electron image. Exsolution in the central part and irregular round shapes with wavy boundaries of the magnetite grain were emphasized in (d). (e) round pyroxene embedded in the magnetite grains; (f) magnetite grain boundaries meet generally at distinct triple junctions with ~120° interfacial angles. In (e) and (f), the magnetite grains display fine exsolutions. mgt=magnetite.

Fig. C-7 (A) Raman spectrum indicating the present of albite crystals and a carbon compound (peak 1587) in the black phase; (B) SEM energy spectrum indicating co-existing carbon and albite. For the SEM energy spectrum and Raman spectrum, thin section was metalized with gold and without metalized, respectively.

Fig. C-8 Mineral paragenetic succession related to the major stages in the CMD.

Fig. C-9 Ternary plots of chemical composition of (a) pyroxene and (c) garnet. The grey area in (c) is Fe skarn which was derived from Meinert (1992). (b) Fe versus Mg for pyroxene in mol.

Fig. C-10 Ternary plots of chemical composition of magnetite. These plots are comparing the wt% composition of magnetite from the Yamansu Fe skarn deposit, Cihai Fe magmatic deposit, Weiya Fe-V-Ti deposit and Panzhihai Fe-V-Ti deposit. Data of Panzhihua Fe-(V-Ti) deposit are from Pang et al. (2008); part of the data of Cihai from Wang et al. (2006), Bushveld from Von Gruenewaldt et al. (1985), Fe-Ti oxide and kiruna from Dupuis and Beaudoin (2011).

Fig.11 Hark diagram of major elements from the skarn, mafic dykes, ore shoot and the black phase.

Fig. C-12 REE patterns and spider diagrams.

Fig. C-13 Nb/Ta-Zr/Hf diagrams (after Gill 1981). The grey zone is correspond to mafic rocks in Cihai district in figure C-1. Data are from Tang et al. (2010) and Yu et al. (1999). The troctolite and the olivine gabbro were sampled by Tang et al. (2010) in the position of 3 and 1 showed in the figure C-1.

Fig. C-14 Schematic model for the formation of the CMD.

Table C-2: EPMA analysis of pyroxene (wt%) and structural formula

Point	SiO_2	Al_2O_3	FeO	K_2O	Na_2O	CaO	MgO	MnO	TiO_2	F	Total
38psk	51.29	0.66	15.25	0.01	0.19	24.08	9.00	0.46	0.02	0.25	101.21
39psk	51.20	0.58	16.78	-	0.19	23.67	8.31	0.17	0.12	0.20	101.23
42psk	49.02	2.17	13.72	-	0.08	24.65	9.12	0.50	0.22	0.24	99.74
66gsk	51.38	1.43	10.29	0.01	0.01	23.40	12.08	0.62	0.09	0.20	99.52
67gsk	49.01	2.72	13.91	-	0.29	23.29	8.55	0.78	0.81	0.12	99.47
68gsk	50.42	2.35	10.72	0.01	-	24.88	11.12	0.40	0.28	0.16	100.33
70gsk	50.97	2.03	9.52	0.02	-	24.83	12.25	0.28	0.06	0.18	100.13
71gsk	51.03	2.06	10.66	-	0.09	24.98	11.42	0.26	0.27	0.25	101.02
72gsk	50.53	1.93	10.02	0.07	0.06	25.01	11.88	0.28	0.14	0.28	100.17
73mf	51.80	0.21	14.76	0.04	0.21	23.25	9.76	0.29	0.02	0.16	100.48
75mf	52.00	0.27	14.71	0.05	0.11	23.45	9.76	0.14	0.05	0.09	100.62
79mf	51.13	0.26	16.21	0.07	0.30	20.81	9.73	0.45	-	0.12	99.07
88psk	51.87	0.76	12.78	-	0.39	23.64	10.46	0.15	-	0.25	100.29
89psk	52.85	0.40	11.77	0.03	0.17	20.40	12.42	0.44	0.09	0.18	98.74
90psk	50.84	0.98	14.94	-	0.35	23.13	9.47	0.31	-	0.32	100.35
93psk	51.65	0.55	10.98	0.05	0.36	23.77	11.41	0.12	0.04	0.18	99.11
94psk	50.11	1.29	12.12	0.01	0.07	24.53	10.22	0.38	0.00	0.30	99.03
97gsk	50.58	0.54	13.04	0.04	0.20	23.61	10.03	0.14	0.02	0.24	98.43
104gsk	49.77	1.63	12.49	0.03	0.08	23.79	10.02	0.40	0.06	0.09	98.35
106gsk	50.09	1.30	13.41	0.01	0.07	24.29	9.84	0.09	0.15	0.21	99.45
111gsk	49.48	0.23	21.75	-	0.07	23.08	3.78	0.89	0.02	0.17	99.48
114gsk	50.25	0.47	19.17	-	0.24	23.58	5.13	0.89	-	0.16	99.88
115gsk	50.31	0.28	21.87	-	0.12	23.60	4.12	0.72	-	0.11	101.12
116gsk	49.85	0.09	15.53	-	0.14	22.18	7.26	0.73	0.08	0.09	95.94
119gsk	50.03	0.06	20.18	-	0.13	23.66	5.10	0.87	-	0.10	100.13
120gsk	50.94	0.06	17.93	-	0.01	24.25	6.25	1.39	-	0.18	101.01
792-5bp	50.07	-	19.66	-		24.67	5.6	-	-	-	-
792-6bp	53.22	3.22	18.58	-	0.41	19.72	4.81	-	-	-	-
792-18bp	50.04	-	19.57	-	-	24.76	5.63	-	-	-	-
792-19bp	52.35	0.88	18.76	-	-	24.39	3.62	-	-	-	-
125-36bp	53.77	-	9.06	-	-	25.86	11.31	-	-	-	-
125-38bp	53.06	1.17	8.11	-	-	26.38	11.28	-	-	-	-
125-44bp	53.88	-	8.24	-	-	26.19	11.69	-	-	-	-
125-45bp	53.08	-	10.55	-	-	24.52	11.85	-	-	-	-
125-46bp	53.35	-	10.44	-	-	25.19	11.03	-	-	-	-
125-50bp	53.14	0.19	9.35	-	-	25.91	11.32	-	-	-	-
125-52bp	53.27	-	9.23	-	-	25.94	11.56	-	-	-	-

Table C-2 continued:

strutural fomula of pyroxene

	Si	Al iv	Al vi	Fe	K	Na	Ca	Mg	Mn	Ti	F	∑ cation
38psk	1.97	0.01	0.00	0.49	0.00	0.01	0.99	0.52	0.02	0.00	0.03	3.98
39psk	1.98	0.01	0.00	0.54	0.00	0.01	0.98	0.48	0.01	0.00	0.02	3.98
42psk	1.90	0.04	0.00	0.45	0.00	0.01	1.03	0.53	0.02	0.01	0.03	3.94
66gsk	1.96	0.03	0.00	0.33	0.00	0.00	0.96	0.69	0.02	0.00	0.02	3.96
67gsk	1.90	0.05	0.00	0.45	0.00	0.02	0.97	0.50	0.03	0.02	0.01	3.93
68gsk	1.91	0.05	0.00	0.34	0.00	0.00	1.01	0.63	0.01	0.01	0.02	3.94
70gsk	1.93	0.04	0.00	0.30	0.00	0.00	1.01	0.69	0.01	0.00	0.02	3.95
71gsk	1.93	0.04	0.00	0.34	0.00	0.01	1.01	0.64	0.01	0.01	0.03	3.95
72gsk	1.92	0.04	0.00	0.32	0.00	0.00	1.02	0.67	0.01	0.00	0.03	3.95
73mf	1.99	0.00	0.00	0.47	0.00	0.02	0.96	0.56	0.01	0.00	0.02	3.99
75mf	1.99	0.01	0.00	0.47	0.00	0.01	0.96	0.56	0.00	0.00	0.01	3.99
79mf	2.00	0.00	0.00	0.53	0.00	0.02	0.87	0.57	0.02	0.00	0.02	3.99
88psk	1.99	0.01	0.00	0.41	0.00	0.03	0.97	0.60	0.01	0.00	0.03	3.98
89psk	2.04	0.00	0.01	0.38	0.00	0.01	0.84	0.71	0.01	0.00	0.02	3.99
90psk	1.97	0.02	0.00	0.48	0.00	0.03	0.96	0.55	0.01	0.00	0.04	3.97
93psk	1.98	0.01	0.00	0.35	0.00	0.03	0.98	0.65	0.00	0.00	0.02	3.99
94psk	1.95	0.03	0.00	0.39	0.00	0.01	1.02	0.59	0.01	0.00	0.04	3.97
97gsk	1.98	0.01	0.00	0.43	0.00	0.02	0.99	0.59	0.01	0.00	0.03	3.99
104gsk	1.94	0.03	0.00	0.41	0.00	0.01	0.99	0.58	0.01	0.00	0.01	3.96
106gsk	1.94	0.03	0.00	0.44	0.00	0.01	1.01	0.57	0.00	0.00	0.03	3.97
111gsk	2.01	0.00	0.01	0.74	0.00	0.01	1.00	0.23	0.03	0.00	0.02	3.99
114gsk	2.00	0.00	0.01	0.64	0.00	0.02	1.01	0.30	0.03	0.00	0.02	3.99
115gsk	2.00	0.01	0.00	0.73	0.00	0.01	1.00	0.24	0.02	0.00	0.01	3.99
116gsk	2.03	0.00	0.00	0.53	0.00	0.01	0.97	0.44	0.03	0.00	0.01	4.00
119gsk	1.99	0.00	0.00	0.67	0.00	0.01	1.01	0.30	0.03	0.00	0.01	4.00
120gsk	2.00	0.00	0.00	0.59	0.00	0.00	1.02	0.37	0.05	0.00	0.02	4.00
792-5bp	1.98	0.00		0.65			1.04	0.33				4.00
792-6bp	2.09		0.06	0.61		0.03	0.83	0.28				3.91
792-18bp	1.98			0.65			1.05	0.33				4.00
792-19bp	2.08		0.02	0.62			1.04	0.21				3.98
125-36bp	2.03		0.00	0.29			1.05	0.64				4.00
125-38bp	2.00		0.02	0.26			1.06	0.63				3.97
125-44bp	2.03			0.26			1.06	0.66				4.00
125-45bp	2.01			0.33			0.99	0.67				4.00
125-46bp	2.02			0.33			1.02	0.62				4.00
125-50bp	2.01			0.30			1.05	0.64				4.00
125-52bp	2.01			0.29			1.05	0.65				4.00

Symbols after the number represent its origin where is present.

psk=pyroxene-rich skarn, gsk=garnet-pyroxene skarn, mf=mafic dyke, bp=black phase.

Normalization of total cation to 4.

Table C-3: EPMA analysis of garnet (wt%) and structural formula

Point No	c44	c45	c46	c47	c48	c49	c50	c51	c56	c61	c64
K_2O	0.00	0.04	0.00	0.00	0.02	0.02	0.00	0.00	0.00	0.00	0.00
SiO_2	37.81	37.90	37.71	37.41	37.61	37.77	37.90	37.89	37.98	38.17	38.36
FeO	10.31	10.01	9.92	10.43	10.14	10.17	9.54	10.00	13.44	8.61	8.39
F	0.25	0.39	0.27	0.32	0.17	0.24	0.22	0.32	0.25	0.14	0.23
Na_2O	0.01	0.00	0.01	0.02	0.00	0.03	0.00	0.00	0.05	0.00	0.04
CaO	33.92	33.92	34.18	34.35	34.18	34.11	33.72	34.50	34.66	33.68	33.26
Al_2O_3	14.35	14.59	14.73	13.71	13.60	13.91	15.48	14.01	12.91	16.44	16.52
MgO	0.26	0.17	0.23	0.20	0.17	0.27	0.23	0.23	0.00	0.47	0.46
MnO	0.64	0.46	0.81	0.57	0.53	0.35	0.31	0.60	0.60	0.56	0.58
Cl	0.00	0.00	0.00	0.00	0.00	0.00	0.00	0.01	0.00	0.01	0.00
P_2O_5	0.35	0.32	0.35	0.31	0.28	0.23	0.33	0.34	0.30	0.25	0.29
CoO	0.09	0.02	0.12	0.00	0.04	0.05	0.00	0.00	0.00	0.00	0.02
TiO_2	1.58	1.14	1.22	1.57	2.15	1.65	0.77	1.43	0.00	0.69	0.58
Total	99.56	98.94	99.55	98.88	98.91	98.79	98.49	99.31	100.17	99.01	98.71
strutural fomula of garnet											
Si	2.99	3.03	2.98	2.99	2.99	3.01	3.01	3.01	3.00	2.99	3.02
Al^{IV}	0.01	0.00	0.02	0.01	0.01	0.00	0.00	0.00	0.00	0.01	0.00
Al^{VI}	1.33	1.37	1.36	1.28	1.27	1.31	1.45	1.31	1.20	1.51	1.54
Fe^{III}	0.57	0.56	0.57	0.62	0.60	0.60	0.50	0.60	0.80	0.45	0.43
Ti	0.09	0.07	0.07	0.09	0.13	0.10	0.05	0.09	0.00	0.04	0.03
Ca	2.88	2.90	2.90	2.94	2.91	2.91	2.87	2.94	2.93	2.83	2.81
Fe^{II}	0.11	0.11	0.09	0.07	0.07	0.08	0.13	0.06	0.08	0.11	0.12
Mn	0.04	0.03	0.05	0.04	0.04	0.02	0.02	0.04	0.04	0.04	0.04
Mg	0.03	0.02	0.03	0.02	0.02	0.03	0.03	0.03	0.00	0.05	0.05
F	0.06	0.10	0.07	0.08	0.04	0.06	0.05	0.08	0.06	0.03	0.06
And	0.33	0.31	0.32	0.36	0.37	0.35	0.28	0.34	0.40	0.25	0.23
Gro	0.63	0.65	0.65	0.62	0.61	0.62	0.68	0.64	0.58	0.70	0.70
Alm	0.04	0.04	0.03	0.02	0.02	0.03	0.04	0.02	0.03	0.04	0.04

Table C-3 continued:

Point No	c65	c99	c103	c100	c121	c122	c123	c124	c125	c129	c130
K_2O	0.00	0.00	0.01	0.05	0.00	0.00	0.05	0.01	0.01	0.00	0.00
SiO_2	38.27	37.25	36.86	36.42	38.19	37.92	39.06	38.51	37.89	38.32	37.93
FeO	8.59	15.41	16.57	16.73	9.68	10.50	8.01	7.64	8.68	7.77	9.66
F	0.30	0.17	0.15	0.23	0.19	0.18	0.21	0.24	0.16	0.15	0.18
Na_2O	0.02	0.00	0.00	0.03	0.04	0.00	0.04	0.00	0.00	0.00	0.03
CaO	33.12	29.55	29.79	30.31	23.97	24.46	22.88	24.14	23.94	23.54	23.82
Al_2O_3	16.27	12.57	13.27	12.85	24.81	24.01	26.87	26.43	25.52	26.61	24.57
MgO	0.46	0.24	0.04	0.10	0.00	0.00	0.03	0.01	0.01	0.00	0.02
MnO	0.47	0.82	0.83	0.86	0.10	0.07	0.46	0.10	0.09	0.25	0.08
Cl	0.00	0.01	0.05	0.00	0.02	0.00	0.02	0.03	0.00	0.00	0.00
P_2O_5	0.25	0.18	0.32	0.31	0.16	0.28	0.15	0.17	0.16	0.28	0.19
CoO	0.06	0.05	0.00	0.02	0.12	0.00	0.08	0.00	0.00	0.00	0.00
TiO_2	0.55	0.09	0.07	0.05	0.03	0.02	0.03	0.04	0.00	0.01	0.02
Total	98.35	96.33	97.96	97.96	97.30	97.42	97.89	97.32	96.44	96.93	96.49
strutural fomula of garnet											
Si	3.04	3.07	2.99	2.96	3.03	3.01	3.07	3.04	3.02	3.03	3.03
Al^{IV}	0.00	0.00	0.01	0.04	0.00	0.00	0.00	0.00	0.00	0.00	0.00
Al^{VI}	1.52	1.22	1.26	1.19	2.32	2.25	2.49	2.46	2.40	2.48	2.31
Fe^{III}	0.44	0.77	0.74	0.80	0.00	0.00	0.00	0.00	0.00	0.00	0.00
Ti	0.03	0.01	0.00	0.00	0.00	0.00	0.00	0.00	0.00	0.00	0.00
Ca	2.82	2.61	2.59	2.64	2.04	2.08	1.93	2.04	2.04	1.99	2.04
Fe^{II}	0.13	0.29	0.39	0.34	0.64	0.70	0.53	0.50	0.58	0.51	0.65
Mn	0.03	0.06	0.06	0.06	0.01	0.00	0.03	0.01	0.01	0.02	0.01
Mg	0.05	0.03	0.00	0.01	0.00	0.00	0.00	0.00	0.00	0.00	0.00
F	0.08	0.04	0.04	0.06	0.05	0.04	0.05	0.06	0.04	0.04	0.04
And	0.24	0.39	0.37	0.40	0.00	0.00	0.00	0.00	0.00	0.00	0.00
Gro	0.70	0.48	0.49	0.48	0.68	0.69	0.64	0.68	0.68	0.66	0.68
Alm	0.04	0.10	0.13	0.11	0.21	0.23	0.18	0.17	0.19	0.17	0.22

Structural formula are calculated based upon 8 cations, $Fe^{3+} = 2 - (Al^{3+})^{VI} - Ti^{4+}$ and $Fe^{2+} = Fe(total) - Fe^{3+}$.

Table C-4: Representive EPMA analysis result of magnetite (wt%) and structural formula

	SiO_2	FeO	CaO	Al_2O_3	MnO	TiO_2	MgO	V_2O_3	Total
li73	0.08	90.35	0.03	0.70	0.15	2.59	0.00	0.13	94.03
li74	0.08	88.18	0.06	0.68	0.05	2.56	0.05	0.21	91.86
E02	0.17	91.61	0.07	1.04	0.11	0.09	0.19	0.00	93.28
E03	0.17	91.56	0.10	1.25	0.42	0.00	0.31	0.00	93.81
E04	0.13	91.79	0.00	0.70	0.35	0.00	0.10	0.00	93.07
E05	0.44	86.32	0.22	8.37	0.17	0.00	1.47	0.00	96.99
E06	0.23	90.86	0.08	0.76	0.29	0.00	0.20	0.00	92.43
E07	0.06	91.14	0.00	1.59	0.10	0.00	0.18	0.02	93.09
E08	0.42	90.12	0.18	1.01	0.17	0.00	0.23	0.00	92.13
F05	3.40	83.04	1.34	0.88	0.05	0.15	0.43	0.00	89.29
F06	0.56	87.91	0.03	0.35	0.00	0.22	0.10	0.00	89.16
F07	1.63	84.41	0.01	1.21	0.04	0.04	0.23	0.01	87.58
F08	5.50	79.11	0.05	3.32	0.06	0.16	1.27	0.05	89.52
F10	0.58	88.12	0.06	0.71	0.10	0.31	0.10	0.00	89.98
F11	0.03	87.64	0.05	0.49	0.20	0.81	0.05	0.00	89.26
F12	0.61	87.13	0.09	0.86	0.11	0.18	0.13	0.00	89.10
F13	0.04	90.70	0.01	0.58	0.00	0.30	0.00	0.01	91.65
F14	5.36	81.12	0.07	4.60	0.01	0.07	0.71	0.11	92.05
F15	0.80	89.09	0.18	0.71	0.10	0.37	0.12	0.00	91.36
F17	0.54	89.65	0.08	0.72	0.01	0.11	0.14	0.03	91.27
F18	0.00	84.34	0.06	0.91	0.11	0.39	0.01	0.00	85.81
F19	0.01	85.08	0.00	1.02	0.08	0.46	0.00	0.01	86.66
F20	0.52	84.30	0.03	0.88	0.18	0.39	0.00	0.00	86.30
F21	0.03	85.15	0.01	0.83	0.12	0.34	0.01	0.01	86.50
F22	0.19	84.76	0.06	0.51	0.16	0.43	0.03	0.00	86.15
F23	2.94	79.05	0.02	1.82	0.26	0.35	0.00	0.01	84.44
F24	0.25	85.47	0.00	0.90	0.23	0.15	0.02	0.02	87.03
F25	0.24	86.11	0.00	0.74	0.28	0.09	0.02	0.00	87.48
F26	0.08	86.93	0.00	2.14	0.22	0.14	0.25	0.00	89.76
F27	0.31	82.05	0.01	1.57	0.35	0.22	0.10	0.00	84.60
F28	0.06	85.99	0.00	0.69	0.06	0.23	0.05	0.05	87.13
F29	0.13	85.34	0.00	7.65	0.66	0.52	0.89	0.02	95.21
F30	1.62	89.37	0.04	1.30	0.20	0.32	0.32	0.01	93.17
F31	0.77	86.59	0.00	0.72	0.08	0.31	0.12	0.02	88.62
F32	0.16	88.78	0.11	0.35	0.13	0.44	0.02	0.00	89.98

F33	0.56	88.17	0.00	0.61	0.14	0.87	0.21	0.00	90.55
F34	0.28	89.80	0.03	0.49	0.00	0.15	0.04	0.00	90.79
F35	0.08	89.57	0.15	0.42	0.00	0.28	0.01	0.05	90.56
F36	0.00	90.44	0.11	0.59	0.15	0.29	0.03	0.01	91.61
F37	0.03	89.56	0.07	0.57	0.05	0.42	0.06	0.00	90.77
F38	3.09	84.21	1.87	0.81	0.00	2.95	0.19	0.02	93.15
F39	0.07	88.75	0.05	0.44	0.00	0.27	0.04	0.00	89.63
F40	0.03	89.79	0.23	0.34	0.01	0.37	0.00	0.00	90.78
F46	0.14	90.12	0.00	1.51	0.14	0.39	0.05	0.00	92.35
F47	0.12	89.61	0.05	1.46	0.03	0.38	0.07	0.00	91.72
F48	0.21	90.38	0.13	1.33	0.16	0.49	0.02	0.07	92.79
F49	0.69	89.90	0.21	1.29	0.19	0.45	0.15	0.00	92.88
F50	1.54	85.64	0.07	2.09	0.12	0.44	0.16	0.01	90.07
F51	0.05	91.44	0.06	1.07	0.16	0.51	0.01	0.00	93.30
F52	0.10	89.40	0.06	2.55	0.08	0.44	0.07	0.00	92.69
F53	0.11	89.07	0.01	2.30	0.23	0.30	0.06	0.00	92.09
F54	0.59	87.14	0.12	0.68	0.00	0.21	0.17	0.06	88.95

strutural formula

	Fe^{3+}	Fe^{2+}	Si	Ca	Al	Mn	Ti	Mg	V
li73	1.823	1.075	0.003	0.001	0.016	0.005	0.075	0.000	0.002
li74	1.817	1.078	0.003	0.002	0.016	0.002	0.075	0.003	0.003
E02	1.958	0.992	0.007	0.003	0.023	0.004	0.003	0.011	0.000
E03	1.959	0.971	0.007	0.004	0.028	0.014	0.000	0.018	0.000
E04	1.974	0.988	0.005	0.000	0.016	0.011	0.000	0.006	0.000
E05	1.783	0.920	0.016	0.009	0.185	0.005	0.000	0.082	0.000
E06	1.964	0.985	0.009	0.003	0.017	0.009	0.000	0.011	0.000
E07	1.958	0.989	0.002	0.000	0.036	0.003	0.000	0.010	0.000
E08	1.944	0.990	0.016	0.008	0.023	0.006	0.000	0.013	0.000
F05	1.701	1.055	0.135	0.057	0.021	0.002	0.004	0.025	0.000
F06	1.933	1.023	0.023	0.001	0.008	0.000	0.007	0.006	0.000
F07	1.835	1.052	0.067	0.001	0.029	0.001	0.001	0.014	0.000
F08	1.475	1.145	0.218	0.002	0.077	0.002	0.005	0.075	0.001
F10	1.918	1.021	0.023	0.002	0.017	0.003	0.009	0.006	0.000
F11	1.937	1.014	0.001	0.002	0.012	0.007	0.024	0.003	0.000
F12	1.919	1.015	0.025	0.004	0.020	0.004	0.006	0.008	0.000
F13	1.965	1.010	0.002	0.001	0.013	0.000	0.009	0.000	0.000
F14	1.469	1.169	0.208	0.003	0.105	0.000	0.002	0.041	0.002
F15	1.899	1.025	0.031	0.008	0.016	0.003	0.011	0.007	0.000
F17	1.933	1.014	0.021	0.003	0.017	0.000	0.003	0.008	0.001
F18	1.953	1.005	0.000	0.003	0.022	0.004	0.012	0.001	0.000
F19	1.945	1.012	0.000	0.000	0.025	0.003	0.014	0.000	0.000
F20	1.911	1.026	0.022	0.001	0.022	0.006	0.012	0.000	0.000
F21	1.955	1.007	0.001	0.000	0.020	0.004	0.011	0.001	0.000

F22	1.945	1.011	0.008	0.003	0.013	0.006	0.013	0.002	0.000
F23	1.682	1.126	0.125	0.001	0.045	0.009	0.011	0.000	0.000
F24	1.948	1.006	0.010	0.000	0.022	0.008	0.005	0.001	0.000
F25	1.957	1.001	0.010	0.000	0.018	0.010	0.003	0.001	0.000
F26	1.935	0.985	0.003	0.000	0.051	0.007	0.004	0.015	0.000
F27	1.920	1.001	0.013	0.000	0.039	0.012	0.007	0.006	0.000
F28	1.961	1.006	0.003	0.000	0.017	0.002	0.007	0.003	0.001
F29	1.786	0.949	0.005	0.000	0.173	0.021	0.015	0.051	0.000
F30	1.827	1.045	0.062	0.002	0.029	0.007	0.009	0.018	0.000
F31	1.901	1.031	0.031	0.000	0.017	0.003	0.009	0.007	0.000
F32	1.952	1.010	0.006	0.004	0.008	0.004	0.013	0.001	0.000
F33	1.889	1.031	0.022	0.000	0.014	0.005	0.026	0.012	0.000
F34	1.958	1.012	0.011	0.001	0.011	0.000	0.004	0.003	0.000
F35	1.965	1.006	0.003	0.007	0.010	0.000	0.008	0.001	0.001
F36	1.969	0.998	0.000	0.004	0.014	0.005	0.008	0.001	0.000
F37	1.959	1.006	0.001	0.003	0.013	0.002	0.012	0.003	0.000
F38	1.575	1.116	0.118	0.077	0.018	0.000	0.085	0.011	0.000
F39	1.967	1.007	0.003	0.002	0.010	0.000	0.008	0.002	0.000
F40	1.968	1.002	0.001	0.010	0.008	0.000	0.011	0.000	0.000
F46	1.932	1.010	0.005	0.000	0.035	0.005	0.012	0.003	0.000
F47	1.934	1.009	0.005	0.002	0.034	0.001	0.011	0.004	0.000
F48	1.921	1.013	0.008	0.005	0.030	0.005	0.014	0.001	0.001
F49	1.891	1.016	0.027	0.009	0.029	0.006	0.013	0.009	0.000
F50	1.801	1.058	0.061	0.003	0.049	0.004	0.013	0.010	0.000
F51	1.942	1.009	0.002	0.002	0.024	0.005	0.015	0.001	0.000
F52	1.908	1.008	0.004	0.002	0.059	0.003	0.013	0.004	0.000
F53	1.920	1.002	0.004	0.000	0.053	0.008	0.009	0.004	0.000
F54	1.921	1.017	0.024	0.005	0.016	0.000	0.006	0.010	0.001

Recalculated chemical data

	Fe_2O_3	FeO	SiO_2	CaO	Al_2O_3	MnO	TiO_2	MgO	V_2O_5	sum
li73	63.15	33.52	0.14	0.03	0.35	0.18	2.59	0.00	0.07	100.02
li74	61.50	32.84	0.14	0.06	0.34	0.05	2.56	0.00	0.10	97.59
E02	67.58	30.81	0.29	0.07	0.52	0.12	0.09	0.00	0.00	99.49
E03	68.03	30.35	0.29	0.10	0.62	0.48	0.00	0.00	0.00	99.88
E04	67.99	30.61	0.22	0.00	0.35	0.39	0.00	0.00	0.00	99.57
E05	63.28	29.39	0.74	0.22	4.19	0.20	0.00	0.02	0.00	98.02
E06	67.26	30.35	0.40	0.08	0.38	0.33	0.00	0.00	0.00	98.80
E07	67.30	30.58	0.10	0.00	0.79	0.12	0.00	0.00	0.01	98.90
E08	66.37	30.40	0.71	0.18	0.51	0.19	0.00	0.00	0.00	98.37
F05	56.95	31.80	5.78	1.34	0.44	0.06	0.15	0.05	0.00	96.56
F06	63.89	30.41	0.96	0.03	0.18	0.00	0.22	0.00	0.00	95.69
F07	59.62	30.76	2.77	0.01	0.61	0.04	0.04	0.01	0.00	93.86
F08	49.49	34.57	9.33	0.05	1.66	0.07	0.16	0.22	0.03	95.58

F10	63.91	30.62	0.99	0.06	0.36	0.11	0.31	0.00	0.00	96.35
F11	63.94	30.11	0.05	0.05	0.25	0.23	0.81	0.00	0.00	95.43
F12	63.33	30.14	1.04	0.09	0.43	0.12	0.18	0.00	0.00	95.33
F13	66.58	30.80	0.07	0.01	0.29	0.00	0.30	0.00	0.00	98.06
F14	50.19	35.96	9.10	0.07	2.30	0.01	0.07	0.12	0.06	97.87
F15	64.32	31.22	1.36	0.18	0.35	0.11	0.37	0.00	0.00	97.91
F17	65.36	30.83	0.91	0.08	0.36	0.01	0.11	0.00	0.02	97.68
F18	61.89	28.65	0.00	0.06	0.45	0.13	0.39	0.00	0.00	91.57
F19	62.18	29.13	0.02	0.00	0.51	0.09	0.46	0.00	0.01	92.39
F20	60.96	29.45	0.88	0.03	0.44	0.20	0.39	0.00	0.00	92.35
F21	62.45	28.95	0.06	0.01	0.41	0.13	0.34	0.00	0.00	92.37
F22	61.99	28.98	0.32	0.06	0.26	0.19	0.43	0.00	0.00	92.23
F23	52.63	31.69	4.98	0.02	0.91	0.29	0.35	0.00	0.00	90.89
F24	62.63	29.12	0.42	0.00	0.45	0.26	0.15	0.00	0.01	93.04
F25	63.31	29.15	0.40	0.00	0.37	0.32	0.09	0.00	0.00	93.63
F26	64.02	29.32	0.13	0.00	1.07	0.25	0.14	0.00	0.00	94.94
F27	59.94	28.11	0.52	0.01	0.79	0.39	0.22	0.00	0.00	89.98
F28	63.17	29.15	0.11	0.00	0.34	0.07	0.23	0.00	0.03	93.10
F29	61.94	29.60	0.22	0.00	3.83	0.75	0.52	0.00	0.01	96.88
F30	63.18	32.51	2.74	0.04	0.65	0.23	0.32	0.02	0.00	99.70
F31	62.39	30.45	1.31	0.00	0.36	0.09	0.31	0.00	0.01	94.92
F32	65.03	30.26	0.27	0.11	0.18	0.15	0.44	0.00	0.00	96.44
F33	63.38	31.13	0.95	0.00	0.30	0.16	0.87	0.00	0.00	96.80
F34	65.80	30.60	0.47	0.03	0.24	0.00	0.15	0.00	0.00	97.29
F35	65.84	30.32	0.13	0.15	0.21	0.00	0.28	0.00	0.03	96.96
F36	66.71	30.41	0.00	0.11	0.30	0.17	0.29	0.00	0.00	97.99
F37	65.77	30.38	0.06	0.07	0.28	0.06	0.42	0.00	0.00	97.05
F38	54.78	34.92	5.25	1.87	0.41	0.00	2.95	0.02	0.01	100.20
F39	65.25	30.04	0.12	0.05	0.22	0.00	0.27	0.00	0.00	95.96
F40	66.12	30.30	0.06	0.23	0.17	0.02	0.37	0.00	0.00	97.26
F46	65.78	30.94	0.24	0.00	0.75	0.16	0.39	0.00	0.00	98.25
F47	65.45	30.71	0.21	0.05	0.73	0.03	0.38	0.00	0.00	97.56
F48	65.77	31.20	0.36	0.13	0.66	0.18	0.49	0.00	0.03	98.82
F49	64.98	31.43	1.18	0.21	0.65	0.21	0.45	0.00	0.00	99.11
F50	59.96	31.69	2.61	0.07	1.04	0.14	0.44	0.01	0.00	95.97
F51	66.88	31.26	0.09	0.06	0.53	0.18	0.51	0.00	0.00	99.51
F52	65.02	30.90	0.16	0.06	1.28	0.10	0.44	0.00	0.00	97.94
F53	65.05	30.54	0.19	0.01	1.15	0.27	0.30	0.00	0.00	97.51
F54	63.33	30.16	0.99	0.12	0.34	0.00	0.21	0.00	0.03	95.18

The structural formulae are calculated on the basis of 4 oxygen (equivalent to 8 electrovalency), $Fe^{3+} = 8 - Si^{4+} - Fe^{2+}(total) - Ca^{2+} - Al^{3+} - Mn^{2+} - Ti^{4+} - Mg^{2+}$; $Fe^{2+} = Fe(total) - Fe^{3+}$.

Table C-5: EPMA analysis of albite (wt%) and structural formula

point No.	140	141	142	144	146
K_2O	0.05	0.06	0.05	0.06	0.05
SiO_2	68.91	67.40	68.79	67.84	68.12
FeO	0.23	0.60	0.00	0.22	0.01
F	0.04	0.01	0.00	0.07	0.13
Na_2O	11.89	11.41	11.04	11.41	11.60
CaO	0.20	0.00	0.25	0.18	0.28
Al_2O_3	19.41	19.07	19.10	18.73	19.16
MgO	0.00	0.15	0.00	0.06	0.03
MnO	0.08	0.04	0.00	0.00	0.06
Cl	0.00	0.00	0.00	0.00	0.00
P_2O_5	0.05	0.02	0.02	0.00	0.00
CoO	0.00	0.04	0.07	0.00	0.11
TiO_2	0.01	0.00	0.03	0.00	0.00
Total	100.87	98.80	99.35	98.57	99.54

strutural fomula mushy silicate basing plagioclase

K	0	0	0	0	0
Si	2.99	2.99	3.04	3.02	3.00
Fe	0.01	0.02	0.00	0.01	0.00
F	0.04	0.01	0.00	0.07	0.13
Na	1.00	0.98	0.95	0.98	0.99
Ca	0.01	0.00	0.01	0.01	0.01
Al	0.99	1.00	1.00	0.98	0.99

Table C-6: EPMA analysis of chlorite (wt%) and structural formula

point	55	52	53	54	107	108	109	110	128
SiO_2	23.09	23.81	23.46	24.29	24.13	25.16	24.50	24.68	24.76
Al_2O_3	18.66	19.59	19.68	19.34	18.20	18.06	15.70	18.39	18.49
TiO_2	0.00	0.03	0.00	0.00	0.00	0.00	0.00	0.02	0.00
FeO	39.85	37.70	36.37	36.38	36.34	36.57	36.90	37.73	37.81
MnO	0.66	0.65	0.67	0.83	0.41	0.56	0.28	0.36	0.47
MgO	4.85	6.57	6.09	6.64	6.30	6.57	6.59	6.52	6.67
CaO	0.04	0.07	0.02	0.03	0.04	0.02	0.40	0.14	0.04
Na_2O	0.05	0.00	0.00	0.10	0.02	0.06	0.06	0.18	0.02
K_2O	0.00	0.04	0.02	0.00	0.00	0.00	0.00	0.02	0.00
F	0.06	0.14	0.09	0.12	0.16	0.12	0.12	0.04	0.06
Cl	0.01	0.00	0.01	0.00	0.02	0.03	0.04	0.04	0.01
Total	87.25	88.60	86.40	87.73	85.61	87.15	84.57	88.12	88.32
strutural fomula of chlorite and related parameter									
Si	5.37	5.37	5.39	5.49	5.60	5.72	5.81	5.58	5.58
Al (IV)	2.63	2.64	2.61	2.51	2.40	2.28	2.19	2.42	2.42
Al	2.49	2.57	2.73	2.64	2.58	2.56	2.19	2.48	2.49
Ti	0.00	0.01	0.00	0.00	0.00	0.00	0.00	0.00	0.00
Fe	7.75	7.10	6.99	6.87	7.06	6.95	7.31	7.14	7.13
Mn	0.13	0.12	0.13	0.16	0.08	0.11	0.06	0.07	0.09
Mg	1.68	2.21	2.09	2.24	2.18	2.23	2.33	2.20	2.24
Ca	0.01	0.02	0.00	0.01	0.01	0.01	0.10	0.03	0.01
Na	0.02	0.00	0.00	0.05	0.01	0.03	0.03	0.08	0.01
K	0.00	0.01	0.01	0.00	0.00	0.00	0.00	0.01	0.00
F	0.04	0.10	0.07	0.09	0.12	0.08	0.09	0.03	0.04
Cl	0.00	0.00	0.00	0.00	0.01	0.01	0.02	0.01	0.00
OH	15.96	15.90	15.93	15.91	15.88	15.91	15.90	15.96	15.95
(Fe+Mn)/(Fe+Mn+Mg)	0.82	0.77	0.77	0.76	0.77	0.76	0.76	0.77	0.76

Table C-7: Chemical analyses of major elements (wt%) and trace elements (ppm) for Cihai deposit

sample name	CH37	CH47	CH72	CH235	CH241	CH246	CH247	CH248	CH 204B	CH 204A
litho.	gsk	bpsb	gsk	mgt	mds	gsk	mds	psk	bp	bp
SiO_2	45.84	52.24	43.71	14.47	50.13	32.96	49.11	39.66	56.11	50.77
TiO_2	0.61	0.93	0.38	0.59	2.05	0.47	1.91	0.27	0.95	0.22
Al_2O_3	10.34	15.12	8.67	4.46	13.27	6.9	13.8	7.75	14.98	7.43
Fe_2O_3	4.99	3.82	6.90	51.01	3.86	16.83	3.41	6.21	2.17	3.13
FeO	8.91	5.64	7.42	23.85	7.91	15.81	6.29	12.95	6.26	10.7
MnO	0.47	0.16	0.42	0.2	0.26	0.27	0.19	0.33	0.14	0.38
MgO	5.13	4.31	5.51	3.12	5.39	5.55	4.71	7.3	2.49	4.31
CaO	21.69	7.76	26.27	8.44	9.4	15.22	13.13	21.47	6.18	17.17
Na_2O	0.69	2.82	0.18	0.21	4.05	0.52	3.94	0.15	3.68	2.05
K_2O	0.8	4.23	0.13	0.33	0.61	0.97	0.24	0.36	5.41	1.45
P_2O_5	0.11	0.07	0.26	0.29	0.26	0.37	0.25	0.56	0.18	0.06
LOI	1.51	3.41	1.53	0.62	3.48	7.03	3.78	4.26	1.96	3.01
Total	100.58	100.13	100.69	102.5	100.26	101.22	100.43	100.65	100.29	100.37
ZnO		0.0059		0.025						
S		0.76591		0.68225						
CuO		0.04432		0.02506						
V_2O_5		0.02083		0.02078						
NiO		0.00754		0.01517						
BaO		0.19905								
SrO		0.02868								
Co_3O_4		0.01134								
Cr_2O_3		0.00707								

gsk: garnet-pyroxene skarn; psk: pyroxene-rich skarn; bpsb: black phase with skarn breccia; mgt: magnetite; mds: mafic dyke swarm; bp: black phase.

table C-7 continued:

sample name	CH37	CH47	CH72	CH235	CH241	CH246	CH247	CH248	CH 204B	CH 204A
litho.	gsk	bpsb	gsk	mgt	mds	gsk	mds	psk	bp	bp
La	12.23	36.19	29.24	16.99	17.27	22.89	13.58	37.82	33.69	22.26
Ce	31.67	73.93	70.49	25.93	40.43	47.82	32.27	67.17	62.47	38.79
Pr	4.78	9.05	9.12	2.9	5.77	5.54	4.95	8.37	7.76	4.68
Nd	23.18	35.72	35.3	10.78	28.27	22.97	24.71	32.16	29.26	16.6
Sm	5.4	6.36	6.91	1.49	7.09	3.91	6.48	5.62	5.22	3.84
Eu	1.3	1.21	3	0.57	1.94	1.85	1.9	2.57	0.83	0.43
Gd	5.45	5.87	6.41	1.51	8.13	4.48	7.7	6.18	5.43	3.42
Tb	0.9	0.91	0.96	0.24	1.4	0.67	1.38	0.94	0.88	0.57
Dy	5.21	4.8	5.52	1.21	8.18	4.03	8.2	5.08	4.77	3.74
Ho	1.01	0.97	1	0.28	1.87	0.78	1.79	1.03	1	0.77
Er	2.98	2.89	2.76	0.76	4.9	2.1	5.35	2.85	3.09	2.13
Tm	0.42	0.47	0.4	0.11	0.81	0.29	0.83	0.44	0.45	0.34
Yb	2.59	3.12	2.62	0.75	4.8	1.71	4.92	2.81	2.93	2.37
Lu	0.37	0.46	0.37	0.11	0.7	0.25	0.78	0.42	0.43	0.4
Y	26.8	24.95	25.01	7.01	43.2	18.66	40.67	23.67	26.92	21.67
Li	7.63	18.79	5.92	9.07	17.4	19.19	19.65	12.76	11.68	5.28
Be	1.9	2.51	1.23	0.21	1	0.64	1.05	0.64	1.61	3.01
Sc	17.18	23.18	11.29	2.25	33.82	7.7	32.74	9.98	18.58	8.06
Ti	3653	6069	2162	2946	12711	2580	11849	1209	5093	880.9
V	151.7	148.9	77	114.88	253.36	108.31	263.92	52.3	619.83	147.18
Cr	84.81	289.14	326.03	159.66	155.83	48.96	118.25	34.62	263.18	328.46
Mn	4031	1330	3586	1590	2060	2159	1526	2645	1027	3063
Co	37.47	116.68	20.9	87.94	28.02	114.96	28.48	51.49	66.38	26.83
Ni	74.44	215.74	238.48	189.43	67.55	209.99	50.09	66.09	171.93	240.29
Cu	175.88	425.25	111.81	153.09	27.02	99.68	14.93	37.85	195.66	138.17
Zn	64.99	287.9	155.1	235.31	56.93	75.84	45.47	61.15	118.64	93.05
Ga	13.53	19.09	14.67	26.38	18.61	24.69	19.11	14.66	11.53	10.58
Rb	41.96	149.69	5.12	4.81	15.44	9.48	8.15	4.5	128.38	31.65
Sr	126.1	851.86	39.64	33.31	130.31	55.62	68.57	43.1	451.96	150.62
Zr	125.56	200.36	100.5	20.67	207.63	65.35	200.37	64.47	185.99	31.92
Nb	10.5	14.81	6.48	6.18	5	10.68	4.8	2.21	15.33	3.28
Mo	3.86	21.85	29.9	16.44	7.6	3.02	2.74	2.04	29.31	41.65
Cd	0.06	0.14	0.14	0.02	0.1	0.04	0.11	-	0.14	0.12
Sn	4.51	1.21	13.64	14.11	1.88	28.96	1.39	13.3	1.18	0.78
Cs	1.74	1.59	0.33	0.29	1.59	0.38	0.7	0.24	0.75	0.41
Ba	74.48	1945.64	52.32	45.52	80.82	140.63	38.41	38.21	1765.75	225.52
Hf	3.91	6.34	3.06	0.64	6.58	2.23	6.53	1.99	6.15	1.01
Ta	0.98	1.41	0.58	0.48	0.45	0.83	0.41	0.28	1.63	0.29

W	0.76	1.82	2.89	2.54	1.33	1.03	1.84	0.4	3.06	2.45
Pb	1.17	3.66	2.36	2.77	1.75	4.1	2.38	1.86	1.89	6.03
Bi	0.15	0.46	0.15	0.21	0.16	0.3	0.11	0.1	0.34	0.07
Th	10.83	18.37	12.05	5.86	2.2	7.97	2.11	9.95	21.93	5.12
U	4.81	3.63	4.31	1.43	0.58	1.62	0.74	3.03	23.74	2.96

Fig. C-1

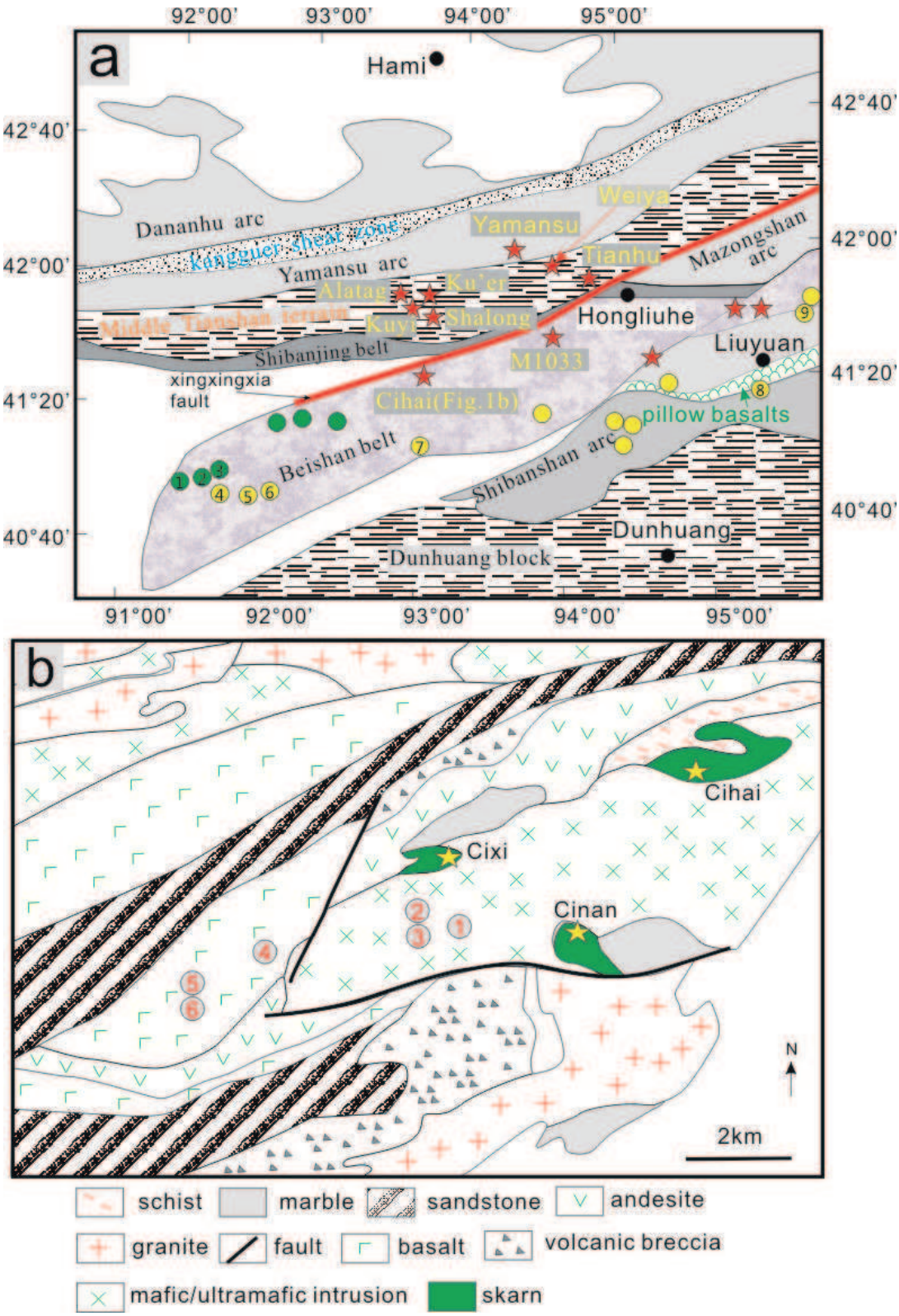
a
Hami
92°00'
93°00'
94°00'
95°00'
42°40'
42°00'
41°20'
40°40'
Dananhu arc
Kangguer shear zone
Yamansu arc
Middle Tianshan terrain
Shibanjing belt
xingxingxia fault
Beishan belt
Yamansu
Weiya
Tianhu
Mazongshan arc
Alatage
Ku'er
Kuyi
Shalong
M1033
Cihai(Fig.1b)
Hongliuhe
Liuyuan
pillow basalts
Shibanshan arc
Dunhuang
Dunhuang block
b
Cihai
Cixi
Cinan
N
2km
schist
marble
sandstone
andesite
granite
fault
basalt
volcanic breccia
mafic/ultramafic intrusion
skarn

Fig. C-2

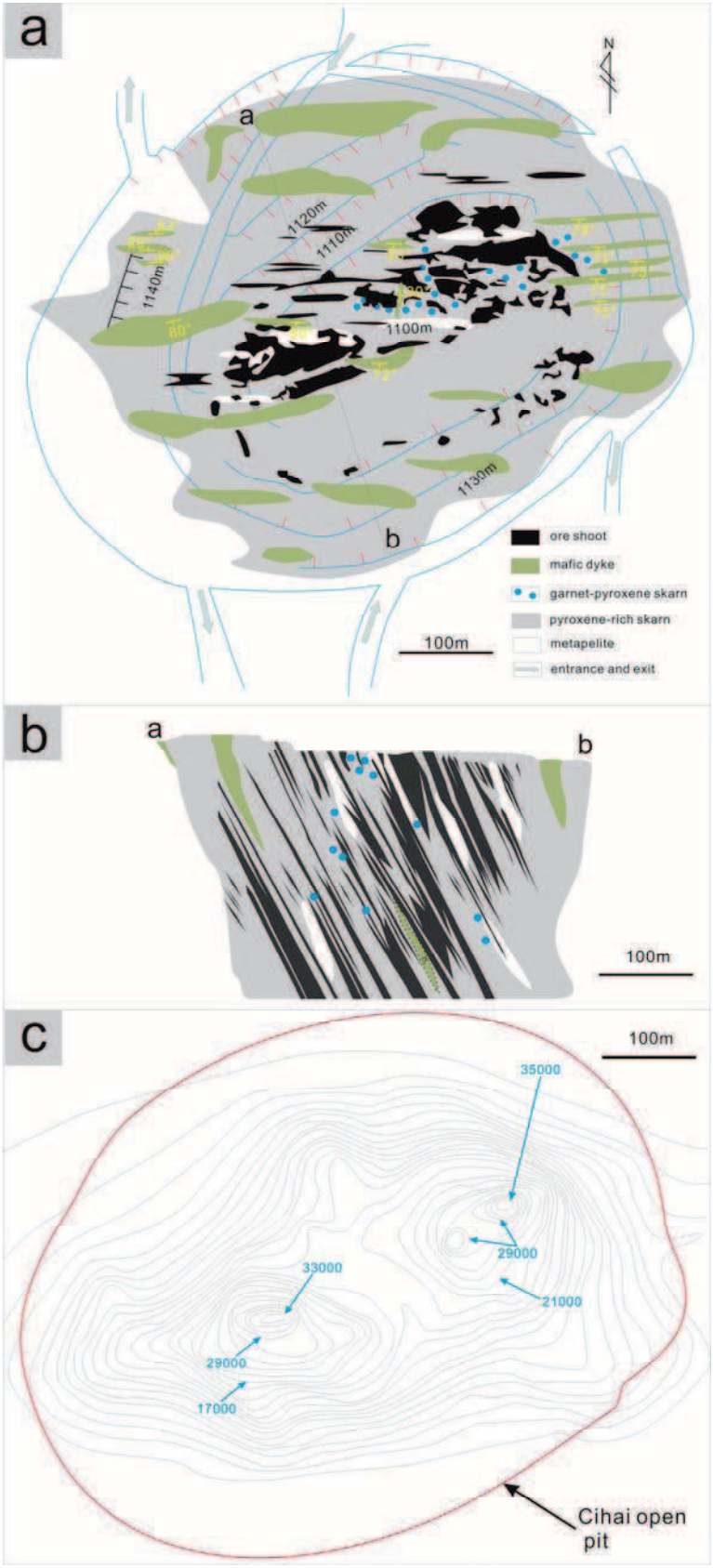
a
N
a
1120m
1110m
1140m
1100m
1130m
b
ore shoot
mafic dyke
garnet-pyroxene skarn
pyroxene-rich skarn
metapelite
entrance and exit
100m
b
a
b
100m
c
100m
35000
29000
33000
21000
29000
17000
Cihai open pit

Fig. C-3

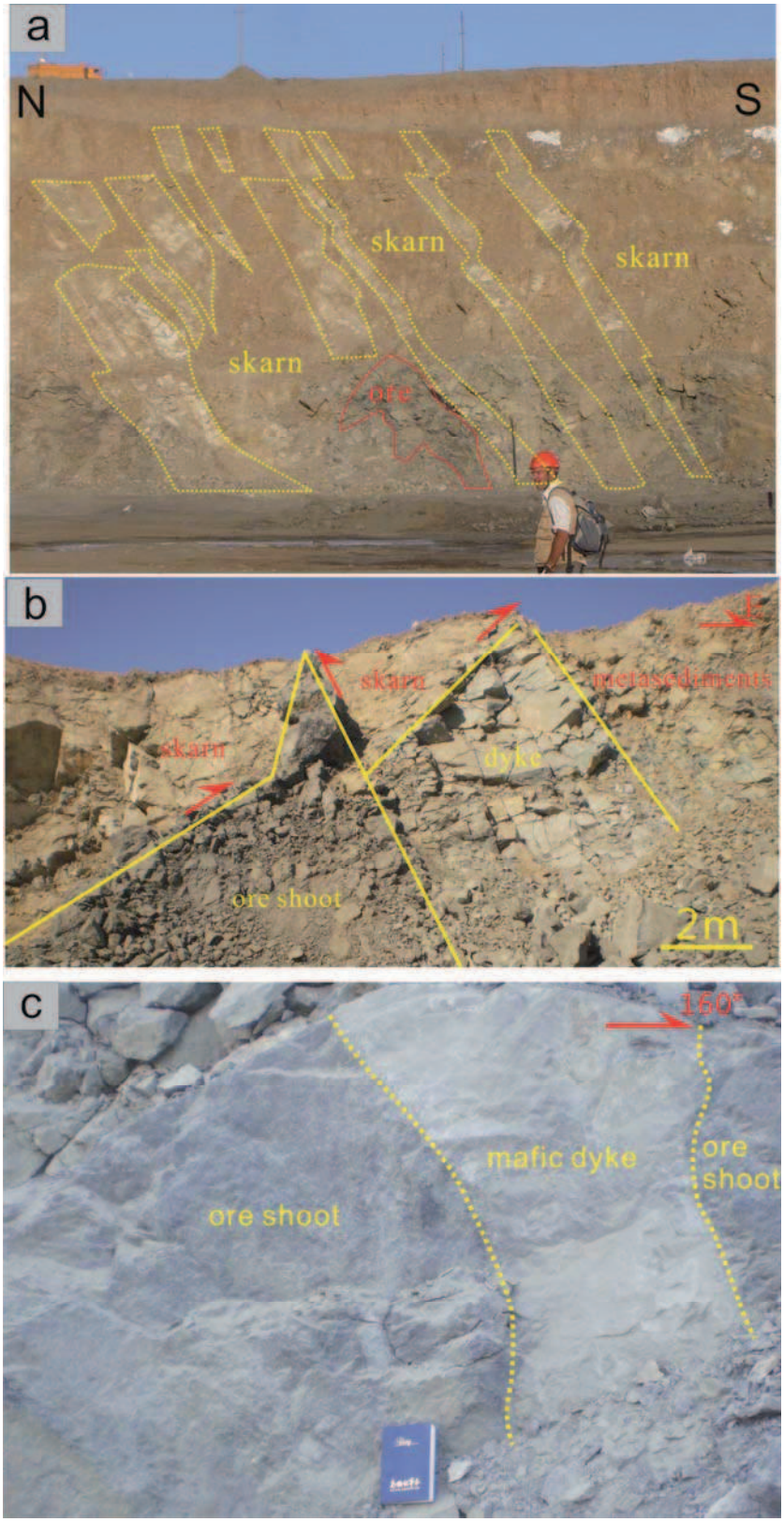
a
N
S
skarn
skarn
skarn
ore
b
skarn
skarn
metasediments
dyke
ore shoot
2m
c
160°
mafic dyke
ore shoot
ore shoot

Fig. C-4

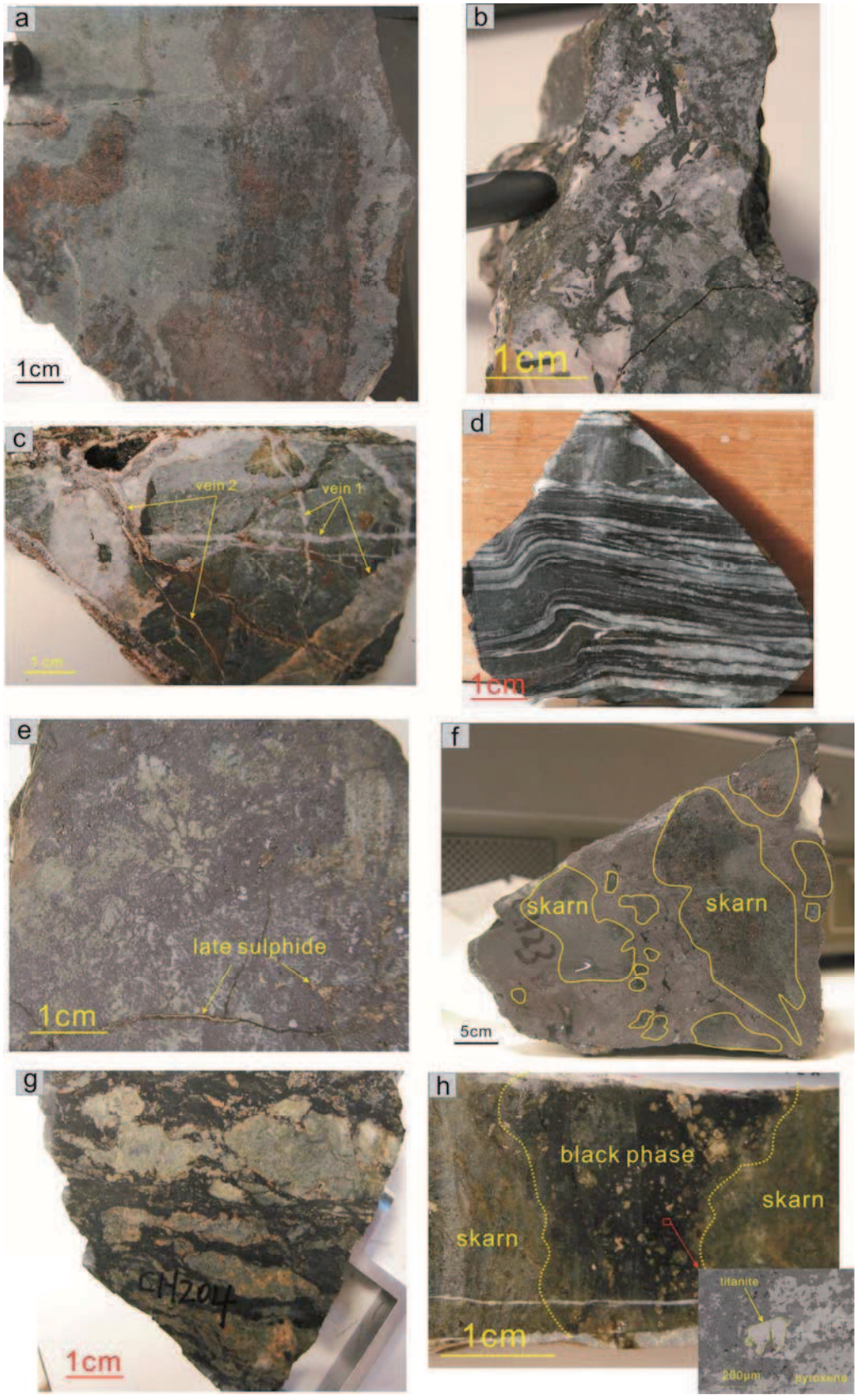
a
1cm
b
1cm
c
vein 2
vein 1
1cm
d
1cm
e
late sulphide
1cm
f
skarn
skarn
5cm
g
1cm
h
black phase
skarn
skarn
1cm
titanite
200μm
pyroxene

Fig. C-5

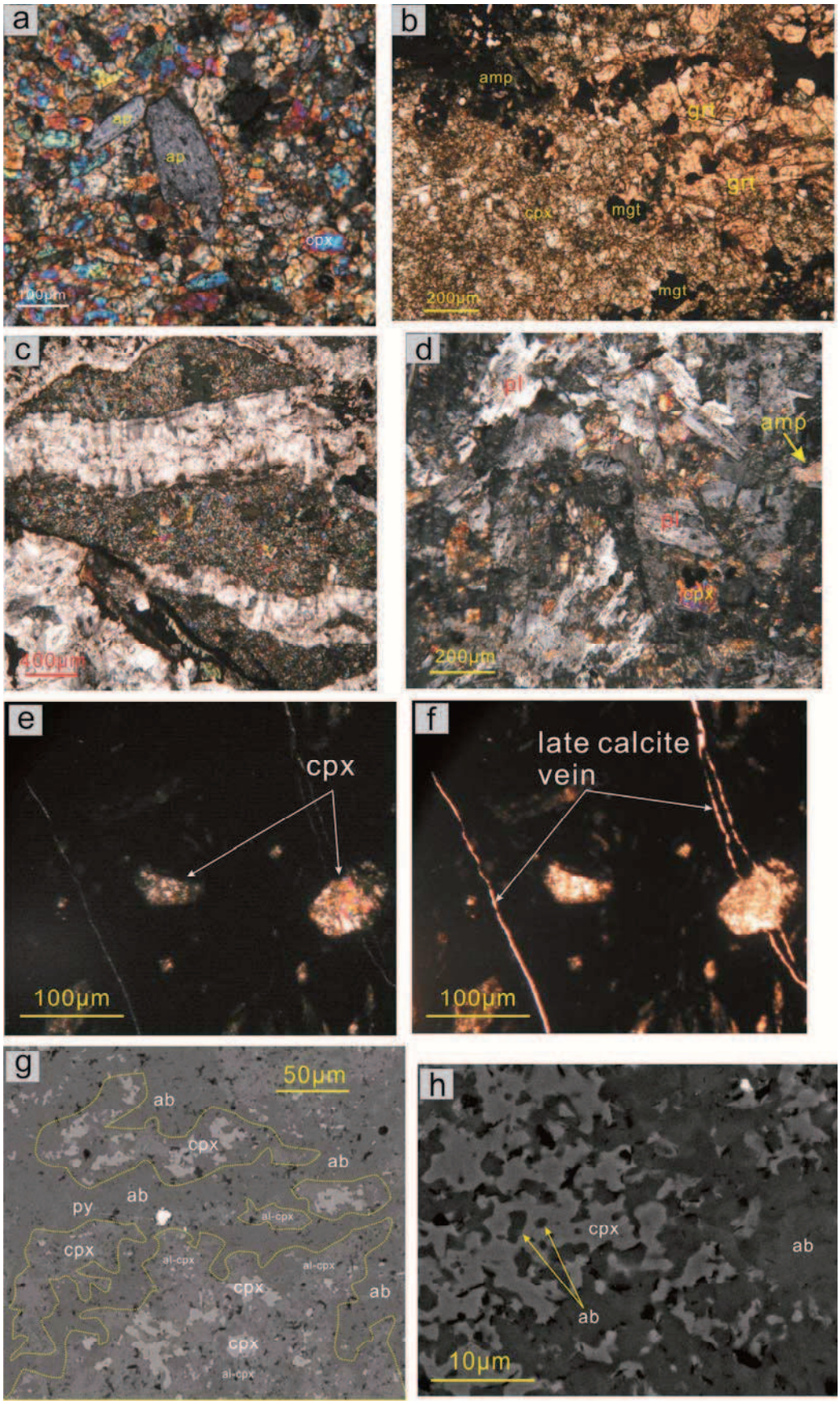
a
ap
ap
cpx
100μm
b
amp
grt
grt
cpx
mgt
mgt
200μm
c
400μm
d
pl
amp
pl
cpx
200μm
e
cpx
100μm
f
late calcite
vein
100μm
g
50μm
ab
cpx
ab
ab
py
al-cpx
cpx
al-cpx
al-cpx
cpx
ab
cpx
al-cpx
h
cpx
ab
ab
10μm

Fig. C-6

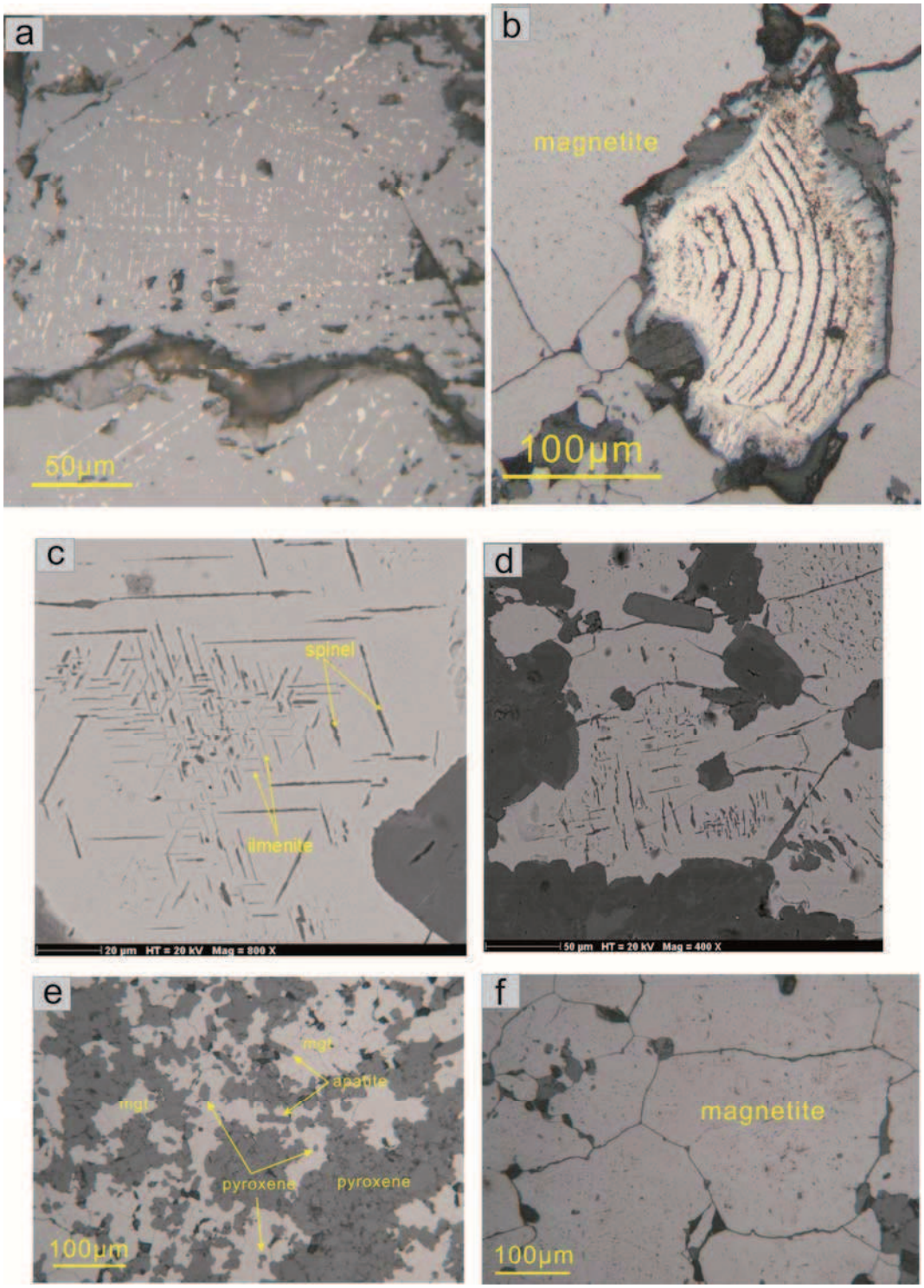
a
50μm
b
magnetite
100μm
c
spinel
ilmenite
20 μm HT = 20 kV Mag = 800 X
d
50 μm HT = 20 kV Mag = 400 X
e
mgt
apatite
mgt
pyroxene
pyroxene
100μm
f
magnetite
100μm

Fig. C-7

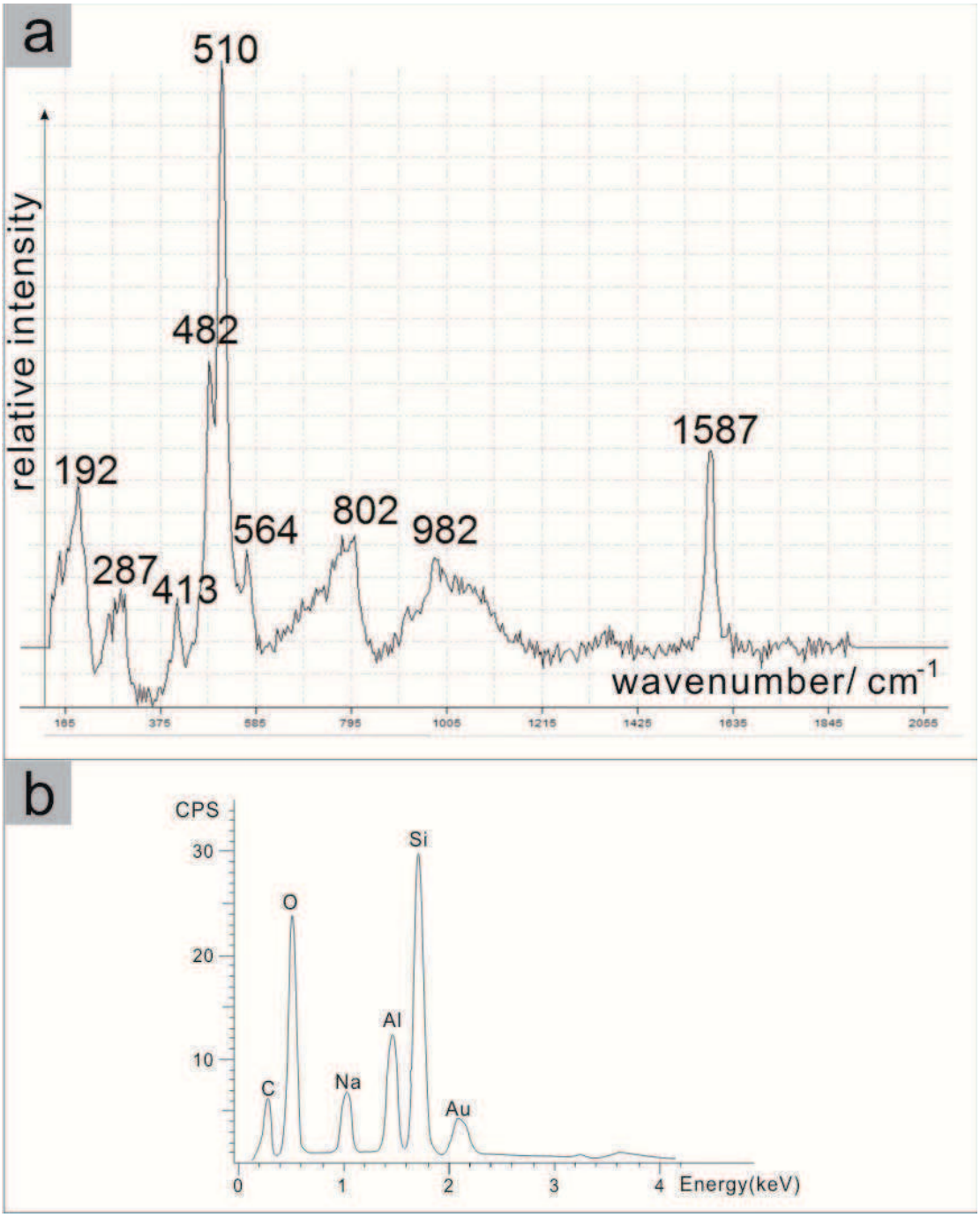
a
510
482
192
287
413
564
802
982
1587
relative intensity
wavenumber/ cm-1
165
375
585
795
1005
1215
1425
1635
1845
2055
b
CPS
30
20
10
O
Si
Al
C
Na
Au
0
1
2
3
4
Energy(keV)

Fig. C-8

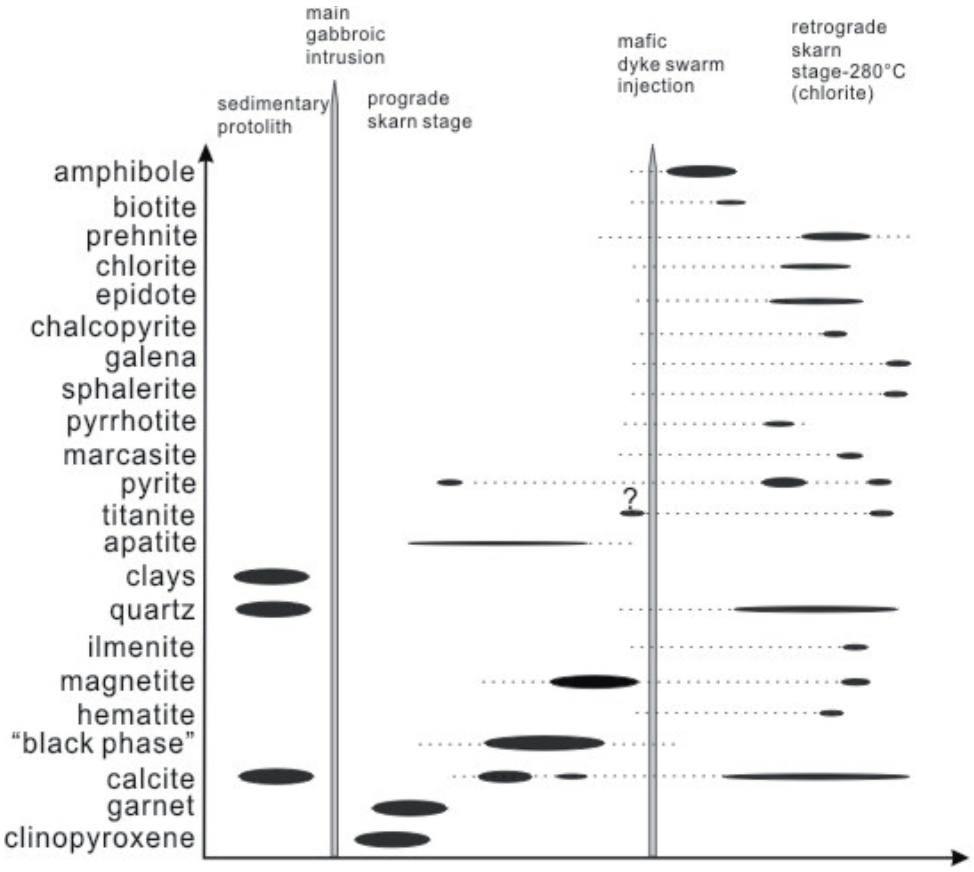
main
gabbroic
intrusion
sedimentary
protolith
prograde
skarn stage
mafic
dyke swarm
injection
retrograde
skarn
stage-280°C
(chlorite)
amphibole
biotite
prehnite
chlorite
epidote
chalcopyrite
galena
sphalerite
pyrrhotite
marcasite
pyrite
titanite
apatite
clays
quartz
ilmenite
magnetite
hematite
"black phase"
calcite
garnet
clinopyroxene
?

Fig. C-9

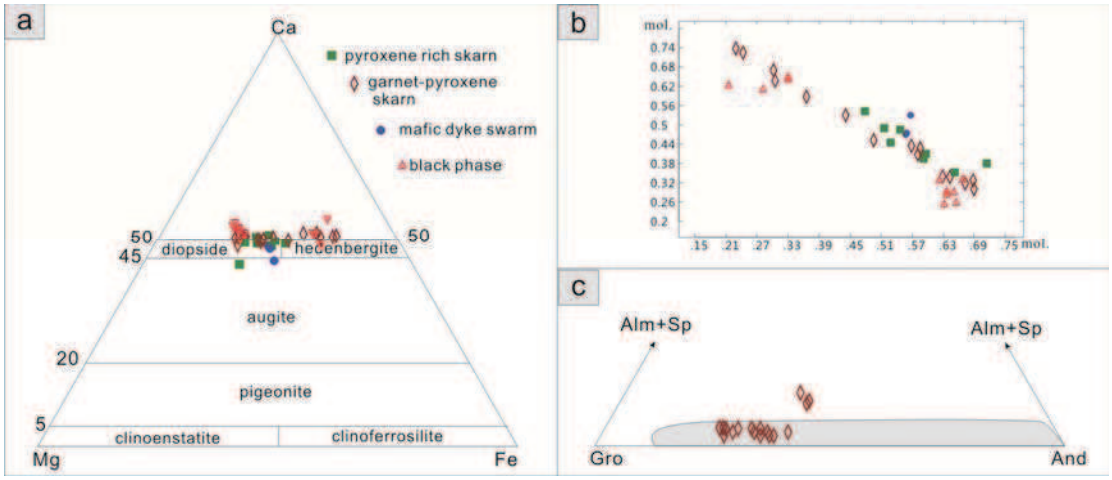
a
Ca
pyroxene rich skarn
garnet-pyroxene
skarn
mafic dyke swarm
black phase
50
45
diopside
hedenbergite
50
augite
20
pigeonite
5
clinoenstatite
clinoferrosilite
Mg
Fe
b
mol.
0.74
0.68
0.62
0.56
0.5
0.44
0.38
0.32
0.26
0.2
.15 .21 .27 .33 .39 .45 .51 .57 .63 .69 .75 mol.
c
Alm+Sp
Alm+Sp
Gro
And

Fig. C-10

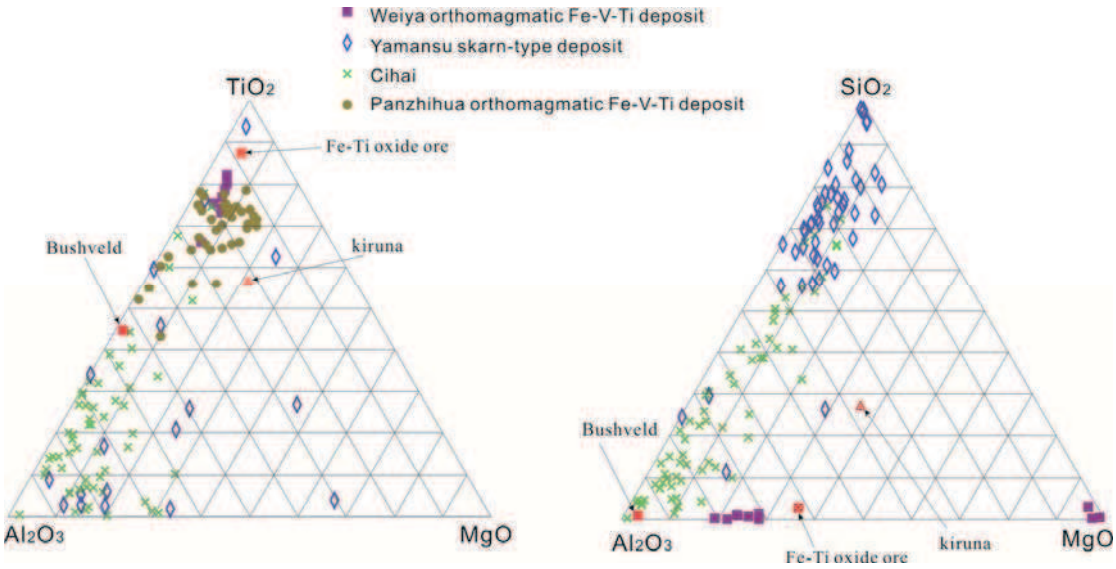

Fig. C-11

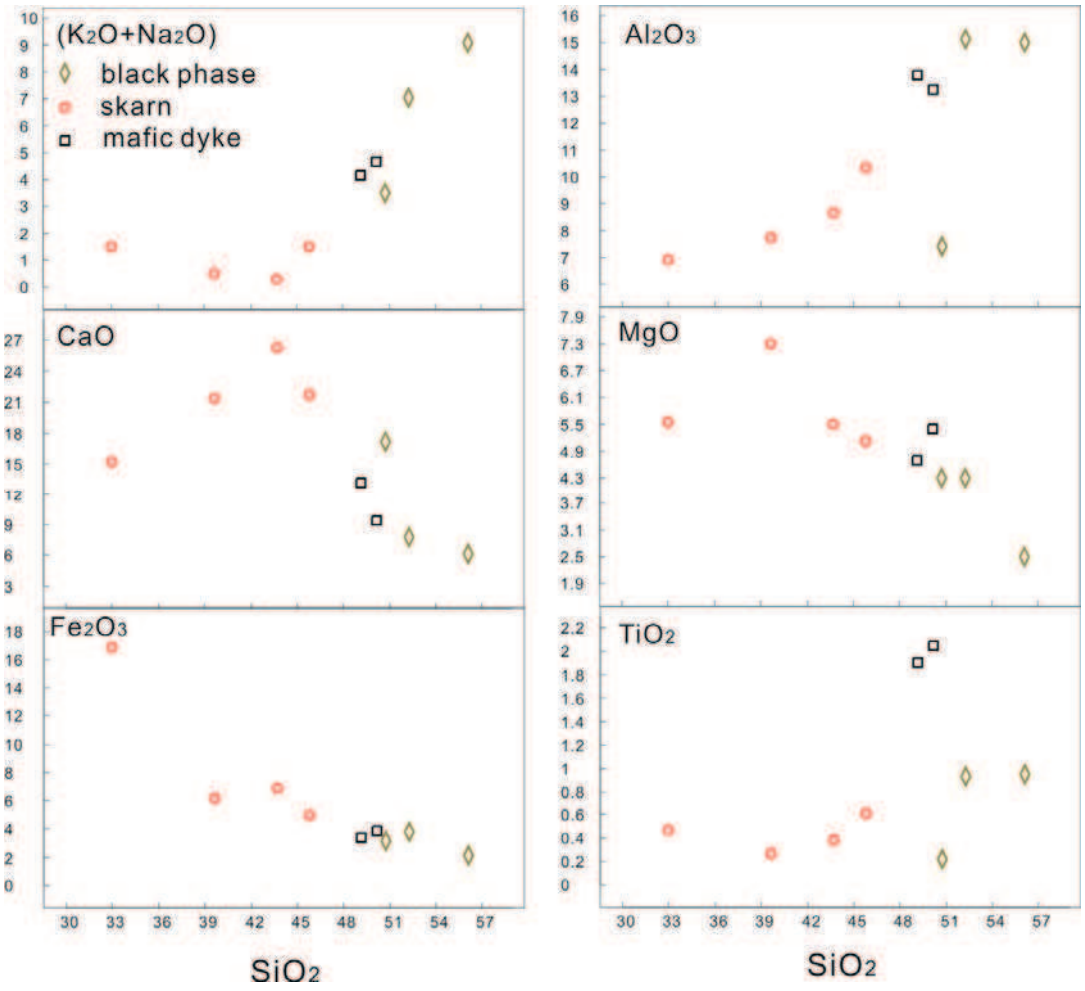

Fig. C-12

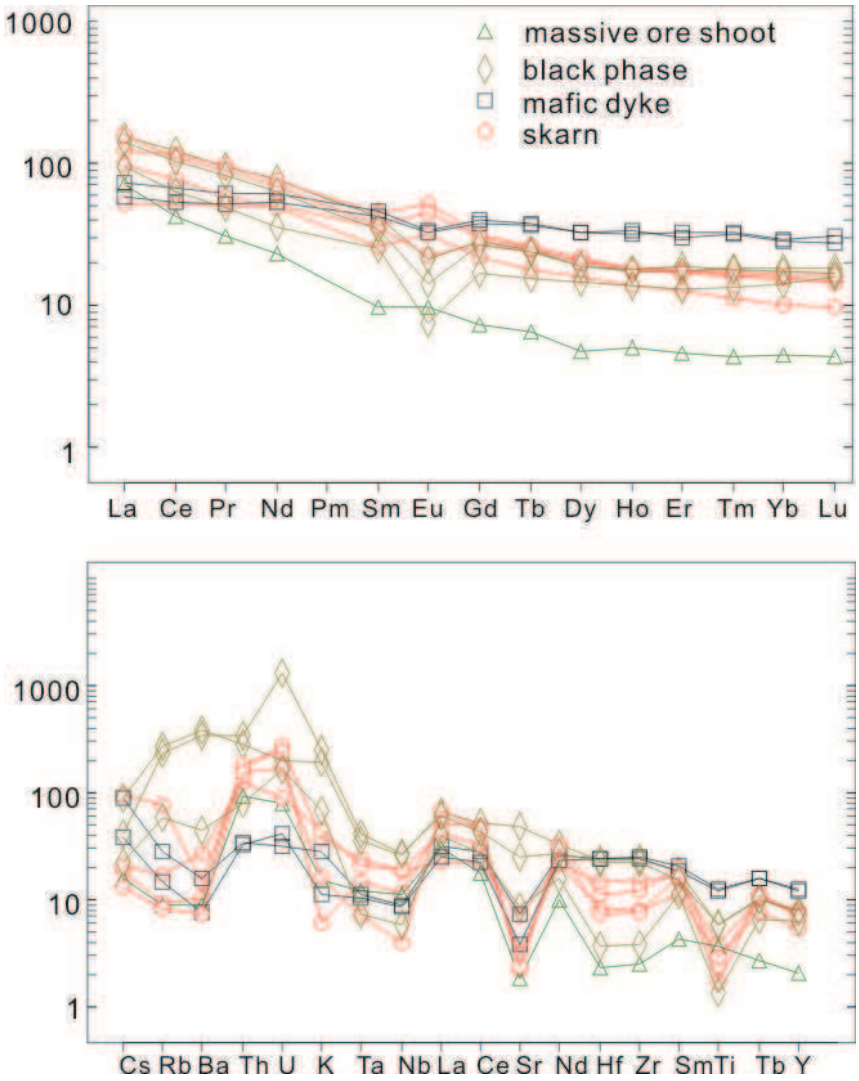

Fig. C-13

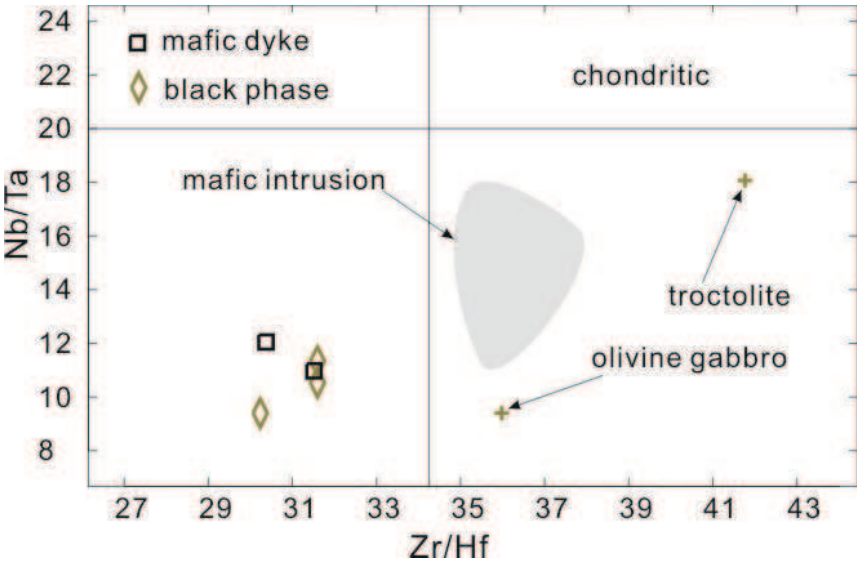

Fig. C-14

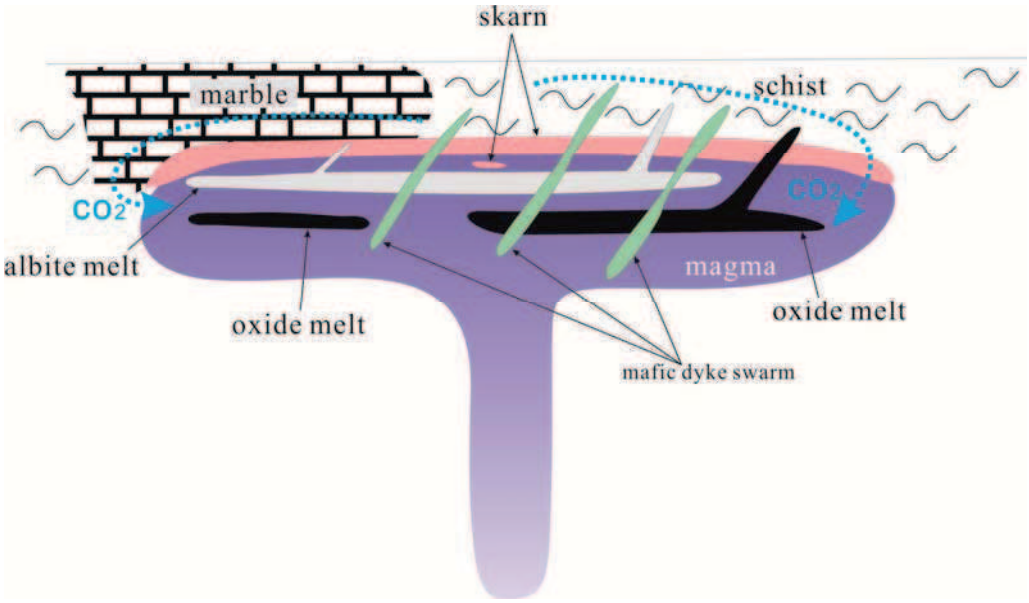
skarn
marble
schist
CO2
CO2
albite melt
magma
oxide melt
oxide melt
mafic dyke swarm

Chapter 5 Metallogenic implication and geodynamical significance of iron skarn-related deposits in eastern Tianshan

Résumé:

Dans ce chapitre, les minéralisations de Yamansu et Cihai sont comparées. Dans le premier gisement, l'origine de la concentration en magnétite semble associé à la circulation d'un fluide riche en fer qui par ailleurs induit une skarnification pervasive de l'encaissant. A Cihai, par contre, la genèse du minerai paraît plus intimement liée à des processus magmatique à travers des processus d'immiscibilité magmatique et probablement d'assimilation. Les minéralisations étudiées sont ensuite replacées dans l'évolution géodynamique du Tianshan oriental.

Abstract:

A brief synthesis has been made in the chapter. Both the Yamansu magnetite deposit (YMD) and Cihai magnetite deposit (CMD) share similar features, however, they are different. Comparisons between YMD and CMD showed that, for the skarnization, pervasive iron-rich fluid and assimilation-immiscibility play an important role for concentration of iron, respectively. In this chapter, a schematic geodynamic evolution and mineralization model in eastern Tianshan has been proposed.

5.1 Short reviews on Yamansu and Cihai magnetite deposits

Comparisons between Yamansu magnetite deposit (YMD) and Cihai magnetite deposit (CMD) showed that:

(1) Both of them hold massive ore shoots. For the skarn, the former one contains massive garnet skarn, from contact part to peripheral part, zonation was relatively clear: high temperature prograde zone to low temperature retrograde zone. CMD hold massive pyroxene-rich skarn and zonation was not clear, however, later hydrothermal alteration well developed;

(2) In CMD, the massive ore shoots were later than the pyroxene-rich skarn and garnet-pyroxene skarn. In addition, magnetite ore shoots corroded the earlier skarn. While in the YMD, it was the iron-fluid that corroded the limestone and gave birth to the massive garnet skarn;

(3) It seems that the massive garnet skarn forming temperature in YMD was about 500-550°C. In CMD, the forming temperature of pyroxene-skarn and garnet-pyroxene was probably higher. The exsolution of spinel and ilmenite in magnetite which corroded the skarn indicated very high forming temperature;

(4) Sedimentary assimilation and iron oxide-melt separation may play an important role during economic iron concentration in CMD; in YMD, extensive metasomatism controlled the skarn forming process;

(5) It seems that both the two deposit related to mafic-ultramafic magmatism; obviously, CMD was formed deeper then YMD (Fig. 5-1);

(6) Both the two deposits originated from iron rich fluid/melt which contributed to the massive magnetite ore shoots. In YMD, the iron rich fluid front reacted with limestone and produced garnet; in CMD, the iron melt brecciated and corroded the skarn (pyroxene-rich skarn and garnet-pyroxene skarn). A hydrothermal fluid can be defined as a hot (~50 to > 500°C) aqueous solution, containing solutes that are commonly precipitated as the solution changes its properties in space and time. It must be pointed out at the outset that the terms fluid and solution are

used interchangeably, although fluid sensu stricto refers to a phase at supercritical temperature in which a liquid no longer exists. It seems that the skarnization is always associated with fluid which has especial contributions to late hydrous alteration. Both in Yamansu and Cihai magnetite deposit, the late retrograde stages were dominated by chlorite, calcite ± epidote ± amphibole. In Yamansu magnetite deposit, the iron-rich fluid front is outline by garnet. The fluid caused extensive metasomatism, as well as extraction of iron from the basalt according to mass balance calculation. In the CMD, the magnetite stage was formed at high temperature. This iron source seems to be a residual part of mafic-ultramafic magma. It means that the mafic-ultramafic intrusion contacted with pelite and limestone leading to the formation of pyroxene-rich skarn and garnet-pyroxene skarn, and then, the iron rich phase altered the pre-existing skarn.

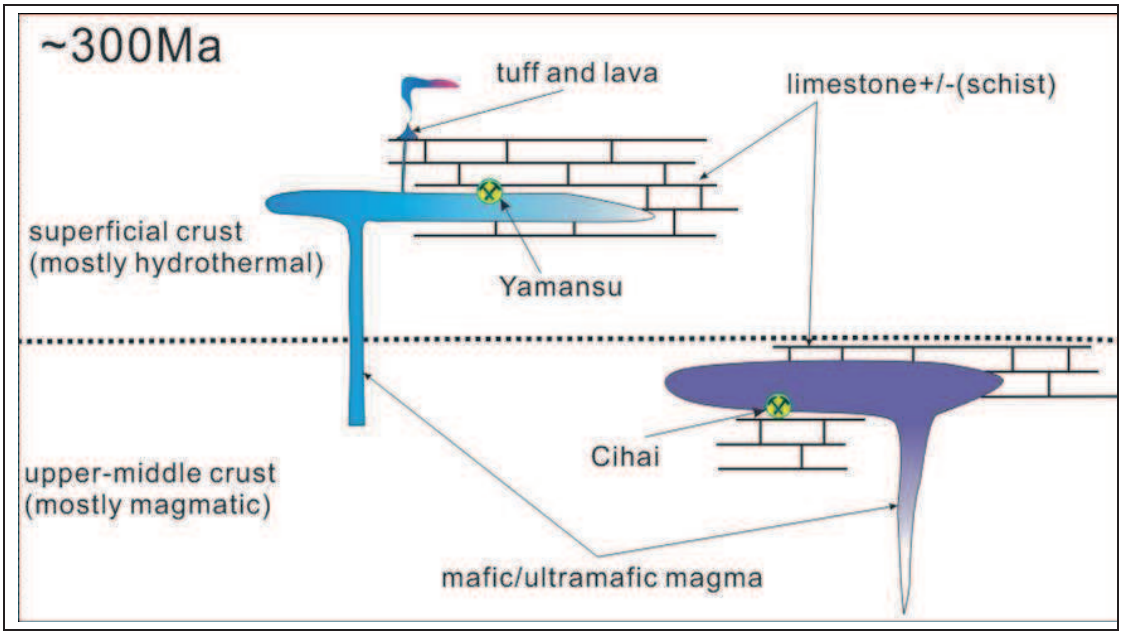

Fig. 5-1: A cartoon showing the forming depth of CMD and YMD.

5.2 Short review on ore deposits of eastern Tianshan

5.2.1 Iron deposits

Iron deposits which are now exploited in eastern Tianshan are distributed spanning tectonic units. In addition, these iron deposits are ascribed into different deposit types. The biggest one is Tianhu iron deposit which produced 800000t (with grade 50%) ore per year; it was a Precambrian sedimentary metamorphic deposit (Jia, 1991; Wu, 2008). Kumutage (also called Shanglong) iron deposit was a Precambrian BIF (XBGMR, 1993). Weiya is a typicall magmatic fractional V-Ti magnetite deposit (Wang et al., 2006; Wang et al., 2006) and dated to be 236Ma (Zhang et al., 2005). Alatag iron deposit is a skarn-type deposit caused by Carboniferous granite (unpublished data from Wu Changzhi). Skarn-related iron deposits in this region includes: Yamansu, Bailingshan, Heijianshan, Chilongfeng, Hongyuntan, Aqishan, Heilongfeng, Shuangfengshan (Mao et al. 2005). Skarnization extensively developed in this region, especially with magnetite mineralization, such as the biotite granite nearby the Shanglong BIF (Fig. 5-2).

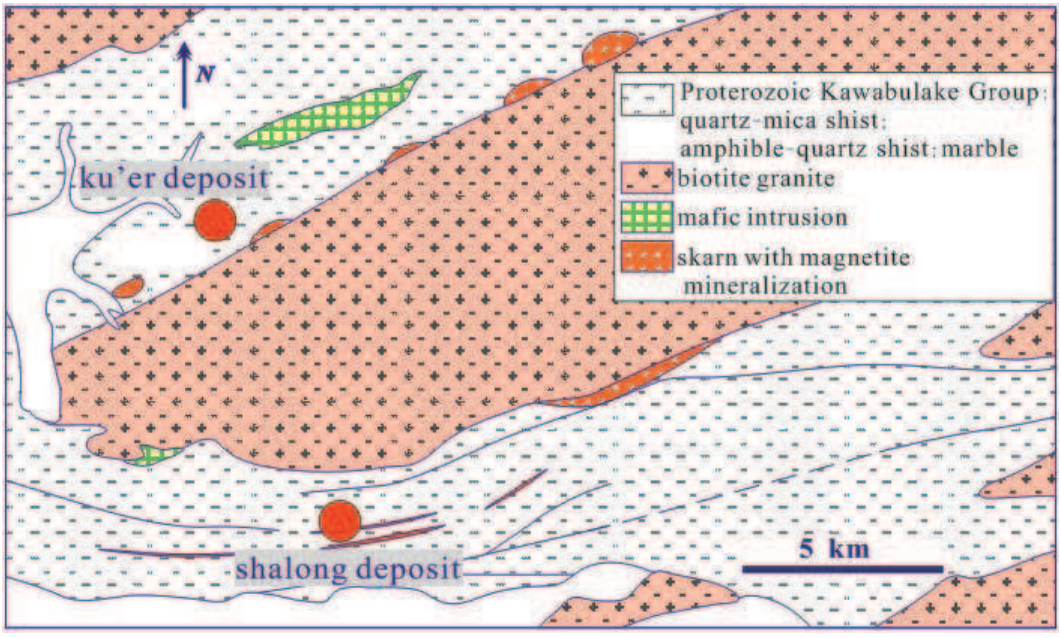

Fig. 5-2: Skarnization near the granite pluton in Centre Tianshan (Wu et al., 2011, report).

5.2.2 Cu-Ni-V-Ti-Au deposits

In addition to iron deposits, the eastern Tianshan was exploited for Cu, Ni, Pb, Zn, Au and Ag, as indicated in chapter 2. All the orthomagmatic Cu-Ni deposits seem relate to small size mafic-ultramafic magma. A case study (Branquet et al., 2012 submitted) from the Huangshandong deposit displayed that:

(1) The Ni-Cu-bearing mafic/ultramafic complexes are not layered intrusions, instead, they are sheeted intrusions emplaced by injection of successive mafic/ultramafic magma bathes. They emplaced through opening of extensional fractures during the course of Permian regional scale dextral inhomogeneous simple shearing;
(2) A rifting event during post-orogenic extension is not required;
(3) Huangshandong Ni-Cu-bearing mafic/ultramafic intrusions are neither parts of ophiolitic suture zone, nor dunite-core Alaskan-type ore deposits.

The Au-(Ag) deposits, mostly epithermal, seem to associate with the large scale shearing, such as Kanguer and Shiyingtan (Pirajno et al., 1997). Porphyry Cu deposits (Tuwu, Yandong, Chihu) are hosted by early Carboniferous granodiorite- and plagiogranite-porphyries which probably related to subduction and arc (Han et al., 2006). Cu-Ag-Pb-Zn skarn-related deposits in eastern Tianshan include: Weiquan, Shuangqing, Heiyingshan and Lubaishan. Their formations probably were caused by diorite dykes which were dated to be Permian (Mao et al., 2002; Li and Liu, 2003).

5.3 Geochronology and ore forming in eastern Tianshan

At the end of Carboniferous and in Permian it was a blooming period of mineralization for Fe-Cu-Ni-Ti-Au (Fig. 5-3). Tectonically, the developments of these late Paleozoic deposits were closely associated with the subduction and collision of the ancient north Tianshan ocean (Wang et al., 2010; Charvet et al., 2011) that intervened between the Tarim craton and the Siberian block. Mostly, these

mineralizations were skarn related iron deposits, porphyry Cu, magmatic Cu-Ni, Orogenic Au Ag and epithermal Au. In the early to mid-Carboniferous, probably the N-dipping subduction beneath the Dananhu arc generated magmatic intrusions, leading to formation of the porphyry Cu deposits (Yangdong and Tuwu Cu deposits) (Xiao et al., 2004). The magmatic front migrated southward to form the Yamansu arc in the late Carboniferous during the closure of the ancient Tianshan Ocean. Large mafic-ultramafic complexes were emplaced, resulting in several magmatic Cu-Ni-Ti-V deposits during a post collisional period. Gold deposits of the shear-zone-type are controlled by the Kanggurtag ductile shear zone. This mineralization series of eastern Tianshan is different from the IOCG defined by Groves et al. (2010).

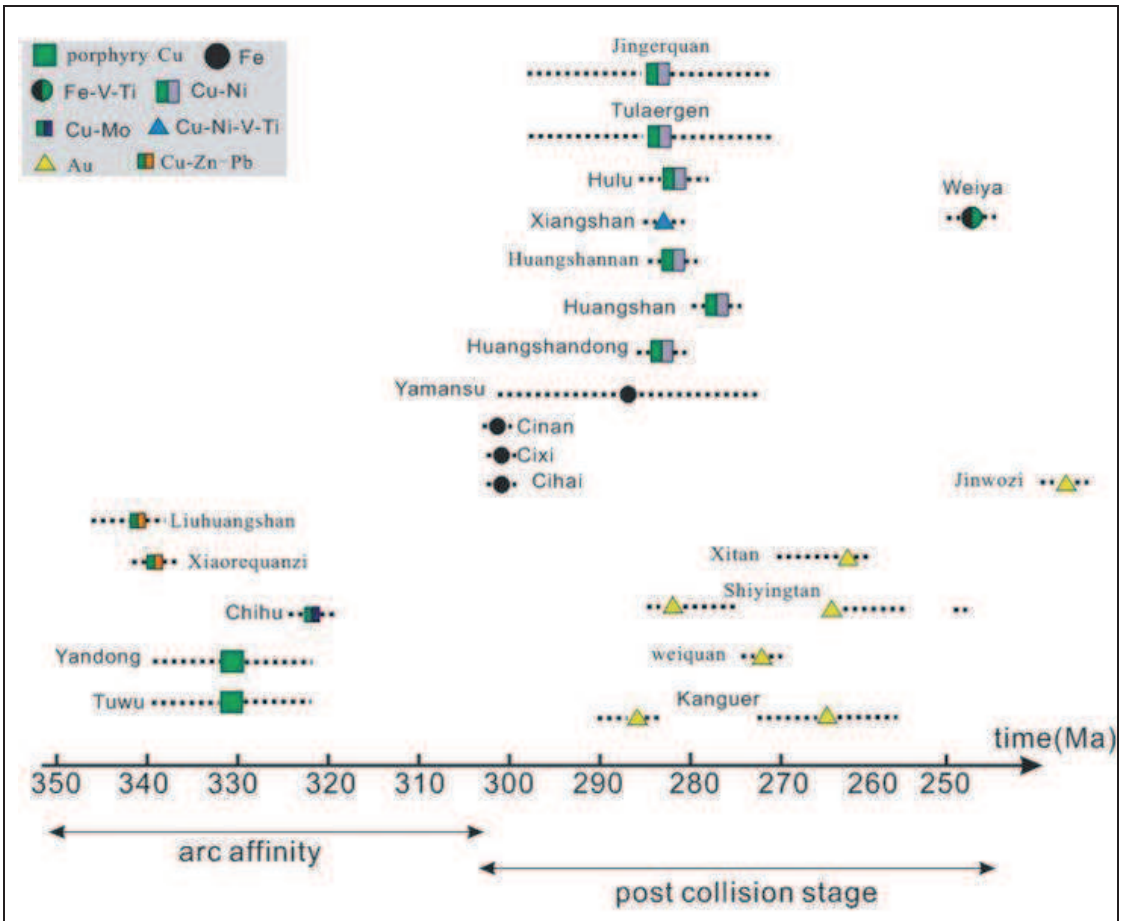

Fig. 5-3: Selective major ore deposits and forming time in eastern Tianshan showing mineralization blooming in late Paleozoic. This diagram is compiled using data from Han et al. (2006) Wu et al. (2010 report), Mao et al. (2005) and data therein.

5.4 Discussion

5.4.1 Source of the magma

The eastern Tianshan, as well as the whole Central Asian Orogenic belt, is known as the most important region of juvenile crustal growth during the Palaeozoic. Numerous geochemical data displayed that these Paleozoic magma probably was affected by mantle materials (Han et al., 1997; Chen et al., 2000; Hu et al., 2000). Among these data, most Nd(T) showed positive value (Jahn, 2004; Gu et al., 2006; Gu et al., 2007) partially leading some studies to conclude plume tectonic environment (Mao et al., 2006; Pirajno, 2007; Su et al., 2011) or mantle magma underplating (Zhao et al., 2008). Majority of granitoids of Phanerozoic time in the eastern Tianshan seems show to contain high proportions of the mantle component in their generaltion (Jahn, 2004). Gu et al. (2007) indicated an intraplated body of mantle magma in the crust in Permain in the eastern Tianshan, rather than underplated body. This intraplated body lead to the low pressure and high temperature metamorphism, migmatisation and partial melting of crustal rocks; heat and fluids from the intraplated magma facilitated formation of the ductile shear zone at a higher crustal level; gneissose granites were formed by reaction of grain-reduced crustal rocks in the ductile shear zone with up-moving fluids and melts released due to metamorphism and ultrametamorphism driven by intraplating; mineralisations characterised by rare metals, such as Li and Be in pegmatites, were genetically affiliated to peraluminous granites produced by partial melting of crustal rocks; co-existence of calc-alkaline to high potassium calc alkaline granites with peraluminous granites indicates that underplating accompanied intraplating in this region; numerous mafic-ultramafic intrusions are high-level representatives of the underplated and intraplated magmas at depth (Gu et al., 2007).

5.4.2 Plume VS. post-collisional stage

The blooming mineralization in eastern Tianshan orogen seems to be linked to certain macro tectonic events. Pirajno (Pirajno, 2007; Pirajno et al., 2008) ascribed the magmatism and related Cu-Ni mineralization to plume. However, Wang et al. (2008) argued that the metallogenic period spanned at least 40Ma which a normal plume would not survive so long (Foulger, 2010). Compared with related deposits of the Emeishan mantle plume, the eastern Tianshan mineralization series has a similar ore-forming element assemblage but has preferable developed Cu-Ni sulphide deposits rather than V-Ti deposits. And in eastern Tianshan, Fe-Au-Cu-Ni deposits occurred with consecutive age which seems not likely happen in plume environment.

5.4.3 Skarn and mafic/ultramafic magmatism

The skarn related iron deposits in eastern Tianshan exploited for magnetite are relative small in size, meanwhile, they associated with mafic/ultramafic magmatism. Skarn minerals consist dominantly of garnet (mostly Fe end-member) and pyroxene, with lesser epidote and actinolite. These skarn related iron deposit developed mostly in the arc where limestone extensive distributed, especially the Carboniferous limestone. In some place, even the Cu-Ni-containing plutons caused skarnization during their emplacement, such as the Huangshandong ultramafic pluton (Branquet et al. 2012 submitted). Average composition of plutons statistics showed that the iron-skarn-related-plutons are about 60% SiO_2 content (Meinert et al. 2005). Many studies showed that iron was probably stripped from the mafic country rocks, such as the Paleoproterozoic iron skarns in the Misi region, northern Finland (Niiranen et al., 2005).

5.4.4 Geodynamic evolution and mineralization

Geodynamic evolution of eastern Tianshan is closely related to that of neighbouring

terrain. Proof from strata, geochronology, structural geology showed that there was no any more oceans in this region at the end of Carboniferous (Laurent-Charvet et al., 2002; Wang et al., 2010; Charvet et al., 2011).

Taking the tectonic and geochronological data into consideration, the metallic mineral deposits in the eastern Tianshan are recognized to be parts of two age groups in late Paleozoic: (1) porphyry copper group formed at about 330-320Ma (Rui et al., 2002; Liu et al., 2003; Han et al., 2006) which indicated the subduction arc. Geochemical compositions of the volcanic rocks and plutons (Wu et al. 2006) which were late Carboniferous in age indicated they are calc-alkaline in composition, thus also suggesting an arc; (2) the Fe-Cu-Ni-V-Ti-Au group formed at about 300-250Ma which reflected post-collisional strike-slip stage (Mao et al., 2005; Wang et al., 2008). A schematic geodynamic model has been proposed (Fig. 5-4). The Dananhu arc belt (Fig. 5-4A) probably formed as a result of north-dipping subduction (Han et al., 2006). However, Charvet et al. (2011) suggested the south-dipping subduction according to the structure observation that the pre-Permian deformation of northern Tianshan belt volcanic arc is north-verging thrusting and folding.

Lower Carboniferous Yamansu Formation exposed well in the Aqishan-Yamansu belt contains magnetite ore deposits, such as Yamansu magnetite deposit. This unit is composed of sedimentary rocks at the base and overlain by andesitic volcanics and tuffs, and was unconformably overlain by the Permian.

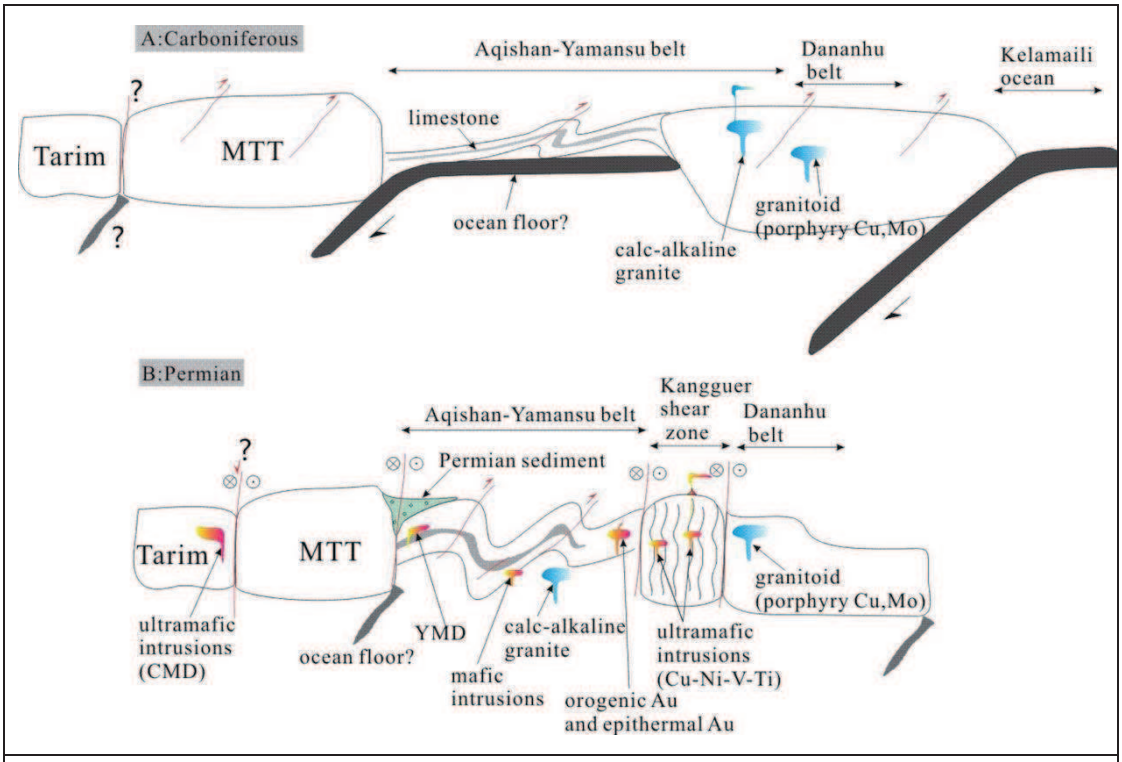

Fig. 5-4: Schematic diagrams showing the Carboniferous and Permian evolution and mineralization model for the eastern Tianshan. This diagram is based on the data from Wu et al. (2006), Laurent-Charvet et al. (2002), Wang et al.(2010), Charvet et al.(2011), Han et al. (2006) and Mao et al. (2005). MTT=Middle Tianshan Terrain, CMD=Cihai magnetite deposit, YMD=Yamansu magnetite deposit.

In the Kangguer shear zone, mafic/ultramafic rocks cross cut the Carboniferous series including limestone (Fig. 5-3B). These mafic/ultramafic rocks were thought to be “ophiolites” (Xiao et al. 2010). However they are not derived from ocean floor. The peridotites, surrounded by serpentinite, are cut by diorites. In some places, the intrusive contact of diorite and gabbro with the deformed Ganduang formation is very clear (Charvet et al. 2011). Branquet et al. (2012) indicated that the Huangshandong ultramafic intrusion, which intruded a host-rock composed of limestone, displayed a contact metasomatism expressed by skarn. These mafic/ultramafic rocks were proposed to be coeval with the Permian strike-slip according to structure and geochronology studies (Branquet et al. 2012 submitted, Qin et al. 2011). At the surface extremely large scale strike-slip shear zones might be associated with deep marine pull-apart basins, filled with pillow basalts, olistotromes and turbidites (Branquet et al., 2012 submitted), and similarly to those

described at Baiyanggou by Shu et al. (2011).

Conclusions and perspectives

A literature survey and an analysis of published data on skarn displayed that the concept of skarn is expanding with time and that characteristic mineral assemblage is an important key for defining the skarn. After the studies on YMD and CMD, conclusions are as following:

1. In the Yamansu iron skarn deposit, the skarn has genetic relation with the limestone and basalt. It was the iron-rich fluid that caused extensive skanization and massive magnetite deposition. The basalt probably was horizontall emplacement according to paleomagnetism and AMS study. Coincidely, the massive garnet skarn was form horizontally. Deteric zircon U-Pb dating on the arkose displayed that the arkose was form later than 312±11 Ma indicating the skarnization probably was later than this age. Later felsic fluid dated to be about 246Ma by Ar-Ar method altered the earlier skarn minerals;
2. For the Cihai magnetite deposit, it seems that CO2 fluid circulation, which derived from decarbonation of sediment, play an important role during the iron-rich melt separation from silicate chamber. Dating on the amphibole by Ar-Ar method indicated the skarn forming time probably was about 300Ma;
3. In the eastern Tianshan orogenic belt, Fe-Cu-Ni-Ti-V-Au mineralization presented successively which may related to a post collisional stage rather than mantle plume.

This thesis contributes to the skarn and mineralization in eastern Tianshan, however, there are still some works in future:

1 More accurate forming age of the skarn. It concerns to the relation with the large crustal scale strike slip shearing in the eastern Tianshan region;

2 Fluid and/or melt inclusions measurement (such as homogenization temperature, composition, salinity) in the skarn minerals.

References:

Ague, J. J. and van Haren, J. L. M. (1996). "Assessing metasomatic mass and volume changes using the bootstrap, with application to deep crustal hydrothermal alteration of marble." Economic Geology 91(7): 1169-1182.

Aksyuk, A. M. (2000). "Estimation of Fluorine Concentrations in Fluids of MineralizedSkarn Systems." Economic Geology 95(6): 1339-1347.

Allan, B. D. and Clarke, D. B. (1981). "Occurrence and origin of garnets in the South Mountain Batholith, Nova Scotia." Can Mineral 19(1): 19-24.

Amelin, Y. V., Neymark, L. A., Ritsk, E. Y. and Nemchin, A. A. (1996). "Enriched Nd-Sr-Pb isotopic signatures in the Dovyren layered intrusion (eastern Siberia, Russia): evidence for source contamination by ancient upper-crustal material." Chemical Geology 129(1–2): 39-69.

Andersen, D. J. and Lindsley, D. H. (1988). "Internally consistent solution models for Fe-Mg-Mn-Ti oxides; Fe-Ti oxides." American Mineralogist 73(7-8): 714-726.

Anderson, A. L. (1947). "Cobalt mineralization in the Blackbird District, Lemhi County, Idaho." Economic Geology 42(1): 22-46.

Anovitz, L. M. and Essene, E. J. (1990). "Thermobarometry and Pressure-Temperature Paths in the Grenville Province of Ontario." Journal of Petrology 31(1): 197-241.

Anovitz, L. M. and Grew, E. S. (1996). "Mineralogy, petrology and geochemistry of boron; an introduction." Reviews in Mineralogy and Geochemistry 33(1): 1-40.

Ashworth, J. R. (1985). Migmatites Glasgow, London: Blackie.

Balen, D. and Broska, I. (2011). "Tourmaline nodules: products of devolatilization within the final evolutionary stage of granitic melt?" Geological Society, London, Special Publications 350(1): 53-68.

Baosteel-Company (1977). geological report.

Barbey, P., Nachit, H. and Pons, J. (2001). "Magma–host interactions during differentiation and emplacement of a shallow-level, zoned granitic pluton (Tarçouate pluton, Morocco): implications for magma emplacement." Lithos 58(3–4): 125-143.

Barton, M. D., Ilchik, R. P. and Marikos, M. A. (1991). "Metasomatism." Reviews in Mineralogy and Geochemistry 26(1): 321-349.

Barton, M. D. and Johnson, D. A. (1996). "Evaporitic-source model for igneous-related Fe

oxide-(REE-Cu-Au-U) mineralization." Geology 24(3): 259-262.

Baskaran, M. (2011). “Environmental Isotope Geochemistry”: Past, Present and Future Handbook of Environmental Isotope Geochemistry. Baskaran, M., Springer Berlin Heidelberg: 3-10.

Best, M. G. (2003). Igneous and metamorphic rock. HongKong, Blackwell Publishing company.

Bird, D. K. and Spieler, A. R. (2004). "Epidote in Geothermal Systems." Reviews in Mineralogy and Geochemistry 56(1): 235-300.

Bohlen, S. R., Dollase, W. A. and Wall, V. J. (1986). "Calibration and Applications of Spinel Equilibria in the System FeO-Al2O3-SiO2." Journal of Petrology 27(5): 1143-1156.

Borradaile, G. J. and Tarling, D. H. (1981). "The influence of deformation mechanisms on magnetic fabrics in weakly deformed rocks." Tectonophysics 77(1-2): 151-168.

Borrok, D. M., Kelser, S. E., Boer, R. H. and Essene, E. J. (1998). "The Vergenoeg magnetite-fluorite deposit, South Africa; support for a hydrothermal model for massive iron oxide deposits." Economic Geology 93(5): 564-586.

Bowers, J. R., Kerrick, D. M. and Furlong, K. P. (1990). "Conduction model for the thermal evolution of the Cupsuptic aureole, Maine." Am J Sci 290(6): 644-665.

Brady, J. B. and Cherniak, D. J. (2010). "Diffusion in Minerals: An Overview of Published Experimental Diffusion Data." Reviews in Mineralogy and Geochemistry 72(1): 899-920.

Branquet, Y., Gumiaux, C., Sizaret, S., Barbanson, L., Wang, B., Cluzel, D., Li, G. and Launay, A. D. (2012 sumitted). "Synkinematic mafic/ultramafic sheeted intrusions: emplacement mechanism and strain restoration of the Permian Huangshan Ni-Cu ore belt (Eastern Tianshan, NW China)."

Buchan, C., Cunningham, D., Windley, B. and Tomurhuu, D. (2001). "Structural and lithological characteristics of the Bayankhongor ophiolite zone, central Mongolia." Journal of the Geological Society(158): 445-460.

Bucher, K. and Grapes, R. (2011). Definition, Conditions and Types of Metamorphism Springer Heidelberg Dordrecht London New York.

Buick, I. S. and Cartwright, I. (2000). "Stable isotope constraints on the mechanism of fluid flow during contact metamorphism around the Marulan Batholith, NSW, Australia." Journal of Geochemical Exploration 69–70(0): 291-295.

Burt, D. M. (1982). "Skarn deposits; historical bibliography through 1970." Econ Geol 77(4): 755-763.

Burtman, V. S. (1975). "Structural geology of variscan Tienshan, USSR." Am J Sci 275-A: 157-186.

Burton, J. C. and Taylor, L. A. (1982). "The f O2 -T and f S2 -T stability relations of hedenbergite and of hedenbergite-johannsenite solid solutions." Economic Geology 77(4): 764-783.

Callegari, E. and Pertsev, N. N. (2007). A systematic nomenclature for metamorphic rocks: 10 Contact Metamorphic Rocks, Recommendations by the IUGS Subcommission on the Systematics of Metamorphic Rocks. Recommendations (www.bgs.ac.uk/scmr/home.html).

Callot, J. P. and Guichet, X. (2003). "Rock texture and magnetic lineation in dykes: a simple analytical model." Tectonophysics 366(3-4): 207-222.

Cañón-Tapia, E. and Herrero-Bervera, E. (2009). "Sampling strategies and the anisotropy of magnetic susceptibility of dykes." Tectonophysics 466(1-2): 3-17.

Cao, G. (1997). "Kanggurtage ophiolites and thermal emplacement of Palaeozoic ophiolites in Xinjiang." Xinjiang Geology 15(3): 269-275.

Cathelineau, M. (1988). "Cation site occupancy in chlorites and illites as a function of temperature." Clay Minerals 23(4): 471-485.

Cathelineau, M. and Nieva, D. (1985). "A chlorite solid solution geothermometer the Los Azufres (Mexico) geothermal system." Contributions to Mineralogy and Petrology 91(3): 235-244.

Charlier, B., Duchesne, J. C. and Vander Auwera, J. (2006). "Magma chamber processes in the Tellnes ilmenite deposit (Rogaland Anorthosite Province, SW Norway) and the formation of Fe-Ti ores in massif-type anorthosites." Chemical Geology 234(3-4): 264-290.

Charlier, B., Duchesne, J. C. and Vander Auwera, J. (2006). "Magma chamber processes in the Tellnes ilmenite deposit (Rogaland Anorthosite Province, SW Norway) and the formation of Fe–Ti ores in massif-type anorthosites." Chemical Geology 234(3–4): 264-290.

Charvet, J., Shu, L. and Laurent-Charvet, S. (2007). "Paleozoic structural and geodynamic evolution of eastern Tianshan (NW China): welding of the Tarim and Junggar plates." Episodes 30(3): 162-186.

Charvet, J., Shu, L., Laurent-Charvet, S., Wang, B., Faure, M., Cluzel, D., Chen, Y. and De Jong, K. (2011). "Palaeozoic tectonic evolution of the Tianshan belt, NW China." Science

China Earth Sciences 54(2): 166-184.

Chaussidon, M., Albarède, F. and Sheppard, S. M. F. (1989). "Sulphur isotope variations in the mantle from ion microprobe analyses of micro-sulphide inclusions." Earth and Planetary Science Letters 92(2): 144-156.

Chaussidon, M. and Lorand, J.-P. (1990). "Sulphur isotope composition of orogenic spinel lherzolite massifs from Ariege (North-Eastern Pyrenees, France): An ion microprobe study." Geochimica et Cosmochimica Acta 54(10): 2835-2846.

Cheilletz, A. and Giuliani, G. (1988). Les skarns tungstiferes stratiformes du Djebel Aouam (Maroc central): model de developpement metasomatique en deux etapes Document du BRGM no 158 -1988.

Chen, F., He, G. and Li, H. (2003). "Tectonic attribute of the Qoltag orogenic belt in the East Tianshan M ountains，northwestern China (in Chinese)." Geology in China 30(4): 361-366.

Chen, F., Li, H., Chen, Y., Wang, D., Wang, J., Liu, D., Tang, Y. and Zhou, R. (2005). "Zircon SHRIMP U-Pb dating and its geological significance of mineralization in Tuwu-Yandong porphyry copper mine, East Tianshan Mountain." Acta Geologica Sinica (in Chinese with English abstract) 79(2): 256-261.

Chen, H. L., Yang, S. F., Wang, Q. H., Luo, J. C., Jia, C. Z., Wei, G. Q. and Li, Z. L. (2006). "Sedimentary response to the Early-mid-Permian basaltic magmatism in the Tarim plate (in Chinese with English abstract)." Geology in China 33(3): 545–552.

Chen, J., Zhou, T., Xie, Z., Zhang, X. and Guo, X. (2000). "Formation of positive εNd(T) granitoids from the Alataw Mountains, Xinjiang, China, by mixing and fractional crystallization: implication for Phanerozoic crustal growth." Tectonophysics 328(1–2): 53-67.

Chen, S., Wang, D., Qu, W., Chen, Z. and Gao, X. (2005). "Geological features and ore formation of the Hulu Cu-Ni sulfide deposit, eastern Tianshan, Xinjiang (in Chinese with English abstract)." Xinjiang Geology 23(3): 230-233.

Chen, W., Sun, S., Zhang, Y., Xiao, W., Wang, Y. and Wang, Q. (2005). "40Ar-39Ar Geochronology of the Qiugemingtashi—Huangshan Ductile Shear Zone in East Tianshan, Xinjiang, NW China." Acta Geologica Sinica (in Chinese with English abstract) 79(6): 790-804.

Cheng, S., Wang, X., Wu, H., Mao, Q., Ao, S. and Han, C. (2008). "Late Paleozoic endogenic metallogenic series in the North Mountains, Xinjiang, NW China." Xinjiang Geology

26(1): 43-48.

Choulet, F., Chen, Y., Wang, B., Faure, M., Cluzel, D., Charvet, J., Lin, W. and Xu, B. (2010). "Late Paleozoic paleogeographic reconstruction of Western Central Asia based upon paleomagnetic data and its geodynamic implications." Journal of Asian Earth Sciences In Press, Corrected Proof.

Chung, S.-L. and Jahn, B.-m. (1995). "Plume-lithosphere interaction in generation of the Emeishan flood basalts at the Permian-Triassic boundary." Geology 23(10): 889-892.

Cifelli, F., Rossetti, F., Mattei, M., Hirt, A. M., Funiciello, R. and Tortorici, L. (2004). "An AMS, structural and paleomagnetic study of quaternary deformation in eastern Sicily." Journal of Structural Geology 26(1): 29-46.

Ciobanu, C. L. and Cook, N. J. (2004). "Skarn textures and a case study: the Ocna de Fier-Dognecea orefield, Banat, Romania." Ore Geology Reviews 24: 315-370.

Clive F, B. (1974). "Plate tectonics and the fusion of Asia." Earth and Planetary Science Letters 21(2): 181-189.

Cole, A., Wilkinson, J. J., Halls, C. and Serenko, T. J. (2000). "Geological characteristics, tectonic setting and preliminary interpretations of the Jilau gold–quartz vein deposit, Tajikistan." Mineralium Deposita 35(7): 600-618.

Coleman, R. G. (1989). "Continental growth of northwest China." Tectonics 8(3): 621-635.

Cooke, D. R., Hollings, P. and Walshe, J. L. (2005). "Giant Porphyry Deposits: Characteristics, Distribution, and Tectonic Controls." Economic Geology 100(5): 801-818.

Corbett, G. and Leach, T. (1998). Southwest acific rim gold-copper systems: structure, alteration,and mineralization, Society of Economic Geologists.

Craddock, J. P., Kennedy, B. C., Cook, A. L., Pawlisch, M. S., Johnston, S. T. and Jackson, M. (2008). "Anisotropy of magnetic susceptibility studies in Tertiary ridge-parallel dykes (Iceland), Tertiary margin-normal Aishihik dykes (Yukon), and Proterozoic Kenora-Kabetogama composite dykes (Minnesota and Ontario)." Tectonophysics 448(1-4): 115-124.

Craddock, J. P., Kennedy, B. C., Cook, A. L., Pawlisch, M. S., Johnston, S. T. and Jackson, M. (2008). "Anisotropy of magnetic susceptibility studies in Tertiary ridge-parallel dykes (Iceland), Tertiary margin-normal Aishihik dykes (Yukon), and Proterozoic Kenora–Kabetogama composite dykes (Minnesota and Ontario)." Tectonophysics 448(1–4): 115-124.

Dahlquist, J. A., Galindo, C., Pankhurst, R. J., Rapela, C. W., Alasino, P. H., Saavedra, J. and

Fanning, C. M. (2007). "Magmatic evolution of the Peñón Rosado granite: Petrogenesis of garnet-bearing granitoids." Lithos 95(3-4): 177-207.

Deer, W., Howie, R. and Zussman, J. (1982). Rock-forming minerals - 2A Single-chain silicates. London and New York, Longman.

Deer, W., Howie, R. and Zussman, J. (1982). Rock-forming minerals - orthosilicates. London and New York, Longman.

Deer, W., Howie, R. and Zussman, J. (2009). Rock-forming minerals: Layered silicates excluding micas and clay minerals, The Geological Society Publishing House.

Deer, W. A., Howie, R. A. and Zussman, J. (1992). An introduction to the rock-forming minerals, Longman Scientific & Technical.

Deer, W. A., Howie, R. A. and Zussman, J. (1997). Rock-forming minerals: disilicates and ring silicates Longman Scientific & Technical.

Derrill, M. and Kerrick, p. (1991). "Overview of Contact Metamorphism " Reviews in Mineralogy and Geochemistry 26: 1 - 12.

Ding, T. (1990). "The geological characteristics of stratabound iron deposits in the Yamansu formation in Xinjiang." (3): 269-272.

Dodson, M. H. (1973). "Closure temperature in cooling geochronological and petrological systems." Contributions to Mineralogy and Petrology 40(3): 259-274.

Duchesne, J. C. (1999). "Fe-Ti deposits in Rogaland anorthosites (South Norway): geochemical characteristics and problems of interpretation." Mineralium Deposita 34(2): 182-198.

Dunlop, D. J. (2002). "Theory and application of the Day plot (Mrs/Ms versus Hcr/Hc) 1. Theoretical curves and tests using titanomagnetite data." J. Geophys. Res. 107(B3): 2056.

Dupuis, C. and Beaudoin, G. (2011). "Discriminant diagrams for iron oxide trace element fingerprinting of mineral deposit types." Mineralium Deposita 46(4): 319-335.

Durand, C. (2006). Circulations fluides, transferts de matière et évolution minéralogique entre deux réservoirs à géochimie contrastée, l'universite de Franche-comte. doctor.

Durand, C., Marquer, D., Baumgartner, L., Goncalves, P., Boulvais, P. and Rossy, M. (2009). "Large calcite and bulk-rock volume loss in metacarbonate xenoliths from the Quérigut massif (French Pyrenees)." Contributions to Mineralogy and Petrology 157(6): 749-763.

E.T.C, S. (1993). "Magmatic sulphide/volatile interaction as a mechanism for producing chalcophile element enriched, Archean Au-quartz, epithermal Au Ag and Au skarn

hydrothermal ore fluids." Ore Geology Reviews 7(5): 359-379.

Ehlers, K., Stüwe, K., Powell, R., Sandiford, M. and Frank, W. (1994). "Thermometrically inferred cooling rates from the Plattengneis, Koralm region, Eastern Alps." Earth and Planetary Science Letters 125(1-4): 307-321.

Einaudi, M. T., Meinert, L. D. and Newberry, R. J. (1981). "Skarn deposits." Economic Geology 75th Anniversary: 317-391.

Einaudi, M. T., Meinert, L. D. and Newberry, R. J. (1981). "Skarn deposits." Econ. Geol., 75th Anniv: 317-391.

Essalhi, M., Sizaret, S., Barbanson, L., Chen, Y., Branquet, Y., Panis, D., Camps, P., Rochette, P. and Canals, A. (2009). "Track of fluid paleocirculation in dolomite host rock at regional scale by the Anisotropy of Magnetic Susceptibility (AMS): An example from Aptian carbonates of La Florida, Northern Spain." Earth and Planetary Science Letters 277(3-4): 501-513.

Ettlinger, A. D. and Ray, G. E. (1989). Precious Metal Enriched Skarns in British Columbia. An overview and geological study, Ministry of Energy, Mines and Petroleum Resources: 128.

Feng, X., Yang, R., Song, G., Li, C. and Lu, G. (1986). "Erlianite-a new vanadium- and iron-bearing silicate mineral." Acta Mineralogica Sinica 6(4): 333-337.

Ferry, J. M. (1994). "Role of fluid flow in the contact metamorphism of siliceous dolomitic limestones." American Mineralogist 79(7-8): 719-736.

Ferry, J. M., Sorensen, S. S. and Rumble Iii, D. (1998). "Structurally controlled fluid flow during contact metamorphism in the Ritter Range pendant, California, USA." Contributions to Mineralogy and Petrology 130(3): 358-378.

Fisher, R. (1953). "Dispersion on a Sphere." Proceedings of the Royal Society of London. Series A. Mathematical and Physical Sciences 217(1130): 295-305.

Foucault, A. and Raoult, J.-F. (2001). Dictionnaire de géologie. Paris, dunod.

Foulger, G. R. (2010). Plates vs Plumes: A Geological Controversy, Wiley-Blackwell.

Franchini, M. B., de Barrio, R. E., Pons, M. J., Schalamuk, I. B., Rios, F. J. and Meinert, L. (2007). "Fe Skarn, Iron Oxide Cu-Au, and Manto Cu-(Ag) Deposits in the Andes Cordillera of Southwest Mendoza Province (34°–36°S), Argentina." Exploration and Mining Geology 16(3-4): 233-265.

Fulignati, P., Kamenetsky, V., Marianelli, P., Sbrana, A. and Mernagh, T. (2001). "Melt inclusion record of immiscibility between silicate, hydrosaline, and carbonate melts:

Applications to skarn genesis at Mount Vesuvius." Geology 29(11): 1043-1046.

Fulignati, P., Marianelli, P., Santacroce, R. and Sbrana, A. (2000). "The skarn shell of the 1944 Vesuvius magma chamber. Genesis and P-T-X conditions from melt and fluid inclusion data." Eur J Mineral 12(5): 1025-1039.

Gaeta, M., Di Rocco, T. and Freda, C. (2009). "Carbonate Assimilation in Open Magmatic Systems: the Role of Melt-bearing Skarns and Cumulate-forming Processes." Journal of Petrology 50(2): 361-385.

Gamble, R. P. (1982). "An experimental study of sulfidation reactions involving andradite and hedenbergite." Economic Geology 77(4): 784-797.

Ganino, C., Arndt, N., Zhou, M.-F., Gaillard, F. and Chauvel, C. (2008). "Interaction of magma with sedimentary wall rock and magnetite ore genesis in the Panzhihua mafic intrusion, SW China." Mineralium Deposita 43(6): 677-694.

Gao, J. F., Lu, J. J. and Lai, M. Y. (2003). "Analysis of Trace Elements in Rock Samples Using HR-ICPMS (in Chinese)." Journal of Nanjing University (Nature Science)(39): 844-850.

Garcia-Casco, A., Torres-Roldan, R., Millan, G., Monie, P. and Schneider, J. (2002). "Oscillatory zoning in eclogitic garnet and amphibole, Northern Serpentinite Melange, Cuba: a record of tectonic instability during subduction?" Journal of Metamorphic Geology 20(6): 581-598.

Gary, T., R, A. J., Xieyan, S. and W., J. D. (2001). "Emeishan Basalts, SW China: reappraisal of the formation's type area stratigraphy and a discussion of its significance as a large igneous province." Journal of the Geological Society 158(4): 593-599.

Gill, J. B. (1981). Orogenic Andesites and Plate Tectonics, Springer-Verlag.

Goldfarb, R. J., Phillips, G. N. and Nokleberg, W. J. (1998). "Tectonic setting of synorogenic gold deposits of the Pacific Rim." Ore Geology Reviews 13(1-5): 185-218.

Gong, X., Yang, X., Chen, Q. and Li, Z. (2004). "Structure deformation and metallogenic prognosis of gold ore zone in Jueluotage of Eastern Tianshan." Journal of Earth Science and Environment 26(2): 6-10.

Grabezhev, A. (2010). "The Gumeshevo skarn-porphyry copper deposits in the Central Urals, Russia: Evolution of the ore-magmatic system as deduced from isotope geochemistry (Sr, Nd, C, O, H)." Geology of Ore Deposits 52(2): 138-153.

Grant, J. A. (1986). "The isocon diagram; a simple solution to Gresens' equation for metasomatic alteration." Economic Geology 81(8): 1976-1982.

Gresens, R. L. (1967). "Composition-volume relationships of metasomatism." Chemical Geology 2: 47-65.

Groves, D. I., Bierlein, F. P., Meinert, L. D. and Hitzman, M. W. (2010). "Iron Oxide Copper-Gold (IOCG) Deposits through Earth History: Implications for Origin, Lithospheric Setting, and Distinction from Other Epigenetic Iron Oxide Deposits." Economic Geology 105(3): 641-654.

Groves, D. I., Goldfarb, R. J., Gebre-Mariam, M., Hagemann, S. G. and Robert, F. (1998). "Orogenic gold deposits: A proposed classification in the context of their crustal distribution and relationship to other gold deposit types." Ore Geology Reviews 13(1-5): 7-27.

Gu, L., Yang, H., Wang, J. and Lui, Y. (1990). "Rb-Sr geochronology of granites in the east section of the mid-Tianshan belt and its tectonic evolution." Journal of Guilin college of Geology 10(1): 49-55.

Gu, L., Zhang, Z., Wu, C., Tang, J., San, J., Wang, C. and Zhang, G. (2007). "Permian geological, metallurgical and geothermal events of the Huangshang-Jingerquan area, eastern Tianshan: indications for magma intraplating and its effects on the crust." Acta Petrologica Sinica 23(11): 2869-2880.

Gu, L., Zhang, Z., Wu, C., Wang, Y., Tang, J., Wang, C., Xi, A. and Zheng, Y. (2006). "Some problems on granites and vertical growth of the continental crust in the Eastern Tianshan Mountains, NW China." Acta Petrologica Sinica 22(5): 1103-1120.

Gu, L., Zhu, J., Guo, J., Liao, J., Yan, Z., Yang, H. and Wang, J. (1995). "Geology and genesis of the mafic-ultramafic complexes in the Huangshan-Jingerquan (HJ) belt, East Xinjiang." Chinese Journal of Geochemistry 14(2): 97-116.

Guo, Z., Shi, H., Zhang, Z. and Zhang, J. (2006). "The tectonic evolution of the south Tianshan Paleo-oceanic crust inferred from the spreading structures and Ar-Ar dating of the Hongluihe ophiolite, NW china." Acta Petrologica Sinica 22(1): 95-102.

Gurenko, A. A., Chaussidon, M. and Schmincke, H.-U. (2001). "Magma ascent and contamination beneath one intraplate volcano: evidence from S and O isotopes in glass inclusions and their host clinopyroxenes from Miocene basaltic hyaloclastites southwest of Gran Canaria (Canary Islands)." Geochimica et Cosmochimica Acta 65(23): 4359-4374.

Gustafson, W. (1972). "The Stability of Andradite, Hedenbergite, and Related Minerals in the System Ca-Fe-Si-O-H." Journal of Petrology 15(3): 455-496.

Hames, W. E., Tracy, R. J. and Bodnar, R. J. (1989). "Postmetamorphic unroofing history deduced from petrology, fluid inclusions, thermochronometry, and thermal modeling: An example from southwestern New England." Geology 17(8): 727-730.

Han, B.-F., Guo, Z.-J., Zhang, Z.-C., Zhang, L., Chen, J.-F. and Song, B. (2010). "Age, geochemistry, and tectonic implications of a late Paleozoic stitching pluton in the North Tian Shan suture zone, western China." Geological Society of America Bulletin 122(3-4): 627-640.

Han, B.-f., Wang, S.-g., Jahn, B.-m., Hong, D.-w., Kagami, H. and Sun, Y.-l. (1997). "Depleted-mantle source for the Ulungur River A-type granites from North Xinjiang, China: geochemistry and Nd–Sr isotopic evidence, and implications for Phanerozoic crustal growth." Chemical Geology 138(3–4): 135-159.

Han, B., Ji, J., Song, B., Chen, L. and Li, Z. (2004). "SHRIMP zircon U-Pb ages of Kalatongke No. 1 and Huangshandong Cu-Ni-bearing mafic-ultramafic complexes, North Xinjiang, and geological implications." Chinese Science Bulletin 49(22): 2424-2429.

Han, C. (2002). Research on Metallogenic series of cppper deposits in East Tianshan Mountains. Beijing, China University of Geosciences. doctor.

Han, C. (2003). Research on metallogenic series of copper deposits in East Tianshan Mountains. Beijing, China University of Geosciences (Beijing). Doctor of philosophy.

Han, C., Xiao, W., Bin, C., Mao, Q., Zhang, J. and Ao, S. (2006). "Major Types and Characteristics of Late Paleozoic Copper Deposits in North Xinjiang, Northwest China." Acta Geologica Sinica (in Chinese with English abstract) 80(1): 74-89.

Han, C., Xiao, W., Zhao, G., Mao, J., Yang, J., Wang, Z., Yan, Z. and Mao, Q. (2006). "Geological characteristics and genesis of the Tuwu porphyry copper deposit, Hami, Xinjiang, Central Asia." Ore Geology Reviews 29(1): 77-94.

Hanson, R. B. and Ferry, J. M. (1995). "Role of fluid flow in the contact metamorphism of siliceous dolomitic limestones; discussion and reply." American Mineralogist 80(11-12): 1222-1228.

Harlov, D. E. and Forster, H.-J. (2002). "High-Grade Fluid Metasomatism on both a Local and a Regional Scale: the Seward Peninsula, Alaska, and the Val Strona di Omegna, Ivrea–Verbano Zone, Northern Italy. Part I: Petrography and Silicate Mineral Chemistry." Journal of Petrology 43(5): 769-799.

He, S. P., Ren, B. S., Yao, W. G. and Fu, L. P. (2002). "The division of tectonic units of Beishan area,Gansu-Inner Mongolia (in Chinese with English abstract)." Northwest Geology 35:

29-40.

He, Y. (2007). "Geochemical features of Yamansu magnetite deposit, Hami city (in chinese)." Western Exploration Engineering(11): 142-144.

Henry, D. J. and Dutrow, B. L. (1992). "Tourmaline in a low grade clastic metasedimentary rock: an example of the petrogenetic potential of tourmaline." Contributions to Mineralogy and Petrology 112(2): 203-218.

Henry, D. J. and Dutrow, B. L. (1996). "Metamorphic tourmaline and its petrologic applications." Reviews in Mineralogy and Geochemistry 33(1): 503-557. Henry, D. J. and Guidotti, C. V. (1985). "Tourmaline as a petrogenetic indicator mineral: an example from the staurolite-grade metapelites of NW Maine." American Mineralogist 70(1-2): 1-15. Herrington, R. J., Zaykov, V. V., Maslennikov, V. V., Brown, D. and Puchkov, V. N. (2005). "Mineral deposits of the Urals and Links to Geodynamic Evolution." Econ Geol One Hundredth Anniversary Volume: 1069-1095.

Hildebrand, R. S. (1986). "Kiruna-type deposits; their origin and relationship to intermediate subvolcanic plutons in the Great Bear magmatic zone, Northwest Canada." Economic Geology 81(3): 640-659.

Hitzman, M. W., Oreskes, N. and Einaudi, M. T. (1992). "Geological characteristics and tectonic setting of proterozoic iron oxide (Cu - U - Au - REE) deposits." Precambrian Research 58(1-4): 241-287.

Hochella, M. F., Liou, J. G., Keskinen, M. J. and Kim, H. S. (1982). "Synthesis and stability relations of magnesium idocrase." Economic Geology 77(4): 798-808.

Holten, T., Jamtveit, B. and Meakin, P. (2000). "Noise and oscillatory zoning of minerals." Geochimica et Cosmochimica Acta 64(11): 1893-1904.

Hou, G., Tang, H. and Liu, C. (2006). "Geochemical characteristics of the Late Paleozoic Volcanics in Jueluotage tectonic belt: eastern Tianshan and its implication." Acta Geologica Sinica (in Chinese with English abstract) 22(5): 1167-1177.

Hou, G., Tang, H. and Liu, C. (2007). "Study on the mineralogy of volcanics of the Yamansu group in the Jueluotage tectonic belt , East Tianshan." Acta Mineralogica Sinica 27(2): 189-194.

Hou, G., Tang, L., Lui, C. and Wang, Y. (2005). "Geochronological and geochemical study on the wallrock of Tuwu-Yandong porphyry copper deposits, Eastern Tianshan mountains." Acta Petrologica Sinica 21(6): 1729-1736.

Hou, T., Zhang, Z., Encarnacion, J., Du, Y., Zhao, Z. and Liu, J. (2010). "Geochemistry of Late

Mesozoic dioritic porphyries associated with Kiruna-style and stratabound carbonate-hosted Zhonggu iron ores, Middle–Lower Yangtze Valley, Eastern China: Constraints on petrogenesis and iron sources." Lithos 119(3–4): 330-344.

Hrouda, F. (1982). "Magnetic anisotropy of rocks and its application in geology and geophysics." Surveys in Geophysics 5(1): 37-82.

Hu, A., Jahn, B.-m., Zhang, G., Chen, Y. and Zhang, Q. (2000). "Crustal evolution and Phanerozoic crustal growth in northern Xinjiang: Nd isotopic evidence. Part I. Isotopic characterization of basement rocks." Tectonophysics 328(1-2): 15-51.

Hu, A., Jahn, B.-m., Zhang, G., Chen, Y. and Zhang, Q. (2000). "Crustal evolution and Phanerozoic crustal growth in northern Xinjiang: Nd isotopic evidence. Part I. Isotopic characterization of basement rocks." Tectonophysics 328(1–2): 15-51.

Hu, A., Wei, G., Zhang, J., Deng, W. and Chen, L. (2007). "SHRIMP U-Pb age for zircons of East Tianhu granitic gneiss and tectoic evolution significance from the eastern Tianshan Mountains，Xinjiang， China." Acta Petrologica Sinica 23(8): 1795-1802.

Hu, A., Zhang, G., Zhang, Q. and Chen, Y. (1998). "Constraints on the age of basement and crustal growth in Tianshan Orogen by Nd isotopic composition." Science in China Series D: Earth Sciences 41(6): 648-657.

Hu, A., Zhang, Z., Liu, J., Peng, J., Zhang, J., Zhao, D., Yang, S. and Zhou, W. (1986). "U-Pb age and evolution of Precambrian metamorphic rocks of middle tianshan uplift zone, Eastern Tianshan,." Geochimica(01): 23-35.

Hu, B. (2007). Tectonomagmatic Evolution and Gold Metallogeny in South Beishan Mountain, Northwest China. Chinese Academy of Geological Sciences. Beijing, Chinese Academy of Geological Sciences. doctor.

Iacono Marziano, G., Gaillard, F. and Pichavant, M. (2007). "Limestone assimilation and the origin of CO2 emissions at the Alban Hills (Central Italy): Constraints from experimental petrology." Journal of Volcanology and Geothermal Research 166(2): 91-105.

Iacono Marziano, G., Gaillard, F. and Pichavant, M. (2008). "Limestone assimilation by basaltic magmas: an experimental re-assessment and application to Italian volcanoes." Contributions to Mineralogy and Petrology 155(6): 719-738.

Ito, M. and Ganguly, J. (2006). "Diffusion kinetics of Cr in olivine and 53Mn-53Cr thermochronology of early solar system objects." Geochimica et Cosmochimica Acta 70: 799-809.

Jahn, B.-M. (2004). "The Central Asian Orogenic Belt and growth of the continental crust in the Phanerozoic." Geological Society, London, Special Publications 226(1): 73-100.

Jahn, B.-m., Wu, F. and Chen, B. (2000). "Massive granitoid generation in Central Asia:Nd isotope evidence and implication for continental growth in the Phanerozoic." Episodes 23(2): 82-92.

Jakobsen, J. K., Veksler, I. V., Tegner, C. and Brooks, C. K. (2005). "Immiscible iron- and silica-rich melts in basalt petrogenesis documented in the Skaergaard intrusion." Geology 33(11): 885-888.

Jamtveit, B. (1991). "Oscillatory zonation patterns in hydrothermal grossular-andradite garnet; nonlinear dynamics in regions of immiscibility." American Mineralogist 76(7-8): 1319-1327.

Jamtveit, B. and Andersen, T. (1992). "Morphological instabilities during rapid growth of metamorphic garnets." Physics and Chemistry of Minerals 19(3): 176-184.

Jamtveit, B. and Hervig, R. L. (1994). "Constraints on Transport and Kinetics in Hydrothermal Systems from Zoned Garnet Crystals." Science 263(5146): 505-508.

Jamtveit, B., Ragnarsdottir, K. V. and Wood, B. J. (1995). "On the origin of zoned grossular-andradite garnets in hydrothermal systems." Eur J Mineral 7(6): 1399-1410.

Jamtveit, B., Wogelius, R. A. and Fraser, D. G. (1993). "Zonation patterns of skarn garnets: Records of hydrothermal system evolution." Geology 21(2): 113-116.

Jebrak, M. and Marcoux, E. (2008). Géologie des ressources minérales. Québec, Association géologique du Canada.

Jelinek, V. (1981). "Characterization of the magnetic fabric of rocks." Tectonophysics 79(3-4): T63-T67.

Ji, J., Li, H., Zhang, L., Yang, X. and Feng, C. (1999). "Sm-Nd and Rb-Sr isotopical ages of magnetite-chlorite formation gold deposit in the volcanic rock area of Late Paleozoic Era, East Tianshan." Chinese Science Bulletin 44(19): 1801-1804.

Ji, J., Xue, C., Zeng, Z. and Yang, X. (1997). "Study on the Kanggurtag gold zone in the Eastern Tianshan Mountains." Geological Review 43(1): 69-77.

Ji, J., Zhang, L., Zeng, Z., Lu, D. and Yang, X. (1996). "Chronology study of Kangultage gold metallogenic belt, East Tianshan." Scientia Geologica Sinica 31(1): 80-89.

Jia, C. Z. (1997). Tectonic characteristics and oil-gas in the Tarim Basin, China (in Chinese). Beijing, Petroleum Industry Press.

Jia, Q. (1991). "The features of magnetite from Tianhu magnetite deposit." Northwestern

Geology 12(1): 19-25.

Jiang, C., Cheng, S., Ye, S., Xia, M., Jiang, H. and Dai, Y. (2006). "Lithogeochemistry and petrogenesis of Zhongshanbei mafic rock body, at Beishan region, Xinjiang." Acta Petrologica Sinica 22(1): 115-126.

Jiang, F., Qin, K., Fang, T. and Wang, S. (2002). "Types, geological characteristics, metallogenic regularity and exploration target of iron deposits in Eastern Tianshan mountains." Xinjiang Geology 20(4): 379-383.

Karimzadeh Somarin, A. (2004). "Geochemical effects of endoskarn formation in the Mazraeh Cu–Fe skarn deposit in northwestern Iran." Geochemistry: Exploration, Environment, Analysis 4(4): 307-315.

Kebede, T., Koeberl, C. and Koller, F. (2001). "Magmatic evolution of the suqii-wagga garnet-bearing two-mica granite, wallagga area, western Ethiopia." Journal of African Earth Sciences 32(2): 193-221.

Kerrich, R. and Cassidy, K. F. (1994). "Temporal relationships of lode gold mineralization to accretion, magmatism, metamorphism and deformation — Archean to present: A review." Ore Geology Reviews 9(4): 263-310.

Kingma, K. and Downs, J. (1989). "Crystal-structure of a birefrigent andradite." American Mineralogist 74: 1307-1316.

Kirschvink, J. L. (1980). "The least-squares line and plane and the analysis of palaeomagnetic data." Geophysical Journal of the Royal Astronomical Society 62(3): 699-718.

Knauth, L. P. (2005). "Temperature and salinity history of the Precambrian ocean: implications for the course of microbial evolution." Palaeogeography, Palaeoclimatology, Palaeoecology 219(1-2): 53-69.

Koděr, P., Rankin, A. H. and Lexa, J. (1998). "Evolution of fluids responsible for iron skarn mineralisation: An example from the Vyhne-Klokoc deposit, Western Carpathians, Slovakia." Mineralogy and Petrology 64(1): 119-147.

Kohn, M. J., Catlos, E. J., Ryerson, F. J. and Harrison, T. M. (2001). "Pressure-temperature-time path discontinuity in the Main Central thrust zone, central Nepal." Geology 29(7): 571-574.

Kolker, A. (1982). "Mineralogy and geochemistry of Fe-Ti oxide and apatite (nelsonite) deposits and evaluation of the liquid immiscibility hypothesis." Econ Geol 77(5): 1146-1158.

Kolker, A. (1982). "Mineralogy and geochemistry of Fe-Ti oxide and apatite (nelsonite) deposits and evaluation of the liquid immiscibility hypothesis." Economic Geology 77(5):

1146-1158.

Koroteev, V. A., de Boorder, H., Necheukhin, V. M. and Sazonov, V. N. (1997). "Geodynamic setting of the mineral deposits of the Urals." Tectonophysics 276(1-4): 291-300.

Kräutner, H. G. and Mede§an, A. (1969). "On stilpnomelane in some Romanian Carpathian crystalline formations." Mineralogy and Petrology 13(3): 203-217.

Krogh, E. J. (1988). "The garnet-clinopyroxene Fe-Mg geothermometer — a reinterpretation of existing experimental data." Contributions to Mineralogy and Petrology 99(1): 44-48.

Krogh, R. (2000). "The garnet–clinopyroxene Fe2+–Mg geothermometer: an updated calibration." Journal of Metamorphic Geology 18(2): 211-219.

Krug, H., Brandstädter, H. and Jacob, K. (1996). "Morphological instabilities in pattern formation by precipitation and crystallization processes." Geologische Rundschau 85(1): 19-28.

Kuscu, I., Gençalioglu Kuscu, G., Meinert, L. D. and Floyd, P. A. (2002). "Tectonic setting and petrogenesis of the Çelebi granitoid, (KIrIkkale-Turkey) and comparison with world skarn granitoids." Journal of Geochemical Exploration 76(3): 175-194.

Kwak, T. A. P. (1986). "Fluid inclusions in skarns (carbonate replacement deposits)." Journal of Metamorphic Geology 4(4): 363-384.

Kwak, T. A. P. (1987). W-Sn skarn deposits and related metamorphic skarns and granitoids

Lasaga, A. C., Ed. (1983). Geospeedometry: an extension of geothermometry. Kinetics and equilibrium in mineral reactions P82-114. Berlin Heidelberg New York, Springer.

Laurent-Charvet, S., Charvet, J., Shu, L., Ma, R. and Lu, H. (2002). "Palaeozoic late collisional strike-slip deformations in Tianshan and Altay, Eastern Xinjiang, NW China." Terra Nova 14(4): 249-256.

Laznicka, P. (2010). Giant Metallic Deposits second edition. London New York, Springer.

Leeman, W. P. and Sisson, V. B. (1996). "Geochemistry of boron and its implications for crustal and mantle processes." Reviews in Mineralogy and Geochemistry 33(1): 645-707.

Lei, R.-X., Wu, C.-Z., Gu, L.-X., Zhang, Z.-Z., Chi, G.-X. and Jiang, Y.-H. "Zircon U-Pb chronology and Hf isotope of the Xingxingxia granodiorite from the Central Tianshan zone (NW China): Implications for the tectonic evolution of the southern Altaids." Gondwana Research In Press, Corrected Proof.

Lei, R.-X., Wu, C.-Z., Gu, L.-X., Zhang, Z.-Z., Chi, G.-X. and Jiang, Y.-H. (2011). "Zircon U–Pb chronology and Hf isotope of the Xingxingxia granodiorite from the Central Tianshan zone (NW China): Implications for the tectonic evolution of the southern

Altaids." Gondwana Research 20(2-3): 582-593.

Lentz, D. R. (2005). Mass-balance analysis of mineralized skarn systems: Implications for replacement processes, carbonate mobility, and permeability evolution Mineral Deposit Research: Meeting the Global Challenge. Mao, J. and Bierlein, F. P., Springer Berlin Heidelberg: 421-424.

Levashova, N. M., Degtyarev, K. E., Bazhenov, M. L., Collins, A. Q. and Van der Voo, R. (2003). "Middle Paleozoic paleomagnetism of east Kazakhstan: post-Middle Devonian rotations in a large-scale orocline in the central Ural-Mongol belt." Tectonophysics 377(3): 249-268.

Levresse, G., González-Partida, E., Carrillo-Chavez, A., Tritlla, J., Camprubí, A., Cheilletz, A., Gasquet, D. and Deloule, E. (2004). "Petrology, U/Pb dating and (C-O) stable isotope constraints on the source and evolution of the adakite-related Mezcala Fe-Au skarn district, Guerrero, Mexico." Mineralium Deposita 39(3): 301-312.

Li, H., Chen, F., Cai, H. and Liu, H. (1999). "Study on isotopic chronology of the mazhuangshan gold mineralization,eastern Xinjiang " Scientia Geologica Sinica 34(2): 251-256.

Li, H., Chen, F., Lu, Y., Yang, H., Guo, J. and Mei, Y. (2004). "Zircon shrimp U-Pb age and strontium isotopes of mineral ized granitoids in the sanchakou copper polymetallic depoist , East tianshan Mountains." Acta Geologica Sinica (in Chinese with English abstract) 25(2): 191-195.

Li, H., Chen, F., Lu, Y., Yang, H., Guo, J. and Mei, Y. (2005). "New Chronological Evidence for Indosinian Diagenetic Mineralization in Eastern Xinjiang, NW China." Acta Geologica Sinica - English Edition 79(2): 264-275.

Li, H. Q. and Liu, D. Q. (2003). "Newsletter of Research Project of Exploration and Assessment for Xinjiang Mineral Resources. Urumqi, p. 6. (in Chinese)."

Li, H. Q., Xie, C. F., Chang, H. L., Cai, H., Zhu, J. P. and Zhou, S. (1998). Study on metallogenetic chronology of nonferrous and precious metallic ore deposits in north Xinjiang, China. Beijing, Geological Publishing House.

Li, J. (2004). "Late Neoproterozoic and Paleozoic Tectonic framework and evolution of Eastern Xinjiang NW China." Geological review 50(3): 304-322. Li, J. (2004). "Late Neoproterozoic and Paleozoic tectonic framework and evolution of Eastern Xinjiang, NW China." Geological Review 50(3): 304-322.

Li, J., Qin, K., Xu, X., Sun, H., Cheng, S., Wu, H. and Mo, X. (2007). "Geochemistry of

Baishiquan Cu-Ni-bearing mafic-ultramafic complex in east Tianshan, Xinjiang; constraints on ore genesis and tectonic setting." Mineral Deposits = Kuangchuang Dizhi 26(1): 43-57.

Li, J., Qin, K., Xu, X., Sun, H., Cheng, S., Wu, H. and Mo, X. (2007). "Geochemistry of Baishiquan Cu-Ni bearing mafic-ultramafic complex in East Tianshan, Xinjiang: Constraints on ore genesis and tectonic setting." Mineral Deposits(1): 43-57.

Li, J., Song, B., Wang, K., Li, Y., Sun, G. and Qi, D. (2006). "Permian mafic-ultramafic complexes on the southern margin of the Tu-Ha basin, East Tianshan Mountains: Geological records of vertical crustal growth in Central Asia." Acta Geologica Sinica (in Chinese with English abstract) 27(5): 424-446.

LI, Q., LIU, S., WANG, Z., YAN, Q., GUO, Z., ZHANG, Z., ZHENG, H., JIANG, C., WANG, T. and CHU, Z. (2007). "Geochemical constraints on the petrogenesis of the Proterozoic granitoid gneisses from the eastern segment of the Central Tianshan Tectonic Zone, northwestern China." Geological Magazine 144(2): 305-317.

Li, W., Xia, B., Wu, G. Q., Wang, H. and Wang, R. (2005). "Kangguertage ophiolite and tectornic significance，Shanshan，Xinjiang China." Acta Petrologica Sinica 21(6): 1617-1632.

Li, X., Xia, L., Xia, Z., Xu, X., Ma, Z. and Wang, L. (2004). "Zircon U-Pb geochronology of volcanic rocks of the Qieshan Group in the East Tianshan Mountains." Geological Bulletin of China 23(12): 1215-1220.

Li, Y., Sun, D. and Zheng, J. (1999). "Paleomagnetic study and tectonic evolution of Xinjiang and its neighboring regions." Xinjiang Geology 17(3): 192-235.

Li, Y., Zhao, G., Qu, W., Pan, C., Mao, Q. and Du, A. (2006). "Re-Os isotopic dataing of the Xiangshan deposit, East Tianshan-NW China." Acta Petrologica Sinica 22(1): 245-251.

Li, Z. (1983). Cihai iron ore deposit geological characteristics, Hami, Xinjiang province, China. report.

Li, Z., Zhao, R., Huo, R. and Wang, Q. (2006). "Geological characters of Tuwu-Yandong copper deposit in Xinjiang." Geology and Prospecting 42(6): 1-4.

Liang, X. (2000). Experimental studies on the mechanism of the formation of skarns and skarn ore deposits in China. Beijing, Academy Press (Xue Yuan).

Liang, X. and Qiao, L. (1991). "Experimental study on the formation of metasomatic rocks and related iorn deposits in volcanic rock." Acta petrologica et Mineralogica(in Chinese with Englisth abstract) 1991(10): 4.

Liang, Y., Huang, X., Xu, K., Yu, X., Wang, Y., Zhang, W. and Cai, Y. (2001). "Geophysical field and deep geology of the Kanggur Tag fault zone, Xinjiang." Regional Geology of China 20(4): 398-403.

Lin, S. (1982). "A contribution to the chemistry, origin and evolution of magnetite." Acta Geologica Sinica (in Chinese with English abstract) (3): 166-174.

Lin, X. and Xu, G. (1989). "A preliminary investigation on some characteristics and forming mechanism of the magma genetic skarn." Geoscience 3(3): 351-358.

Lindsley, D. H. and Dixon, S. S. (1976). "Diopside-enstatite equilibria at 850-1400 and 5-35 kbar." Am J Sci 276: 1285-1301

Liou, J. (1973). "Synthesis and stability relations of epidote Ca2Al2FeSi3O12(OH)12." Journal of Petrology 14: 381-413.

Lister, G. F. (1966). "The composition and origin of selected iron-titanium deposits." Economic Geology 61(2): 275-310.

Liu, C., Zhao, Z. and Guo, Z. (2006). "Chronology and geochemistry of lamprophyre dykes from Beishan area，Gansu province and implications for the crust-mantle interaction." Acta Geologica Sinica (in Chinese with English abstract) 22(5): 1294-1306.

Liu, D., Chen, Y., Wang, D., Tang, Y., Zhou, R., Wang, J., Li, H. and Chen, F. (2003). "A discussion on problems related to mineralization of Tuwu-Yandong Cu-Mo ore field in Hami, Xinjiang (in Chinese with English abstract)." Mineral Deposits 22(4): 334-344.

Liu, S., Guo, Z., Zhang, Z., Li, Q. and Zheng, H. (2004). "Nature of the Precambrian metamorphic blocks in the eastern segment of Central Tianshan: Constraint from geochronology and Nd isotopic geochemistry." Science in China Series D: Earth Sciences 47(12): 1085-1094.

Liu, Y. G., Miah, M. R. U. and Schmitt, R. A. (1988). "Cerium: A chemical tracer for paleo-oceanic redox conditions." Geochimica et Cosmochimica Acta 52(6): 1361-1371.

London, D., Morgan, G. B. and Wolf, M. B. (1996). "Boron in granitic rocks and their contact aureoles." Reviews in Mineralogy and Geochemistry 33(1): 299-330.

Lu, D., Ji, J., Lu, R. and Tao, H. (1995). "Geochemical characteristics and metallogeny of the Yamansu iron deposit, Xinjiang (in Chinese)." Northwestern Geology 16(1): 15-19.

Lu, D., Ji, J., Lu, R. and Tao, H. (1996). "Geochemical characteristics of the rare earth elements of the Yamansu iron deposit (in Chinese with English abstract)." Journal of Xi'an college of geology 18: 12-16.

Lu, H.-Z., Liu, Y., Wang, C., Xu, Y. and Li, H. (2003). "Mineralization and Fluid Inclusion

Study of the Shizhuyuan W-Sn-Bi-Mo-F Skarn Deposit, Hunan Province, China." Economic Geology 98(5): 955-974.

Ludwig, K. R. (2001). "A Geochronological Toolkit for Microsoft Excel." Berkeley Geochronology Center Special Publication: 1-56.

Lui, D. and Chen, T. (1979). "Metallogeny and exploring perspective of Yamansu magnetite deposit, Xinjiang (in Chinese)." Dongjiang Dizhi(1): 315-316.

Lund, K., Tysdal, R. G., Evans, K. V., Kunk, M. J. and Pillers, R. M. (2011). "Structural Controls and Evolution of Gold-, Silver-, and REE-Bearing Copper-Cobalt Ore Deposits, Blackbird District, East-Central Idaho: Epigenetic Origins." Economic Geology 106(4): 585-618.

Ma, R. S., Shu, L. S. and Sun, J. Q. (1997). Tectonic evolution and mineralization of Eastern Tianshan. Beijing, Geological Publishing House.

Maher, K. C. (2010). "Skarn Alteration and Mineralization at Coroccohuayco, Tintaya District, Peru." Economic Geology 105(2): 263-283.

Maher, K. C. and Larson, P. B. (2007). "Variation in Copper Isotope Ratios and Controls on Fractionation in Hypogene Skarn Mineralization at Coroccohuayco and Tintaya, Perú." Economic Geology 102(2): 225-237.

Manning, D. (1982). "Chemical and morphological variations in tourmalines from the Hub Kapong batholith of peninsular Thailand." Mineralogical Magazine(45): 139-147.

Mao, J., Goldfarb, R., Wang, Y., Hart, C., Wang, Z. and Yang, J. (2005). "Late Paleozoic base and precious metal deposits,East Tianshan,Xinjiang,China:Characteristics and geodynamic setting." Episodes 28(1): 23-36.

Mao, J., Pirajno, F., Zhang, Z., Chai, F., Yang, J., Wu, H., Chen, S., Cheng, S. and Zhang, C. (2006). "Late variscan post-collisional Cu-Ni sulfide deposits in East Tianshan and Altay in China: principal characteristics and possible relationship with mantle plume." Acta geologica Sinica 80(7): 925-942.

Mao, J., Xie, G., Duan, C., Pirajno, F., Ishiyama, D. and Chen, Y. (2011). "A tectono-genetic model for porphyry–skarn–stratabound Cu–Au–Mo–Fe and magnetite–apatite deposits along the Middle–Lower Yangtze River Valley, Eastern China." Ore Geology Reviews 43(1): 294-314.

Mao, J., Yang, J., Qu, W., Du, A., Wang, Z. and Chunming, H. (2002). "Re-Os dating of Cu- Ni sulfide ores from Huangshandong deposit in Xinjiang and its geodynamic significance." Mineral Deposits 21(4): 323-331.

Mao, J. W., Pirajno, F., Zhang, Z. H., Chai, F. M., Wu, H., Chen, S. P., Cheng, L. S., Yang, J. M. and Zhang, C. Q. (2008). "A review of the Cu-Ni sulphide deposits in the Chinese Tianshan and Altay orogens (Xinjiang Autonomous Region, NW China): Principal characteristics and ore-forming processes." Journal of Asian Earth Sciences 32(2-4): 184-203.

Mao, J. W., Pirajno, F., Zhang, Z. H., Chai, F. M., Wu, H., Chen, S. P., Cheng, L. S., Yang, J. M. and Zhang, C. Q. (2008). "A review of the Cu–Ni sulphide deposits in the Chinese Tianshan and Altay orogens (Xinjiang Autonomous Region, NW China): Principal characteristics and ore-forming processes." Journal of Asian Earth Sciences 32(2-4): 184-203.

Mao, J. W., Yang, J. M., Wang, Z. L., Han, C. M. and Ma, T. L. (2002). "Geological setting and metallogenic process of the copper-gold mineralization in the East Tianshan. Scientific Report, 289p (in Chinese).".

Mao, Q., Fang, T., Wang, J., Wang, S. and Wang, N. (2010). "Geochronology studies of the Early Paleozoic Honghai massive sulfide deposits and its geological significance in Kalatage area, eastern Tianshan Mountian." Acta Geologica Sinica (in Chinese with English abstract) 26(10): 3017-3026.

Mapani, B. E. S. and Wilson, C. J. L. (1998). "Evidence for externally derived vein forming and mineralising fluids: An example from the Magdala gold mine, Stawell, Victoria, Australia." Ore Geology Reviews 13(1-5): 323-343.

Meinert, L. D. (1984). "Mineralogy and petrology of iron skarns in western British Columbia, Canada." Economic Geology 79(5): 869-882.

Meinert, L. D. (1992). "Skarns and skarn deposits." Geoscience Canada 19(4): 145-162.

Meinert, L. D., Dipple, G. M. and Nicolescu, S. (2005). "World skarn deposits." Economic Geology one hundredth anniversary volume: 299-336.

Meinert, L. D., Hedenquist, J. W., Satoh, H. and Matsuhisa, Y. (2003). "Formation of Anhydrous and Hydrous Skarn in Cu-Au Ore Deposits by Magmatic Fluids." Economic Geology 98(1): 147-156.

Mercier, J.-C. (1976). "Single-pyroxene geothermometry and geobarometry." American Mineralogist 61(7-8): 603-615.

Merrill, R. T., McElhinny, M. W. and McFadden, P. L. (1996). The Magnetic Field of the Earth: Paleomagnetism, the Core, and the Deep Mantle Academic Press.

Miyano, T. and Klein, C. (1989). "Phase equilibria in the system

K2O-FeO-MgO-Al2O3-SiO2-H2O-CO2 and the stability limit of stilpnomelane in metamorphosed Precambrian iron-formations." Contributions to Mineralogy and Petrology 102(4): 478-491.

Morimoto, N. (1988). "Nomenclature of Pyroxenes." Mineralogy and Petrology 39(1): 55-76.

Mücke, A. and Younessi, R. (1994). "Magnetite-apatite deposits (Kiruna-type) along the Sanandaj-Sirjan zone and in the Bafq area, Iran, associated with ultramafic and calcalkaline rocks and carbonatites." Mineralogy and Petrology 50(4): 219-244.

Mueller, A. G., Nemchin, A. A. and Frei, R. (2004). "The Nevoria Gold Skarn Deposit, Southern Cross Greenstone Belt, Western Australia: II. Pressure-Temperature-Time Path and Relationship to Postorogenic Granites." Economic Geology 99(3): 453-478.

Mukhopadhyay, B. (1991). "Garnet-clinopyroxene geobarometry; the problems, a prospect, and an approximate solution with some applications." American Mineralogist 76(3-4): 512-529.

Murphy, K. and Dymond, J. (1984). "Rare earth element fluxes and geochemical budget in the eastern equatorial Pacific." Nature 307(5950): 444-447.

Nadège, N. (1997). Structural study of the Zn-Pb mineralzations of the paleozoic of the pierrefitte dome (Hautes Pyrenee)-Texture goniometry applied to transparent and opaque minerals. Orléans, Université d'Orléans. doctor: 303.

Naranjo, J. A., Henríquez, F. and Nyström, J. O. (2010). "Subvolcanic contact metasomatism at El Laco Volcanic Complex,Central Andes." Andean Geology 37(1): 110-120.

Neumann, E. R., Dunworth, E. A., Sundvoll, B. A. and Tollefsrud, J. I. (2002). "B1 basaltic lavas in Vestfold–Jeløya area, central Oslo rift: derivation from initial melts formed by progressive partial melting of an enriched mantle source." Lithos 61(1–2): 21-53.

Newberry, N. G., Peacor, D. R., Essene, E. J. and Geissman, J. W. (1982). "Silicon in magnetite: High resolution microanalysis of magnetite-ilmenite intergrowths." Contributions to Mineralogy and Petrology 80(4): 334-340.

Nicolescu, Ş. and Cornell, D. H. (1999). "P–T conditions during skarn formation in the Ocna de Fier ore district, Romania." Mineralium Deposita 34(8): 730-742.

Niiranen, T., Mänttäri, I., Poutiainen, M., Oliver, N. S. and Miller, J. (2005). "Genesis of Palaeoproterozoic iron skarns in the Misi region, northern Finland." Mineralium Deposita 40(2): 192-217.

Nimis, P. and Taylor, W. R. (2000). "Single clinopyroxene thermobarometry for garnet peridotites. Part I. Calibration and testing of a Cr-in-Cpx barometer and an

enstatite-in-Cpx thermometer." Contributions to Mineralogy and Petrology 139(5): 541-554.

Nystroem, J. O. and Henriquez, F. (1994). "Magmatic features of iron ores of the Kiruna type in Chile and Sweden; ore textures and magnetite geochemistry." Economic Geology 89(4): 820-839.

Nystroem, J. O. and Henriquez, F. (1995). "Magmatic features of iron ores of the Kiruna type in Chile and Sweden; ore textures and magnetite geochemistry; reply." Economic Geology 90(2): 473-475.

Oen, I. S., de Maesschalck, A. A. and Lustenhouwer, W. J. (1986). "Mid-Proterozoic exhalative-sedimentary Mn skarns containing possible microbial fossils, Grythyttan, Bergslagen, Sweden." Economic Geology 81(6): 1533-1543.

Ouyang, Z., Zhou, D., Lin, J. and Feng, J. (2006). "Geochemistry and geological implications of the Baiyanche basic-indermediate dyke swarm in the Bogda orogenic belt in xingjiang, China." Geoteconica et Metallogenia 30(4): 495-503.

Pang, K.-N., Zhou, M.-F., Lindsley, D., Zhao, D. and Malpas, J. (2008). "Origin of Fe–Ti Oxide Ores in Mafic Intrusions: Evidence from the Panzhihua Intrusion, SW China." Journal of Petrology 49(2): 295-313.

Parak, T. (1984). "On the magmatic origin of iron ores of the kiruna type--a discussion." Econ Geol 79: 1945-1949.

Parak, T. (1985). "Phosphorus in different types of ore, sulfides in the iron deposits, and the type and origin of ores at Kiruna." Economic Geology 80(3): 646-665.

Piper, D. (1974). "Rare earth elements in the sedimentary cycle: A summary." Chemical Geology 14(4): 285-304.

Pirajno, F. (2007). "Mantle plumes, associated intraplate tectono-magmatic processes and ore systems." Episodes 30(1): 6-19.

Pirajno, F. (2010). "Intracontinental strike-slip faults, associated magmatism, mineral systems and mantle dynamics: examples from NW China and Altay-Sayan (Siberia)." Journal of Geodynamics 50(3-4): 325-346.

Pirajno, F., Luo, Z., Liu, S. and Dong, L. (1997). "Gold Deposits in the Eastern Tian Shan, Northwestern China." International Geology Review 39: 891-904.

Pirajno, F., Mao, J., Zhang, Z., Zhang, Z. and Chai, F. (2008). "The association of mafic–ultramafic intrusions and A-type magmatism in the Tian Shan and Altay orogens, NW China: Implications for geodynamic evolution and potential for the discovery of

new ore deposits." Journal of Asian Earth Sciences 32(2-4): 165-183.

Poldervaart, A. and Hess, H. H. (1951). "Pyroxenes in the Crystallization of Basaltic Magma." The Journal of Geology 59(5): 472-489.

Powell, R. and Powell, M. (1977). "Geothermometry and oxygen barometry using coexisting iron-titanium oxides: A reappraisal." Mineralogical Magazine 41: 257-263.

Price, M., Walsh, K. and Nature, P. (2005). Rocks and Minerals, Dorling Kindersley.

Qin, K.-z., Peng, X.-m., San, J.-z., Xu, X.-w., Fang, T.-h., Wang, S.-l. and Yu, H.-f. (2003). "Types of major ore deposits, division of metallogenic belts in eastern tianshan, and discriminatioon of potential prospects of Cu,Au, Ni mineralization(in Chinese with English abstract)." Xinjiang Geology 21(2): 143-150.

Qin, K.-z., Su, B.-x., Sakyi, P. A., Tang, D.-m., Li, X.-h., Sun, H., Xiao, Q.-h. and Liu, P.-p. (2011). "SIMS zircon U-Pb geochronology and Sr-Nd isotopes of Ni-Cu-Bearing Mafic-Ultramafic Intrusions in Eastern Tianshan and Beishan in correlation with flood basalts in Tarim Basin (NW China): Constraints on a ca. 280 Ma mantle PLUME." Am J Sci 311(3): 237-260.

Qin, K., Fang, T., Wang, S., Zhu, b., Feng, Y., Yu, H. and Xiu, Q. (2002). "Plate tectonics division, evolution and metallogenic settings in Eastern Tianshan mountains, NW China." Xinjiang Geology 20(4): 302-308.

Qin, K., Sun, S., Li, J., Fang, T., Wang, S. and Liu, W. (2002). "Paleozoic Epithermal Au and Porphyry Cu Deposits in North Xinjiang, China: Epochs, Features, Tectonic Linkage and Exploration Significance." Resource Geology 52(4): 291-300.

Råheim, A. and Green, D. H. (1974). "Experimental determination of the temperature and pressure dependence of the Fe-Mg partition coefficient for coexisting garnet and clinopyroxene." Contributions to Mineralogy and Petrology 48(3): 179-203.

Ray, G. E. and Webster, I. C. L. (1991). An overview of skarn deposits. Ore deposits, tectonics and metallogeny in the Canadian cordillera, British Columbia Ministry of Energy Mines and Petroleum Resources: 213-252.

Ren, B., Xingke, Y., Li, W., Li, Y. and Wu, J. (2002). "The mineralization geological characteristics and deposit comparison of Tuwu largest type porphyry copper deposit in eastern Tianshan mountain." Northwestern Geology 35(3): 67-75.

Ren, J., Jiang, C., Zhang, Z. and QIan, D. (1980). Geotectonic evolution of China. Beijing, Science Publish House.

René, M. and Stelling, J. (2007). "Garnet-bearing granite from the Třebíč pluton, Bohemian

Massif (Czech Republic)." Mineralogy and Petrology 91(1): 55-69.

Reynolds, R. C. (1965). "Geochemical behaviour of boron during the metamorphism of carbonate rocks." Geochimica et Cosmochimica Acta 29(9): 1101-1114.

Rhazi, M. E. L. and Hayashi, K. i. (2002). "Mineralogy, Geochemistry, and Age Constraints on the Beni Bou Ifrour Skarn Type Magnetite Deposit, Northeastern Morocco." Resource Geology 52(1): 25-39.

Robb, L. (2005). Introduction to Ore-Forming Processes, Blackwell Publishing.

Robl, J., Hergarten, S., Stüwe, K. and Hauzenberger, C. (2007). "THERMAL HISTORY: A new software to interpret diffusive zoning profiles in garnet." Computers & Geosciences 33(6): 760-772.

Rollinson, H. (2003). "Metamorphic history suggested by garnet-growth chronologies in the Isua Greenstone Belt, West Greenland." Precambrian Research 126: 181-196.

Romer, R. L., Martinsson, O. and Perdahl, J. A. (1994). "Geochronology of the Kiruna iron ores and hydrothermal alterations." Econ Geol 89(6): 1249-1261.

Rubin, J. N. and Kyle, J. R. (1988). "Mineralogy and geochemistry of the San Martin skarn deposit, Zacatecas." Econ Geol 83(8): 1782-1801.

Rui, Z., Goldfarb, R., Qiu, Y., Zhou, T., Chen, R., Pirajno, F. and Yun, G. (2002). "Paleozoic-early Mesozoic gold deposits of the Xinjiang Autonomous Region, northwestern China." Mineralium Deposita 37(3): 393-418.

Rui, Z., Wang, L. and Wang, Y. (2002). "Discussion on Metallogenic Epoch of Tuwu and Yandong Porphyry Copper Deposits in Eastern Tianshan Mountains , Xinjiang." Mineral Deposits 21(1): 16-22.

Rye, R. O. (1993). "The evolution of magmatic fluids in the epithermal environment; the stable isotope perspective." Economic Geology 88(3): 733-752.

Sabau, G., Negulescu, E. and Massonne, H. (2006). "Chemical zonation and relative timing of growth sections in garnets from eclogites of the Leaota Massif, South Carpathians." Mineralogical Magazine 70(6): 655-667.

San, J., Hui, W., Qin, K., Sun, H., Xu, X., Liang, G., Wei, J., Kang, F. and Xiao, Q. (2007). "Geological characteristics of Tulargen magmatic Cu-Ni-Co deposit in eastern Xinjiang and its exploration direction." Mineral Deposits 26(3): 307-316.

Saxena, S. K. (1979). "Garnet-clinopyroxene geothermometer." Contributions to Mineralogy and Petrology 70(3): 229-235.

Schmidt, V., Günther, D. and Hirt, A. M. (2006). "Magnetic anisotropy of calcite at

room-temperature." Tectonophysics 418(1-2): 63-73.

Sengor, A. M. C., Natal'in, B. A. and Burtman, V. S. (1993). "Evolution of the Altaid tectonic collage and Palarozoic crustal growth in Eurasia." Nature(364): 299-307.

Shi, Y., Liu, D., Zhang, Q., Jian, P., Zhang, F. and Miao, L. (2007). "SHRIMP zircon U-Pb dating of the Gangou granitoids, Central Tianshan Mountains, Northwest China and tectonic significances." Chinese Science Bulletin 52(11): 1507-1516.

Shiga, Y. (1989). "Further study on silician magnetite." Mining Geology 39: 305-309.

Shimazaki, H. (1998). "On the Occurrence of Silician Magnetites." Resource Geology 48(1): 23-29.

Shimazaki, H. and Kusakabe, M. (1990). "Oxygen isotope study of the Kamioka Zn-Pb skarn deposits, Central Japan." Mineralium Deposita 25(3): 221-229.

Shoji, T., Mariko, T. and Ooishi, T. (1985). "Stability of grandite garnet in H2O-CO2 mixtures at 600°C under 100 MPa." Mineralogical Journal 12(6): 260-268.

Shtukenberg, A., Popov, D. and Yu, P. (2002). "An application of the point-dipole model to the problem of optical anomalies in grandite garnets." Mineralogical Magazine 66(2): 275-286.

Shtukenberg, A. G., Popov, D. Y. and Punin, Y. O. (2005). "Growth ordering and anomalous birefringence in ugrandite garnets." Mineral Mag 69(4): 537-550.

Shu, L., Charvet, J., Guo, L., Lu, H. and Charvet, L. (1999). "A Large-Scale Palaeozoic Dextral Ductile Strike-Slip Zone:the Aqqikkudug-Weiya Zone along the Northern Margin of the Central Tianshan Belt,Xinjiang,NW China." Acta Geologica Sinica (in Chinese with English abstract) 73(2): 148-162.

Shu, L., Wang, B., Zhu, W., Guo, Z., Charvet, J. and Zhang, Y. (2011). "Timing of initiation of extension in the Tianshan, based on structural, geochemical and geochronological analyses of bimodal volcanism and olistostrome in the Bogda Shan (NW China)." International Journal of Earth Sciences 100(7): 1647-1663.

Shulters, J. C. and Bohlen, S. R. (1989). "The Stability of Hercynite and Hercynite-Gahnite Spinels in Corundum- or Quartz-Bearing Assemblages." Journal of Petrology 30(4): 1017-1031.

Sillitoe, R. (2003). "Iron oxide-copper-gold deposits: an Andean view." Mineralium Deposita 38(7): 787-812.

Sizaret, S., Chen, Y., Barbanson, L., Henry, B., Camps, P. and Marcoux, E. (2006). "Crystallization in flow – I. Palaeocirculation track by texture analysis and magnetic

fabrics." Geophysical Journal International 167(2): 605-612.

Sizaret, S., Fedioun, I., Barbanson, L. and Chen, Y. (2006). "Crystallization in flow – II. Modelling crystal growth kinetics controlled by boundary layer thickness." Geophysical Journal International 167(2): 1027-1034.

Slack, J. F. (1996). "Tourmaline associations with hydrothermal ore deposits." Reviews in Mineralogy and Geochemistry 33(1): 559-643.

Soloviev, S. G. (2011). "Geology, Mineralization, and Fluid Inclusion Characteristics of the Kensu W-Mo Skarn and Mo-W-Cu-Au Alkalic Porphyry Deposit, Tien Shan, Kyrgyzstan." Economic Geology 106(2): 193-222.

Song, B., Li, J., Li, W., Wang, K. and Wang, Y. (2002). "Shrimp dating of zircons from Dananhu and Kezirkalasayi granitoid batholith in Southern margin of Tuha basin and their geological implication." Xinjiang Geology 20(4): 342-345.

Spencer, K. J. and Lindsley, D. H. (1981). " A solution model for coexisting iron-titanium oxides." American Mineralogist 66: 1189-1201.

Su, B., Qin, K., Sakyi, P. A., Liu, P., Tang, D., Malaviarachchi, S. P. K., Xiao, Q., Sun, H., Dai, Y. and Yan, H. (2011). "Geochemistry and geochronology of acidic rocks in the Beishan region, NW China: Petrogenesis and tectonic implications." Journal of Asian Earth Sciences 41(1): 31-43.

Sun, H., Qin, K., Li, J., Tang, D., Fan, X. and Xiao, Q. (2008). "Constraint of mantle partial melting on PGE mineralization of mafic-ultramafic intrusions in Eastern Tianshan: Case study on Tulargen and Xiangshan Cu-Ni deposits." Yanshi Xuebao = Acta Petrologica Sinica 24(5): 1079-1086.

Sun, H., Qin, K., Xu, X., Li, J., Ding, K., Xu, Y. and San, J. (2007). "Petrological characteristics and copper nickel ore forming processes of Early Permian mafic ultramafic intrusion belts in East Tianshan." Mineral Deposits 26(1): 98-108.

Sun, H., Qin, K. Z., Xu, X. W., Li, J. X., Ding, K. S., Xu, Y. X. and San, J. Z. (2007). "Petrological characteristics and copper-nickel ore-forming processes of Early Permian mafic-ultramafic intrusion belts in East Tianshan." Mineral Deposits 26(1): 98-108.

Sun, S. S. and McDonough, W. F. (1989). Chemical and isotopic systematics of oceanic basalts: implications for mantle composition and processes. London, Geological Society Special Publication.

Tang, J., Gu, L., Zhang, Z., Wu, C., San, J., Wang, C., LUi, S. and Zhang, G. (2007). "Characteristics, age and origin of the Xianshuiquan geneissose granite in esteran

Tianshan." Acta Petrologica Sinica 23(8): 1803-1820.

Tang, P.-z., Wang, J.-b., Wang, Y.-w. and Long, L.-l. (2010). "Geochemical characteristics of mafic-ultramafic rocks in the Cihai ore district, Xinjiang, and their geological significance." Geochimica (in Chinese with English abstract) 39(6): 542-552.

Tarling, D. H. and Hrouda, F. (1993). The magnetic anisotropy of rocks, Chapman and Hall.

Taylor, B. and Liou, J. (1978). "The low temperature stablility of andradite in C-O-H fluids." American Mineralogist 63: 378-393.

Taylor, B. E. (1976). Origin and significance of C-O-H fluids in the formation of Ca-Fe-Si skarn, Osgood Mountains, Humboldt County, Nevada, Stanford University. PHD: 149.

Taylor, B. E. and Slack, J. F. (1984). "Tourmalines from Appalachian-Caledonian massive sulfide deposits; textural, chemical, and isotopic relationships." Economic Geology 79(7): 1703-1726.

Taylor, S. R. and McClennan, S. M. (1985). The continental crust: Its composition and evolution. Oxford, Blackwell Scientific Publications.

Thorne, W., Hagemann, S., Vennemann, T. and Oliver, N. (2009). "Oxygen Isotope Compositions of Iron Oxides from High-Grade BIF-Hosted Iron Ore Deposits of the Central Hamersley Province, Western Australia: Constraints on the Evolution of Hydrothermal Fluids." Economic Geology 104(7): 1019-1035.

Trestman-Matts, A., Dorris, S. E., Kumarakrishnan, S. and Mason, T. O. (1983). "Thermoelectric Determination of Cation Distributions in." Journal of the American Ceramic Society 66(12): 829-834.

Turner, F. J., Griggs, D. T. and Heard, H. (1954). "Experimental deformation of calcite crystals." Geological Society of America Bulletin 65(9): 883-934.

Turnock, A. C. and Eugster, H. P. (1962). "Fe—Al Oxides: Phase Relationships below 1,000°C." Journal of Petrology 3(3): 533-565.

Verkaeren, J. and Bartholome, P. (1979). "Petrology of the San Leone magnetite skarn deposit (S.W. Sardinia)." Economic Geology 74(1): 53-66.

Vernon, R. H. and Clarke, G. L. (2008). Principles of metamorphic petrology. London, Cambridge University Press.

Vidal, O., Parra, T. and Vieillard, P. (2005). "Thermodynamic properties of the Tschermak solid solution in Fe-chlorite: Application to natural examples and possible role of oxidation." American Mineralogist 90(2-3): 347-358.

Vidale, R. (1969). "Metasomatism in a chemical gradient and the formation of calc-silicate

bands." Am J Sci 267(8): 857-874.

Vielzeuf, D. and Holloway, J. R. (1988). "Experimental determination of the fluid-absent melting relations in the pelitic system." Contributions to Mineralogy and Petrology 98(3): 257-276.

Von Gruenewaldt, G. (1993). "Ilmenite-Apatite Enrichments in the Upper Zone of the Bushveld Complex: A Major Titanium-Rock Phosphate Resource." International Geology Review 35(11): 987-1000.

Von Gruenewaldt, G., Klemm, D. D., Henckel, J. and Dehm, R. M. (1985). "Exsolution features in titanomagnetites from massive magnetite layers and their host rocks of the upper zone, eastern Bushveld Complex." Econ Geol 80(4): 1049-1061.

Wang, B., Chen, Y., Zhan, S., Shu, L., Faure, M., Cluzel, D., Charvet, J. and Laurent-Charvet, S. (2007). "Primary Carboniferous and Permian paleomagnetic results from the Yili Block (NW China) and their implications on the geodynamic evolution of Chinese Tianshan Belt." Earth and Planetary Science Letters 263(3-4): 288-308.

Wang, B., Cluzel, D., Shu, L., Faure, M., Charvet, J., Chen, Y., Meffre, S. and de Jong, K. (2009). "Evolution of calc-alkaline to alkaline magmatism through Carboniferous convergence to Permian transcurrent tectonics, western Chinese Tianshan." International Journal of Earth Sciences 98(6): 1275-1298.

Wang, B., Faure, M., Shu, L., Cluzel, D., Charvet, J., De Jong, K. and Chen, Y. (2008). "Paleozoic tectonic evolution of the Yili Block, western Chinese Tianshan." Bulletin de la Societe Geologique de France 179(5): 483-490.

Wang, C., Gu, L., Zhang, Z., Wu, C., Tang, J., San, J., Li, G. and Li, Z. (2009). "Petrogenesis and tectonic implications of the Permian alkaline granite and quartz-syenite assemblage in Harlik Mountains, Xinjiang." Acta Petrologica Sinica 25(12): 3166-3181.

Wang, D. H., Li, C. J., Chen, S., Xiao, K., Li, H. Q. and Liang, T. (2006). "Metallogenic characteristics and direction in mineral search in the East Tianshan, Xinjiang, China." Geological Bulletin of China 25(8): 910-915.

Wang, Q., Shu, L. and Charvet, J. (2010). "Understanding and study perspectives on tectonic evolution and crustal structure of the Paleozoic Chinese Tianshan." Episodes 33(4): 242-266.

Wang, X. (2005). "Analysis of the geology and genesis of Yamansu Fe-deposit." Contributions to Geology and Mineral Resources Research 20: 125-128.

Wang, X. (2005). "Analysis of the geology and genesis of Yamansu Fe-deposit (in Chinese with

English abstract)." Contributions to geology and mineral resources research 20 sup: 125-128.

Wang, Y., Li, J. and Sun, G. (2008). "Postcollisional eastward extrusion and tectonic exhumation along the eastern Tianshan Orogen, Central Asia: constraints from dextral strike-slip motion and 40Ar-39Ar geochronological evidence." The Journal of Geology 116: 599-618.

Wang, Y., Mao, J. W., Chen, W., Yang, F. Q. and Yang, J. M. (2006). "Tectonic constrants on minerallization of the Kanggurtag gold belt in the Eastern Tianshan, Xinjiang, NW China." Acta Petrologica Sinica 22(1): 236-244.

Wang, Y., Sha, J. and Cheng, C. (2006). "Composition of magnetite from the Cihai Fe (Co) deposit, Xinjiang, and its genetic significance." Mineral Deposits (in Chinese with English abstract) 25 special 321-324.

Wang, Y., Wang, J. and Wang, L. (2006). "Comparison of host rocks on the two types of vanadic titianomagnetite deposits in eastern Tien Shan, China." Yanshi Xuebao = Acta Petrologica Sinica 22(5): 1425-1436.

Wang, Y., Wang, J., Wang, L. and Long, L. (2008). "Metallogenic Series Related to Permian Mafic Complex in North Xinjiang: Post-collisional Stage or Mantle Plume Result?" Acta Geologica Sinica - English Edition 82(4): 788-795.

Wang, Y., Wang, J., Wang, L., Peng, X., Hui, W. and Qin, Q. (2006). "A intermediate type of Cu-Ni sulfide and V-Ti magnetite deposit: Xiangshanxi deposit, Hami, Xinjiang, China." Acta Geologica Sinica (in Chinese with English abstract) 80(1): 61-73.

Wang, Y. T., Mao, J., Bierlein, F. P., Mao, J. W., Chen, W., Yang, J. M., Wang, Z. L. and Yang, F. Q. (2005). Strike-slip fault controls on mineralization in the Kanggurtag gold belt in the Eastern Tianshan, Xinjiang, NW China. Mineral Deposit Research: Meeting the Global Challenge, Springer Berlin Heidelberg: 1347-1349.

Wartes, M. A., Carroll, A. R. and Greene, T. J. (2002). "Permian sedimentary record of the Turpan-Hami basin and adjacent regions, northwest China: Constraints on postamalgamation tectonic evolution." Geological Society of America Bulletin 114(2): 131-152.

Weidner, J. R. (1982). "Iron-oxidem agmasin the system Fe-C-O." Canadian Mineralogist 20: 555-566.

Wenk, H. R., Takeshita, T., Bechler, E., Erskine, B. G. and Matthies, S. (1987). "Pure shear and simple shear calcite textures. Comparison of experimental, theoretical and natural data."

Journal of Structural Geology 9(5–6): 731-745.

Wenzel, T., Baumgartner, L. P., Brugmann, G. E., Konnikov, E. G. and Kislov, E. V. (2002). "Partial Melting and Assimilation of Dolomitic Xenoliths by Mafic Magma: the Ioko-Dovyren Intrusion (North Baikal Region, Russia)." Journal of Petrology 43(11): 2049-2074.

Westendorp, R. W., Watkinson, D. H. and Jonasson, I. R. (1991). "Silicon-bearing zoned magnetite crystals and the evolution of hydrothermal fluids at the Ansil Cu-Zn mine, Rouyn-Noranda, Quebec." Economic Geology 86(5): 1110-1114.

Wilson, A. H. and Prendergast, M. D. (2001). "Platinum-Group Element Mineralisation in the Great Dyke, Zimbabwe, and its Relationship to Magma Evolution and Magma Chamber Structure." South African Journal of Geology 104(4): 319-342.

Windley, B. F., Alexeiev, D., Xiao, W., Kröner, A. and Badarch, G. (2007). "Tectonic models for accretion of the Central Asian Orogenic Belt." Journal of the Geological Society 164(1): 31-47.

Wright, J. E. and Haxel, G. (1982). "A garnet-two-mica granite, Coyote Mountains, southern Arizona: Geologic setting, uranium-lead isotopic systematics of zircon, and nature of the granite source region." Geological Society of America Bulletin 93(11): 1176-1188.

Wu, C. (2008). Recent progress in Centre Tianshan belt. Nanjing.

Wu, C., Zhang, Z., Zaw, K., Della-Pasque, F., Tang, J., Zheng, Y., Wang, C. and San, J. (2006). "Geochronology，geochemistry and tectonic significances of the Hongyuntan granitoids in the Qoaag area Eastern Tianshan." Acta Petrologica Siniea 22(5): 1121-1134.

Wu, C. C. and Mason, T. O. (1981). "Thermopower Measurement of Cation Distribution in Magnetite." Journal of the American Ceramic Society 64(9): 520-522.

Wu, Y. and Chang, Y. (1998). "On the magmatic skarn." Earth Science Frontiers (China University of Geosciences, Beijing) 5(4): 291-301.

XBGMR (1993). Xinjiang Bureau of Geology and Mineral Resources:Regional Geology of Xinjiang Uygur Autonomous Region (in Chinese with English abstract). Beijing, Geological Publishing House.

Xia, J. (2010). Contact Zone Structure and Mineralization Significance of Lingxiang Iron Deposit in Daye, Hubei Province. China University of Geosciences Hubei, China University of Geosciences Master.

Xia, L.-Q., Xu, X.-Y., Xia, Z.-C., Li, X.-M., Ma, Z.-P. and Wang, L.-S. (2004). "Petrogenesis of Carboniferous rift-related volcanic rocks in the Tianshan, northwestern China."

Geological Society of America Bulletin 116(3-4): 419-433.

Xiao, W.-J., Zhang, L.-C., Qin, K.-Z., Sun, S. and Li, J.-L. (2004). "Paleozoic accretionary and collisional tectonics of the eastern Tianshan (China): Implications for the continental growth of central Asia." Am J Sci 304(4): 370-395.

Xiao, W., Han, C., Yuan, C., Sun, M., Lin, S., Chen, H., Li, Z., Li, J. and Sun, S. (2008). "Middle Cambrian to Permian subduction-related accretionary orogenesis of Northern Xinjiang, NW China: Implications for the tectonic evolution of central Asia." Journal of Asian Earth Sciences 32(2-4): 102-117.

Xiao, W., Windley, B. F., Badarch, G., Sun, S., Li, J., Qin, K. and Wang, Z. (2004). "Palaeozoic accretionary and convergent tectonics of the southern Altaids: implications for the growth of Central Asia." Journal of the Geological Society 161(3): 339-342.

Xiao, W. J., Mao, Q. G., Windley, B. F., Han, C. M., Qu, J. F., Zhang, J. E., Ao, S. J., Guo, Q. Q., Cleven, N. R., Lin, S. F., Shan, Y. H. and Li, J. L. (2010). "Paleozoic multiple accretionary and collisional processes of the Beishan orogenic collage." Am J Sci 310(10): 1553-1594.

Xirouchakis, D., Lindsley, D. H. and Andersen, D. J. (2001). "Assemblages with titanite (CaTiOSiO4), Ca-Mg-Fe olivine and pyroxenes, Fe-Mg-Ti oxides, and quartz: Part I. Theory." American Mineralogist 86(3): 247-253.

Xirouchakis, D., Lindsley, D. H. and Frost, B. R. (2001). "Assemblages with titanite (CaTiOSiO4), Ca-Mg-Fe olivine and pyroxenes, Fe-Mg-Ti oxides, and quartz: Part II. Application." American Mineralogist 86(3): 254-264.

Xu, G. and Lin, X. (2000). "Geology and geochemistry of the Changlongshan skarn iron deposit, Anhui Province, China." Ore Geology Reviews 16(1-2): 91-106.

Xu, X. Y., He, H. P., Wang, H. L. and Chen, J. L. (2009). Geological settings of the metallogeny of the Eastern Tian Shan and Beishan areas, scale 1:1,000,000. Beijing, Geological Publishing House.

Xu, X. Y., He, S. P., Wang, H. L., Chen, J. L., Zhang, E. P. and Feng, Y. M. (2008). Outline of the geology of NW China—Qinling, Qilian and Tian Shan areas. Beijing, Science in China Press.

Xue, C., Ji, J. and Yang, Q. (2000). "Subvolcanic hydrothermal metallogeny of the Cihai iron (cobalt) deposit, Xinjiang." Northwestern Geology 19(2): 156-164.

Yakubchuk, A. S., Shatov, V. V., Kirwin, D., Tomurtogoo, O., Badarch, G. and Buryak, A. A. (2005). "Gold and Base Metal Metallogeny of the Central Asian Orogenic

Supercollage." Economic Geology 100th Anniversary: 1035-1068.

Yang, F., Mao, J., Bierlein, F. P., Pirajno, F., Zhao, C., Ye, H. and Liu, F. (2009). "A review of the geological characteristics and geodynamic mechanisms of Late Paleozoic epithermal gold deposits in North Xinjiang, China." Ore Geology Reviews 35(2): 217-234.

Yang, H., Li, Y., Yan, g., Li, W., Yang, L., Zhao, G., Ye, D., Zhao, Y., Zhao, J., Shen, C., Wang, X. and Su, X. (2006). "Main metallogenic characteristics in the beishan orogen." Northwestern Geology 39(2): 78-95.

Yang, T., LI, J., Sun, G. and Wang, Y. (2006). "Earlier Devonian active continental arc in Central Tianshan: evidence of geochemical analyses and Zircon SHRIMP dating on mylonitized granitic rock." Acta Petrologica Sinica 22(1): 41-48.

Yu, H. (1985). "The skarn in Xujiachong picrite body from Jingshan country, Hubei Province (in Chinese with English abstract)." Rock and Mineral Analysis(2): 108-114.

Yu, S., Li, Q., Yang, Q. and Lui, H. (1999). Open-pit mining geological survey report for Cihai magnetite deposit (second stage).

Yuan, C., Sun, M., Wilde, S., Xiao, W., Xu, Y., Long, X. and Zhao, G. (2010). "Post-collisional plutons in the Balikun area, East Chinese Tianshan: Evolving magmatism in response to extension and slab break-off." Lithos 119(3-4): 269-288.

Zarayskiy, G. P., Zharikov, V. A., Stoyanovskaya, F. M. and Balashov, V. N. (1987). "THE EXPERIMENTAL STUDY OF BIMETASOMATIC SKARN FORMATION." International Geology Review 29(7): 761-858.

Zhang, A. and Ding, T. (1984). "Xinjiang Yamansu ancient volcanic dome and its ore-controlling characteristics." Northwestern Geology(3): 19-24.

Zhang, C.-L., Li, Z.-X., Li, X.-H., Xu, Y.-G., Zhou, G. and Ye, H.-M. (2010). "A Permian large igneous province in Tarim and Central Asian orogenic belt, NW China: Results of a ca. 275 Ma mantle plume?" Geological Society of America Bulletin 122(11-12): 2020-2040.

Zhang, G., Zhang, B. and Li, Z. "Fundamental characteristics and its geological significance of Kangguertage fault zone in the Eastern Xinjiang." Journal of Chengdu college of Geology 19(3): 41-49.

Zhang, H., Wei, G., Li, Y., Du, Z. and Chai, D. (2010). "Carboniferous lithologic association and tectonic evolution of Dananhu arc in the East Tianshan Mountains." Acta petrologica et Mineralogica(in Chinese with Englisth abstract) 29(1): 1-14.

Zhang, L., Ji, J., Li, H. and Shen, Y. (2000). "Geochemical characteristics and source of two-type oreforming fluids in Kanggultage gold ore belt, east Tianshan." Acta Petrologica Sinica 16(4): 535-541.

Zhang, L., Qin, K. and Xiao, W. (2008). "Multiple mineralization events in the eastern Tianshan district, NW China: Isotopic geochronology and geological significance." Journal of Asian Earth Sciences 32(2-4): 236-246.

Zhang, L., Qin, K., Ying, J., Xia, B. and Shu, J. (2004). "The relationship between ore forming processes and adakitic rock in Tuwu-Yandong porphyry copper metallogenic belt, eastern Tianshan mountains." Acta Petrologica Sinica 20(2): 259-268.

Zhang, M., Li, C., Fu, P., Hu, P. and Ripley, E. (2011). "The Permian Huangshanxi Cu–Ni deposit in western China: intrusive–extrusive association, ore genesis, and exploration implications." Mineralium Deposita 46(2): 153-170.

Zhang, M., Zhang, J., Wu, J., Chen, S., Jin, H. and Li, s. (1980). "The preliminary study of geological characteristics about Cihai-type iron deposit (in Chinese)." Geol Prospect 16(6): 25-32.

Zhang, S. and Ling, Q. (1993). "Characteristics of skarn copper deposit: an example from dongshizishan copper deposit in tongling county, anhui province." Earth Science Journal of China University of Geosciences 18(6): 801-814.

Zhang, Z. (2010). "A discussion on the genetic mechanism of Tonglüshan skarn Cu-Fe deposits,Hubei Province." Earth Science Frontiers (China University of Geosciences, Beijing)(5): 296-305.

Zhang, Z., Gu, L., Wu, C., Li, W., Xi, A. and Wang, S. (2005). "Zircon SHRIMP Dating for the Weiya Pluton, Eastern Tianshan: Its Geological Implications." Acta Geologica Sinica - English Edition 79(4): 481-490.

Zhang, Z., Gu, L., Yang, H., Wu, C., Wang, Y. and Min, M. (2004). "Characteristics and genesis of the Chengjiangian gneissic granites in the east section of the Middle Tianshan Mountain areas: Taking the Tianhudong granite as am example." Acta Petrologica Sinica 20(2): 595-608.

Zhao, a. (1990). "A study on the mineral chemistry of magnetite from Tieshan iron copper mineral deposit, Daye hubei and its origin." Earth Science Journal of China University of Geosciences 15(4): 358-396.

Zhao, B. (1989). Skarns and skarn deposits of China, Science Press. Zhao, B., Li, T. and Li, Z. (1985). "Experimental study of the physico-chemical conditions of skarn formation."

Chinese Journal of Geochemistry 4(2): 114-126.

Zhao, B., Zhao, J., Li, Z., Zhang, Z. and Peng, Z. (2003). "Characteristics of melt inclusions in skarn minerals from Fe, Cu(Au) and Au(Cu) ore deposits in the region from Daye to Jiujiang." Science in China Series D: Earth Sciences 46(5): 481-497.

Zhao, J., Qiu, X., Zhao, B., Tu, X., Yu, J. and Lu, T. (2007). "Ree geochemistry of mineralzed skarns from Daye to Wushan region, China." Geochimica 36(4): 400-412.

Zhao, J., Zhao, B., Zhang, C. and Wang, R. (2003). "Compositions of melt inclusions in garnet and pyroxene from skarn deposits distributed in the area from Daye to Chengmenshan." GEOCHIMICA 32(6): 540-550.

Zhao, Y., Bi, C. and Li, D. (1983). "The characteristics of volatile components and alkaline metasomatism in main skarn-type iron deposits of China and their role in ore deposit fromation." Geological Review (Chinese) 29(1): 66-74.

Zhao, Y., Bi, C. and Li, D. (1984). "The characteristics of volatile components and alkaline metasomatism in main skarn-type iron deposits in China and their role in ore formation." Chinese Journal of Geochemistry 3(1): 14-23.

Zhao, Y., Lin, W., Bi, C. and Li, D. (1986). "Basic geological characteristics of skarn deposits of China." Bulletin of the Chinese academy of geological sciences 8(3): 59-87.

Zhao, Y., Lin, W., Bi, C., Li, D. and Jiang, C. (1990). Skarn deposits of China.

Zhao, Z., Guo, Z., Han, B., Wang, Y. and Liu, C. (2006). "Comparative study on Permian basalts from Eastern Xinjiang-Beihan area of Gansu province and its tectonic implications." Acta Petrologica Sinica 22(5): 1279-1193.

Zhao, Z. H., Xiong, X. L., Wang, Q., Wyman, D. A., Bao, Z. W., Bai, Z. H. and Qiao, Y. L. (2008). "Underplating-related adakites in Xinjiang Tianshan, China." Lithos 102(1-2): 374-391.

Zharikov, V. A., 1970, Skarns: Int'l. Geol. Rev., v. 12, p. 541-559, 619-647, 760-775. (1970). "Skarns." International Geology Review 12: 541-559.

Zharikov, V. A., Pertsev, N. N., Rusinov, V. L., Callegari, E. and Fettes, D. J. (web version 01.02.07). Metasomatism and metasomatic rocks.

Zharikov, V. A. and Zaraisky, G. P. (2003). Experimental Modelling of Wall-Rock Metasomatism Chapter 9 in Progress in Metamorphic and Magmatic Petrology; A Memorial volume in Honor of D. S. Korzhinskiy (L. L. Perchuk, Ed.). Cambridge University Press, Cambridge, England. 503 p.

Zhou, J., Cui, B., Xiao, H. and Chen, S. (2000). "The rift evolution and au ore-forming regular

in East part of beishan, Ganshu and Xingjiang (in Chinese with English abstract)." Volcanology and Mineral Resources 21(1): 7-17.

Zhou, M.-F., Michael Lesher, C., Yang, Z., Li, J. and Sun, M. (2004). "Geochemistry and petrogenesis of 270 Ma Ni-Cu-(PGE) sulfide-bearing mafic intrusions in the Huangshan district, Eastern Xinjiang, Northwest China: implications for the tectonic evolution of the Central Asian orogenic belt." Chemical Geology 209(3-4): 233-257.

Zhou, M.-F., Michael Lesher, C., Yang, Z., Li, J. and Sun, M. (2004). "Geochemistry and petrogenesis of 270 Ma Ni–Cu–(PGE) sulfide-bearing mafic intrusions in the Huangshan district, Eastern Xinjiang, Northwest China: implications for the tectonic evolution of the Central Asian orogenic belt." Chemical Geology 209(3–4): 233-257.

Zhou, M.-F., Zhao, J.-H., Jiang, C.-Y., Gao, J.-F., Wang, W. and Yang, S.-H. (2009). "OIB-like, heterogeneous mantle sources of Permian basaltic magmatism in the western Tarim Basin, NW China: Implications for a possible Permian large igneous province." Lithos 113(3-4): 583-594.

Zhou, T., Yuan, F., Tan, L., Fan, Y. and Yue, S. (2006). "Geodynamic significance of the A-type granites in the Sawuer region in west Junggar, Xinjiang: Rock geochemistry and SHRIMP zircon age evidence." Science in China Series D: Earth Sciences 49(2): 113-123.

Zou, G., Liang, G., Chen, J., Zheng, Y., Gao, J., Xing, D. and Li, S. (2006). "Late paleozoic tectonic framword and evolution in the Jiabaishan area, Qoltag, eastern Tianshan, Northwest China." Geological Bulletin of China 25(1-2): 48-57.

Zuo, G. and He, G. (1990). Plate Tectonics and Metallogenic Regularities in Beishan Region（ in Chinese with English abstract）. Beijing, Peking University Press.

Zuo, G., Li, S., Yu, S. and Li, Q. (2004). "The occurrence characteristics and metallotectonic evolution of Cihai iron ore deposit in Xinjiang." Northwestern Geology (in Chinese with English abstract) 37(1): 53-61.

Zuo, G., Liu, Y. and Liu, C. (2003). "Framework and evolution of the tectonic structure in Beishan area across inner Mongolia autonomous region (in Chinese with English abstract)." Acta Geological Gansu 12(1): 1-15.

Абдулла Алиев Х. М.(translated by Xu, W. (1953). The relationship between ore-forming process and granitoid pluton, Geological Publishing House.

APPENDIX A: Method of rock magmatism

The term “magnetic field” simply describes a volume within which there is a change in magnetic energy. This change in energy can be detected and measured. The location where a magnetic field can be detected exiting or entering a material is called a magnetic pole. Magnetic poles have never been detected in isolation but always occur in pairs, which are referred to as dipoles. A dipole has a magnetic pole on one end and a second, equal but opposite, magnetic pole on the other. A bar magnet can be considered a dipole with a north pole at one end and south pole at the other. A magnetic field can be measured leaving the dipole at the North Pole and returning to the magnet at the South Pole. All matter is composed of atoms, and atoms are composed of protons, neutrons and electrons. Protons and neutrons are located in an atom’s nucleus and electrons are in constant motion around the nucleus. Electrons carry a negative charge, based on Ampère’s Law, and produce a magnetic field as they move through space. A magnetic field is produced whenever an electrical charge is in motion. The strength of this field is called the magnetic moment, which is the sum of individual magnetic moments from multiple atoms. Ampère’s Law is a simple approximation to the modern physical interpretation of magnetism and is applicable to diamagnetic materials. However, our understanding of paramagnetism and ferromagnetism is based on the quantum spin of atomic electrons.

When a material is placed into a magnetic field H, the field will induce a magnetization $M = \chi H$, where χ is the bulk magnetic susceptibility of the material. The total measurable magnetic flux, which has contributions from the applied field and the induced magnetization, is the magnetic induction $B = \mu 0*(M + H)$, where $\mu 0$ is the magnetic constant. Most materials produce their own magnetization in

response to the applied external field. Typically, the response is weak and exists only when the magnetic field is applied. The term “magnetism” is used to describe how these materials respond on the microscopic level and is used to categorize the type of magnetic behaviour of a material.

1: Magnetic anisotropy

The magnetic energy of a ferromagnetic grain is minimized by aligning its magnetic moment in the direction of the ambient magnetic field. In the absence of other controls on the orientation of their magnetization, ferromagnetic grains would always align with the ambient geomagnetic field and no older remanence would be preserved. However, the energy required to magnetize a grain is usually not constant in all orientations; there are ‘easy’ directions of magnetization in which the associated energy is lower. Alignment of magnetization along the easy axis of magnetization in a ferromagnetic grain enables recording of long-term remanent magnetizations. There are three principal sources of magnetic anisotropy.

Magnetocrystalline anisotropy occurs when the exchange energy between coupled spins is minimized when spins are aligned along particular crystallographic axes.

Shape anisotropy can be considered as follows. If atomic magnetic moments are modeled as pairs of magnetic charges, a magnetized grain will have a surface distribution of charges, which not only produces an external field but also an internal demagnetizing field that opposes the overall magnetization. The strength of this field depends on the surface charge distribution. Therefore an elongated grain has a smaller demagnetizing field along its long axis. The long axis of the grain then becomes the easy axis of magnetization because a smaller percentage of the surface is covered by magnetic charges.

Magnetostrictive anisotropy occurs because spin realignment exerts stresses on the

magnetic crystal, which changes its shape. Conversely, therefore, applied stresses, which further alter the shape of the crystal, can affect the spin alignment and give rise to magnetostrictive anisotropy.

2:The Earth's magnetic field

If we could place a bar magnet inside the Earth, inclined approximately 11° to the rotational axis and offset about 550 km from the Earth's centre, we could account for 90% of the observed magnetic field. The other ~10% of the field is contributed by the Earth's crust. The magnetic field strength at the Earth's surface is 30-60 μT. The Earth's magnetic field is a vector quantity, with both strength and a direction at any point in space. To completely describe it we need to know three quantities (Fig. A-1). These are usually described in one of three ways:

- three orthogonal strength components: X, Y, and Z; or
- the total field strength and two angles: B, D, and I; or
- two strength components and an angle: H, Z, and D.

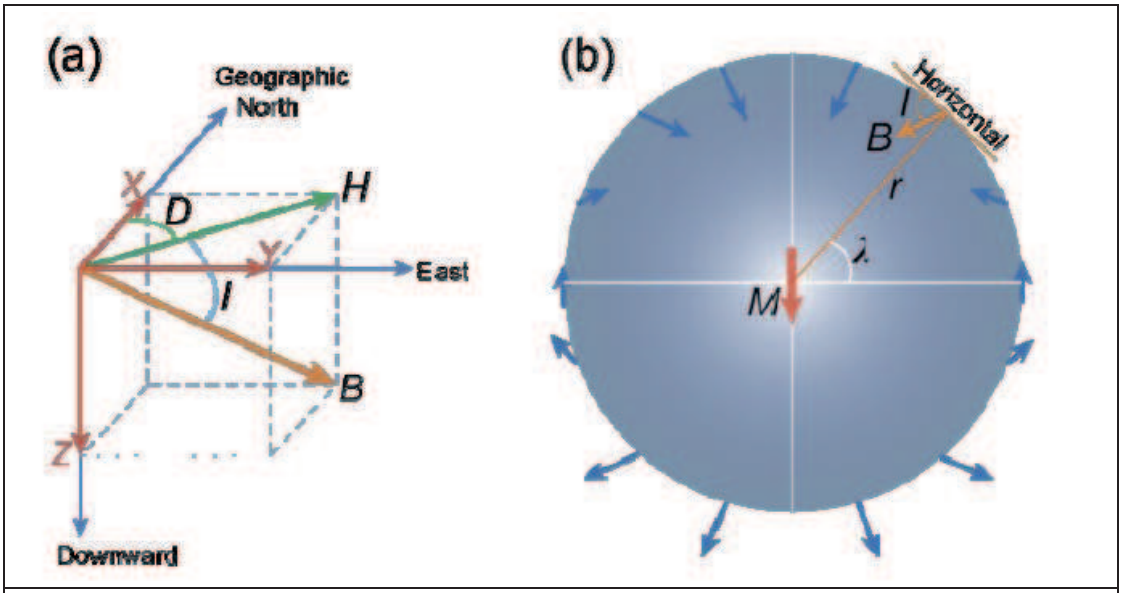

Fig A-1: (a) Schematic illustration of the main elements of the geomagnetic field. (b) Geocentric axial dipole model. A magnetic dipole M is placed at the centre of the Earth and is aligned with the rotation axis. λ is the geographic latitude; r is the mean radius of the Earth; I represents the inclination at that point. After Butler (1992).

In these representations, X is the north component, Y is the east component and Z is the vertical component of the magnetic field vector (by convention Z is positive

downward); B is the total intensity of the magnetic field vector; H is the horizontal component of the magnetic field vector; D is the magnetic declination, which is defined as the angle between true north and the horizontal component of the field measured eastward from true north; I is the magnetic inclination, which is defined as the angle measured from the horizontal plane to the magnetic field vector (and is positive downward).

3: Geocentric axial dipole model

The geocentric axial dipole (GAD) model is a fundamental hypothesis in paleomagnetism. In this model, the Earth's magnetic field, when its variation is averaged over a sufficiently long period of time, is represented by a single magnetic dipole at the centre of the Earth that is aligned with the rotation axis. A GAD field has the following properties:

$H = M \cos \lambda / r3$, $Z = 2M \sin \lambda / r3$, and $B = M (1 + 3\sin2 \lambda)1/2/r3$,

where M is the dipole moment of the geocentric axial dipole; λ is the geographic latitude, which ranges from -90˚ at the south geographic pole to +90˚ at the north geographic pole; and r is the Earth's mean radius.

The lengths of the arrows in Figure 2.4b schematically illustrate the factor of 2 increase in magnetic field strength from equator to poles. The inclination of the field can be determined by: $\tan I = Z / H = 2 \sin \lambda / \cos \lambda = 2 \tan \lambda$, where I increases from -90˚ at the geographic south pole to +90˚ at the geographic north pole. The relationship between I and λ is essential to understanding many paleogeographic and tectonic applications of paleomagnetism. For a GAD, D = 0˚ everywhere.

4: Demagnetization methods

The total NRM of a sample does not always only have a single magnetization component. Instead, it can comprise the vector sum of a number of different components. For sediments such as Chinese loess, the NRM may consist of a DRM

and/or a PDRM from or shortly after the time of deposition, a CRM caused by pedogenic magnetite formation and a VRM that carries a present-day field overprint. It is necessary to separate these different components to extract useful paleomagnetic information. This is usually achieved through the use of stepwise demagnetization, which relies on the principle that different magnetic components are carried by distinct populations of grains, with different mineralogies and grain sizes, and therefore different stabilities. Stepwise demagnetization progressively removes low stability NRM components, and isolates the more stable components that are more likely to record an ancient magnetization. The most stable component is referred to as the ChRM. The two techniques commonly used to isolate the ChRM are thermal and **AF demagnetization:**

Thermal demagnetization: The characteristic relaxation time τ is inversely proportional to temperature. Therefore, grains that are stable at room temperature will become unstable when heated to their unblocking temperature Tb, which is higher for more stable grains. Thermal demagnetization involves heating a sample to temperature T then cooling it back to room temperature in zero magnetic field. All grains with blocking temperature $Tb < T$ have their directions randomized, thereby erasing the NRM carried by these grains and allowing more stable components to be isolated.

AF demagnetization: When a sample is exposed to a sinusoidally varying magnetic field, which is smoothly reduced to zero from a specified peak value to randomize the magnetization of the sample, it is being subjected to AF demagnetization. This process effectively randomizes the magnetization of grains with coercivities below the peak AF intensity, which allows the remanence of higher coercivity grains to be isolated. In this study, we used an in-line AF demagnetizer on a 2G-Enterprises cryogenic magnetometer (Roberts, 2006), with which an AF was applied along three mutually perpendicular sample axes at progressively increasing fields after each measurement step.

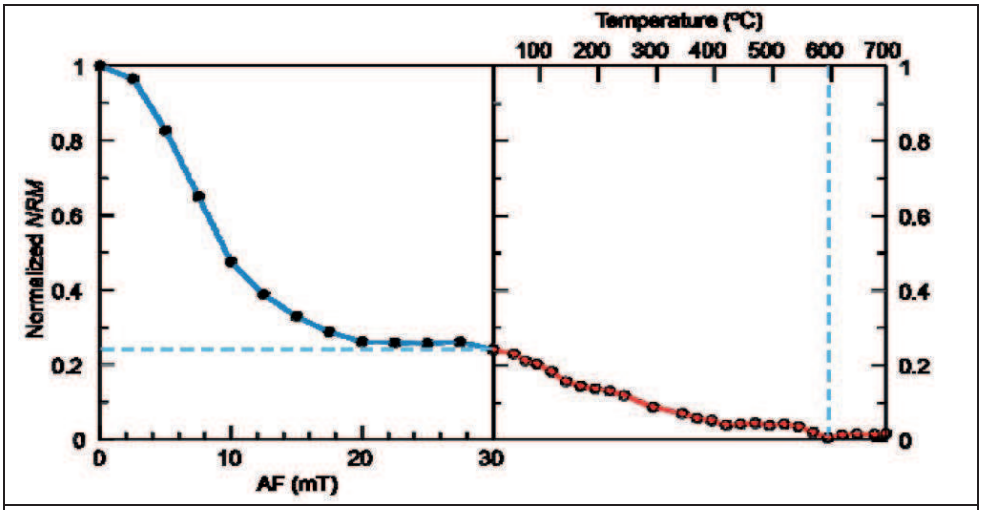

Fig A-2: An example of combined AF and thermal demagnetization for a paleosol sample. The sample was first treated using AF demagnetization up to a 30 mT peak field, followed by stepwise heating up to 700 C.

The relative effectiveness of the thermal and AF demagnetization methods can differ depending on the mineralogy of the remanence-carrying grains, and on the distribution of coercivities and unblocking temperatures for the different components. For example, AF treatment is less effective at removing the remanence carried by hematite compared to the thermal method. This is because hematite has high coercivities, but its remanence will be totally removed by heating above the Néel temperature of 680˚C. An example is given in Fig A-2 for a Chinese loess sample that has been subjected to combined AF and thermal treatment.

5: IRM acquisition curves

Rock magnetism involves the study of the magnetic properties of rock-forming magnetic minerals. Analysis of the rock magnetic properties of Paleomagnetic samples is recognized as being fundamentally important for understanding Paleomagnetic signals. A wide range of parameters and properties are analyzed in rock magnetic studies. These parameters and properties are briefly summarized belows.

As discussed above, in a gradually increasing field, a sample will acquire an IRM as it progresses from a demagnetized to a saturated state; this IRM acquisition process provides much useful information about the magnetic minerals in a sample. Robertson and France (1994) suggested that if a population of magnetic materials has a log-normally distributed coercivity spectrum and if the IRM is the linear sum of the IRM of all contributing grains, then an IRM acquisition curve can be "unmixed" into its constituent components. It is straightforward to rapidly measure IRM acquisition curves using a vibrating sample magnetometer or alternating gardient magnetometer. Several important developments in unmixing IRM acquisition curves have been made (e.g., Kruiver et al., 2001; Heslop et al., 2002; Egli, 2003; Heslop et al., 2007) since the original work of Robertson and France (1994).

A problem with analysis of IRM acquisition curves method is that measurements are discrete with systematic errors. When calculating a derivative, these errors are enlarged, which makes it difficult to judge how many components should be modelled and how good is the modelling. Egli (2003) proposed a useful method to avoid this problem. Discrete data are first fitted with a hyperbolic curve, and are then subtracted from the raw data to obtain a difference between the curves. The residual data are then filtered using a least-squares collocation method to produce one best fitting residual curve. The sum of these two curves produces the best modelling of the raw data; we can then calculate the derivative of this curve with minimized errors. Details of this mathematical procedure can be found in Egli (2003).

6: Magnetic minerals

Numerous magnetic minerals occur in nature and can be found in various environments. These minerals have contrasting magnetic properties that determine their ability to carry paleomagnetic signals. The basic magnetic properties and

composition of geologically common magnetic minerals are listed in Table A-1.

Table A-1: Physical properties of common natural magnetic minerals

Mineral	composition	Density (Kg/m^3)	Ms (Am^2/Kg)	T_c/T_N (°C)	Bc(mT)	Other
Magnetite	Fe_3O_4	5197	92	580	10's	Tv = 110-120K
Hematite	αFe_2O_3	5271	0.4	675	highly variable	T_N = 250-260K
Maghemite	γFe_2O_3	5074	74	590-675		
Goethite	αFeOOH	4264	<1	70-125	very large	Breaks down to hematite
Greigite	Fe_3S_4	4079	~59	>350	<70	Breaks down at: 270-350°C
Pyrrhotite	Fe_7S_8	4662	<20	270	100's	Transition at 34K
Titano-magnetite	$Fe_{2.4}Ti_{0.6}O_4$	4939	24	150	8	

APPENDIX B: U-Pb dating result

Table 3-2: U-Pb dating results for zircons from Yamansu felsic vulcanite

	corrected isotope ratio					
	$^{207}Pb/^{206}Pb$	1σ	$^{207}Pb/^{235}Pb$	1σ	$^{206}Pb/^{238}Pb$	1σ
y300-1	0.05255	0.00154	0.35902	0.01102	0.04957	0.00089
y300-2	0.05175	0.00183	0.36789	0.01312	0.05157	0.00097
y300-3	0.05235	0.00205	0.34169	0.01353	0.04735	0.00092
y300-4	0.05596	0.00128	0.56157	0.01402	0.0728	0.00123
y300-5	0.05588	0.00168	0.55516	0.01731	0.07206	0.00129
y300-6	0.05618	0.00128	0.5564	0.01392	0.07184	0.00123
y300-7	0.05303	0.00225	0.35286	0.01509	0.04827	0.00092
y300-8	0.05549	0.00185	0.52073	0.01786	0.06807	0.00125
y300-9	0.12521	0.01823	1.21493	0.17377	0.07038	0.00191
y300-10	0.07096	0.00238	0.72333	0.02455	0.07395	0.00139
y300-11	0.07092	0.00413	0.4599	0.02595	0.04709	0.00117
y300-12	0.0844	0.00287	0.80859	0.02779	0.0695	0.00133
y300-13	0.10544	0.0031	0.75848	0.02305	0.0522	0.00099
y300-14	0.05713	0.00234	0.45653	0.0187	0.05795	0.00117
y300-15	0.13018	0.00935	6.13537	0.42462	0.34191	0.01081
y300-16	0.05621	0.00162	0.55752	0.01683	0.07195	0.00128
y300-17	0.0577	0.00124	0.56952	0.01363	0.0716	0.00121
y300-18	0.05536	0.00137	0.38523	0.01023	0.05048	0.00088
y300-19	0.05775	0.00364	0.62131	0.03814	0.07807	0.00199
y300-20	0.05559	0.00261	0.52266	0.02435	0.06821	0.00145
y300-21	0.10205	0.00562	1.00919	0.05262	0.07172	0.00128
y300-22	0.23919	0.00504	13.04066	0.30811	0.39554	0.00676
y300-23	0.05505	0.00177	0.52179	0.01725	0.06878	0.0013
y300-24	0.05495	0.0019	0.4948	0.01744	0.06535	0.00123

continued table 3-2:

	$^{207}Pb/^{206}Pb$		$^{207}Pb/^{235}Pb$		$^{206}Pb/^{238}Pb$	
	age	1σ	age	1σ	age	1σ
y300-1	309	68	311	8	312	5
y300-2	274	83	318	10	324	6
y300-3	301	92	298	10	298	6
y300-4	451	52	453	9	453	7
y300-5	448	68	448	11	449	8
y300-6	459	52	449	9	447	7
y300-7	330	99	307	11	304	6
y300-8	432	76	426	12	425	8
y300-9	2032	273	807	80	438	12
y300-10	956	70	553	14	460	8
y300-11	955	122	384	18	297	7
y300-12	1302	68	602	16	433	8
y300-13	1722	55	573	13	328	6
y300-14	497	92	382	13	363	7
y300-15	2100	130	1995	60	1896	52
y300-16	461	65	450	11	448	8
y300-17	518	48	458	9	446	7
y300-18	427	56	331	7	317	5
y300-19	520	142	491	24	485	12
y300-20	436	107	427	16	425	9
y300-21	1662	105	708	27	447	8
y300-22	3115	34	2683	22	2148	31
y300-23	414	74	426	12	429	8
y300-24	410	79	408	12	408	7

APPENDIX C: Mineral chemistry of Yamansu magnetite deposit

Table 3-3 EPMA analysis of albite (wt%)

sample	N°.	K_2O	SiO_2	FeOT	CaO	Na_2O	Al_2O_3	Total
yn2-1	69	0.05	67.91	0.21	0.38	10.86	19.35	98.83
yL1-1	5	0.16	67.83	0.09	0.93	10.52	20.01	99.69
yn2-1	68	0.23	67.56	0.43	0.24	10.82	19.45	98.82
yn2-1	70	0.31	67.53	0.11	0.22	10.58	19.53	98.3
yn2-1	67	0.31	67.62	0.05	0.15	7	19.39	94.56
yn2-1	71	0.36	68.44	0.14	0.34	10.55	19.75	99.8
yn2-1	72	0.74	67.85	0.17	0.47	10.11	19.56	99.07
yo1-2	84	1.49	64.78	0.26	0.8	9.13	21.46	98.27

structural formula of albite and K-feldspar (based on 5 cations)

sample	N°.	K	Si	Fe	Ca	Na	Al
yn2-1	69	0	3.02	0.01	0.02	0.94	1.01
yL1-1	5	0.01	3	0	0.04	0.9	1.04
yn2-1	68	0.01	3.01	0.02	0.01	0.93	1.02
yn2-1	70	0.02	3.02	0	0.01	0.92	1.03
yn2-1	67	0.02	3.23	0	0.01	0.65	1.09
yn2-1	71	0.02	3.03	0	0.02	0.9	1.03
yn2-1	72	0.04	3.03	0.01	0.02	0.87	1.03
yo1-2	84	0.09	2.93	0.01	0.04	0.8	1.14

Table 3-4: EPMA analysis of pyroxene (wt%) and structural formulae

	yL3-1 21	yL3-1 30	y12b-2 y69	y12b-2 y70	y12b-2 y71	y13d-2 y110	y13d-2 y111
SiO_2	51.9	51.7	50.4	50.6	50.5	51.5	51.9
FeO	8.92	7.86	22.2	21.4	17.3	15.6	15.4
MnO	0.14	0.12	3.78	2.84	1.33	1.04	0.92
MgO	13.1	10.2	6.02	8.14	11.1	13.4	13.4
CaO	24.1	24	11.2	12	10.6	12.4	12.7
Al_2O_3	1.2	1.18	0.5	0.39	0.83	1.92	1.31
Na_2O	0.48	0.3	0.15	0.08	0.16	0.22	0.09
K_2O	0.13	0.03	0.04	0.02	0.02	0.14	0.11
Σ	100	95.4	94.3	95.5	91.8	96.3	95.9
structural formula (based on 4 cations)							
Si	1.94	2.05	2.15	2.1	2.12	2.03	2.06
Al^{IV}	0.05	0	0	0	0	0	0
Al^{VI}	0	0.06	0.03	0.02	0.04	0.09	0.06
Fe^{3+}	0	0	0	0	0	0	0
Fe^{2+}	0.28	0.26	0.79	0.74	0.61	0.52	0.51
Mn	0	0	0.14	0.1	0.05	0.03	0.03
Mg	0.73	0.6	0.38	0.5	0.69	0.79	0.79
Ca	0.97	1.02	0.51	0.53	0.48	0.52	0.54
Na	0.02	0.01	0.01	0	0.01	0.01	0
K	0	0	0	0	0	0	0
sum	4	4	4	4	4	4	4
Fe+Mn+Mg	1.02	0.86	1.31	1.34	1.35	1.34	1.33
Ca	0.97	1.02	0.51	0.53	0.48	0.52	0.54
(Fe+Mn)/Mg	0.39	0.44	2.42	1.67	0.95	0.7	0.68
(Fe+Mn+Mg)/Ca	1.05	0.85	2.56	2.52	2.82	2.55	2.48

Table 3-5 EPMA data of magnetite (wt%) in Yamansu magnetite deposit

occu-rrence	N°	SiO_2	FeO	CaO	Al_2O_3	MnO	TiO_2	MgO	V_2O_3	Total
A	li01	0.8	94.48	0.34	0.32	0	0	0.08	0	96.1
A	li02	1.71	92.59	0.68	0.56	0.05	0.05	0.13	0	95.9
A	li03	0.64	94.32	0.17	0.27	0.11	0.03	0	0	95.6
B	li04	1.04	93.61	0.41	0.4	0.12	0	0.04	0	96.1
B	li06	0.11	95.8	0	0.03	0.03	0	0.02	0	96.1
B	li07	0	90.84	0.03	0.02	0	0	0.01	0.22	91.2
B	li08	0.02	90.95	0.26	0.14	0	0	0.03	0	91.4
B	li09	0	91.22	0.01	0.09	0	0	0	0.36	91.7
C	li10	0.04	91.76	0.01	0.08	0.03	0	0	0.34	92.3
C	li11	0.02	91.68	0.01	0.09	0.04	0.04	0	0.04	92
C	li13	1.71	89.62	0.19	0.85	0.18	0.03	0.1	0.04	92.9
D	li14	0.57	91.04	0.11	0.2	0.23	0.01	0.03	0.04	92.6
D	li15	1.56	90.62	0.45	0.31	0.24	0.16	0.16	0.04	93.7
D	li17	0.27	86.54	0.04	0.15	0.05	5.3	0.05	1.12	93.8
D	li18	1.21	88.42	0.8	0.48	0.02	1.74	0.06	0.35	93.2
D	li19	0.54	87.89	0.29	0.27	0.17	0.4	0	0.22	90.1
D	li20	0.09	87.98	0.01	0.05	0.13	5.31	0.02	0.27	94.1
D	li21	0.13	90.05	0.02	0.04	0.02	4.16	0	0.31	95
D	li22	0.12	87.33	0.01	0.11	0.09	3.48	0	0.26	91.6
D	li23	0.18	90.95	0.03	0.08	0.07	0.03	0.04	0.21	91.7
B	li24	0.16	89.32	0.02	0.01	0.13	0.05	0.02	0.2	90.2
B	li25	0.15	89.02	0.01	0.03	0.07	5.3	0.02	0.22	95
B	li26	0.31	89.52	0	0.94	0.06	0.49	0	0.09	91.5
B	li27	0.47	88.7	0	1.07	0	0.11	0.05	0.04	91
B	li28	0.58	92.91	0.02	0	0.07	0	0.03	0.02	93.7
B	li29	0.71	92.09	0.08	0.09	0.04	0	0.07	0.07	93.6
B	li30	0.55	92.83	0	0.08	0.01	0	0.12	0.01	93.7
B	li31	1.44	90.36	0.06	0.01	0.02	0	0.01	0	91.9
B	li32	2.2	86.72	0.04	0.02	0.08	0	0.02	0.03	89.3
B	li33	1.32	88.15	0.03	0.02	0.12	0.02	0.04	0	89.7
A	li34	0.5	91.96	0.22	0.22	0	0	0.12	0.06	93.3
A	li35	0.23	91.97	0.13	0.12	0.01	0	0	0	92.9
A	li38	1.23	92.48	0.31	0.44	0.13	0	0.06	0	95
E	li40	0.22	94.15	0	0.06	0.03	0	0	0	94.6
E	li41	0.42	94.52	0.34	0.11	0.02	0	0.02	0	95.5
E	li42	2.22	89.86	0.13	0.03	0.04	0	0.01	0	92.5

E	li43	0.3	91.6	0.03	0.02	0.04	0	0.05	0.07	92.2
E	li44	0.19	92.19	0.03	0.02	0.08	0	0.01	0	92.6
E	li45	2.02	90.97	0.09	0.06	0.06	0	0	0	93.5
E	li46	0.38	92.31	0.04	0	0	0	0	0.03	92.9
B	li47	0.17	91.82	0	0	0	0	0	0.12	92.2
B	li48	1.29	92.2	0.13	0	0	0	0	0.03	93.7
B	li50	0.08	87.5	0.08	0.05	0	1.58	0	0.25	89.6
B	li51	0.03	90.45	0	0.04	0	0	0	0.38	91.2
B	li52	0.03	88.74	0.05	0.05	0	1.26	0.03	0.34	90.8
B	li53	0.01	90.48	0.11	0.01	0	0.2	0	0.35	91.2
B	li54	0	89.32	0.05	0.05	0	0.04	0	0.4	90.2
B	li55	0.06	90.13	0.21	0.04	0.04	0.33	0	0.24	91.2
B	li73	0.08	90.35	0.03	0.7	0.15	2.59	0	0.13	94.3
A	li74	0.08	88.18	0.06	0.68	0.05	2.56	0.05	0.21	92
A	li76	3.28	86.43	1.31	0.95	0.16	0	0.38	0	92.6

structural formula

		Fe^{3+}	Fe^{2+}	Si	Ca	Al	Mn	Ti	Mg	V
A	li01	1.93	1.01	0.03	0.01	0.01	0	0	0	0
A	li02	1.86	1.03	0.06	0.03	0.01	0	0	0.01	0
A	li03	1.94	1.01	0.02	0.01	0.01	0	0	0	0
B	li04	1.91	1.02	0.04	0.02	0.01	0	0	0	0
B	li06	1.99	1	0	0	0	0	0	0	0
B	li07	1.99	1.01	0	0	0	0	0	0	0
B	li08	2	0.99	0	0.01	0	0	0	0	0
B	li09	1.98	1.01	0	0	0	0	0	0	0.01
C	li10	1.98	1.01	0	0	0	0	0	0	0.01
C	li11	1.99	1	0	0	0	0	0	0	0
C	li13	1.85	1.05	0.07	0.01	0.02	0.01	0	0.01	0
D	li14	1.95	1.01	0.02	0	0	0.01	0	0	0
D	li15	1.86	1.03	0.06	0.02	0.01	0.01	0	0.01	0
D	li17	1.61	1.19	0.01	0	0	0	0.15	0	0.02
D	li18	1.78	1.07	0.05	0.03	0.01	0	0.05	0	0.01
D	li19	1.92	1.02	0.02	0.01	0.01	0.01	0.01	0	0
D	li20	1.67	1.16	0	0	0	0	0.15	0	0
D	li21	1.74	1.13	0	0	0	0	0.12	0	0
D	li22	1.77	1.11	0	0	0	0	0.1	0	0
D	li23	1.97	1.01	0.01	0	0	0	0	0	0
B	li24	1.97	1.01	0.01	0	0	0	0	0	0
B	li25	1.67	1.16	0.01	0	0	0	0.15	0	0
B	li26	1.92	1.03	0.01	0	0.02	0	0.01	0	0
B	li27	1.93	1.02	0.02	0	0.03	0	0	0	0
B	li28	1.95	1.02	0.02	0	0	0	0	0	0
B	li29	1.94	1.02	0.03	0	0	0	0	0	0
B	li30	1.96	1.01	0.02	0	0	0	0	0.01	0

B	li31	1.89	1.05	0.06	0	0	0	0	0	0
B	li32	1.82	1.08	0.09	0	0	0	0	0	0
B	li33	1.89	1.05	0.05	0	0	0	0	0	0
A	li34	1.95	1	0.02	0.01	0	0	0	0.01	0
A	li35	1.98	1	0.01	0.01	0	0	0	0	0
A	li38	1.9	1.03	0.05	0.01	0.01	0	0	0	0
E	li40	1.98	1.01	0.01	0	0	0	0	0	0
E	li41	1.97	1	0.02	0.01	0	0	0	0	0
E	li42	1.83	1.08	0.09	0.01	0	0	0	0	0
E	li43	1.97	1.01	0.01	0	0	0	0	0	0
E	li44	1.98	1	0.01	0	0	0	0	0	0
E	li45	1.84	1.07	0.08	0	0	0	0	0	0
E	li46	1.97	1.01	0.01	0	0	0	0	0	0
B	li47	1.98	1.01	0.01	0	0	0	0	0	0
B	li48	1.9	1.04	0.05	0.01	0	0	0	0	0
B	li50	1.88	1.06	0	0	0	0	0.05	0	0
B	li51	1.98	1.01	0	0	0	0	0	0	0.01
B	li52	1.9	1.05	0	0	0	0	0.04	0	0.01
B	li53	1.97	1.01	0	0	0	0	0.01	0	0.01
B	li54	1.98	1.01	0	0	0	0	0	0	0.01
B	li55	1.96	1.01	0	0.01	0	0	0.01	0	0
B	li73	1.82	1.08	0	0	0.02	0.01	0.07	0	0
A	li74	1.82	1.08	0	0	0.02	0	0.08	0	0
A	li76	1.73	1.04	0.13	0.05	0.02	0.01	0	0.02	0

re-calculated geochemical data

		Fe_2O_3	FeO	SiO_2	CaO	Al_2O_3	MnO	TiO_2	MgO	V_2O_5	sum
A	li01	68.93	32.45	1.35	0.34	0.16	0	0	0	0	103.24
A	li02	66.21	33.02	2.91	0.68	0.28	0.06	0.05	0.01	0	103.21
A	li03	68.89	32.33	1.08	0.17	0.13	0.12	0.03	0	0	102.76
B	li04	67.94	32.47	1.76	0.41	0.2	0.14	0	0	0	102.92
B	li06	70.84	32.07	0.19	0	0.02	0.04	0	0	0	103.15
B	li07	67.06	30.5	0	0.03	0.01	0	0	0	0.11	97.71
B	li08	67.6	30.12	0.04	0.26	0.07	0	0	0	0	98.09
B	li09	67.13	30.82	0	0.01	0.05	0	0	0	0.18	98.19
C	li10	67.51	31.01	0.07	0.01	0.04	0.04	0	0	0.17	98.85
C	li11	67.82	30.65	0.03	0.01	0.05	0.05	0.04	0	0.02	98.67
C	li13	63.51	32.48	2.91	0.19	0.42	0.21	0.03	0.01	0.02	99.77
D	li14	66.64	31.08	0.97	0.11	0.1	0.26	0.01	0	0.02	99.2
D	li15	64.84	32.28	2.65	0.45	0.16	0.28	0.16	0.01	0.02	100.85
D	li17	55.29	36.79	0.45	0.04	0.08	0.06	5.3	0	0.56	98.58
D	li18	61.32	33.24	2.06	0.8	0.24	0.02	1.74	0	0.18	99.59
D	li19	63.69	30.58	0.91	0.29	0.14	0.19	0.4	0	0.11	96.32
D	li20	57.74	36.03	0.15	0.01	0.02	0.15	5.31	0	0.14	99.55
D	li21	60.59	35.53	0.22	0.02	0.02	0.03	4.16	0	0.15	100.72

D	li22	59.57	33.73	0.21	0.01	0.05	0.1	3.48	0	0.13	97.29
D	li23	66.87	30.78	0.31	0.03	0.04	0.08	0.03	0	0.1	98.24
B	li24	65.72	30.18	0.26	0.02	0.01	0.15	0.05	0	0.1	96.49
B	li25	58.43	36.45	0.25	0.01	0.02	0.07	5.3	0	0.11	100.64
B	li26	64.82	31.19	0.52	0	0.47	0.07	0.49	0	0.05	97.62
B	li27	64.47	30.69	0.8	0	0.54	0	0.11	0	0.02	96.63
B	li28	67.89	31.83	0.98	0.02	0	0.07	0	0	0.01	100.8
B	li29	67.05	31.76	1.21	0.08	0.05	0.05	0	0	0.04	100.23
B	li30	67.94	31.7	0.93	0	0.04	0.01	0	0	0	100.63
B	li31	64.47	32.35	2.45	0.06	0	0.02	0	0	0	99.34
B	li32	60.44	32.34	3.73	0.04	0.01	0.09	0	0	0.01	96.67
B	li33	63.1	31.37	2.24	0.03	0.01	0.14	0.02	0	0	96.92
A	li34	67.49	31.23	0.85	0.22	0.11	0	0	0	0.03	99.93
A	li35	67.83	30.94	0.39	0.13	0.06	0.01	0	0	0	99.35
A	li38	66.69	32.47	2.09	0.31	0.22	0.14	0	0	0	101.92
E	li40	69.37	31.73	0.37	0	0.03	0.03	0	0	0	101.53
E	li41	69.62	31.87	0.71	0.34	0.06	0.02	0	0	0	102.62
E	li42	62.8	33.35	3.76	0.13	0.01	0.05	0	0	0	100.1
E	li43	67.37	30.98	0.5	0.03	0.01	0.04	0	0	0.03	98.97
E	li44	68.05	30.96	0.33	0.03	0.01	0.09	0	0	0	99.47
E	li45	63.94	33.44	3.43	0.09	0.03	0.07	0	0	0	100.99
E	li46	67.72	31.37	0.65	0.04	0	0	0	0	0.01	99.79
B	li47	67.58	31	0.28	0	0	0	0	0	0.06	98.93
B	li48	66.12	32.71	2.19	0.13	0	0	0	0	0.01	101.16
B	li50	62.33	31.41	0.13	0.08	0.02	0	1.58	0	0.12	95.68
B	li51	66.49	30.63	0.04	0	0.02	0	0	0	0.19	97.37
B	li52	63.67	31.45	0.05	0.05	0.03	0	1.26	0	0.17	96.67
B	li53	66.42	30.72	0.02	0.11	0.01	0	0.2	0	0.17	97.65
B	li54	65.66	30.24	0	0.05	0.02	0	0.04	0	0.2	96.21
B	li55	66.16	30.6	0.11	0.21	0.02	0.05	0.33	0	0.12	97.59
B	li73	63.15	33.52	0.14	0.03	0.35	0.18	2.59	0	0.07	100.02
A	li74	61.5	32.84	0.14	0.06	0.34	0.05	2.56	0	0.1	97.59
A	li76	59.85	32.58	5.57	1.31	0.47	0.19	0	0.04	0	100

Sample occurrences: A=massive magnetite; B=disseminated magnetite; C=disseminated magnetite with epidote; D=magnetite in basalt; E=magnetite in garnet. Structural formulae calculation is basing on 3 cations. Details can be refered to the text.

Table 3-6 EPMA analysis data of stilpnomelane (wt%)

	y7a-132	y7a-133	y7a-134	y7a-135
K_2O	5.507	1.703	1.003	2.154
SiO_2	42.705	45.195	40.379	45.387
FeO	26.056	27.689	23.387	27.447
CaO	0.004	0.027	0.098	0
Na_2O	3.041	0.576	0.911	0.565
TiO_2	0	0	0	0.022
Al_2O_3	4.771	4.941	3.815	5.001
MnO	2.143	2.551	1.937	2.483
Cl	0.001	0	0.051	0
MgO	5.48	5.684	5.047	5.788
P_2O_5	0	0	0	0
F	0	0.22	0.096	0.146
Total	89.708	88.586	76.724	88.993
	structural formulae			
Si	3.65	3.72	3.8	3.72
Aliv	0.35	0.28	0.2	0.28
Alvi	0.13	0.2	0.22	0.2
Fe	1.86	1.9	1.84	1.88
Mn	0.15	0.18	0.15	0.17
Mg	0.7	0.7	0.71	0.71
Na	0.25	0.05	0.08	0.04
K	0.3	0.09	0.06	0.11

Number of ions on the basis of 11.

Table 3-7 EPMA analysis of K-feldspar (wt%)

sample	N°.		K_2O	SiO_2	FeO(T)	CaO	Na_2O	Al_2O_3	Total
yo1-2	85	feldspar	7.32	65.42	0.28	0.32	6.58	19.19	99.15
yo1-2	83	feldspar	9.3	65.66	0	0.37	4.74	19.27	99.7
yo1-2	89	feldspar	10.94	64.32	0.32	0.22	3.69	19.26	99.19
yo1-1	81	orthoclase	15.26	62.76	0.06	0	1.04	18.1	97.32
yL1-1	6	orthoclase	15.74	62.7	0	0.03	0.27	17.8	96.69
yL1-1	7	orthoclase	15.75	63.85	0.14	0	0.45	18.04	98.27
yL1-2	12	orthoclase	15.8	62.8	0.15	0	0.25	18.26	97.5
yL1-2	9	orthoclase	16.02	61.73	0.08	0.02	0.46	17.89	96.24
yL3-1	29	orthoclase	16.15	63.47	0.19	0	0.26	18.31	98.54
yL1-1	8	orthoclase	16.15	63.95	0.12	0	0.27	18.15	98.75
yL3-1	22	orthoclase	16.18	63.11	0.14	0	0.33	18.22	98.02
yL3-1	23	orthoclase	16.29	63.34	0.18	0.15	0.3	18.35	98.64
yL3-1	27	orthoclase	16.33	63.23	0.01	0	0.27	18.08	97.98
yg3-1	65	orthoclase	16.61	63.91	0.25	0.02	0.04	18.17	99.15

structural formula of K-feldspar (based on 5 cations)

sample	N°.		K	Si	Fe	Ca	Na	Al
yo1-2	85	feldspar	0.42	2.95	0.01	0.02	0.58	1.02
yo1-2	83	feldspar	0.54	2.99	0	0.02	0.42	1.03
yo1-2	89	feldspar	0.64	2.96	0.01	0.01	0.33	1.04
yo1-1	81	orthoclase	0.92	2.97	0	0	0.1	1.01
yL1-1	6	orthoclase	0.96	3.01	0	0	0.03	1.01
yL1-1	7	orthoclase	0.95	3.01	0.01	0	0.04	1
yL1-2	12	orthoclase	0.96	2.99	0.01	0	0.02	1.02
yL1-2	9	orthoclase	0.98	2.96	0	0	0.04	1.01
yL3-1	29	orthoclase	0.97	2.99	0.01	0	0.02	1.01
yL1-1	8	orthoclase	0.97	3	0	0	0.02	1
yL3-1	22	orthoclase	0.97	2.98	0.01	0	0.03	1.01
yL3-1	23	orthoclase	0.97	2.97	0.01	0.01	0.03	1.01
yL3-1	27	orthoclase	0.98	2.99	0	0	0.02	1.01
yg3-1	65	orthoclase	0.99	2.99	0.01	0	0	1

Table 3-8: EPMA analysis of tourmaline (wt%) and structural formula

sample	yml-2-33	yml-2-34	yml-2-35	yml-2-43	yml-2-49	yml-1-51	yml-1-57	yml-1-58	yml-1-54
N°.	33	34	35	43	49	51	57	58	61
SiO^2	35.59	35.93	35.42	35.51	34.3	34.59	34.52	34.63	34.57
Al^2O^3	23.59	26.83	25.53	23.89	22.35	23.55	23.85	23.14	24.23
TiO^2	0.2	0.16	0.22	0.32	0.25	0.17	0.21	0.29	0.35
FeO	12.04	9.25	11.82	12.79	13.19	14.06	13.98	13.3	13.58
MnO	0.09	0.01	0.12	0.01	0.03	0	0.05	0.03	0.02
MgO	7.12	9.34	8.5	9.13	5.55	8.26	8.35	9.1	7.69
CaO	2.66	2.06	2.4	2.6	6.39	2.6	2.59	2.93	2.48
Na^2O	0.52	1.5	1.37	1.38	1.14	1.35	1.42	1.12	1.32
K^2O	0.05	0.04	0.03	0.06	0.08	0.02	0.03	0.05	0.04
F	0	0.62	0.93	0.64	0	1.24	0.44	0.27	0
sum	81.86	85.74	86.34	86.33	83.28	85.84	85.44	84.86	84.28
T position									
Si	6.35	6.08	6.07	6.12	6.19	6.09	6.05	6.08	6.08
Al(T)	0	0	0	0	0	0	0	0	0
B	3	3	3	3	3	3	3	3	3
Z position									
Al(Z)	4.96	5.35	5.16	4.85	4.75	4.88	4.92	4.79	5.02
Fe3+	1.04	0.652	0.841	1.149	1.249	1.116	1.077	1.213	0.976
Y position									
Al(Y)	0	0	0	0	0	0	0	0	0
Ti	0.03	0.02	0.03	0.04	0.03	0.02	0.03	0.04	0.05
Fe2+	0.755	0.656	0.854	0.694	0.741	0.953	0.97	0.739	1.02
Mn	0.01	0	0.02	0	0	0	0.01	0.01	0
Mg	1.89	2.35	2.17	2.34	1.49	2.17	2.18	2.38	2.02
Li	0.31	0	0	0	0.73	0	0	0	0
X position									
Ca	0.51	0.37	0.44	0.48	1.23	0.49	0.49	0.55	0.47
Na	0.18	0.49	0.45	0.46	0.4	0.46	0.48	0.38	0.45
K	0.01	0.01	0.01	0.01	0.02	0.01	0.01	0.01	0.01
W position									
F	0	0.33	0.5	0.35	0	0.69	0.24	0.15	0
OH	4	3.67	3.5	3.65	4	3.31	3.76	3.85	4

Continued table 3-8:

(Fe+Mn)/(Fe+Mn+Mg)	0.49	0.36	0.44	0.44	0.57	0.49	0.49	0.45	0.5
(Na+K)/Ca	0.38	1.34	1.04	0.99	0.34	0.95	1.01	0.71	0.98
(Na+K)/(Na+K+Ca)	0.27	0.57	0.51	0.5	0.25	0.49	0.5	0.41	0.5
Mg/(Mg+Fe)	0.51	0.64	0.56	0.56	0.43	0.51	0.52	0.55	0.5

Note: B_2O_3 calculated assuming 3 B and W=4 atoms per formula unit. Total Fe measured as FeO.

Table 3-9: EPMA analysis of axinite (wt%) and structural formula

	y13d-2	y13d-2	y12b-4	y12b-1	y12b-1	y12b-1
No.	112	113	59	49	50	55
SiO2	40.865	41.472	42.705	40.567	42.298	41.036
Al2O3	17.421	16.209	16.612	17.887	17.619	16.776
FeO	3.917	5.909	7.626	5.73	5.502	5.543
MnO	9.132	7.196	3.994	6.482	6.539	8.025
MgO	0.292	0.592	1.348	0.368	0.353	0.282
CaO	19.491	18.988	19.843	19.318	19.794	19.478
Na2O	0.032	0.028	0	0.036	0	0.032
K2O	0.007	0.03	0	0.03	0	0
normalisation to Ca+Fe+Mn+Mg=	3	3	3	3	3	3
Ca+Mn+Mg+Fe	0.54	0.54	0.55	0.52	0.53	0.54
	structural formula					
Si	3.79	3.86	3.88	3.86	3.98	3.76
Aliv	0.21	0.14	0.12	0.14	0.02	0.24
Alvi	1.7	1.63	1.66	1.87	1.94	1.57
Fe	0.3	0.46	0.58	0.46	0.43	0.43
Mn	0.72	0.57	0.31	0.52	0.52	0.62
Mg	0.04	0.08	0.18	0.05	0.05	0.04
Ca	1.94	1.89	1.93	1.97	2	1.91
B	1	1	1	1	1	1
OH	1	1	1	1	1	1
	re-calculated geochemical composition					
SiO2	40.87	41.47	42.71	40.57	42.3	41.04
Al2O3	17.42	16.21	16.61	17.89	17.62	16.78
FeO	3.92	5.91	7.63	5.73	5.5	5.54
MnO	9.13	7.2	3.99	6.48	6.54	8.03
MgO	0.29	0.59	1.35	0.37	0.35	0.28
CaO	19.49	18.99	19.84	19.32	19.79	19.48
Na2O	0.03	0.03	0	0.04	0	0.03
K2O	0.01	0.03	0	0.03	0	0
B2O3	6.24	6.23	6.38	6.09	6.16	6.32
H2O	1.61	1.61	1.65	1.57	1.59	1.63
Sum.	99.01	98.26	100.16	98.08	99.85	99.12

Table 3-10: EPMA analysis of epidote (wt%) and structural formula

		N°	SiO_2	Al_2O_3	FeO	MnO	CaO	Σ
grained epidote	y5b-1	20	36.7	23.31	12.7	0.28	23.02	96.51
	y5b-1	21	37.8	22.28	13.7	0.15	23.19	97.42
	y5b-1	22	36.8	21.73	14.6	0.31	22.8	96.47
	y5b-1	24	36.9	21.62	14.4	0.04	23.05	96.36
	y5b-1	27	36.3	21.61	14.6	0.14	22.92	96.11
	y5b-1	29	36.8	21.68	14.8	0.13	23.05	97.16
	y5b-1	23	36.9	21.46	14.8	0.08	23.08	96.69
	y5b-1	25	37.3	22.96	13	0.13	23.36	97.13
	y5b-1	28	37.3	21.45	14.7	0.17	23.6	97.8
flade epidote	y13d-1	99	35.8	20.93	15.2	0.46	22.77	95.69
	y13d-1	100	35.9	20.54	15.6	0.12	23.26	95.63
	y13d-1	106	35.8	20.66	15.7	0.23	23.01	95.59
	yo1-3	91	37.2	21.54	14.2	0.05	23.57	96.8
	yo1-3	93	37.3	22.32	13.5	0.02	23.56	96.92
	yo1-3	95	37.4	22.65	13	0.07	23.39	97.03
	yo1-3	97	37.5	23.02	13	0.09	23.46	97.3
	yo1-3	98	37.2	22.03	13.4	0.04	23.55	96.5
	yo1-3	100	37.3	24.52	10.4	0.01	23.82	96.5
epidote associated with tourmaline and K-feldspar	ym1-2	36	36.6	19.68	14.5	0.35	22.97	94.44
	ym1-2	37	37.1	23.34	11.5	0.58	22.35	95.81
	ym1-2	38	36.6	20.37	14.9	0.53	22.53	95.16
	ym1-2	40	37.1	22.72	12.7	1.04	21.37	95.18
	ym1-2	41	37	19.93	15.3	1.03	20.98	94.83
	ym1-2	44	36.4	19.98	15.2	0.93	21.53	94.34
	ym1-2	47	37.3	20.74	12.8	0.47	22.88	95.08
	ym1-2	48	37	22.16	12.7	1.53	21.85	95.8
	ym1-1	50	36.5	22.06	12.5	0.36	22.78	94.78
	ym1-1	52	36.2	20.6	14	1.37	21.27	93.89
	ym1-1	53	36.7	22.2	12.2	0.88	21.79	94.69
	ym1-1	54	37	22.25	11.9	0.04	22.99	95.08
	ym1-1	55	36.9	21.21	14	0.08	22.73	95.14
	ym1-1	56	36.8	24.44	9.69	0.28	23.37	94.7
	ym1-1	59	35.7	18.37	16.4	0.13	22.92	93.85

continued table 3-10:

Normalisation to sum eq. oxy, =12.5												
	N°.	Si	Al^{IV}	ΣIV	Al^{VI}	Fe^{3+}	Mn^{3+}	ΣVI	Ca^{2+}	Fe^{2+}	Mn^{2+}	ΣVIII
grained epidote	20	2.95	0.05	3	2.15	0.84	0	3	1.98	0.01	0.02	2.01
	21	3.01	0	3.01	2.09	0.91	0.01	3	1.97	0	0.01	1.98
	22	2.97	0.03	3	2.03	0.97	0	3	1.97	0.01	0.02	2
	24	2.98	0.02	3	2.03	0.97	0	3	1.99	0	0	2.01
	27	2.95	0.05	3	2.01	0.98	0	3	1.99	0.01	0.01	2.02
	29	2.96	0.04	3	2.01	0.99	0	3	1.99	0.01	0.01	2.01
	23	2.97	0.03	3	2.01	0.99	0	3	1.99	0.01	0.01	2.01
	25	2.98	0.02	3	2.13	0.86	0	3	2	0	0.01	2.01
	28	2.98	0.02	3	2	0.98	0.01	2.99	2.02	0	0	2.02
flade epidote	99	2.93	0.07	3	1.94	1.04	0.01	3	2	0	0.02	2.02
	100	2.94	0.06	3	1.92	1.07	0.01	2.99	2.04	0	0	2.04
	106	2.93	0.07	3	1.92	1.07	0	3	2.02	0	0.01	2.03
	91	2.99	0.01	3	2.03	0.95	0	2.98	2.03	0	0	2.03
	93	2.98	0.02	3	2.09	0.9	0	2.99	2.02	0	0	2.02
	95	2.99	0.01	3	2.12	0.87	0	3	2	0	0	2
	97	2.98	0.02	3	2.14	0.86	0	3	2	0	0.01	2.01
	98	2.99	0.01	3	2.08	0.9	0	2.98	2.03	0	0	2.03
	100	2.98	0.02	3	2.28	0.7	0	2.98	2.04	0	0	2.04
epidote associated with tourmaline and K-feldspar	36	3.02	0	3.02	1.92	1	0.02	2.95	2.03	0	0	2.04
	37	3	0	3	2.22	0.77	0	3	1.94	0	0.04	1.98
	38	2.99	0.01	3	1.96	1.02	0.02	3	1.97	0	0.02	1.99
	40	3	0	3	2.17	0.83	0	3	1.85	0.02	0.07	1.96
	41	3.03	0	3.03	1.92	1.05	0.03	3	1.84	0	0.04	1.93
	44	3	0	3	1.94	1.05	0	3	1.9	0	0.06	1.97
	47	3.04	0	3.04	1.99	0.87	0.03	2.93	2	0	0	2
	48	2.98	0.02	3	2.09	0.86	0.03	3	1.89	0	0.07	1.97
	50	2.99	0.01	3	2.11	0.85	0.02	3	2	0	0	2.01
	52	3	0	3	2.01	0.97	0.02	3	1.89	0	0.07	1.96
	53	3	0	3	2.14	0.84	0.02	3	1.91	0	0.04	1.97
	54	3.01	0	3.01	2.13	0.81	0	2.97	2	0	0	2.02
	55	3.01	0	3.01	2.04	0.95	0.01	3	1.99	0	0	1.99
	56	2.98	0.02	3	2.31	0.66	0.02	2.99	2.03	0	0	2.03
	59	2.99	0.01	3	1.8	1.15	0.01	2.96	2.06	0	0	2.06

Table 3-11: EPMA analysis of chlorite (wt%) and structural formula

sample	N°.	SiO_2	Al_2O_3	FeO	MnO	MgO	CaO	F	Cl	Total
y5b-1	32	26.69	18.6	28.9	0.61	13.94	0.09	0.02	0.1	89.03
y5b-1	33	26.5	17.75	27.8	0.52	14.55	0.1	0.27	0.06	87.63
y5b-1	34	26.2	18.31	28.49	0.66	13.59	0	0.12	0.08	87.54
y5b-1	35	26.47	17.91	28.57	0.59	14.39	0.03	0.01	0.01	87.97
y6c-2	89	26.24	17.43	28.39	0.57	13.67	0.09	0	0	86.4
y6c-2	90	26.66	18.25	28.42	0.59	14.55	0.06	0	0	88.63
y6c-2	91	27.29	17.7	28.32	0.59	14.27	0.07	0.21	0.01	88.54
y6b-1	94	25	18.32	30.05	0.61	12.98	0.04	0	0.02	87.08
y6b-1	95	25.74	18.17	28.55	0.51	13.92	1.01	0	0	87.92
y6b-1	96	26.07	17.86	28.68	0.53	14.48	0.03	0.05	0	87.74
y5a-1	139	26.57	17.34	28.26	0.56	14.64	0.11	0.08	0.03	87.65
y3b-1	141	23.93	18.36	34.19	0.77	8.91	0.04	0	0.02	86.31
yL1-2	10	27.68	17.34	21.04	2.07	18.23	0.32	0.18	0	86.94
yo1-2	90	29.4	20.23	12.9	2.3	22.67	0.17	0.14	0.02	87.89
yo1-2	87	28.87	20.12	13.44	2.47	22.63	0.09	0.81	0	88.51
yo1-2	88	28.41	19.72	12.37	2.23	22.69	0.12	0	0	85.6
structural formula and related parameter										
sample	N°.	Si	Al(IV)	Al	Fe	Mn	Mg	Ca	OH	M
y5b-1	32	5.67	2.33	2.32	5.13	0.11	4.41	0.02	16	0.54
y5b-1	33	5.71	2.29	2.22	5.01	0.09	4.67	0.02	16	0.52
y5b-1	34	5.66	2.34	2.33	5.15	0.12	4.38	0	16	0.55
y5b-1	35	5.68	2.32	2.21	5.13	0.11	4.6	0.01	16	0.53
y6c-2	89	5.74	2.26	2.23	5.19	0.11	4.46	0.02	16	0.54
y6c-2	90	5.67	2.33	2.24	5.05	0.11	4.61	0.01	16	0.53
y6c-2	91	5.81	2.19	2.26	5.04	0.11	4.53	0.02	16	0.53
y6b-1	94	5.49	2.51	2.23	5.52	0.11	4.25	0.01	16	0.57
y6b-1	95	5.55	2.45	2.18	5.15	0.09	4.48	0.23	16	0.54
y6b-1	96	5.62	2.38	2.17	5.17	0.1	4.66	0.01	16	0.53
y5a-1	139	5.73	2.27	2.13	5.09	0.1	4.7	0.03	16	0.52
y3b-1	141	5.45	2.55	2.38	6.51	0.15	3.02	0.01	16	0.69
yL1-2	10	5.83	2.17	2.13	3.71	0.37	5.72	0.07	16	0.42
yo1-2	90	5.82	2.18	2.55	2.14	0.39	6.69	0.04	16	0.27
yo1-2	87	5.75	2.25	2.48	2.24	0.42	6.72	0.02	16	0.28
yo1-2	88	5.77	2.23	2.49	2.1	0.38	6.87	0.03	16	0.27
Note: M=(Fe+Mn)/(Fe+Mn+Mg)										

APPENDIX D: Whole rock geochemistry of Yamansu deposit

Table 3-12: Chemical analyses of major (wt%) and trace (ppm) elements for Yamansu magnetite deposit

(cc=limestone; bst=basalt; mgt=magnetite; grt=garnet; sk=skarn; epi=epidote; K=K-feldspar; mbl=marble)

	Al_2O_3	CaO	Fe_2O_3	FeO	K_2O	MgO	MnO	Na_2O	SiO_2	P_2O_5	TiO_2	LOI	Sum
Y205 bst	16.73	6.94	6.88	3.39	0.29	6.33	0.38	5.11	49.31	0.09	1.01	4.66	101.12
Y159 bst	21.2	7.68	5.8	3.72	4.38	4.1	0.55	1.78	46.15	0.09	0.85	4.39	100.69
Y133 altered bst	19.78	17.53	4.27	3.95	0.08	4.16	0.69	1.36	42.72	0.11	0.72	5.43	100.8
Y244BD altered bst	12.28	20.67	5.98	2.09	1.84	2.38	0.1	3.01	40.53	0.06	0.46	11.29	100.69
Y71A white cc	4.55	41.84	1.43	0.24	0.03	0.46	0.05	2.39	17	0.04	0.15	31.91	100.09
Y71B black cc	0.37	54.35	0.29	0.14	0.1	0.4	0.04	0.04	1.15	0.02	0.01	42.89	99.8
Y244BA grey cc	0.64	53.68	0.46	0.31	0.01	0.46	0.06	0.1	2.14	0.02	0.02	41.88	99.78
Y244BB white cc	9.7	26.7	2.86	2.18	3.18	1.79	0.09	1.69	34.77	0.05	0.37	16.91	100.29
Y244BC black cc	8.05	34.85	4.29	1.5	1.09	1.99	0.09	1	25.86	0.05	0.36	21.13	100.26
Y244AD white cc	0.47	54.26	0.34	0.32	0.02	0.58	0.11	0.11	2.43	0.02	0.44	40.9	99.8
Y70 cc	1.62	51.46	0.78	0.1	0.3	0.46	0.02	0.29	4.64	0.02	0.06	40.33	100.08
Y72 cc	9.13	31.19	15.56	4.93	0.04	0.51	0.56	0.35	37.55	0.12	0.38	1.97	102.39
Y194 mbl	0.23	54.25	0.18	0.15	0.02	0.15	0.04	0.1	1.14	0.02	0.01	43.47	99.76
Y135B mgt				27.2									27.24
Y90B mgt	2.06	3.58	68.11	25.2	0.03	1.36	0.11	0.28	8.27	0.02	0.08	-1.6	107.54
Y90A grt sk	7.09	12.34	30.28	18.6	0.04	6.44	0.27	0.39	23.87	0.07	0.23	3.44	103.09
Y102 epi sk	15.3	20.32	8.97	3.64	2.1	3.39	0.34	0.23	42.52	0.11	0.58	3.69	101.19
Y105 grt sk	11.77	10.33	2.22	5.45	3.23	2.39	0.51	2.69	57.39	0.07	0.53	3.72	100.3
Y106 grt sk	7.19	34.37	19.73	1.73	0.01	0.3	0.43	0.09	37.5	0.06	0.44	1.22	103.07
Y113 grt sk	7.74	33.08	19.53	3.69	0.02	0.4	0.58	0.34	37.66	0.05	0.41	-0.28	103.22
Y117 K sk	18.81	4.75	1.9	5.3	10.28	1.21	0.34	0.56	54.39	0.02	0.84	1.91	100.31
Y132 grt sk	7.61	33.55	18.82	1.83	0.05	0.23	0.4	0.07	36.81	0.08	0.35	2.7	102.5
Y172 epi K sk	12.96	15.94	6.92	2.77	3.23	4.01	0.29	0.6	47.91	0.19	1.2	4.98	101
Y196 grt sk	4.72	25.04	30.79	8.27	0.09	1.1	0.47	0.1	32.1	0.07	0.32	1.43	104.5
Y216 grt sk	5.14	24.84	32.4	8.5	0.11	0.72	0.38	0.15	30.46	0.09	0.28	1.72	104.79
Y118 dyke	17.71	4.45	3.76	5.08	8.5	3.69	0.68	0.8	51.79	0.02	0.83	3.21	100.52

continued table 3-12:

	La	Ce	Pr	Nd	Sm	Eu	Gd	Tb	Dy	Ho	Er	Tm	Yb	Lu	Y
Y205 bst	3.37	6.93	1.49	8.92	3.2	1.06	4.3	0.71	4.37	0.98	2.61	0.41	2.52	0.39	22.33
Y159 bst	2.6	5.68	1.12	7.22	2.28	1.13	3.16	0.5	3.08	0.65	1.83	0.28	1.83	0.28	16.72
Y133 altered bst	9.91	14.88	1.89	8.75	1.74	0.7	2.45	0.38	2.37	0.48	1.37	0.21	1.26	0.18	13.29
Y244BD altered bst	1.87	3.22	0.85	4.73	1.55	0.31	1.59	0.26	1.73	0.38	0.99	0.16	0.97	0.16	11.28
Y71A white cc	1.41	0.1	0.25	1.3	0.28	0.08	0.31	0.05	0.4	0.1	0.31	0.05	0.3	0.05	4.71
Y71B black cc	3.16	2.9	0.74	3.28	0.82	0.2	0.9	0.15	1.06	0.24	0.73	0.11	0.6	0.09	9.95
Y244BA grey cc	1.96	2.08	0.5	2.16	0.44	0.09	0.51	0.09	0.54	0.11	0.29	0.04	0.29	0.04	4.13
Y244BB white cc	2.02	2.99	0.77	4.32	1.37	0.3	1.38	0.23	1.52	0.31	0.92	0.14	0.84	0.15	9.86
Y244BC black cc	2.65	4.58	0.92	5.05	1.34	0.28	1.32	0.22	1.46	0.28	0.82	0.12	0.81	0.13	9.63
Y244AD white cc	1.52	1.28	0.39	2.07	0.46	0.07	0.43	0.07	0.48	0.12	0.32	0.05	0.28	0.05	3.98
Y70 cc	1.19	0.38	0.3	1.72	0.35	0.11	0.48	0.08	0.65	0.11	0.36	0.06	0.29	0.06	4.99
Y72 cc	6.73	11.88	2.07	15.63	5.08	1.43	5.03	0.76	4.66	0.86	2.68	0.36	2.16	0.33	28.94
Y194 mbl	0.39	0.1	-	0.26	0.06	0.02	0.07	0.01	0.08	0.03	0.08	0.01	0.1	0.02	1.35
Y135B mgt	4.3	5.15	0.58	1.88	0.13	0.04	0.11	0.02	0.14	0.03	0.11	0.01	0.12	0.02	1.16
Y90B mgt	1.8	3.21	0.78	3.42	0.67	0.23	0.55	0.09	0.48	0.1	0.3	0.05	0.31	0.04	3.51
Y90A grt sk	5.54	15.73	2.59	10.91	2.08	0.8	1.92	0.32	1.78	0.35	1.08	0.15	1.06	0.16	10.77
Y102 epi sk	195.62	286.32	23.81	60.9	3.62	0.79	2.53	0.37	2.43	0.38	1.31	0.16	1.04	0.18	11.92
Y105 grt sk	58.92	127.23	11.99	42.38	4.09	0.78	3.23	0.39	2.24	0.44	1.39	0.2	1.28	0.25	16.46
Y106 grt sk	8.32	23.68	3.58	20.38	4.91	1.78	4.7	0.7	4.03	0.72	2.39	0.3	2.24	0.35	22.72
Y113 grt sk	6.22	17.68	3.09	18.68	5.36	1.92	4.75	0.75	4.58	0.87	2.76	0.37	2.26	0.4	28.28
Y117 K sk	3.15	10.05	1.47	7.18	1.49	0.93	1.64	0.28	1.75	0.41	1.28	0.23	1.6	0.27	10.18
Y132 grt sk	3.96	15.03	3.52	23.73	6.29	2.42	6.15	0.86	5.08	0.95	2.8	0.42	2.37	0.35	32.84
Y172 epi K sk	7.58	18.06	2.56	13.9	4.12	1.95	5.22	0.81	5.22	0.97	2.75	0.43	2.52	0.4	24.81
Y196 grt sk	12.4	21.61	2.54	11.59	3.06	1.83	3.52	0.49	3.4	0.81	2.29	0.37	2.32	0.4	25.32
Y216 grt sk	15.41	34.98	3.81	18.87	3.78	1.4	3.69	0.62	3.25	0.58	1.63	0.22	1.55	0.25	17.22
Y118 dyke	4.07	16.27	2.39	12.37	2.84	1.24	2.77	0.44	2.55	0.51	1.44	0.23	1.66	0.25	12.19

continued table 3-12:

	Li	Be	Sc	Ti	V	Cr	Mn	Co	Ni	Cu	Zn	Ga	Rb	Sr
Y205 bst	56.35	0.39	56.02	6371	356.45	103.19	2760.4	8.07	62.61	13.47	16.57	17.01	8.55	164.49
Y159 bst	112.37	0.41	46.82	5910	336.59	3335	5472	23.66	243.32	113.77	324.04	22.88	192.77	483.07
Y133 altered bst	83.89	0.23	40.91	4939	198.11	133.26	5585	6.85	65.54	26.57	60.8	18.23	3.89	62.39
Y244BD altered bst	12.51	0.57	14.42	2358	64.28	663.26	768.1	11.48	427.41	163.3	221.71	9.8	27.43	461.77
Y71A white cc	7.01	0.04	1.01	87.59	5.32	11.68	387.9	2.29	21.49	3.75	-	0.47	5.45	1034.35
Y71B black cc	0.69	0.17	4.28	782.9	31.46	65.37	394.6	2.69	48.34	13.1	22.86	7.52	1.51	833.1
Y244BA grey cc	3.94	0.04	1.14	131.1	5.68	45.38	490.6	3.43	47.07	8.95	33.3	0.96	1.04	537.81
Y244BB white cc	6.93	0.29	10.41	1932	51.66	254.8	678.7	9.17	236.34	157.84	111.25	7.33	49.21	685.4
Y244BC black cc	7.52	0.2	10.08	1873	51.27	266.65	668.4	7.53	231.75	231.66	71.03	6.91	18.97	473.16
Y244AD white cc	2.43	0.11	1.24	108.8	5.17	42.37	514.2	2.9	39.92	11.19	9.48	0.73	1.03	510
Y70 cc	1.28	0.07	3.62	450.3	21.79	45.5	186.6	7.36	47.96	14.33	25.45	1.78	8.52	1610
Y72 cc	6.26	0.74	12.22	2113	146.93	74.98	4805	33.18	92.18	456.96	35.66	11.76	2.26	20.01
Y194 mbl	0.87	0	0.95	57	3.51	128.03	340.3	3.26	103.19	6.49	-	0.38	0.86	163.52
Y135B mgt	4.92	1.22	1.86	390	23.02	937.94	741.6	15.22	590.28	5899.37	63.1	12.41	3.11	38.3
Y90B mgt	1.79	0.3	2.63	367.7	39.86	67.18	786.3	25.04	62.92	145.68	179.69	7.5	1.86	10.12
Y90A grt sk	7.66	0.35	9.32	1294	68.1	47.1	2336	148.27	75.55	428.06	316.67	14.28	5.13	8.02
Y102 epi sk	7.33	1.01	23.59	3587	37.72	46.28	2945	12.24	36.76	26.47	78.99	20.41	48.95	386.61
Y105 grt sk	7.67	1.68	18.1	2905	116.63	37.05	3665	4.41	22.79	9.99	14.86	18.67	75.88	128.81
Y106 grt sk	1.24	0.1	10.17	2058	129.37	206.22	2971	6.39	137.13	19.75	57.82	8.88	2.22	12.97
Y113 grt sk	2.53	0.4	13.8	2453	158.65	186.47	5576	127.46	220.79	953.58	1533.69	11.45	1.5	12.6
Y117 K sk	25.52	1.16	16.08	5060	98.24	123.43	2658	8.4	69.49	50.07	924.67	13.69	191.18	402.57
Y132 grt sk	5.77	0.01	12.79	2423	131.09	514.96	3778	4.47	276.87	20.83	134.59	13.34	3.35	16.87
Y172 epi K sk	6.8	0.83	50.79	8708	381.91	105.81	2309	6.6	66.93	19.62	23.6	22.93	71.26	1148
Y196 grt sk	2.7	0.36	10.08	1779	91.82	55.03	3752.9	23.77	43.84	81.25	24.71	11.96	5.73	16.91
Y216 grt sk	3.51	0.57	6.61	1280	107.32	193.25	3070.9	30.83	165.46	486.7	32.6	10.84	13.88	31.03
Y118 dyke	53.6	1.1	26.68	4997	158.41	183.26	5509	5.8	107.82	29.19	319.85	15.52	188.44	691.24

continued table 3-12:

	Zr	Nb	Mo	Cd	Sn	Cs	Ba	Hf	Ta	W	Pb	Bi	Th	U
Y205 bst	68.82	2.08	7.09	0.04	1.68	0.88	46.26	2.56	0.22	3.82	1.88	0.11	1.59	0.91
Y159 bst	27.04	1.22	328.19	0.78	4.24	9.3	1570	1.1	0.09	14.41	4.98	0.16	0.32	0.44
Y133 altered bst	23.15	0.86	5.68	0	1.13	0.74	73.03	0.84	0.11	3.91	42.02	0.09	0.39	1.08
Y244BD altered bst	68.2	2.5	67.49	0.22	0.82	0.73	227.36	2.24	0.21	2.52	5.65	0.38	2.72	5.69
Y71A white cc	2.5	0.23	2.39	0.07	-	0.54	7.71	0.05	0.03	0.33	1.04	0.01	0.14	0.98
Y71B black cc	15.89	0.86	7.82	0.12	0.21	0.2	7.2	0.53	0.07	1.05	5.89	0.07	0.88	4.67
Y244BA grey cc	3.99	0.23	112.8	0.29	-	0.07	8.49	0.11	0.02	0.37	1.57	0.07	0.28	1.91
Y244BB white cc	53.1	2.21	53.15	0.43	0.92	0.9	391.63	1.85	0.17	3.24	5.88	0.46	2.1	5.73
Y244BC black cc	55.55	1.8	35	0.12	0.63	0.46	145.85	1.84	0.17	1.44	5.14	0.41	2.18	5.74
Y244AD white cc	3.49	0.12	5.18	-	-	0.16	6.87	0.08	0.03	0.26	0.92	0.04	0.21	0.99
Y70 cc	7.3	0.55	5.45	0.23	0.33	0.34	40.09	0.27	0.05	0.88	4.79	0.07	0.44	2.6
Y72 cc	42.9	3.24	10.68	0.09	3.61	0.22	9.26	1.55	0.14	2.29	21.33	0.26	0.69	4.12
Y194 mbl	1.01	0.31	18.31	0.09	-	0.05	6.95	0.02	0.03	1.25	0.79	0.04	0.09	0.09
Y135B mgt	2.81	0.8	224.36	0.85	1.69	0.4	50.9	0.07	0.09	223.68	7.16	0.27	0.33	1.75
Y90B mgt	12.33	0.43	6.48	0.7	0.75	2.19	3.46	0.44	0.07	1.88	47.95	0.12	0.51	2.19
Y90A grt sk	46.18	1.59	5.34	2.08	2.32	2.57	4.16	1.6	0.19	5.59	61.07	0.3	1.81	8.38
Y102 epi sk	134.58	3.25	3.98	0.13	2.25	0.46	660.55	4.23	0.48	2.98	27	0.3	8.56	5.99
Y105 grt sk	61.13	2.26	3.75	0.03	1.55	0.86	299	2.01	0.17	2.17	2.4	0.07	3.95	2.38
Y106 grt sk	52.83	2.48	18.83	0.26	4.96	0.07	14.33	1.92	0.17	7.81	20.76	0.05	1.3	9.07
Y113 grt sk	55.13	3.09	26.93	8.06	5.46	0.2	7.89	1.85	0.17	9.37	1486.96	0.67	1.09	10.42
Y117 K sk	155.22	6.95	13.42	2.78	1.2	2.75	4109	4.86	0.63	2.98	22.46	0.13	6.85	2.6
Y132 grt sk	47.28	2.66	46.26	0.31	6.57	0.69	33.88	1.31	0.22	6.32	244.36	0.07	0.94	7.4
Y172 epi K sk	52.59	1.5	12.87	0.05	2.34	0.36	282.31	1.9	0.17	2.73	5.48	0.25	0.62	0.57
Y196 grt sk	26.09	1.94	16.8	0.04	5.3	5.83	22.01	1.03	0.13	16.11	4.09	0.07	1.4	8.11
Y216 grt sk	37.34	2.2	24.26	0.06	3.52	7.28	102.39	0.99	0.64	8.89	11.47	0.13	2.74	6.84
Y118 dyke	154.02	6.29	19.9	0.37	1.38	3.12	5964	4.87	11.34	3.84	5.06	0.15	7.38	2.28

Table 3-13: Rock major compositions with densities for mass balance calculation.

				Δmi (g)	
	basalt Y205	basalt Y159	skarn Y102	Y205 to Y102	Y159 to Y102
SiO_2	49.31	46.15	42.52	-1.90	-0.55
TiO_2	1.01	0.85	0.58	-0.36	-0.23
Al_2O_3	16.73	21.20	15.30	0.33	-4.79
MgO	6.33	4.10	3.39	-2.55	-0.46
CaO	6.94	7.68	20.32	15.72	14.11
Fe_2O_3	6.19	5.22	8.07	2.81	3.43
FeO	3.39	3.72	3.64	0.67	0.18
MnO	0.38	0.55	0.34	0.00	-0.19
P_2O_5	0.09	0.09	0.11	0.03	0.03
Na_2O	5.11	1.78	0.23	-4.85	-1.53
K2O	0.29	4.38	2.10	2.05	-2.13
LOI	4.66	4.39	3.69	-0.55	-0.43
∑	100.43	100.11	100.29		
ρ (g/cm^3)	2.85	2.82	3.36		
f_V				0.947	0.9

In the volume of gain and loss, compare to the original (basalt), positive value means gain, whereas negative value means loss.

APPENDIX E: Isotope composition

[carbon and oxygen in carbonates of marbles, calciphyres, skarns and products of their endogenetic and hypergenetic alteration (Aleksandrov 1998)]

	region	$\delta^{13}C‰$	$\delta^{18}O‰$	specimen No.
sedimentary carbonate rocks				
Primary sedimentary carbonates		+1 to -1	30-25	
marbleized carbonate rocks				
Dolomite marble	Yalrutia	+1.5	29.2	V-01516
-1.5 20.3 YCh-0212	Chukotka	-1.5	20.3	Cch-0212
Reactive Carbonates of Marbles and calciphyres				
Forsterite-carbonate rhythms	Transbaikal	+0.5	18.7	ZBK-0103
Forsterite calciphyre	Yakutia	-0.9	20.1	V-01363
Periclase marble	Ditto	-1.2	19.2	V-096
Forsterite calciphyre	Ditto	-1.3	17.7	V-0621
Forsterite-carbonate rhythms	Ditto	-1.5	16	V-01459
	Ditto	-1.6	20.2	V-0706
Forsterite calciphyre	Ditto	-2.5	21.6	V-098
	Ditto	-2.6	22.6	V-0245
Fnrsterite-carbonate rhythms	Scotland	-3.0	22.6	Sh-033
Forsterite Calciphyre	Yakutia	-3.0	20.1	V-0707
	Ditto	-3.8	26.3	E-456/1
Dolomite marble	Scotland	-3.9	18	Sh-033
Forsterite calciphyre	Yakutia	-4.0	19	V-01327
Monticellite calciphyre	Ditto	-5.1	22.4	V-0708
Forstente calciphyre	Ditto	-5.1	20.8	V-01566
Surplus carbonates of skarns				
Calclc-diopstde skarn	Yakutia	-9.6	12.9	V-01755
Carbonatoborates				
New formations of Carbonates of Late Alkaline stage and zone of hypergenesis				
Calclphyre with szaibelyite	Yakutia	-11.1	11.6	V-01345
Calclphyre with vonsenite	Ditto	-8.7	10.3	V-01566
Altered sakhaite	Ditto	-8.4	10.2	V-01500
	Ditto	-8.1	11.7	V-0709
Calciphyre with serpentine	Ditto	-7.6	10.9	V-0284
	Ditto	-7.5	14.1	V-01755
Calciphyre with ludwigite	Ditto	-7.4	9.8	V-0292
Calciphyre with paigeite	Ditto	-6.2	10.1	V-01500
Calciphyre with skarnoid	Ditto	-6.2	12.9	V-0309
Brucitized periclase marble	Chukotka	-6.0	10.4	VCh-0284
	Ditto	-5.9	7.7	VCh-0288
Modified sakhaite	Yakutia	-5.8	15.3	V-01055

continued appendix E:

Calciphyre with serpentine	Ditto	-5.8	14.1	V-01755
Carbonatized szaibelyite	Ditto	-5.7	11.2	V-0104
Calciphyre with vonsenite	Ditto	-5.6	11.3	V-0257
Coarse grained calcite	Chukotka	-5.5	11.6	VCh-0284
Marble with amphibole	Yakutia	-5.5	12	V-01354
Marble with chlorite	Ditto	-5.3	7	V-01354
Marble with szaibelyite	North Korea	-4.7	10.3	TN-01
Carbonatized brucite	Chukotka	-4.3	9.6	VCh-0288
Marble with szaibelyite	Romania	-4.1	7.9	R-025
Late veined carbonate	North Korea	-4	10	Kht-030
Marble with chlorite	Scothland	-4	10.5	ShG-01
Late carbonate	Yakutia	-3.8	13.3	V-0983
Carbonate with serpentine	Ditto	-3.6	6.5	V-0295
Calciphyre with serpentine	Ditto	-3.6	6.6	V-0295
	Scothland	-3.4	17.8	Sh-033
	Yakutia	-3.2	7.5	V-0629
Late calcite	Ditto	-2.2	12.2	V-01516
Marble with paigeite	Alaska	-2.1	11.6	As-01200
Altered borcarite	Yakutia	-1.3	13.8	V-0569
Altered sakhaite	Ditto	-1	13.7	V-01451

APPENDIX F:

Table 3-14: K-feldspar Ar-Ar dating result

	Sample 19g						
Tempera-ture	^{36}Ar	^{37}Ar	^{38}Ar	^{39}Ar	^{40}Ar	Age(Ma)	fraction ^{39}Ar
600	0.01305	0.00008	0.00325	0.05853	4.63655	157.791	0.013826
700	0.00623	0.00019	0.00479	0.28199	6.44065	216.9369	0.066614
800	0.0046	0.00033	0.00511	0.33068	6.93565	225.1254	0.078116
850	0.00371	0.00022	0.00487	0.32449	6.62079	227.5346	0.076654
900	0.00296	0.00021	0.00466	0.3209	6.38923	229.8869	0.075806
950	0.00214	0.00017	0.0044	0.31237	6.07079	233.1417	0.073791
1000	0.00151	0.00018	0.00418	0.30449	5.78814	235.1171	0.071929
1030	0.00153	0.00018	0.00497	0.36092	6.78373	235.1737	0.085259
1070	0.00117	0.00017	0.00347	0.2514	4.76938	235.8466	0.059388
1100	0.00162	0.00019	0.00456	0.32707	6.23108	235.7045	0.077263
1150	0.00169	0.00016	0.00442	0.31548	6.05321	235.891	0.074525
1200	0.00182	0.00014	0.00433	0.30683	5.92723	235.306	0.072482
1300	0.00182	0.00008	0.00375	0.26047	5.15588	237.4201	0.06153
1400	0.00394	0.00015	0.00499	0.32093	6.82769	235.8038	0.075813
1500	0.00699	0.00006	0.00341	0.15665	4.84954	234.4052	0.037005

Sample y247

Temperature	^{36}Ar	^{37}Ar	^{38}Ar	^{39}Ar	^{40}Ar	Age(Ma)	fraction ^{39}Ar
600	0.00423	0.00002	0.00121	0.02042	1.59961	214.6892	0.014274
700	0.00721	0.00065	0.00315	0.12148	4.25156	230.0913	0.084919
800	0.00554	0.00049	0.00307	0.14748	4.19558	230.197	0.103094
850	0.00571	0.00053	0.00361	0.18617	4.93509	232.008	0.13014
900	0.00426	0.00031	0.00316	0.1703	4.24975	234.0006	0.119046
950	0.00358	0.00018	0.00304	0.16977	4.07043	236.7359	0.118675
1000	0.00449	0.00016	0.00371	0.19823	4.90471	240.7097	0.13857
1030	0.00469	0.00012	0.00315	0.15044	4.14961	244.4005	0.105163
1070	0.00455	0.00009	0.00253	0.09336	3.11044	250.4165	0.065262
1100	0.00325	0.00002	0.00158	0.04979	1.9284	256.277	0.034805
1150	0.00354	0.00004	0.00146	0.03245	1.70151	263.2086	0.022684
1200	0.00354	0.00004	0.00146	0.03245	1.70151	263.2086	0.022684
1300	0.00355	0.00002	0.0015	0.03226	1.72311	272.4972	0.022551
1400	0.00266	0.00003	0.00099	0.01743	1.1373	259.3981	0.012184
1500	0.0042	0.00002	0.00105	0.00851	1.42845	259.315	0.005949

Sample 19L

Temperature	^{36}Ar	^{37}Ar	^{38}Ar	^{39}Ar	^{40}Ar	Age(Ma)	fraction ^{39}Ar
600	0.0054	0.00005	0.00218	0.08049	2.85514	204.164	0.018851
700	0.0035	0.00015	0.00489	0.32166	6.53878	228.8357	0.075335
800	0.00176	0.00015	0.00447	0.31252	6.02894	236.2086	0.073194
850	0.00128	0.00016	0.00385	0.26963	5.17013	238.2325	0.063149
900	0.00109	0.00012	0.00403	0.28907	5.52512	241.3687	0.067702
950	0.00137	0.00017	0.00529	0.377	7.23761	243.0578	0.088296
1000	0.00117	0.00012	0.00423	0.29697	5.77652	245.2229	0.069552
1030	0.00125	0.00018	0.0042	0.28865	5.67976	246.6653	0.067604
1070	0.00127	0.00016	0.00392	0.26982	5.38061	248.6904	0.063194
1100	0.00144	0.00021	0.0046	0.31498	6.30472	250.2427	0.07377
1150	0.00157	0.00008	0.00491	0.33906	6.81296	251.044	0.07941
1200	0.00159	0.00015	0.00494	0.33861	6.86124	253.0527	0.079305
1300	0.00124	0.00013	0.00382	0.25811	5.27151	254.7685	0.060451
1400	0.00129	0.0001	0.00349	0.23429	4.83285	254.6624	0.054872
1500	0.0026	0.00013	0.0043	0.27887	6.05225	253.6132	0.065313

Sample y153

Temperature	^{36}Ar	^{37}Ar	^{38}Ar	^{39}Ar	^{40}Ar	Age(Ma)	fraction ^{39}Ar
600	0.00646	0.00004	0.00266	0.1092	3.35226	172.2386	0.025064
700	0.00229	0.00013	0.00418	0.29193	5.73489	231.9771	0.067006
750	0.00168	0.00016	0.00457	0.33169	6.41062	238.9878	0.076132
800	0.00106	0.00009	0.00353	0.25637	4.96886	243.4933	0.058844
850	0.00125	0.00013	0.00476	0.34854	6.72506	244.5539	0.079999
900	0.00093	0.00015	0.00413	0.30397	5.87372	247.0729	0.069769
950	0.00104	0.00017	0.00499	0.3642	7.0279	247.5439	0.083594
1000	0.00084	0.00015	0.00389	0.28005	5.42237	247.8375	0.064279
1030	0.00092	0.00014	0.00398	0.28113	5.45766	247.4166	0.064527
1070	0.00141	0.00018	0.00536	0.3868	7.51244	246.0215	0.088781
1100	0.00092	0.0001	0.00337	0.23888	4.67005	246.9012	0.054829
1150	0.00097	0.00015	0.00343	0.23992	4.70112	246.7244	0.055068
1200	0.00102	0.00016	0.00356	0.25175	4.94453	247.3086	0.057784
1300	0.00131	0.00017	0.00391	0.27469	5.43922	246.5558	0.063049
1400	0.00135	0.00007	0.00326	0.22328	4.50119	246.1829	0.051249
1500	0.00227	0.00011	0.00282	0.17438	3.86782	245.0403	0.040025

Guangrong LI

Gisements de fer dans la ceinture orogénique de l'Est Tianshan (Chine): l'Association magnétite-skarn-magmatisme

Résumé :

L'objectif de cette thèse est l'étude de l'association magnétite-skarn-magmatisme. Dans ce but, deux gisements de magnétite (Yamansu et Cihai) ont été sélectionnés dans l'Est du Tianshan (NW Chine). Dans les deux gisements, l'assemblage grenat-pyroxène-magnétite a été reconnu, mais les mécanismes de formation de la minéralisation y sont différents. Cet assemblage a ensuite été altéré par un stade hydrothermal. Les études minéralogiques et géochimiques ainsi que les zonations observées suggèrent, que dans le gisement de Yamansu (YMD), le skarn et la minéralisation sont liés à la circulation d'un fluide riche en fer; alors que pour le gisement de Cihai (CMD), la mise en place du minerai est probablement associée à un magmatisme mafique/ultramafique. A YMD, selon l'anisotropie de la susceptibilité magnétique (AMS) et une étude paléomagnétique, le basalte et le skarn massif à grenat, tout deux encaissant les corps à magnétite massive, étaient en position horizontale lors de leur formation. L'attitude actuelle de ce gisement serait donc due à la phase tectonique majeure. La magnétite dans CMD présente les caractéristiques d'une magnetite magmatique, plutôt qu'hydrothermale. Dans ce gisement, la contamination du magma par des formations sédimentaires a pu contribuer à séparer efficacement un liquide riche en oxyde de fer d'un bain silicaté.

Mots clés : skarn, magnétite, magma mafique/ultramafique, AMS, paléomagnétisme, Tianshan Est

Iron Ore Deposits in the Eastern Tianshan Orogenic Belt (China): the Magnetite-Skarn-Magmatism Association

Abstract:

The aim of this thesis was to investigate the magnetite-skarn-magmatism association, of which two study objects (Yamansu and Cihai magnetite deposits) were selected from eastern Tianshan, China. Both of the Yamansu and Cihai magnetite deposit illustrate garnet-pyroxene-magnetite assemblage in prograde stage and hydrothermal assemblage in retrograde stage which essentially defined as skarn-related deposit, but with different forming mechanisms. Yamansu magnetite deposit (YMD) is a typical metasomatic skarn deposit confirmed by the mineral assemblage and chemical composition, zonation etc., whereas to Cihai magnetite deposit (CMD) probably associated to sedimentary assimilation into mafic/ultramafic magma and fractionation. According to anisotropy of magnetic susceptibility (AMS) and paleomagnetic study, the basalt and the massive garnet skarn which clamp massive magnetite ore bodies were coincidently horizontal in YMD. In addition, it was the Fe-rich fluid caused extensive skarnization in YMD. The magnetite in CMD is magmatic origin, rather than hydrothermal according to mineralogy and geochemical study. External material contamination of the mafic/ultramafic magma probably efficiently separated the magnetite and silicate at the peripheral part of the large mafic/ultramafic pluton in high temperature.

Keywords : skarn, magnetite, mafic/ultramafic magma, AMS, paleomagnetism, eastern Tianshan

OSUC-CNRS (UMR 6113)
45071, Orléans, France
Nanjing University
Nanjing city,210093, China